ULTRA-HIGH-PERFORMANCE CONCRETE AND ADVANCED MANUFACTURING METHODS FOR MODULAR CONSTRUCTION

By

Jamshaid Sawab, Ing Lim, Y.L. Mo and Mo Li

University of Houston

Hong Wang

Oak Ridge National Laboratory

Maria Guimaraes

Electric Power Research Institute

Project FY-ID 13-5282

Project Title: Ultra-High Performance Concrete & Advanced Manufacturing Methods for Modular Construction

Performed in cooperation with the Department of Energy

April 2016

Department of Civil and Environmental Engineering

University of Houston

Houston, Texas

DISCLAIMER

This research was performed in cooperation with the Department of Energy, Oak Ridge National Laboratory and Electric Power Research Institute. The contents of this report reflect the views of the authors, who are responsible for the facts and accuracy of the data presented herein. The contents do not necessarily reflect the official view or policies of the DOE. This report does not constitute a standard, specification or regulation, nor is it intended for construction, bidding or permit purposes. Trade names were used solely for information and not product endorsement.

ACKNOWLEDGEMENTS

This research, Project No. 13-5282, was conducted in cooperation with the Department of Energy, Oak Ridge National Laboratory and Electric Power Research Institute. Alison Hahn Krager (Federal Manager) and Jack Lance (Technical POC) served as the project monitoring committee.

ABSTRACT

Small modular reactors (SMR) allow for less onsite construction, increase nuclear material security, and provide a flexible and cost-effective energy alternative. SMR can be factory-built as modular components, and shipped to desired locations for fast assembly. This project successfully developed a new class of ultra-high performance concrete (UHPC), which features a compressive strength greater than 22 ksi (150 MPa) without special treatment and self-consolidating characteristics desired for SMR modular construction. With an ultra-high strength and dense microstructure, it will facilitate rapid construction of steel plate-concrete (SC) beams and walls with thinner and lighter modules, and can withstand harsh environments and mechanical loads anticipated during the service life of nuclear power plants. In addition, the self-consolidating characteristics are crucial for the fast construction and assembly of SC modules with reduced labor costs and improved quality.

Following the UHPC material development, the capacity of producing self-consolidating UHPC in mass quantities was investigated and compared to accepted self-consolidating concrete standards. With slightly adjusted mixing procedure using large-scale gravity-based mixers (compared with small-scale force-based mixer), the self-consolidating UHPC has been successfully processed at six cubic yards; the product met both minimum compressive strength requirements and self-consolidating concrete standards. Steel plate-UHPC beams (15 ft. long, 12 in. wide and 16 in. deep) and wall panels (40 in. X 40 in. X 3 in.) were then constructed using the self-consolidating UHPC without any external vibration. Quality control guidelines for producing UHPC in large scale were developed.

When the concrete is replaced by UHPC in a steel plate concrete (SC) beam, it is critical to evaluate its structural behavior with both flexure and shear-governed failure modes. In recent years, SC has

been widely used for buildings and nuclear containment structures to resist lateral forces induced by severe earthquakes and heavy winds. SC modules have good potential for SMR because of their cost-effectiveness and reduced construction time. However, the minimum shear reinforcement (i.e. cross tie) ratio needs to be determined for the steel plate-UHPC (S-UHPC) beams to exhibit a ductile failure mode. In this project, S-UHPC beams were designed and constructed. The beams were tested to evaluate structural capacity and identify the minimum cross ties ratios. In addition, as the bond between UHPC and steel plate is essential for ensuring structural integrity under shear and flexure, it was measured and examined in this project through digital image correlation system and smart piezoelectric aggregate sensors. Large-scale testing and finite element simulation were also performed on S-UHPC wall panels. New bond slip-based constitutive models of steel plate were developed for S-UHPC, which were used in finite element analysis program to predict S-UHPC behavior under shear. The results were well validated through experimental data.

The long-term durability of UHPC were established in this project. UHPC specimens were tested under free shrinkage, restrained shrinkage, elevated temperature, water permeation, chloride diffusion, corrosion, and alkali silica reaction. UHPC has demonstrated significantly improved durability compared with control concrete specimens.

This research led to a new generation of steel plate-UHPC modules for SMR that can provide large benefits to the electric power industry. Taking advantage of the high strength and durability of UHPC, their modularity and ease of assembly can address the high cost barriers of typical nuclear power plants.

TABLE OF CONTENTS

List of Figures

List of Tables

1. Introduction

1.1. Significance of Research

Research on high performance concrete (HPC) with compressive strength higher than 100MPa has been carried out over the past several decades. However, their direct application in Nuclear Power Plants (NPP) construction does not yet exist. First, attaining compressive strengths over 150MPa without special treatment such as high pressure curing, heat curing and extensive vibration, has been nearly out of reach. Second, lack of standardized processing and quality control methods to produce robust HPC materials in large quantities has limited its factory prefabrication application. Finally, there is no long-term durability data of HPC in typical nuclear power plant environment, especially under shrinkage, alkali silica reaction, elevated temperature, chemical attack, and corrosion effects. This research fills in these knowledge gaps. For the first time, a new class of ultra-high performance concrete (UHPC) materials has been developed based on a systematic approach specifically for small modular reactor (SMR) construction. The approach integrates micromechanics theory, design of experiments, hydration chemistry, and rheology tailoring methods as well as time-dependent computed micro-tomography (Micro-CT) that can characterize material 3D microstructure formation and degradation. The newly developed UHPC possess a compressive strength exceeding 150MPa (22ksi) without special heat and pressure treatment, by using a conventional concrete mixer and ingredients commercially available in the U.S. Accelerated durability testing was conducted on multi-scales to understand UHPC long-term behavior in the SMR environment. Furthermore, to bridge the gap between laboratory development and construction application, quality control methods were developed to ensure robust production of UHPC modules in mass quantities.

SMR is “where the most innovation is going on in nuclear energy” and “a very promising direction that we need to pursue,” said U.S. Energy Secretary Ernest Moniz in April. SMRs allow for less onsite construction, increase nuclear material security, and provide a flexible and cost-effective energy alternative. Steel plate and concrete (SC) structures have been employed in new nuclear power plants, such as the AP1000. SC modules have a good potential for SMR because of their cost-effectiveness and reduced construction time. This research led to the development of new steel plate-UHPC modules for SMR that can provide large benefits to the electric power industry. Their modularity and ease of assembly addresses the high cost barriers of typical nuclear power plants. The SMR can be factory-built as modular components, then shipped to the desired locations for assembly. The UHPC provides high potential for SMR design to generate maximum power output with the least amount of steel and concrete, taking advantage of the high strength and durability of UHPC that were accomplished in this project. As a result, the SMR design and construction with optimized efficiency, compactness and reduced costs can be achieved.

1.1.Scope of the Research

This report is divided into six chapters. The logical path of the project is shown in Figure 1.

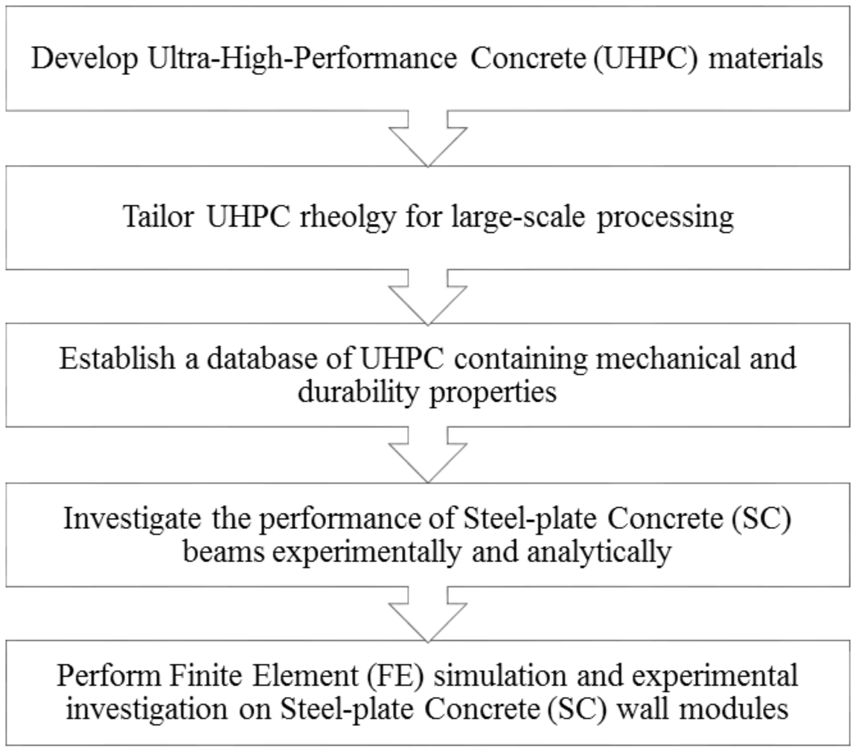

Figure 1. Logical path of the research

Chapter 1 introduces the significance and objectives of the research, and presents the roadmap of the report.

Chapter 2 describes the material development of UHPC integrating ultra-high compressive strength with self-consolidating properties.

Chapter 3 describes the long-term behavior of UHPC under hostile environments based on accelerated durability tests.

Chapter 4 presents a literature study of the past relevant work related to Steel-plate Concrete (SC) structural system. It describes the understanding of steel-plate UHPC (S-UHPC) behavior under out-of-plane shear, based on large-scale experiments and finite element simulation.

Chapter 5 presents the experimental program conducted to understand the in-plane shear behavior of Steel-plate S-UHPC wall panels, using the Universal Panel Tester at the University of Houston. It also describes the development of a new analytical model to predict the structural behavior of S-UHPC wall panel, which were validated with the experimental data.

Chapter 6 presents major conclusions.

2. DEVELOPMENT OF SELF-CONSOLIDATING ULTRA-HIGH PERFORMANCE CONCRETE

2.1. Introduction

There is more than a three-decade history of studies on High Performance Concrete (HPC). In its early development, high performance concrete was defined as a type of concrete that is self-compactable during its fresh stage, has no initial defects during its early age and has protection against external factors after hardening [1]. This highly flowable concrete with low yield stress is capable of flowing into congested reinforcements without external vibration. Researchers later on adopted the term "self-compacting high performance concrete" that is well-known as "self-compacting concrete" or 'self-consolidating concrete" (SCC) [2, 3] Other definitions of high performance concrete include high strength and high durability. ACI defines high performance concrete as a concrete which meets a specific combination of performance and uniformity requirements that cannot always be achieved routinely using conventional constituents and normal mixing, placing and curing practices. This definition includes a series of concrete products that are designed to have specific desired characteristics such as high workability, high early strength, high toughness and high durability to exposure conditions [4, 5].

Further attempts to achieve very high compressive strengths and durability brought in UHPC [6]. The basic principle to gain the ultra-high strength was by increasing the packing density, decreasing the voids in the mixture. Compressive strength of cementitious material is governed by matrix initial porosity; thus minimal voids would result in maximum strength [7]. In general, UHPC contains Portland cement, fine sand, ground quartz, high-range water reducer, water and other concrete admixtures. Micro scale aggregate is used as micro filler along with silica fume for pore size minimization. Low water-to-binder ratio is required to achieve high strength in accordance with Abram's law [8-10].

However, in order to increase the compressive strength, modulus of elasticity, abrasion resistance and other properties, existing techniques require the use of special mixing procedures such as the vacuum mixing process [11, 12], and special curing methods such as hot temperature steam and pressure curing with different timings and temperatures [13]. These unconventional methods have limited the use of UHPCs in practical construction. By incorporating a different blend of ingredients, a new class of UHPC was created without special heat and pressure treatment [14, 15]. Ultra-high performance fiber reinforced concrete (UHPFRC) was also developed without steam curing, which showed improved ductility and energy absorption capacity [16, 17].

Another property desired besides ultra-high strength is the self-consolidating property in concrete, which was achieved by using High-Range Water Reducers (HRWR) or superplasticizer [18, 19] as well as proper aggregate, sand and powder proportion [20, 21], which leads to reduction in both yield stress and plastic viscosity of the paste. This results in high flowability and deformability. Low viscosity and yield stress leads to increased potential of segregation that can be mitigated by adding mineral admixtures such as silica fume, ground-granulated blast furnace slag or fly ash [22]. A viscosity modifying agent was also used in SCC to prevent segregation from bringing viscosity back to an optimum level [23].

After analyzing the previous research work, the constituent materials and preliminary mixture proportions for UHPC were selected. The objective was to achieve dense packing density by determining the particle size distribution and the combined amount of water and chemical admixtures. Furthermore, through ingredient proportioning and chemical admixtures, the yield stress and plastic viscosity of UHPC during its fresh state was to be tailored so that a self-consolidating property could be achieved. Self-consolidating properties were determined using standardized tests.

2.2.Constituent Materials for UHPC

Materials used in the study for development of UHPC are introduced below.

2.2.1. Cement

Tricalcium silicate (C_3S) and dicalcium silicate (C_2S) are the most important compounds in cement and are responsible for strength. Together they constitute 70-80 percent of cement. The amount of C_3S for developing UHPC in this study is more than 61%. Higher values of C_3S in the range of 67.23 and 74% have been used by Larrard and Wille et al., respectively [15, 24]. Although the higher amount of C_3S resulted in higher compressive strength, its availability in the United States market is very limited. We used the types of cement that were easily available in the U.S market.

Blaine fineness is another factor that was considered while selecting the type of cement. Higher fineness means a larger surface area and thus the requirement of more water by the cement which may reduce the rheology of the mixture. Higher cement particle fineness will also lead to fast setting and higher early-age hydration. An average fineness of $400 m^2/kg$ or less is thus used in this study.

A lower amount of tricalcium aluminate (C_3A) resulted in a higher spread value due to its slower reaction with water. C_3A content in the range of 3-7% resulted in a higher spread value without affecting the compressive strength. The lower the amount of C_3A, the higher will be the spread value. Although the C_3A amount as low as 0% could result in a higher spread value as in the case of class-H cement, it may be accompanied by a lower C_3A and C_2A amount which will result in reduced compressive strength.

Two types of cement that could be easily found in the U.S. market are mainly used for the mixtures: Type I Ordinary Portland Cement and Class-H oil well cement. Class-H Oil well cement was used in the mixtures to examine the effect of a lower C_3A content and a lower Blaine fineness. The important chemical and physical properties of Type I Portland cement and Class-H cement are summarized in Table 1.

Table 1. Specifications for type I Portland cement and Class-H cement

Specification/Type	Portland cement type-I	Class-H oil well cement
C_3S	61	56
C_2S	12	18
C_3A	6	0
C_4AF	12	-
$C_4AF + 2(C_3A)$	-	18
$C_3S + 4.75(C_3A)$	90	-
Blaine fineness (cm^2/g)	394	265
SiO_2 %	20.3	21.3
Al_2O_3 %	4.7	3.3
Fe_2O_3 %	3.9	5.9
CaO %	64	63.3

Class-H cement resulted in a better rheology due to its very low C_3A content (0%) as compared to Type I Portland cement, which has 6% C_3A. On the other hand, Type I Portland cement resulted in a higher compressive strength because of its higher C_3S amount. The test results can be compared in mixture 22 and 30 of Table 4 for Type I Portland cement and Class-H cement, respectively. Type-I Portland cement resulted in a compressive strength of 22ksi and thus was selected for further study.

2.2.2. Silica Fume

Silica fume, also known as microsilica, is a by-product of silicon metal or ferrosilicon alloys production. Silica fume on average has more than 85% SiO_2 and therefore it is a very reactive pozzolan. The particle size of silica fume is very small, approximately 1/100th the size of a cement particle. Silica fume has been found in this study to be the most effective addition in terms of development of very high strength concrete. As ultra-fine particles, silica fume physically functions as filler, and its pozzolanic reaction chemically improves the packing density of the matrix. It also reduces the segregation or bleeding tendency that is caused by the use of a large quantity of superplasticizer.

The effect of silica fume can be explained by its reaction with calcium hydroxide released from the hydration of cement and its filling effect in the voids among the other ingredient particles. This will improve the transition zone between the cement and other ingredients and thus will result in decreased porosity and refinement of capillary pores in the UHPC matrix. Therefore, adding silica fume in the concrete mixture also increases the durability of the matrix. Previous research has found the optimum proportion of silica fume to be 20-25% by weight of cement [24].

Three types of silica fume were used in the mixtures:

1) Densified silica fume (DSF)
2) Undensified silica fume (USF)
3) White silica fume (WSF)

Although densified and undensified silica fume have the same chemical properties, undensified silica fume resulted in a better rheology due to the requirement of lesser shear energy to break down the silica fume agglomerates during mixing. The specifications of gray silica fume (densified and undensified) and white silica fume are presented in Table 2. The densified white silica fume may improve the flowability of the mixture as compared to densified gray silica fume, due to a smaller surface area and lower levels of carbon.

Table 2. Summary of specifications for different types of silica fume

	USF	DSF	WSF
Color	Light to medium gray	Light to medium gray	Off white to white
Solubility in Water	Insoluble	Insoluble	Insoluble
Bulk Density	128-769 kg/m^3	-	400 – 700 kg/m^3
Carbon (C)	< 6%	1.75-2.25%	$\leq$ 0.20 %
Iron Oxide (Fe_2O_3)	< 2 %	1-1.5%	$\leq$ 0.25 %
Aluminum Oxide (Al_2O_3)	< 2 %	0.5-1.5%	-
Sodium Oxide (Na_2O)	< 2 %	-	-
Melting Point	1200 C – 1300 C	-	1200 C – 1300 C
Specific Gravity	2.2 – 2.50	2.3	2.2 g/cm^3
Specific surface area	-	22-30 m^2/g	20 m^2/g
Particle Size	Approx. 0.4 µm	0.02-0.09 µm	-
Silicon Dioxide (SiO_2)	> 85%	90-96%	96.0 – 99.0 %
Potassium Oxide (K^2O)	< 2%	-	-
Magnesium Oxide (MgO)	< 2%	-	-
Calcium Oxide (CaO)	< 2%	0.2-1.5%	-

A comparison between the two types of grey silica fume is given in Figure 2 and Figure 3. The images were obtained through scanning electron microscopy (SEM). This comparison provides physical explanation of the particle size distribution theory that will be discussed in section 2.4.1. DSF with a strong bond between particles that was introduced during the designed agglomeration process behaves as micron-scale particles, while USF behaves as separate nanoparticles with a size smaller by an order of magnitude compared with DSF.

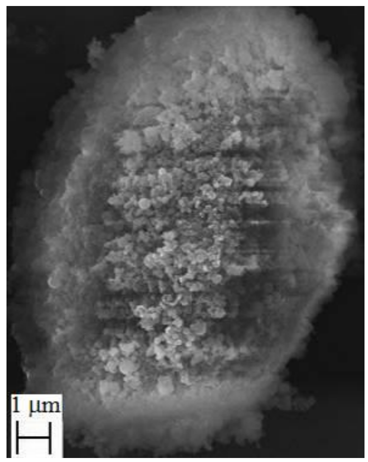

Figure 2. SEM image of one grain of densified silica fume

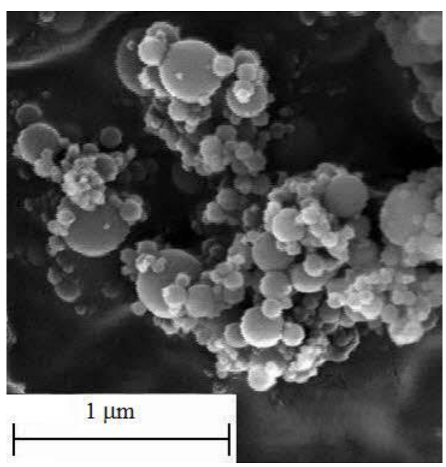

Figure 3. SEM image of grains of undensified silica fume particles

2.2.3. Fly Ash

Fly ash is one of the by-product materials produced in the combustion of powdered coal in modern thermal power plants as fine particles that fly out with the flue gas steam. The material is generally categorized into two types based on its CaO content: low calcium that is highly pozzolanic, meaning that it reacts with excess lime generated in the hydration of portland cement and Class C fly ash which is pozzolanic and also can be self-cementing. Most of fly ash particles have a spherical shape as confirmed in Figure 4, which provides rheological enhancement due to the "ball bearing effect." It has been used as a Portland cement replacement in high volume to reduce construction of carbon emission.

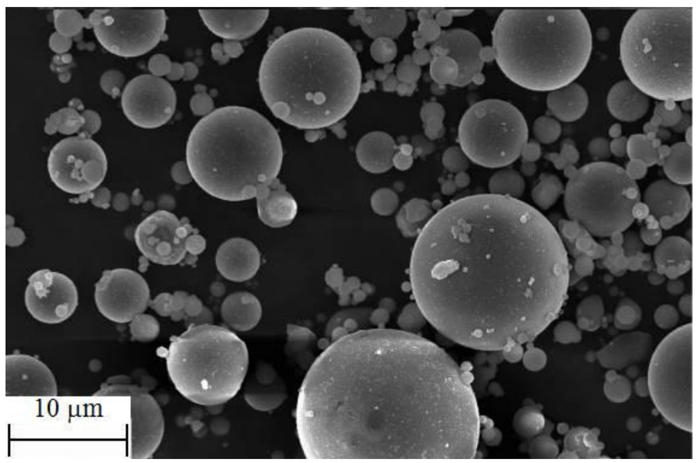

Figure 4. SEM image of fly ash particles

Low calcium Type-F fly ash with 5.13% CaO content was used to improve the rheology of the mixture. Different proportions of fly ash were tested to determine the optimum amount of fly ash to be used for UHPC. An addition of 5% and 10% fly ash resulted in about a similar spread value. Though 20% fly ash improved the spread value of the mixture as compared to 5% and 10%, it may reduce the strength of the mixture by 2 to 3ksi at 28 days, due to the characteristics of pozzolanic materials that require more time to develop its strength.

2.2.4. Aggregates

Round quartz crystalline silica with >99.7% of silicon dioxide content is used as aggregates. F-35 unground silica as the coarse sand passed the sieve size of 850 micrometers, and ground silica as the fine sand passed the sieve size of 212 micrometers. The combination of these two types of aggregate is selected for the purpose of obtaining a better packing density [15].

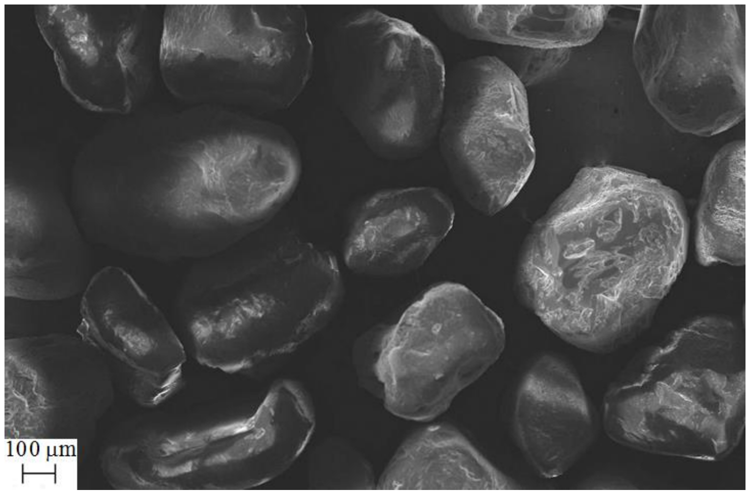

Figure 5. SEM image of whole grain silica sand used in UHPC mixture

2.2.5. Fine Ground Silica

Fine ground silica containing 99.2% of silicon dioxide, in the form of white powder, is used as filler for better packing density. Median diameter of the fine ground silica is 1.6 micron, and 96% of the powder has a smaller diameter than 5 micron.

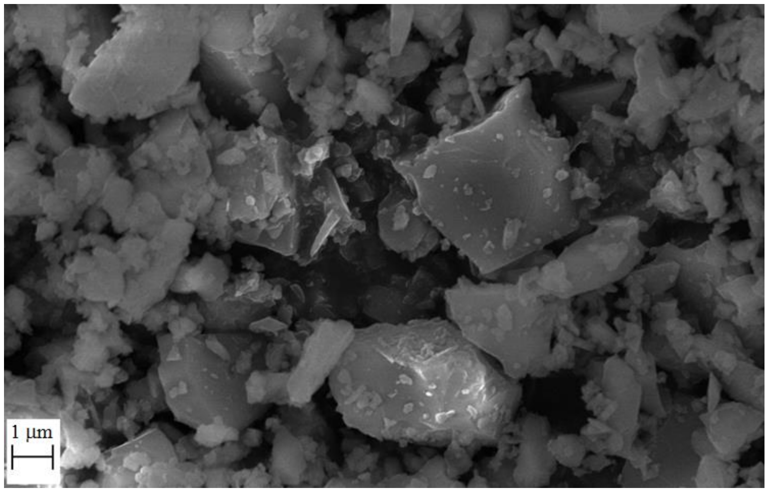

Figure 6. SEM image of fine ground silica used in UHPC mixture

2.2.6. High Range Water Reducer (HRWR) - Superplasticizer

Polycarboxylate ether-based superplasticizers are used for this study. Four various types of superplasticizer produced in the U.S. are investigated. Superplasticizer has a high influence on the fresh properties of the mixture. It can facilitate using lower w/c ratio while maintaining the required workability. If used in optimum range, it will lead to optimized packing of the mixture. Various proportions of superplasticizer are tested and the optimum range is used for the purpose of developing UHPC. The range of superplasticizer proportions used for the mixtures in this study is 2% to 7%.

2.3.Experimental Procedures

2.3.1. Mixing

The mixing order of the ingredients in UHPC is crucial for attaining a homogeneous mix at fresh state. The mixing process started with dry mixing of the first two types of sand and fine ground silica at a speed of 60RPM for about five minutes. Then cement, fly ash and silica fume were added and mixed for another five minutes. In the UHPC mixture, the number of ingredients is higher and the fineness of the material is greater; therefore it is important to practice dry mixing for several minutes in order to uniformly distribute the ingredients. This is crucial due to the fact that powder materials tend to agglomerate and lesser shear energy is required to break them apart when they are in dry condition. Therefore, water and superplasticizer should be added to the mixture after dry mixing. Water and superplasticizer were mixed together and then slowly added to the mixture in about two minutes. The mixing time between the ingredients depends on the type of material used and the mixing sequence, varying between 5 to 15 minutes. Mixing was carried on until all the ingredients were mixed and a uniformity could be observed in the mixture. Figure 7 illustrates the mixing sequence for UHPC.

Dry mixing of Sand 1, Sand 2 and Silica Powder for 5 mins

Dry mixing of all the ingredients + Cement, Fly Ash and Silica fume for 5 mins.

Mixture of water and superplasticizer to be added in about 2 mins

Completion of Mixing (5-15 mins)

Figure 7. Mixing procedure for UHPC

2.3.2. Flow Test

In order to measure the spread value of the mixture, flow tests conforming to ASTM C230/230M [25] were conducted. The mixture was carefully placed in the flow mold on a plexiglass surface, and the surface of the paste on the mold was flattened (Figure 8). The flow mold was then carefully lifted so that the mortar flowed sideways forming a pancake shape on the plexiglass surface, and then the diameter of the spread was measured (Figure 9). The measurement was done twice in two directions perpendicular to each other. The average value of the two measurements is reported in Table 4.

Figure 8. Material casted into the flow mold

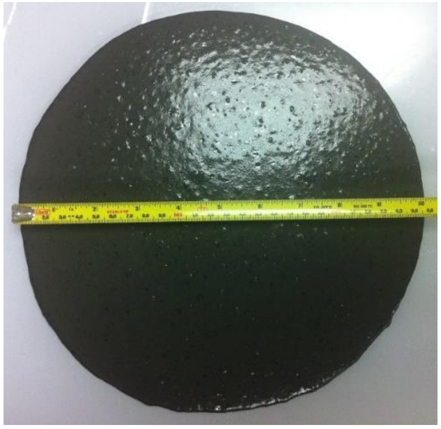

Figure 9. Measurement of spread value

For structural scale casting, the same procedure was performed with Abram's cone on a baseplate. According to ASTM 1611 [26], spread values of self-consolidating concrete measured are within 480-740mm. Measurement of spread value needs to be done for each batch as a mean of mixture control, where the measurement results from different batches have to be within a 75mm tolerance.

2.3.3. Casting

The fresh UHPC mixture was cast into a 2×4-inch mold. The molds were lubricated to facilitate easier de-molding. Manual tamping and tapping was performed for the mixtures that didn’t match the self-consolidating requirement (spread value < 25cm). For the large-scale casting, the UHPC mixture was cast into 4×8-inch, 3×6-inch and 2×4-inch molds.

2.3.4. Curing

The specimens were de-molded two days after casting and then were immersed in water for 28 days under room temperature (23°C/73°F).

2.3.5. Grinding

Grinding was done on the specimens to obtain a smooth finish for an even distribution of compressive loads during uniaxial compressive testing. A 7-inch table top tile saw and a 4-1/2-inch portable angle grinder was used for the purpose of grinding the cylinder specimens.

Figure 10. Before and after grinding

2.3.6. Capping

To increase the accuracy of the results and for the compressive force to be uniformly distributed throughout the cross-sectional area of the specimens, the specimens were capped on the top and bottom. Two different capping methods were used.

The first capping method used in this study is the use of a vertical cylinder capping kit with a sulfur-based capping compound that conforms to ASTM C617 [27]. Specimens were put on the capping plate and a molten capping compound was poured. The mold was removed after the capping compound was hardened. This was done for both the ends. This method resulted in the capping material crushing first due its lower compressive strength as compared to UHPC. Another method is un-bonded capping with a neoprene elastomeric pad that is restrained within steel restraints. This method was done according to ASTM C1231 [28]. The results obtained from this method were consistent.

2.3.7. Compression Testing

All the specimens were tested using the compression testing machine by Tinius Olsen Company. The material testing machine is automatically controlled by Tinius Olsen Test Navigator software. The base plate was set at zero position and the top plate was moved up to the suitable position to allow sufficient space for the capped specimens to be set up in the machine. The top plate was then lowered to slightly touch the upper end of the specimen. Load and position readings were then calibrated to zero.

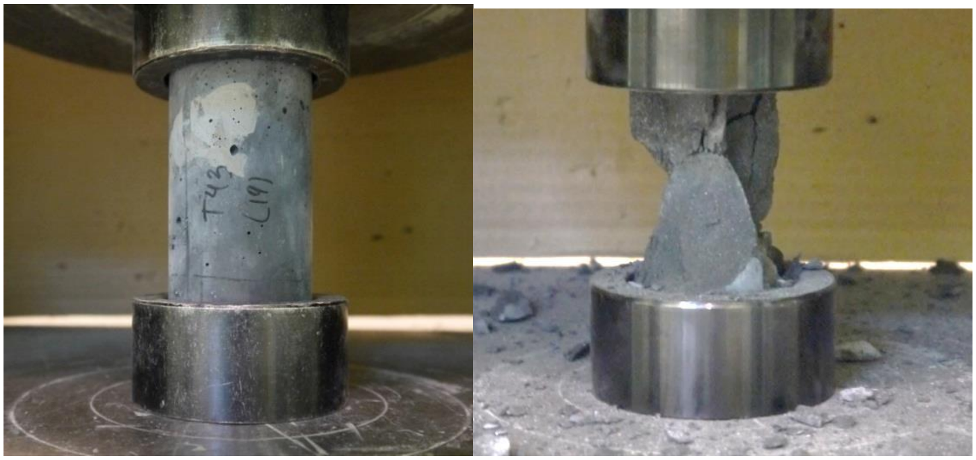

Figure 11. Compression test before and after failure

All the specimens were tested using the displacement control mechanism. The displacement rate was set to 0.2in/min until the top plate was fully in contact with the specimen. The position reading was readjusted to zero after the contact. The compression test then continued with a displacement rate of 0.025in/min when an un-bonded neoprene pad cap was used and 0.01in/min when a bonded cap was used. The specimens were loaded until there was a sudden drop in load by 20% of the peak load. Three to four specimens were tested in compression for each trial.

2.4.UHPC Design Approach and Mix Proportions

After conducting literature review and summarizing the state of the arts on self-consolidating concrete and ultra-high performance concrete, a total of 60 mixes were designed based on the packing density and ingredient properties. The objective was to achieve the compressive strength of 22ksi with self-consolidating properties. The preliminarily ingredient proportions were selected based on previous research work. The ingredients and the ingredient proportions were then modified subsequently based on the test results.

Table 3. UHPC design considerations

Fundamental Principles for developing UHPC:
• Optimum packing density by selecting ingredients such that all the voids are densely packed. • A low w/b ratio. • Application of round quartz crystalline silica as high strength aggregates. • Achieving an optimum amount of superplasticizer.

The mixture design of UHPC differs from conventional concrete as it incorporates high amounts of cement, silica fume and superplasticizer. The design is based on the principle of optimizing the particle packing density of the constituent ingredients in the UHPC mixture. The objective here is to obtain a particle packing of the greatest density.

Packing density is defined as the volume fraction of the mixture occupied by solids and is an important property in a multi-particle system. The particle density, also known as true density, may also be expressed as 1 minus the porosity. Mathematical models have been developed in the past for the purpose of optimization. These models were developed to find the best packing density of particles. One such model is known as The Linear Packing Density Model for grain mixtures (LPDM). In this model, the grains were considered identically shaped particles of varying sizes and it is assumed that the mixtures are composed of n components of equal density, identically shaped, non-deformable grains [29]. The packing density of the mixture is written as $\rho = \sum_{i=1}^{n} \emptyset_i$ where $\emptyset_i$ is the partial volume of grain component i contained in the packing. The fractional solid volume of the grain component i can be obtained from: $\eta i = \frac{\emptyset_i}{\rho}$. Here, the packing densities of compacted mixtures are calculated. Therefore $\sum_{i=1}^{n} \eta_i = 1$.

There could be three particle packing cases. 1) If the larger grains are fully packed as shown in Figure 12, the grains are non-crowding and the packing density is given by $\rho = \frac{\alpha_1}{1-\eta_2}$, where α_1 is the residual packing density of the larger grains and η_2 is the fractional solid volume of the smaller grains [29].

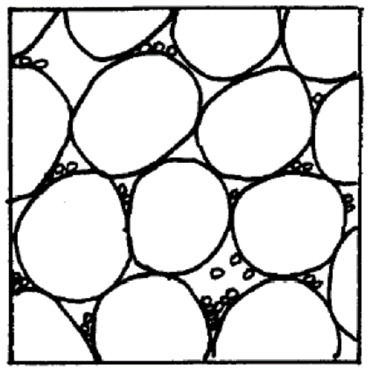

Figure 12. Non-crowding system with larger grains fully packed [29]

2) In the situation pictured in Figure 13, the small grains are fully packed and the packing density in terms of the fractional solid volumes is written as $\rho = \frac{\alpha_2}{1-(1-\alpha_2)\eta_1}$ where $\alpha_2$is the residual packing density of the smaller grains and η_1 is the fractional solid volume of the larger grains.

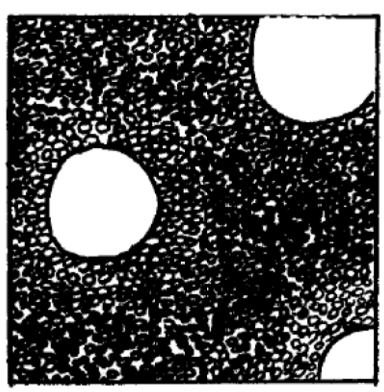

Figure 13. Non-crowding system with smaller grains fully packed [29]

3) When the small particles just fill in the interstitial space left by the larger particles, optimum packing could be achieved as shown in Figure 11 [29].

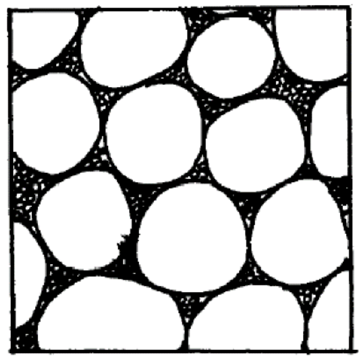

Figure 14. Optimum packing [29]

To achieve optimum packing, each grain should fill the voids between the larger grains. Two types of sand, unground and ground silica, represented the largest particle size in the mixture. Cement as the binder has the next particle size. Fine ground silica was used as the filler material with an average particle diameter of 5μm or 10μm. Silica fume has the smallest particle size amongst all the constituent materials and it acts as a microfiller in UHPC and thus will improve the packing density of the mixture. High packing density was achieved by changing the matrix composition and proportions and by selecting ranges of particle size for cement, silica fume and fine ground silica. It should be noted that silica fume also increases the compressive strength of UHPC by reacting with calcium hydroxide. Furthermore, it helps improve the interfacial transition zone between the cement and the sand.

2.4.1. Particle Size Distribution Analysis

Various design methods have been introduced to control the flowability of SCC [1, 30-32]. These design methods rely on the different proportion arrangement of coarse aggregate, fine aggregate and powder with low water content and high superplasticizer content. The flowability of SCC has been theoretically explained with the packing theory of the solid particles involved in the mixtures [33, 34]. A dense mixture with optimum packing has fine powders filling in large voids, thus less water is required in the mixture. Good packing density is also shown to be related with achieving high strength in ultra-high performance concrete (UHPC).

Size distributions of the constituent materials characterize the packing density in a mixture. According to the reactivity of the materials, solid particles used in this research can be classified into sands and cementitious powder. Figure 15 presents the particle size distribution of three different gradings of sand: unground silica that passes a sieve size of 850 microns (sand), ground silica that passes the sieve size of 250 microns (GS) and fine ground silica with 96% of the powder having a diameter smaller than 5 microns (FGS). Particle size distribution of cementitious powders that consist of cement, low-calcium Type-F fly ash and silica fume is shown in Figure 16. Two types of grey silica fume are considered for particle size distribution analysis: undensified silica fume (USF) and densified silica fume (DSF). Undensified silica fume is the condition of silica fume as produced directly from the bag house. The particles are really fine and dusty causing difficulty in pneumatic handling on the production site. Densified silica fume underwent an intentional controlled reversible agglomeration process for easy handling purposes, causing larger agglomerated particles during application.

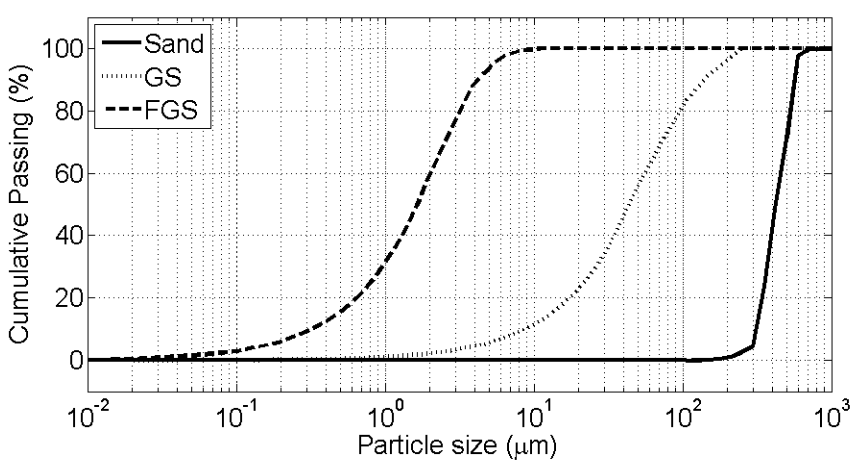

Figure 15. Particle size distribution of sands

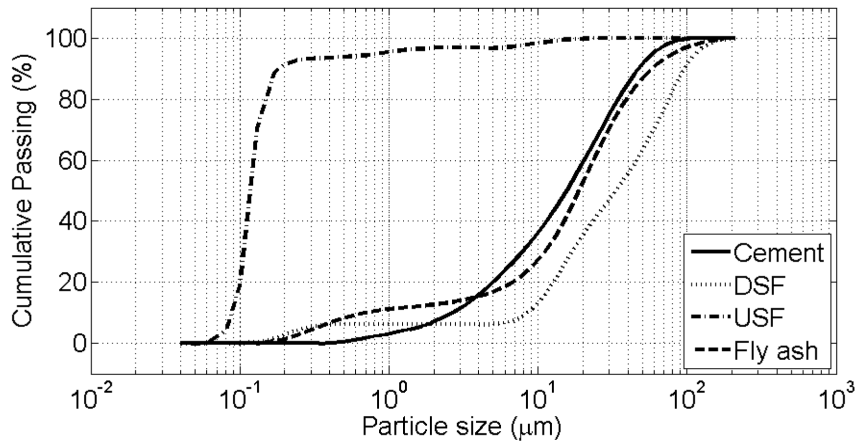

Figure 16. Particle size distribution of cementitious powders

Several packing theories state that to obtain optimal packing density, the particle size distribution of all solid particles shall follow a general packing equation suggested by Andreasen and Andersen:

$$P = \left(\frac{d}{D}\right)^q \times 100 \tag{1}$$

where P is the cumulative passing percentage, d is the corresponding sieve size, D is the diameter of the largest particle and q is the coefficient of distribution that is a selected parameter between 0 and 1. The packing theory by Fuller uses q=0.5, but Andreasen and Andersen found that optimum packing is obtained when q=0.37. In ideal circumstances as modeled by computer simulation, full packing or zero voids can be achieved when the coefficient of distribution is ≤ 0.37[35, 36].

Funk and Dinger recognized that there is a minimum particle size used in a mixture that shall be a considered parameter. Thus a modified model of the Andreasen curve is derived, known as the Dinger-Funk Equation [35]:

$$P = \frac{d^q - dm^q}{D^q - dm^q} \times 100 \tag{2}$$

Distribution modulus q determines the slope of particle distribution curve in both equations. A mixture with more coarse particles better fits the curve with higher distribution modulus, and a mixture with more fine particles better fits the curve with lower distribution modulus. The comparison between distribution curves with different q values is illustrated in the figure below:

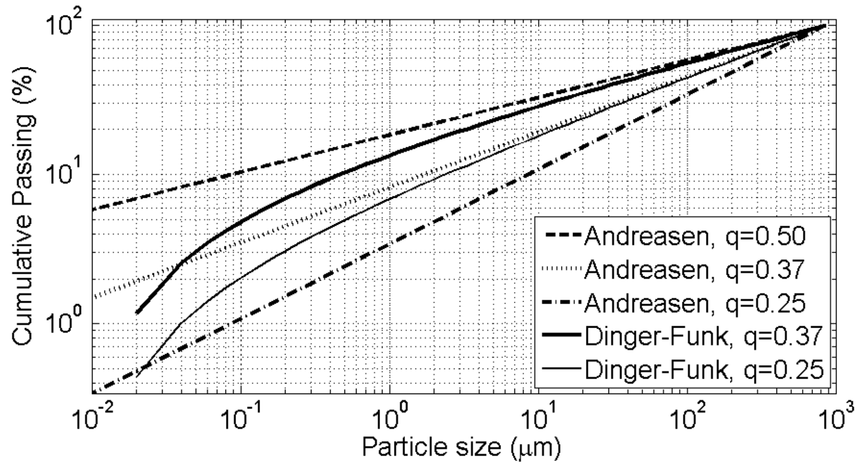

Figure 17. Comparison between different models of particle size distribution curves

To calculate the cumulative passing percentage of total solid particles, proportion by volume of each material needs to be determined. The mixture proportion was designed by the weight of each material compared to cement; thus conversion was done over the specific gravity of each material. The passing percentage of each material was then multiplied with the corresponding volume fraction to obtain the contribution of each constituent to the total mixture. Taking Andreasen and Dinger-Funk models as mean values, standard deviation and the most suitable distribution modulus are compared between the mixtures using undensified silica fume and those using densified silica fume.

Particle size distributions of mixture proportions with 0.25 silica fume and fine ground silica with 0.05 fly ash to cement by weight are shown in Figure 18 (USF) and Figure 19 (DSF).

Both of the curves for USF and DSF are better fitting to the Dinger-Funk model, as observed in the lower standard deviation value. The mixture with USF fits best with the Dinger-Funk model with q=0.23, while DSF fits the Dinger-Funk model with q=0.3. The higher distribution modulus signifies coarser particles and less flowability. Moreover, a comparison between DSF and its best fitted model results in a 5.03 standard deviation, which is significantly higher than USF with a 4.07 standard deviation. This theoretical calculation explains the higher spread value obtained during the flow test of the mixture with USF that reaches 22cm compared with the spread value of DSF at 19.5cm (Mix 22 and 41 in Table 4).

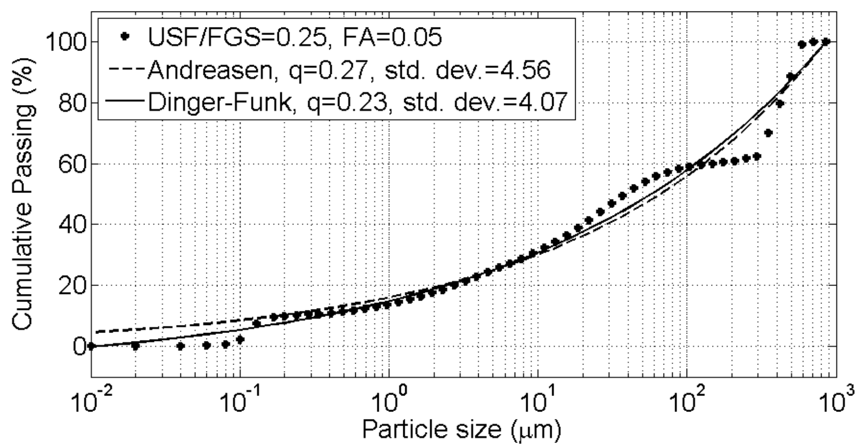

Figure 18. Particle size distribution of mixture with 0.25 USF and fine ground silica with 0.05 fly ash ratio to cement by weight.

A similar story is found in the comparison between another set of mixtures with 0.25 silica fume (differs in type, USF and DSF) and fine ground silica that contains zero amount of fly ash, as seen in Figure 20 and Figure 21. Lower values of standard deviation are on the Dinger-Funk models, but the mixture with USF has the lowest standard deviation at 4.22. Both Andreasen and Dinger-Funk models have a lower slope on the USF mixture, causing this mixture to have better flowability with a spread value of 19cm compared to the DSF mixture at 17cm (Mix 22 and 37 in Table 4).

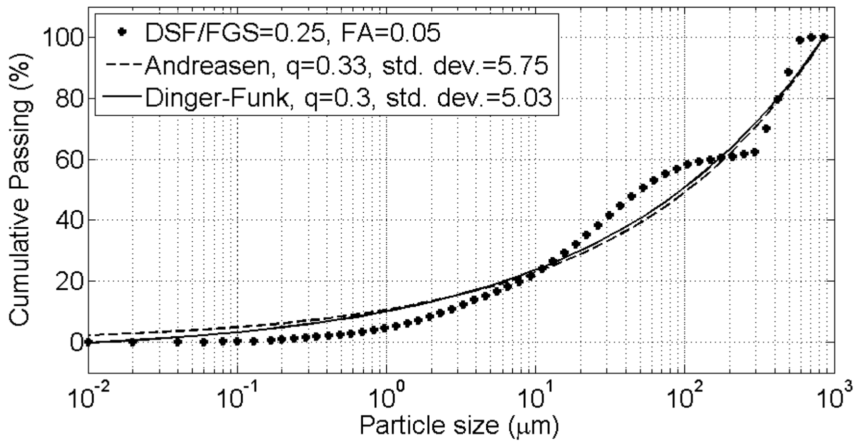

Figure 19. Particle size distribution of mixture with 0.25 DSF and fine ground silica with 0.05 fly ash ratio to cement by weight

Comparing the variation of the amount of fly ash, q values for each model are the same and there is no significant difference in standard deviation due to the very little amount of fly ash addition in the mixture. However, flowability of mixtures with a 0.05 fly ash ratio to cement by weight are better than those without fly ash, which is a 3cm increase in the mixture with USF and a 2.5cm increase in the mixture with DSF. This phenomenon is due to the spherical shape of fly ash particles giving a more dominant positive effect on the flowability compared with its size distribution. Other than particle size distribution, particle shape, a proper amount of water and a high-range water reducer also play an important role in the density and flowability of self-compacting concrete.

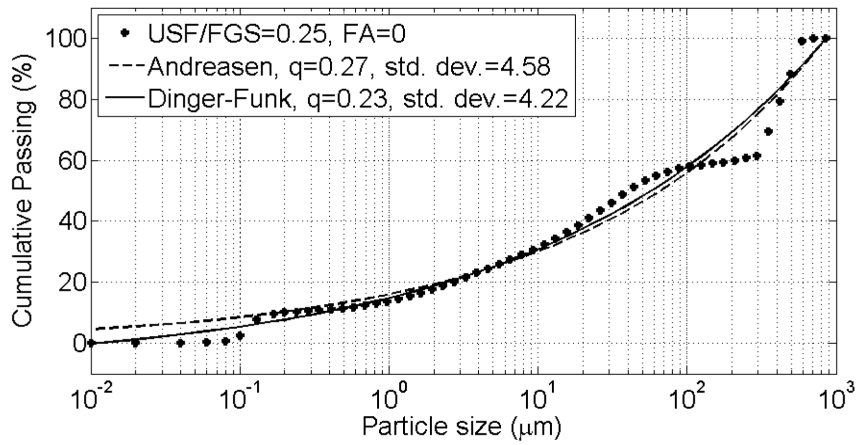

Figure 20. Particle size distribution of mixture with 0.25 USF and fine ground silica ratio to cement by weight, and 0 amount of fly ash

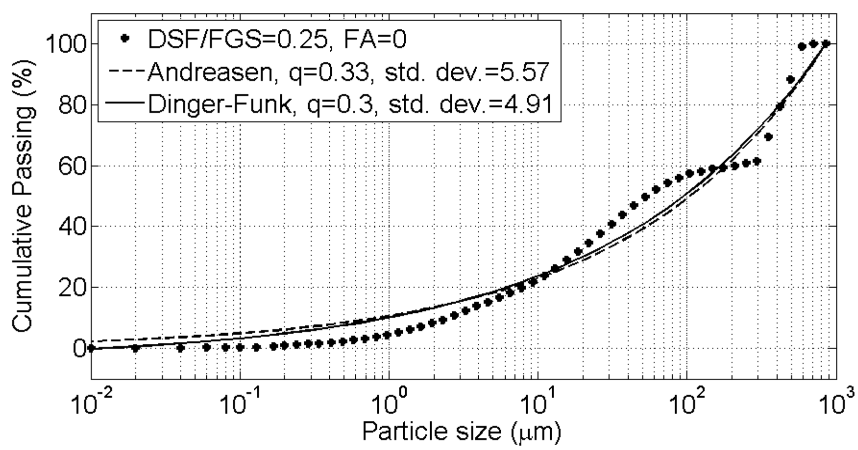

Figure 21. Particle size distribution of mixture with 0.25 DSF and fine ground silica ratio to cement by weight, and 0 amount of fly ash

2.4.2. Mix Proportions

While designing the mixture proportions for UHPC, the aspects mentioned in Table 3 were carefully followed. The parameters that were studied for an optimum amount are as follows:

- Water/binder ratio
- Silica fume/fine ground silica/cement ratio
- Superplasticizer/cement ratio
- Fly ash/cement ratio
- Type of cement
- Type of silica fume
- Type of high range water reducer

The mixtures and the trials of 60 mixes are summarized in Table 4. Unground silica and ground silica are used in ratio 4:1, with a total proportion of 1.4 compared to cement by weight. These trials were designed to achieve a dense packing of the particles for desired strength and flowability. The optimum amount of superplasticizer, fly ash and w/b were obtained from these trials.

Table 4. Mixture proportions and results

No.	C	SF	FA	FGS	w/c	w/b	HRWR	HRWR Type	SF Type	Spread value (cm)	f_c' (ksi)
1	1†	0.25	0.00	0.25	0.229	0.183	0.015	A	DSF	NC	NC
2	1†	0.25	0.00	0.25	0.312	0.250	0.105	A	DSF	23.5	10.1
3	1†	0.25	0.00	0.25	0.303	0.243	0.090	B	DSF	21.5	10.6
4	1†	0.25	0.00	0.25	0.303	0.243	0.090	C	DSF	23.5	10.7
5	1†	0.25	0.00	0.25	0.303	0.243	0.090	D	DSF	19.5	11.0
6	1†	0.25	0.00	0.25	0.363	0.290	0.105	A	DSF	26.0	8.6
7	1†	0.25	0.00	0.25*	0.363	0.290	0.105	A	DSF	27.0	9.0
8	1†	0.25	0.00	0.25	0.354	0.283	0.090	A	DSF	27.0	8.3
9	1†	0.25	0.20	0.25	0.354	0.244	0.090	A	DSF	29.5	9.6
10	1†	0.25	0.05	0.25	0.354	0.272	0.090	A	DSF	30.0	9.8

No.	C	SF	FA	FGS	w/c	w/b	HRWR	HRWR Type	SF Type	Spread value (cm)	f_c’ (ksi)
11	$1^{\dagger}$	0.25	0.00	0.25	0.268	0.214	0.060	A	DSF	16.0	22.8
12	$1^{\dagger}$	0.25	0.00	0.25	0.268	0.214	0.060	B	DSF	NF	25.6
13	$1^{\dagger}$	0.25	0.00	0.25	0.268	0.214	0.060	C	DSF	17.5	25.9
14	$1^{\dagger}$	0.25	0.00	0.25	0.247	0.198	0.040	C	DSF	NF	23.0
15	$1^{\dagger}$	0.25	0.00	0.25	0.250	0.200	0.040	C	DSF	NF	25.0
16	$1^{\dagger}$	0.25	0.00	0.25	0.250	0.200	0.045	C	DSF	NF	26.6
17	$1^{\dagger}$	0.25	0.00	0.25	0.250	0.200	0.050	C	DSF	NF	25.5
18	$1^{\dagger}$	0.25	0.00	0.25	0.250	0.200	0.060	C	DSF	NF	23.0
19	$1^{\dagger}$	0.25	0.10	0.25	0.250	0.185	0.060	C	DSF	17.5	24.7
20	$1^{\dagger}$	0.25	0.00	0.25	0.268	0.214	0.060	C	DSF	15.5	22.9
21	$1^{\dagger}$	0.25	0.05	0.25	0.260	0.200	0.060	C	DSF	17.0	24.6
22	$1^{\dagger}$	0.25	0.00	0.25	0.263	0.210	0.060	C	DSF	17.0	23.7
23	$1^{\dagger}$	0.25	0.05	0.25	0.273	0.210	0.060	C	DSF	19.5	23.0
24	$1^{\dagger}$	0.25	0.10	0.25	0.284	0.210	0.060	C	DSF	20.5	22.1
25	$1^{\dagger}$	0.25	0.20	0.25	0.305	0.210	0.060	C	DSF	18.5	21.5
26	$1^{\dagger}$	0.25	0.05	0.30	0.273	0.210	0.060	C	DSF	16.0	22.5
27	$1^{\dagger}$	0.25	0.00	0.25	0.263	0.210	0.040	C	DSF	14.0	25.2
28	$1^{\dagger}$	0.25	0.00	0.25	0.263	0.210	0.045	C	DSF	NF	24.1
29	$1^{\dagger}$	0.25	0.00	0.25	0.263	0.210	0.050	C	DSF	15.0	24.9
30	1^{Θ}	0.25	0.00	0.25	0.263	0.210	0.060	C	DSF	20.0	19.7
31	1^{Θ}	0.25	0.00	0.25	0.263	0.210	0.060	A	DSF	17.0	19.9
32	1^{Θ}	0.25	0.00	0.25*	0.263	0.210	0.060	A	DSF	17.5	20.3
33	1^{Θ}	0.25	0.00	0.25*	0.263	0.210	0.060	C	DSF	22.0	19.7
34	1^{Θ}	0.25	0.05	0.25	0.273	0.210	0.060	C	DSF	21.5	19.6
35	1^{Θ}	0.25	0.00	0.25	0.263	0.210	0.060	C	DSF	21.5	19.69
36	1^{Θ}	0.25	0.00	0.25	0.263	0.210	0.070	C	DSF	21.0	18.58
37	$1^{\dagger}$	0.25	0.00	0.25	0.263	0.210	0.060	C	USF	19.0	24.77

No.	C	SF	FA	FGS	w/c	w/b	HRWR	HRWR Type	SF Type	Spread value (cm)	f_c' (ksi)
38	$1^{\dagger}$	0.25	0.00	0.25	0.263	0.210	0.060	C	DSF	17.0	23.57
39	$1^{\dagger}$	0.25	0.00	0.25	0.263	0.210	0.060	C	USF	15.0	18.97
40	1^{Θ}	0.25	0.05	0.25	0.273	0.210	0.060	C	DSF	21.5	19.60
41	$1^{\dagger}$	0.25	0.05	0.25	0.273	0.210	0.060	C	USF	22.0	23.38
42	$1^{\dagger}$	0.25	0.05	0.25	0.260	0.200	0.060	C	WSF	20.5	24.32
43	1^{Θ}	0.25	0.05	0.25	0.273	0.210	0.060	C	WSF	24.5	22.65
44	$1^{\dagger}$	0.25	0.10	0.25	0.284	0.210	0.060	C	USF	22.0	23.14
45	1^{Θ}	0.25	0.05	0.20	0.273	0.210	0.060	C	WSF	25.5	20.65
46	1^{Θ}	0.20	0.00	0.20	0.252	0.210	0.060	C	DSF	22.0	19.33
47	$1^{\dagger}$	0.20	0.00	0.20	0.252	0.210	0.060	C	USF	21.5	24.52
48	$1^{\dagger}$	0.20	0.05	0.20	0.263	0.210	0.060	C	USF	26.0	23.24
49	$1^{\dagger}$	0.20	0.05	0.20	0.263	0.210	0.060	C	WSF	25.0	22.45
50	1^{Θ}	0.20	0.05	0.20	0.263	0.210	0.060	C	WSF	27.5	21.04
51	1^{Θ}	0.20	0.05	0.20	0.250	0.200	0.060	C	WSF	27.0	22.01
52	$1^{\dagger}$	0.20	0.10	0.20	0.273	0.210	0.060	C	USF	24.5	24.75
53	1^{Θ}	0.20	0.20	0.20	0.294	0.210	0.060	C	DSF	27.5	18.97
54	$1^{\dagger}$	0.20	0.20	0.20	0.294	0.210	0.060	C	USF	28.5	22.87
55	$1^{\dagger}$	0.20	0.20	0.40	0.294	0.210	0.060	C	USF	22.5	22.43
56	$1^{\dagger}$	0.00	0.05	0.00	0.221	0.210	0.060	C	USF	24.0	16.83
57	$1^{\dagger}$	0.10	0.20	0.10	0.24	0.210	0.060	C	USF	25.5	21.29
58	1^{Θ}	0.20	0.05	0.20	0.238	0.190	0.060	C	WSF	24.0	21.7
59	$1^{\dagger}$	0.25	0.05	0.25	0.273	0.210	0.060	C	WSF	18.0	20.1
60	1^{Θ}	0.25	0.05	0.25	0.273	0.210	0.060	C	USF	25.0	20.7

Note: C=Cement, †Ordinary Portland cement, $^{\Theta}$Class-H cement, SF=Silica Fume, FA=Fly ash, FGS=Fine Ground Silica, HRWR=High range water reducer, *Fine ground silica with maximum 10μ dia., USF=Undensified Silica Fume, DSF=Densified Silica Fume WSF=White Silica Fume, NC=Non-Castable, NF=Non-Flowable (spread value<15cm)

Although compressive strength as high as 26.6ksi was achieved (Mix 16), the mixture did not satisfy the workability requirements for ultra-high performance concrete. The ingredients were further studied in the microstructure level and modified to improve the rheology of the mixture. The modified ingredients included different types and proportions of silica fume and fine ground silica and the addition of an optimum amount of Type-F fly ash. The amount of fly ash between 0 to 20% of cement by weight was experimented. Two series of result are reported in Figure 22 and Figure 23 showing that 5% fly ash was found to be the most effective one in terms of a significant increase in flowability, while maintaining the compressive strength around 22ksi. Portland cement type-I was used in both series, involving two different types and amounts of silica fume. The first series uses a 0.25 densified silica fume ratio to cement by weight, and the second series uses a 0.2 undensified silica fume to cement by weight.

Mixtures 32-36 were cast using Class-H cement, which resulted in an increased spread value for the same proportions as compared to ordinary Portland cement. These mixtures did not only result in increased spread value but would also give longer setting time. The increased spread value was due to the lower amount of Tricalcium Aluminate (C3A) content (0%) and a lower surface area which resulted in the requirement of less water and thus improved rheology. However, the mixtures using Class-H cement resulted in decreased compressive strength as compared to ordinary Portland cement due to a lower percentage of Tricalcium Silicate (C3S), which is mostly responsible for the development of strength in concrete.

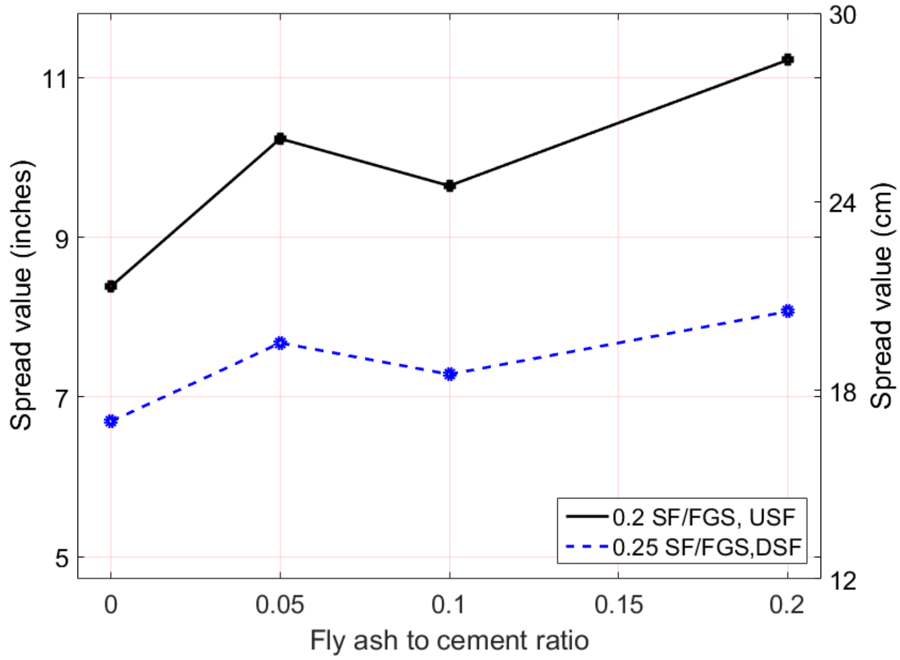

Figure 22. Effect of fly ash content on spread value for different amount and type of silica fume/powder

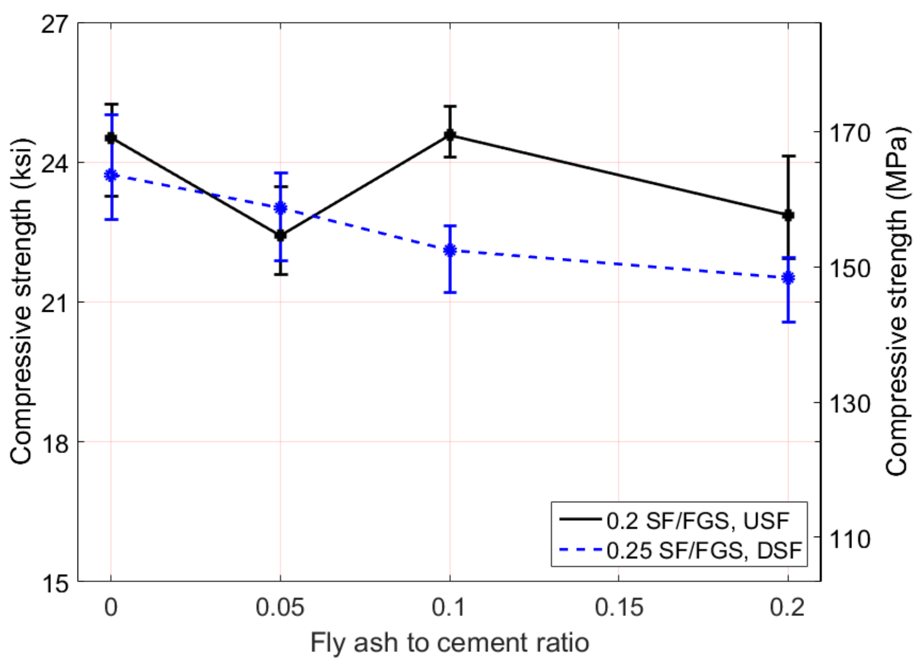

Figure 23. Effect of fly ash content on c for different amount and type of silica fume/powder

Three types of superplasticizer were used for the purpose of studying their effect on the mixtures with DSF:FGS:C = 0.25:0.25:1 without involving fly ash. Comparison of the compressive strength and spread value are shown in Figure 24, and it was found that superplasticizer Type C gave the most satisfying result. The comparison of the superplasticizer amount in the mixture was also compared using superplasticizer Type C. The result in Figure 25 shows that 6% superplasticizer gave a better flowability without reducing the compressive strength of the mixture.

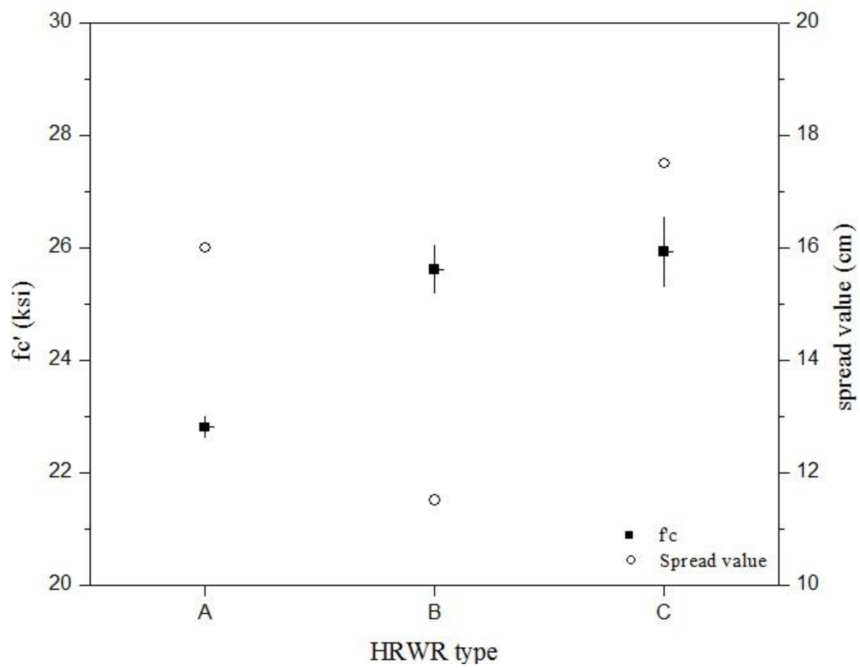

Figure 24. Effect of the type of superplasticizer on compressive strength and spread value

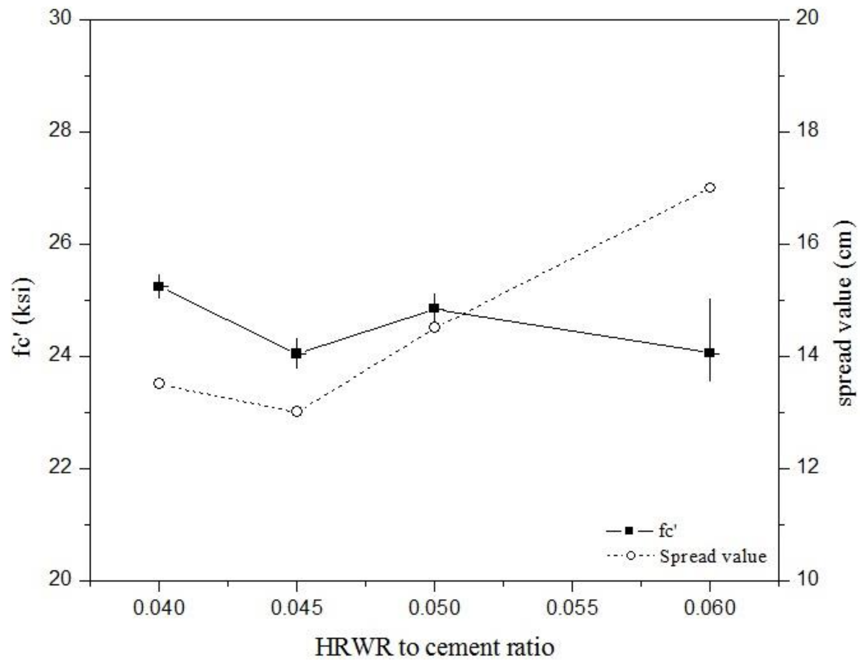

Figure 25. Effect of the amount of superplasticizer on compressive strength and spread value

The type of silica fume does not significantly affect the compressive strength, but it has a great influence on the spread value. This was confirmed through experiments on different mixtures as shown in Table 5 and Figure 26. One series uses the combination of Portland cement type-I and three types of silica fumes while the other uses Class-H cement. It can be seen that compared with DSF, USF gives better flowability and compressive strength. In most cases, a more workable mixture causes less air voids in the mixture that allows it to obtain higher compressive strength. Involving Class-H cement in the mixture gives even better flowability; however there is a consequence of reduced strength due to the low C_3S content in Class-H cement.

Table 5. Effect of the type of silica fume on flowability for two different type of cement

Spread value (cm)	DSF	WSF	USF
Portland cement type I	19.5	18.0	22.0
Class-H cement	21.5	24.5	25.0

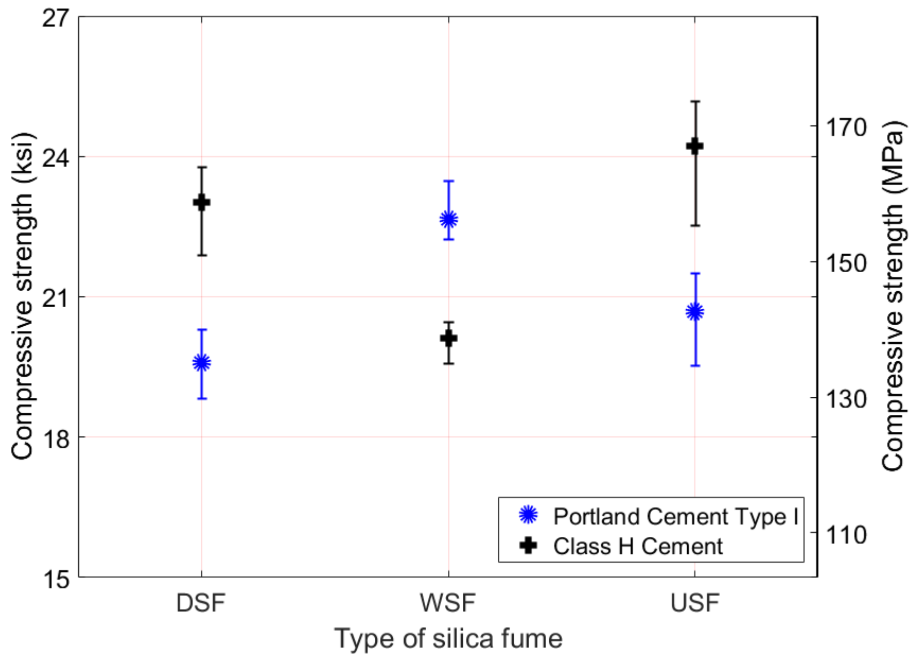

Figure 26. Effect of the type of silica fume on compressive strength for two different type of cement

In order to study the effect of silica fume and fine ground silica on the mechanical properties of UHPC, their content to cement ratio by weight between 0 and 0.25 was investigated. The silica fume to fine ground silica ratio was kept as 1:1 to limit the varying parameters. Figure 27 shows the effect of the amount of silica fume and fine ground silica on the compressive strength and spread value of the UHPC mixture. The optimum amount of silica fume and fine ground silica was found to be 20% of cement by weight for a homogenous self-consolidating concrete without excessive bleeding.

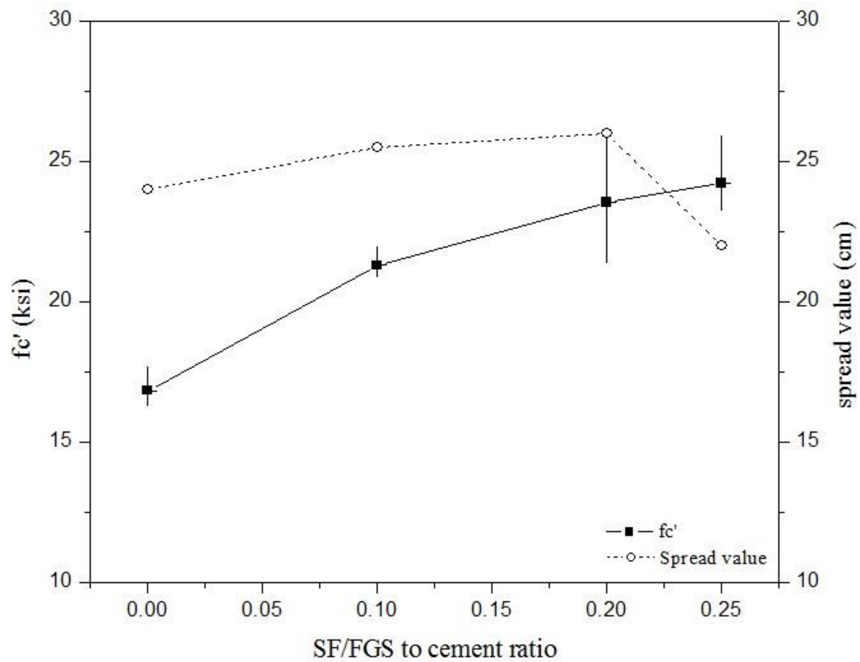

Figure 27. The effect of silica fume and fine ground silica content on compressive strength and spread value

Table 6. Optimum mixture proportions for UHPC

Ingredient	Proportion
Cement	1
Silica Fume (Undensified)	0.200
Fly Ash	0.050
Fine ground silica	0.200
w/b	0.210
Superplasticizer (HRWR)	0.060
Sand 1 (0.212mm)	0.28
Sand 2 (0.85mm)	1.12
Test Results	
Spread Value (cm)	26.0
f_c' (ksi)	23.24

From the results in Table 4, the compressive strength of 22ksi with spread values higher than 25cm were achieved through understanding the material characteristics and modifying the proportions to optimize packing density. An optimum proportion of superplasticizer, fly ash, the type of superplasticizer and water/binder ratio that satisfies the requirements of UHPC were selected based on the compressive strength and spread value for large-scale production and further studies (Table 6).

2.5. Large-scale Production and Self-Consolidating Characterization of UHPC

It is necessary to understand the capability of UHPC in order for it to be produced in bulk quantities for the purpose of pre-fabrication of UHPC modules with controlled quality. The laboratory designed mixture was produced in bulk quantity using a conventional 11 cubic feet gravity-based concrete mixer. The test equipment and setup are shown in Figure 28.

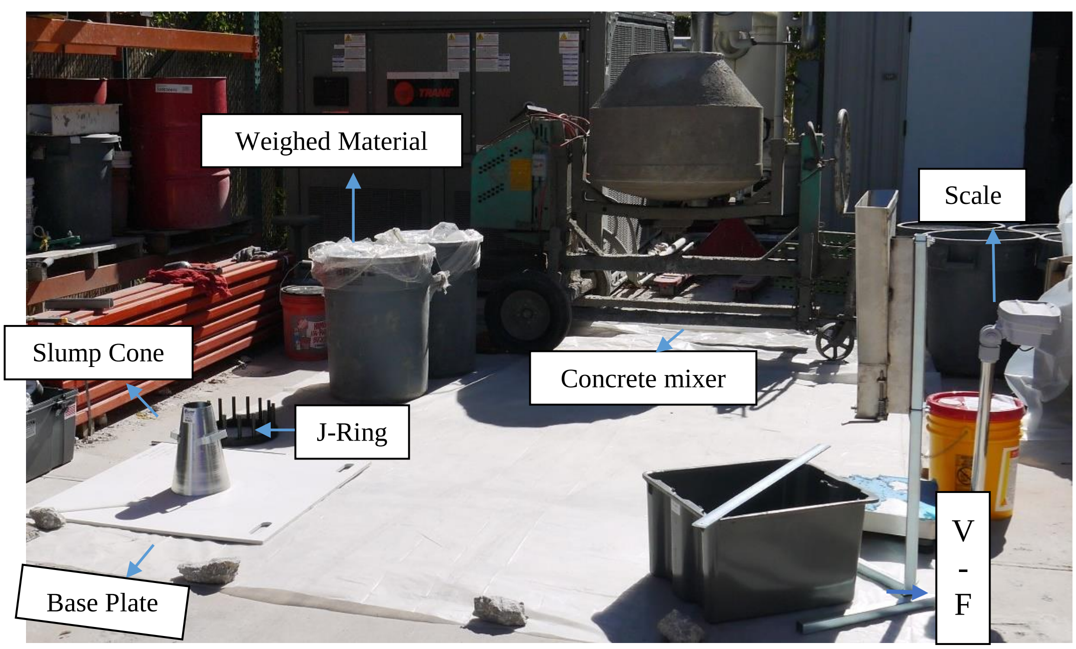

Figure 28. Test facilities

Three classes of aggregates were initially dry mixed for a period of 5 minutes. Cement, fly ash and silica fume were then added, and all the ingredients were dry mixed for another 5 minutes. Laboratory practices demonstrated that different addition methods of superplasticizer had no significant effect on flowability of the mixture. Hence, for small scale mixing in the laboratory, water mixed with superplasticizer was added directly to the uniformly mixed dry ingredients all at once. However, since the gravity-based mixer is not as powerful as the force-based laboratory mixer, it was observed that the gradual addition of the superplasticizer helped to improve the flowability of the mixture, as recommended by Tue et al [37]. Thus, for large scale practice, water and the superplasticizer were first mixed together and then added gradually to the mixer for 2-3 minutes. Mixing was continued for around 10-15 minutes until all the ingredients had reacted and a uniformity could be observed in the mixture.

Figure 29. Completion of mixing

Several tests such as the Slump flow test, J-ring and V-funnel were performed to further investigate different properties of the mixture [38]. The Slump flow test was performed in accordance with ASTM 1611 [26]. This test was aimed to investigate the free, unrestricted deformability of UHPC. The flow-time T50 indicates the rate of deformation within the 50cm inscribed mark.

The slump flow test was performed with the upright mold procedure by using regular Abram's cone, which is a truncated cone with a base diameter of 200mm, a 100mm diameter at the top and a height of 300mm. The slump flow mold was placed on a 40-inch square base plate with a 20-inch (50cm) inscribed circular mark. The freshly mixed UHPC was poured out and the cone was filled to the brim without tamping. The cone was then raised vertically and the UHPC was allowed to flow out freely below the cone (Figure 30). The time required since the first lifting of the mold until the UHPC reached the 20-inch mark was recorded as T50 time. The final diameter of the pancake was measured 30 seconds afterwards in two perpendicular directions. The average of the two measured diameters was calculated.

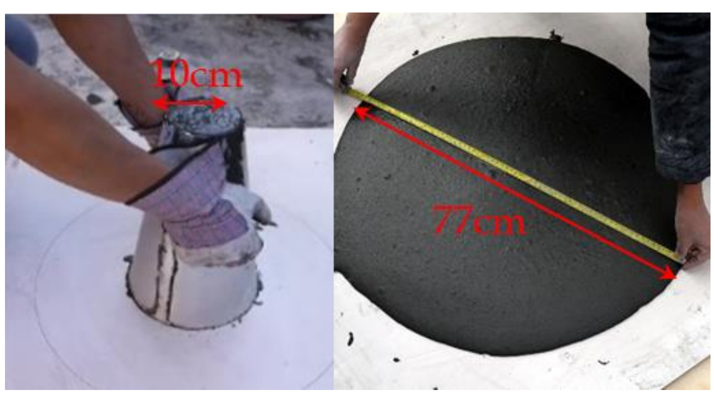

Figure 30. Slump flow measurement

Slump flow signifies the ability of UHPC to fill the formwork under its own weight. A common range of slump flow for self-consolidating concrete is 45-76cm according to ACI 237-07

[23] and 65-80cm as per EFNARC [38]. The flow time T50 indicates the viscosity of the mixture. A material with a flow rate of less than 2 seconds is considered to have low viscosity and is prone to segregation, while a flow rate higher than 5 seconds is considered as too viscous. A tolerance of 5cm in slump flow measurement is used to confirm the consistency of the material. Following the slump-cone measurement, visual observation was carried out to examine the stability of the material. The visual stability index is reported based on the appearance of the concrete spread in accordance with the appendix in ASTM 1611 [26].

The V-funnel test was performed to measure the flow rate of UHPC under its self-weight. The flow time is an indication of its plastic viscosity. The V-funnel flow-time is the amount of time for a defined volume of Self-Consolidating Concrete (SCC) to flow through a narrow opening at the mouth of the funnel and gives an indication of the filling ability of SCC, provided blocking and/or segregation do not take place. The V-funnel was pre-moistened prior to the test. The opening was kept closed as the V-funnel was filled with UHPC to the brim without compacting or tamping. The trap door was opened within 10 seconds after filling, and concrete was allowed to flow out under gravity. Time was measured from the moment the trap door was opened till light could be seen from above through the funnel opening. Shorter flow time indicates higher flowability of concrete. Flow time is expected not to be greater than 10 seconds for good flowability.

Figure 31. V-funnel test

To measure segregation resistance, the V-funnel test was performed at T5 minutes. The funnel was refilled and tested at 5 minutes. The time difference between immediate V-funnel and T5 minute was recorded. The time difference is expected to be less than 3 seconds according to EFNARC [38], since time difference greater than 3 seconds might indicate segregation. However, if there is no appearance of segregation or blockage, increased time in V-funnel T5 minute could also be due to rapid setting time that decreases workability.

A J-ring test was performed to measure the passing ability of UHPC in accordance with ASTM C1621 [39]. The ring has steel rods of 16mm diameter with 100mm height, and they are spaced at 59mm apart around the ring to simulate reinforcing bars. The ring is placed at the centre of the square base plate. The remaining procedure is the same as the slump flow test. The difference in height inside and outside the ring was measured at four locations, and the average was calculated. The spread diameter in two perpendicular directions was also measured. The average of the spread diameter was then subtracted from the average of the spread diameter found from the slump cone test and the difference was recorded. Greater difference in height and spread indicates lower passing ability. Height difference of more than 10mm or spread difference of more than 50mm indicates poor passing ability.

Figure 32. Passing ability test with J-ring

The air content at fresh state for the mixture was also measured in percentage according to ASTM C231 [40] with Type-B air meter. Measurement of air content was done as a standard test to assure the quality of large-scale produced material at the job site as required in ACI 237-07 [23]. A measuring bowl was dampened prior to the test, and filled to the brim without any compacting or tamping. After assembling the apparatus, the main air valve between the air chamber and measuring bowl was closed and petcocks at the sides of air chamber were opened. Water was pumped into the device using a rubber syringe. Both petcocks were then closed and air was pumped into the air chamber until the gauge was at the initial pressure line. The main air valve was released and air content was read on the gauge to the nearest 0.1%. SCC case examples in ACI 237 [23] show an air content range between 1-6%.

Figure 33. Air content measurement

Table 7 shows the different test results for the characterization of self-consolidating UHPC and the standard accepted criteria for self-consolidating concrete by EFNARC [38].

Table 7. Tests on UHPC

No.	Test	UHPC	EFNARC
1	Compressive Strength (ksi)	22.34	-
2	Slump flow by Abram's cone	77cm	65-85cm
3	T_{50cm} slump flow	4sec	2-5sec
4	J-ring, height difference	0-2mm	0-10mm
5	V-funnel	10sec	6-12sec
6	V-funnel increase time at T_{5min}	7sec	3sec
7	J-ring, spread difference	0cm	N/A
8	Visual stability index (ASTM C1611)	0	N/A
9	Air content	4.8%	N/A

2.6. Microstructure Characterization through High-resolution Micro-Computed Tomography

Even though research and development for improving UHPC has been ongoing for decades, an explanation of physical properties behind the ultra-high compressive strength in UHPC is rarely discussed. High-resolution μCT allows us to look at the physical microstructure of the material, and is used as one of the tools in this study to provide a clearer understanding behind one of the possible reasons for the high strength of UHPC that can be produced without any special heat or pressure treatment.

Volume imaging techniques using a penetrating electromagnetic wave have heralded major advancements in many fields of science and engineering. Such volume imaging techniques allow the construction of 3D models from 2D image slices in order to visualize internal details of various objects. In particular, computed tomography (CT), which utilizes X-rays to scan cross-sectional images, have been widely adopted in medical imaging, where cross-sectional images can be used for diagnostic and therapeutic purposes in various medical disciplines[41, 42]. In order to recreate a model of the internal structure of a sample, a series of 2D CT images can be obtained at various different angles to be digitally combined in order to create a 3D model. When each volume pixel or voxel is in the micrometer range, the method is termed as high-resolution micro-computed tomography (μCT) [43, 44].

This method has recently gained traction in materials analysis and particularly in cementitious material study [45-48] due to the high level of three-dimensional information that can be gained, as well as the non-destructive nature of the imaging technique which preserves the sample structure for repeated imaging of the same location after multiple processes.

When a sample is illuminated with an incident x-ray beam, the major component of the beam penetrates through the sample. The beam intensity attenuates due to the absorption by the different constituent material of the sample. The intensity of the transmitted beam is measured by a digital x-ray detector and the value of the attenuation coefficient for each voxel is transformed into a CT numbers according to the Hounsfield scale [49] given by:

$$\text{CT Number} = 1000 \times \frac{\mu_x - \mu_{water}}{\mu_{water}} \tag{3}$$

where μ_x and μ_{water} are the linear attenuation coefficients of the sample material and water, respectively. A set of 2D cross-section images that map the material distribution within the sample can be calculated and constructed. These 2D images are mathematically stacked together to construct a 3D map of the interior structure of the sample. This method produces easily visualized morphological parameters (e.g. surface area and volume) of the sample.

The resolution of a μCT system is an important parameter which affects the accuracy of the analysis and is defined by the dimensions of the voxels. The x–y resolution is defined as the sample cross sectional diameter divided by the image pixel dimension, which depends on the number of detector channels and geometric factors. The z resolution corresponds to the spacing between each 2D cross-section planes, which is equal to the slice thickness of each reading.

The μCT used in this study was a high-energy microtomography scanner, which consists of a 130kV X-ray source and a distortion-free flat panel detector with a 4000×2648 resolution. For the scanning process, the sample was fixed on a micro-positioning stage and scanned in air with an 80kV tube voltage and 125μA tube current. A total of 2200 slice images were obtained while the sample was rotated with an angle step of 0.3°. The thickness and resolution of each slice were 5μm and 2400×2400, respectively, yielding a voxel dimension of 5×5×5μm. The wavelet noise reduction technique [50] was performed on each cross-section image. In addition, a median filter method [51] was applied to remove random noise surrounding the air voids.

For μCT measurements, a 5mm cube was extracted from a cylindrical specimen of UHPC, as shown in Figure 34. The mixture proportion contains 0.25 silica fume to cement ratio by weight, 0.25 fine ground silica to cement ratio by weight and 0.21 water to binder ratio. The compressive strength of the sample was found to be 25ksi. Conventional mortar with a compressive strength of less than 10ksi was used for result comparison.

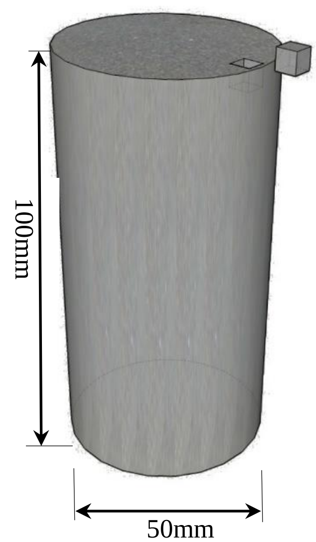

Figure 34. Sample extraction

MicroCT measurements are mathematically regarded as a four-dimensional set, with each 3-dimensional voxel represented by Cartesian coordinates (x, y and z) and its corresponding density at each point.

Figure 35 shows the cross-sectional images of the samples and the area preferred for analysis. Each raw image contains a 2D array of pixels consisting of 256 possible levels (0–255) of gray intensity. The gray level of each pixel represents the density value that corresponds to the linear attenuation coefficient of the element contained in that pixel. The raw images generally contain: (1) gas phase (air pores) that appears black and (2) solid phase, including the cementitious binder and fine aggregates, which appear as different shades of gray. Within the solid phase, the unhydrated clinker has a higher density than the fine aggregates (sand) and hydration products (such as calcium silicate hydrate and calcium hydroxide), thus absorbing a higher dose of x-ray and appearing brighter in the images. In addition, white speckles are observed in the μCT images. These likely stem from high-density metal impurities within the cementitious matrix.

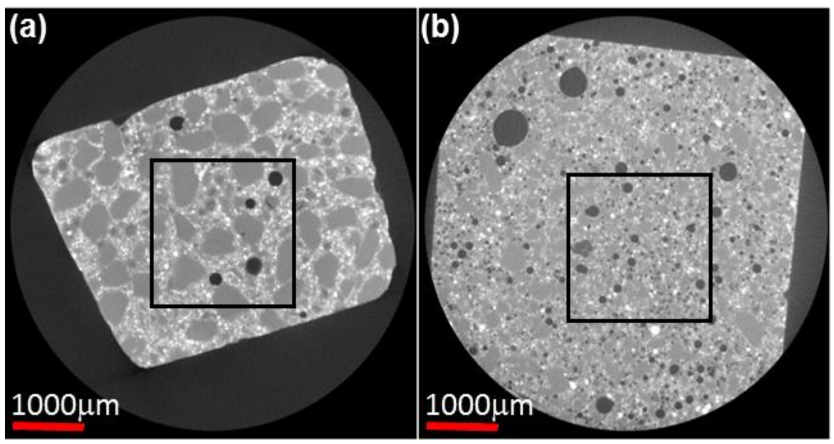

Figure 35. Two dimensional cross section images of (a) UHPC and (b) conventional mortar. Square indicates volume of interest.

Image segmentation was performed to highlight multiple phases within the image in order to visualize a specific component within the inhomogeneous material. To demonstrate the segmentation process, a volume of interest (VOI) of 2×2×2mm was extracted from the sample. A global thresholding method was used to convert grey-scale images to binary images. By examining all the voxels in each grey-scale VOI, a histogram representing the frequency distribution of each intensity level can be generated (Figure 36). The Otsu's method [52] was applied to calculate the threshold values: T1 separates the gas phase from the solid phase, and T2 further divides the solid phases by separating the hydrates and aggregates from unhydrated particles. The threshold intensity values were applied to all the pixels of the gray-scale images. The components of interest were colored white, and other pixels were colored black. By these means, the gas phase was determined as all the pixels with intensity smaller than T1 and was segregated and colored white. After thresholding segmentation, a series of binary images were obtained. In the binary image, a pixel can either have a value of “1” when it is part of the gas phase, or “0” when it is part of the solid phase. Figure 37 to Figure 40 contains a comparison of binary images of pores, sands, hydrates and anhydrates in UHPC and conventional mortar. By aligning and stacking the series of 2D images, a three dimensional reconstruction of the material can be obtained, with the pore distribution clearly visible. These 2D binary cross-section images are combined into a 3D voxel representation, as shown in Figure 41 to Figure 44.

The resolution capacity limits the minimum size of detectable pores to 5 microns. Cracks generate from the largest flaws and connect to other cracks as they develop into a compressive failure in a brittle material [53]; thus macropores as measured in this study have a direct effect on the compressive behavior of the material [54].

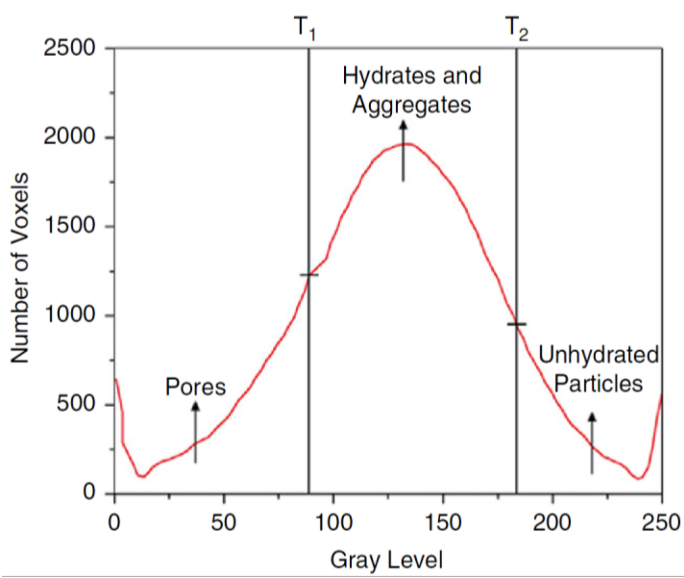

Figure 36. Gray level histogram and threshold values

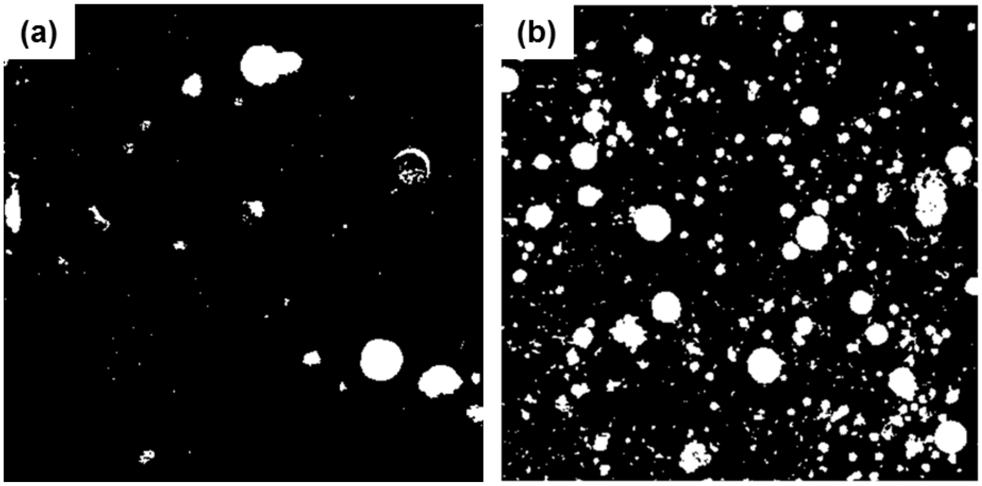

Figure 37. Binary images of pores for (a) UHPC (b) conventional mortar

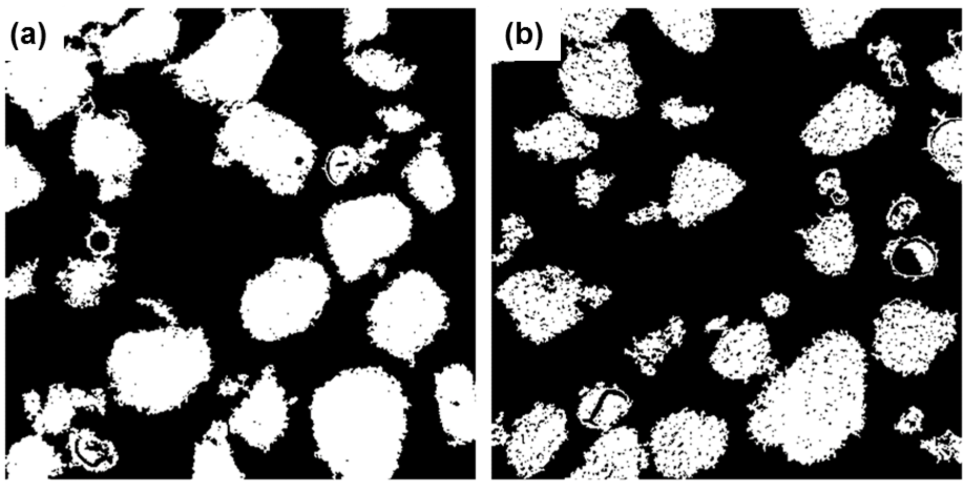

Figure 38. Binary images of sands for (a) UHPC (b) conventional mortar

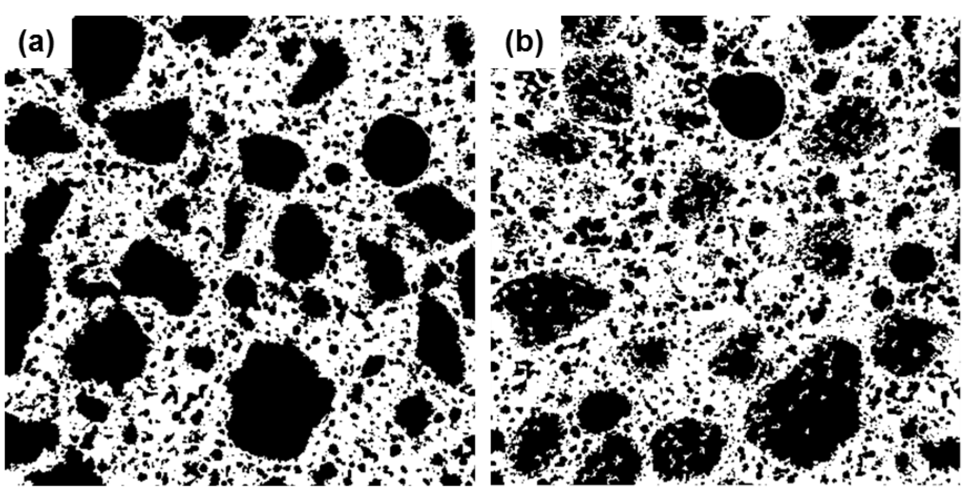

Figure 39. Binary images of hydrates for (a) UHPC (b) conventional mortar

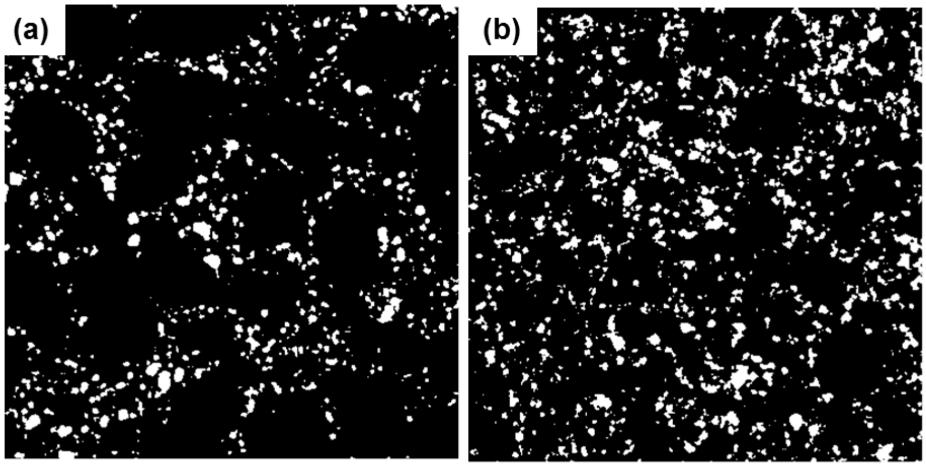

Figure 40. Binary images of anhydrates for (a) UHPC (b) conventional mortar

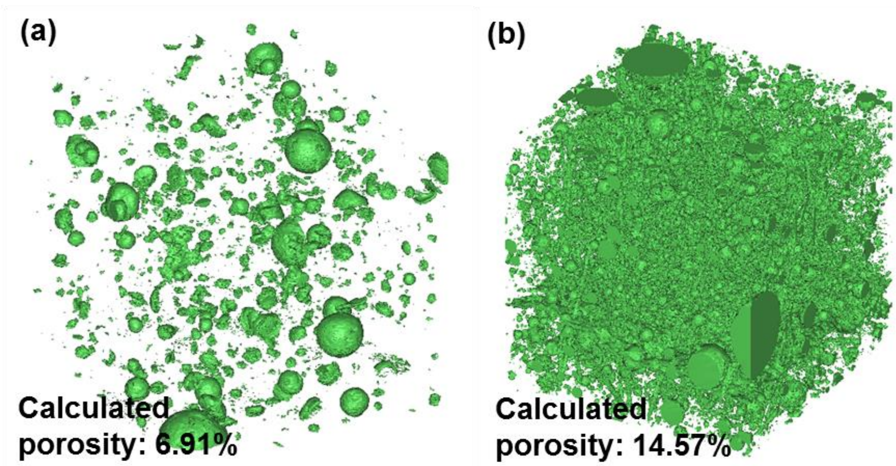

Figure 41. Reconstructed 3D images of pores for (a) UHPC (b) conventional mortar

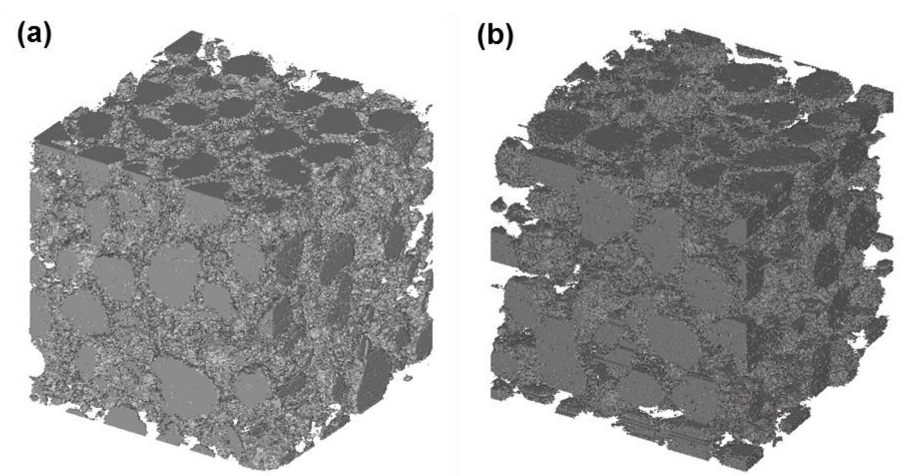

Figure 42. Reconstructed 3D images of sands for (a) UHPC (b) conventional mortar

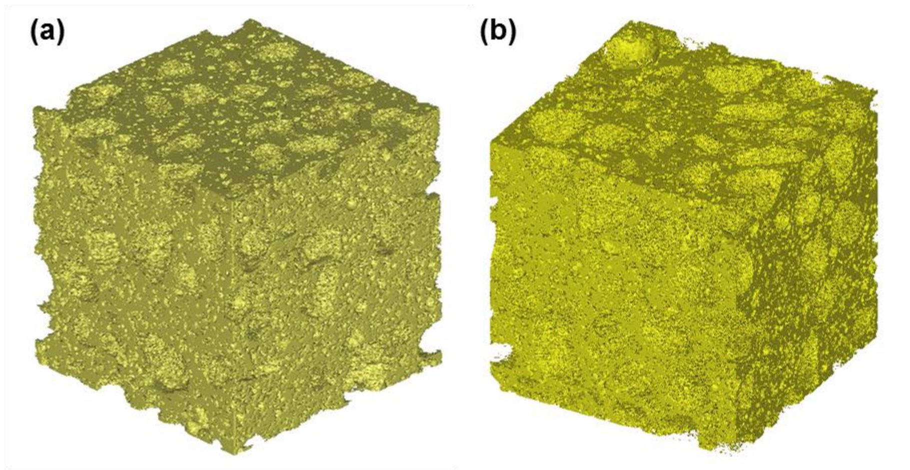

Figure 43. Reconstructed 3D images of hydrates for (a) UHPC (b) conventional mortar

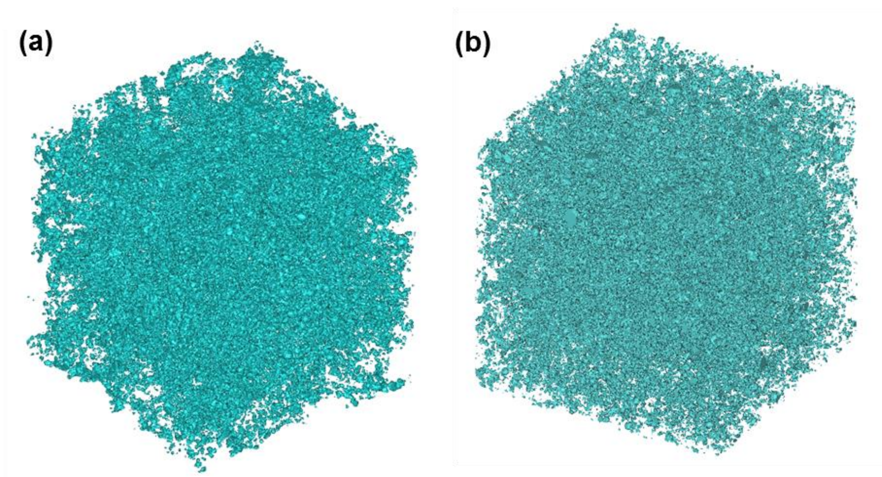

Figure 44. Reconstructed 3D images of anhydrates for (a) UHPC (b) conventional mortar

Figure 41 shows the comparison in the three-dimensional pore distributions of UHPC and control mortar. Image analysis was performed on the two figures to obtain the calculated percentage of porosity in the hardened state, yielding 6.91% for UHPC and 14.57% for the control mortar, showing that the total number of macropores in UHPC is significantly lower than that of conventional mortar. The calculated percentage of porosity gives a direct and qualitative indication of the significantly higher compressive strength of UHPC compared to conventional mortar. This experiment has successfully given a meaningful explanation of the ultra-high strength property of UHPC.

2.7. Microstructure Characterization of UHPC through Scanning Electron Microscopy

In addition to the use of three dimensional micro-CT technology to characterize the internal microstructure of the pores of UHPC, scanning electron microscope (SEM) was also used to analyze the surface microstructure topography of UHPC. An SEM produces images by scanning the sample with a focused beam of electrons, a simplified operating schematic of an SEM is shown in Figure 45. A field-emission electron source creates an electron beam that is filtered and focused through various apertures and beam lenses to ultimately bombard the sample surface with a focused electron beam. Collision between the electrons from the beam and the particles in the sample causes an emission of secondary electrons from the sample [55, 56], which were collected by the detector and displayed on a computer monitor. The SEM images obtained from scanning and detection of the secondary electrons provide information on the surface topography of the samples. The machine used for this project is a LEO 1525 field emission SEM with acceleration voltage between 100V to 30kV. All SEM images in this report were taken at 15kV.

Since SEM imaging relies on the collection of secondary electron emission from samples for samples that are not naturally electrically-conductive, the samples must be either attached to an electrically-conductive base surface, or deposited with another thin conductive material layer to facilitate the production of secondary electrons without interference.

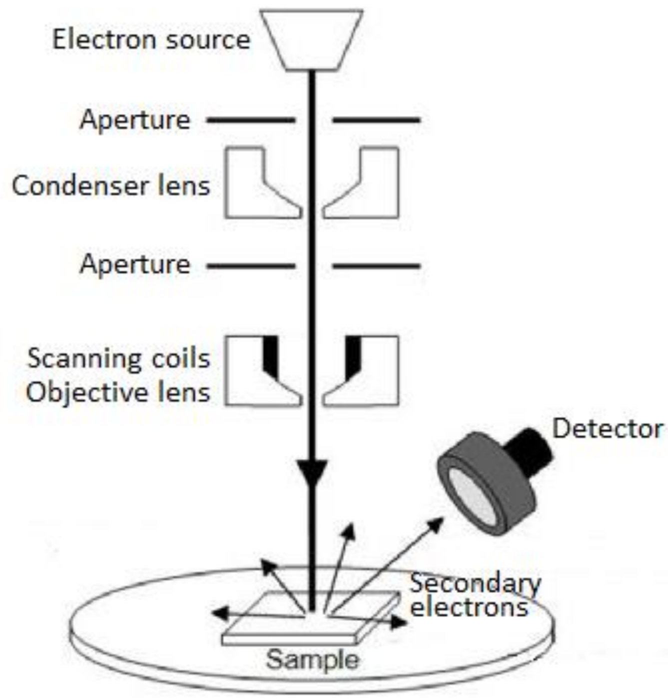

Figure 45. Schematic of scanning electron microscope

2.7.1. Sample preparation

In this study, SEM imaging was performed on UHPC specimens and conventional concrete specimens, as well as their constituent raw materials in powder form. Preparation of the powder sample was performed by depositing a small amount of powder on an electrically-conductive carbon tape that was attached to the specimen holder. The sample was subsequently subject to a stream of air to dislodge excess unattached powder particles.

For larger specimen preparation, small cubed specimens were obtained by cutting the cylindrical specimen with a tile saw. Samples were then cracked by applying impact force using a ball-peen hammer on the cubed specimen, as shown in Figure 46. This method was preferred In order to obtain an untouched surface and to avoid the attachment of any impurity from cutting tools on the studied surface. Solid samples were cleansed thoroughly with isopropyl alcohol to remove any dirt and oil particles on the surface and within the pores of the specimen. Since the porous matrix of concrete may trap liquid, the subsequent cleansed specimens were heated in an environmental chamber for 24 hours at 60ºC in order to thoroughly de-gas the samples to shorten vacuum pumping time in the SEM chamber, which requires an operating condition of 2×10^{-5}Torr pressure. Non-electrically-conductive samples cannot emit secondary electrons; therefore a thin layer of electrically-conductive material is sputter-deposited on the surface of the samples. In this study, 10nm of gold was used as the specimen coating. Dry etching with argon gas was performed before deposition in order to increase surface adhesion of the gold particles on the samples.

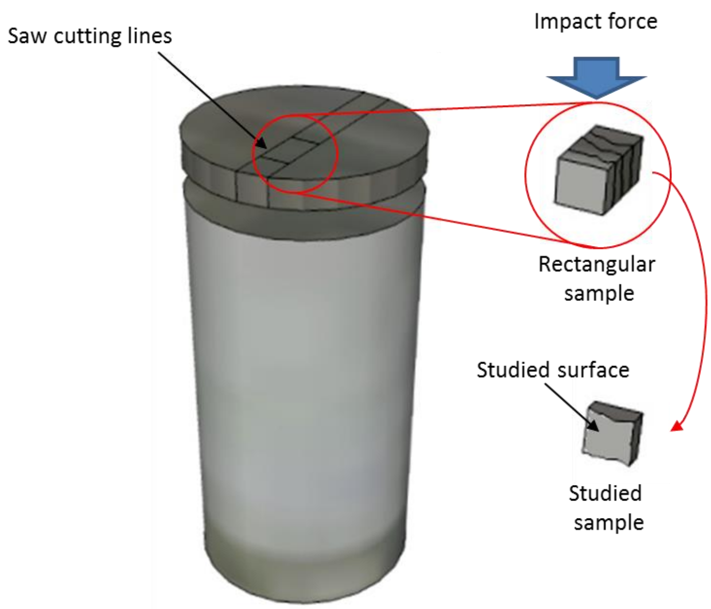

Figure 46. Specimen preparation

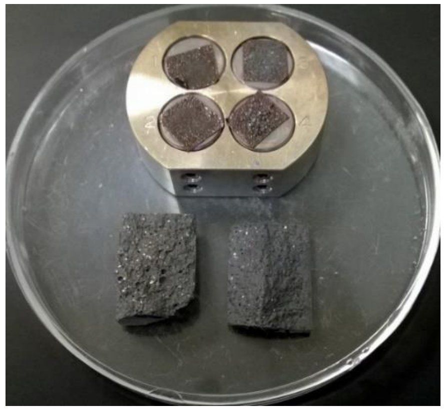

Figure 47. Setup of powder samples on a specimen holder, and larger UHPC samples

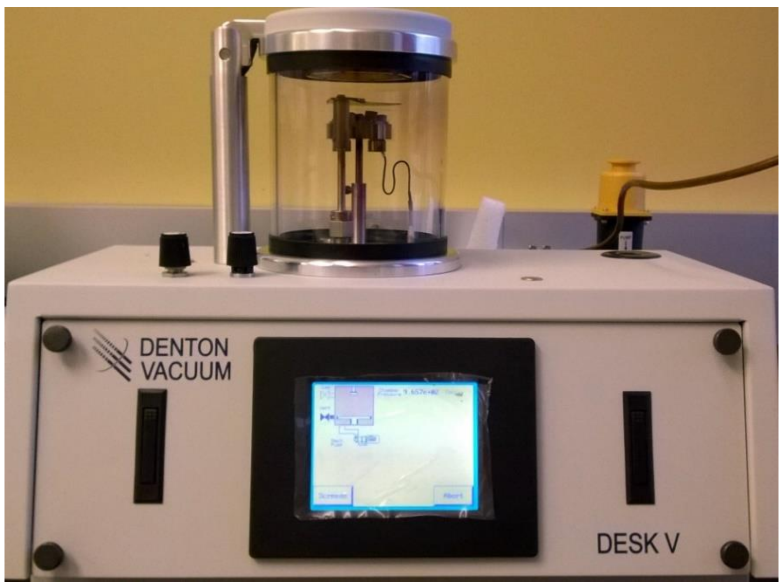

Figure 48. Etching and sputter deposition machine

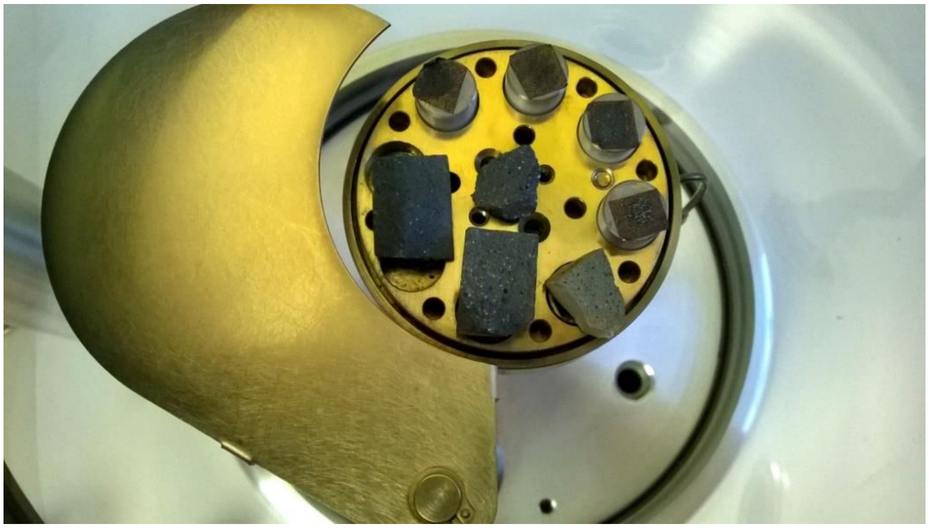

Figure 49. Appearance of samples after gold coating

2.7.2. SEM results

A comparison of the results obtained by SEM of UHPC, conventional concrete and its constituent raw materials provided us with a basis of a qualitative description of the effect of each raw material. Raw material images were reported in Section 2.2. The cracked surface of the UHPC sample compared with conventional concrete can be seen in Figure 50. Through observation of sand particle on the cracked surface of UHPC, it was evident that the silica grains in UHPC were cut through from the impact force introduced by sample preparation. The silica grains were recognizable by comparing the shape and size of the materials to Figure 5 and Figure 6. This denotes that the hydrated cement paste with very a low water cement ratio has higher tensile strength than silica sand particle. In contrast, for the studied surface of conventional concrete, we can see the outer surface of sand and the appearance of detached sand particles, showing the failure of the paste around the sand particles.

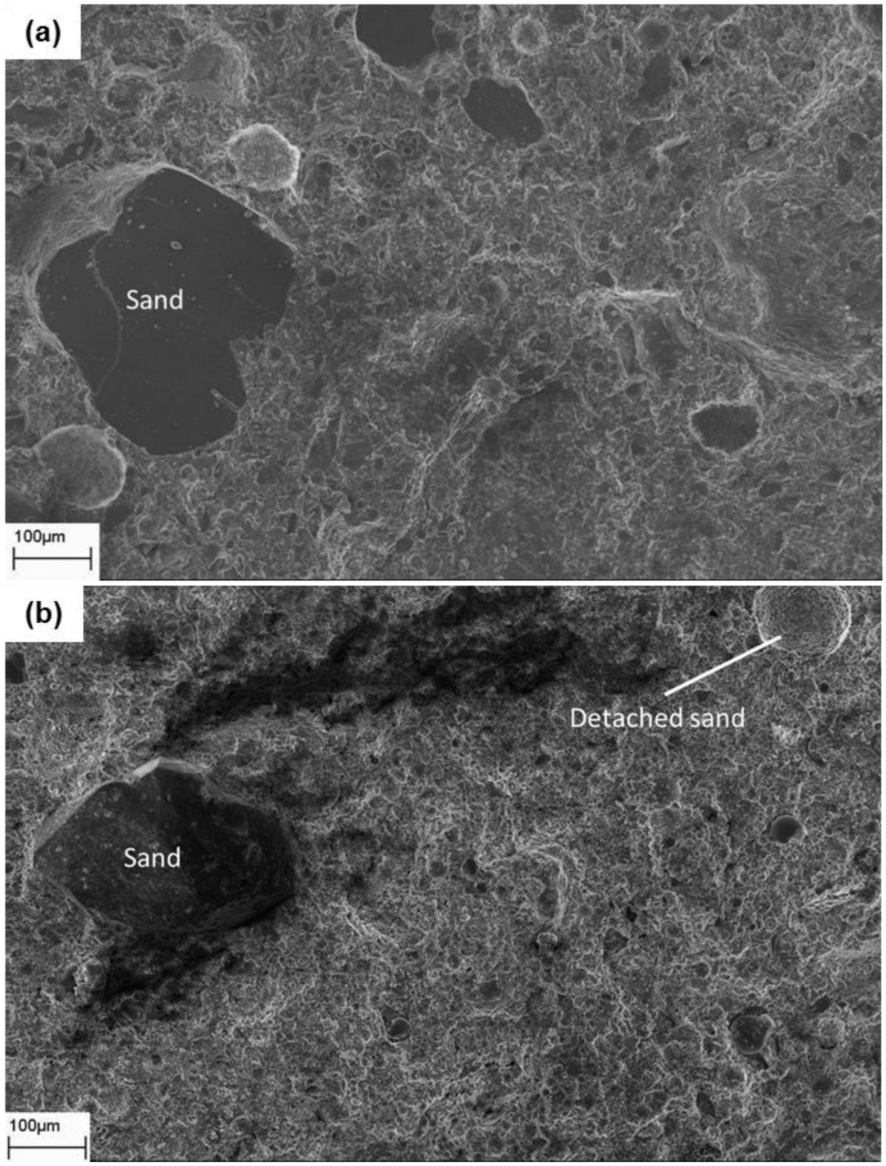

Figure 50. Cracked surface of (a) UHPC (b) conventional mortar sample

In higher magnifications, large numbers of needle-like crystalline ettringite are visible throughout the hydrated compounds, especially around the transition zone of a detached sand particle, as shown in Figure 51. Ettringite is a hydrous calcium aluminum sulfate mineral ($Ca_6Al_2(SO_4)_3(OH)_{12}\cdot 26H_2O$) that is formed in the air voids in concrete. It results from the reaction of calcium aluminate with calcium sulfate, both present in Portland cement. However in UHPC samples only C-S-H layers, small numbers of calcium hydroxide, unhydrates and aggregates are visible (Figure 52). The structure of C-S-H layers in UHPC appears solid, thus explaining the higher tensile resistance it possess.

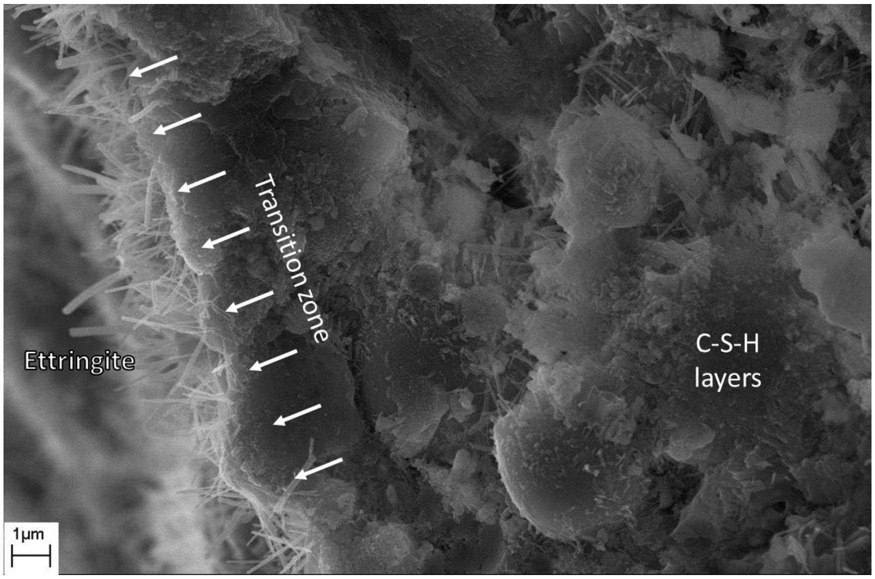

Figure 51. Microstructure of conventional concrete surface at high magnification

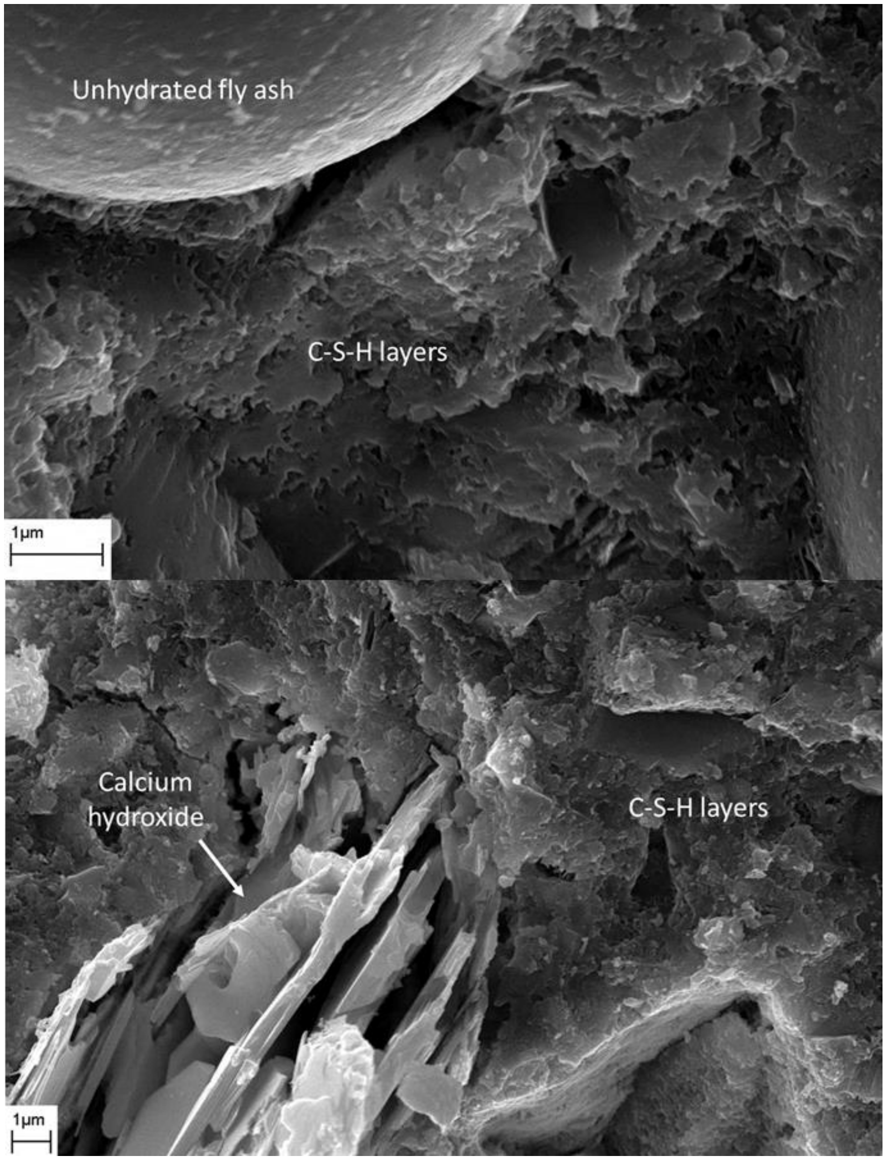

Figure 52. Microstructure of UHPC at high magnification

2.8.Quality Control Guidelines for UHPC Processing

UHPC was produced in bulk quantity of six cubic feet per batch without the need of special heat and pressure treatment by using a conventional concrete mixer and ingredients commercially available in the United States. Equipment, materials and a detailed procedure are described below as quality control guidelines for future material production.

2.8.1. Instruments and apparatus

2.8.1.1. Mixing and casting

- Concrete mixer - gravitation-based mixer with a capacity of 11 cubic feet
- Containers for raw materials - 20 to 30 gallon capacity containers, 5 gallon buckets
- Sample container - a pan or wheelbarrow for transporting materials from mixer to mold
- Weighing scale with capacity higher than 285 lbs.
- Cylinder molds - diameter 4 in. and height 8 in.
- Water tank or curing box, burlap
- Shovels, scoops, trowel and mallet
- Safety equipment (particulate respirator, gloves, safety goggles)

2.8.1.2. Quality measurements

- Slump flow mold (Abram's cone), conforming to description in ASTM C143
- Base plate (non-absorbent, smooth, and rigid) with a 20 in. inscribed circular mark
- Box beam level
- Measurement tape or ruler
- Stopwatch
- Material testing system, capable of carrying out compression test with capacity higher than 300kips
- Concrete cylinder grinder
- Pressure air meter

2.8.2. Materials and source:

- Portland cement type I: TXI, Martin Marietta Materials
- Undensified silica fume: Norchem, Globe Metallurgical, Inc.
- Low calcium, class F- fly ash: Boral Material Technologies
- Whole grain silica, F-35: U.S. Silica
- Ground silica, SIL-CO-SIL 250: U.S. Silica
- Fine ground silica, MIN-U-SIL 5: U.S. Silica
- High range water reducer, ViscoCrete 2110: Sika A.G.
- Tap water

Table 8. Material Proportion

PROPORTION	Weight per ft^3 volume (lb)
Cement	47.51
Silica fume	9.50
Fly ash	2.38
Fine sand 1	53.21
Fine sand 2	13.30
Fine ground silica	9.50
Water	10.76
Superplasticizer	2.85

2.8.3. Mixing and casting procedure

1. Prepare and weigh all ingredient materials according to the required volume (see Table 10).

2. Clean and pre-wet mixer
3. Put all the dry aggregates (whole grain silica, ground silica and fine ground silica) into the mixer. Cover mixer opening to prevent material loss during mixing process and dry mix for 5 minutes.
4. Add all cementitious materials (cement, silica fume and fly ash) into the mixer. Cover the mixer opening and continue to dry mix for another 5 minutes.
5. Add high-range water reducer to the total weighed water, then gradually add the mixture into the dry mix in the mixer while the mixer is still running.
6. Check if there is any dry material that is attached to the mixer wall. Hit the mixer wall with mallet or scrape off the material from the mixer wall if necessary. Adjust the angle of elevation of the mixer as low as possible for better mixing, while preventing the material from spilling out. Continue the mixing for 10 minutes and visually observe until the material forms a uniform paste.
7. Carefully pour the material into the wheelbarrow and cast it into the molds. Carefully flatten the surface with a trowel. Prepare at least three cylinders for compression test. No vibration is needed.
8. Prepare base plate and slump flow mold on a leveled ground. Put the mold in the middle of the base plate and hold the mold firmly.
9. Pour material into the mold up to the brim.
10. Carefully lift the mold upward and count the time since the lifting up of the mold until the material reaches the 20-inch inscribed mark on the base plate. Record the time.
11. Measure the diameter of the spread out UHPC and record the spread value.

12. Take measurement of the air content with the pressure method according to ASTM C231, if required.
13. Remove the specimens from the mold at 48±4 hours after casting and cure specimens according to ASTM C31. Protect the surface of structural member specimens from water loss with wet burlap and store cylinder specimens in a water tank or a moist-curing box at temperature 23±2ºC.
14. At 28 days after casting, take the cylinder specimens out from the curing environment. Flatten the top surface of cylinder specimen by using a concrete grinder. Carry out compression test in accordance with ASTM C39.

2.8.4. Suggested acceptance criteria:

- Slump flow: 25.5–28.5in.
- Compressive strength: >22ksi
- Air content: 5±1%

2.9.Summary

A new class of ultra-high performance concrete (UHPC) that possesses a compressive strength of more than 22ksi (150MPa) with self-consolidating property was developed, and it is suitable for modular construction. The material can be mass produced by using a conventional concrete mixer and commercially available ingredients in the United States. The material design approach includes packing density and particle size distribution analysis. Various parameters were studied through 60 mixture proportions to obtain the optimum mixture that reaches the desired compressive strength and acceptable flowability. An optimum proportion was selected for large-scale processing and self-consolidating property characterization of UHPC.

X-ray micro-computed tomography (micro-CT) was adopted to derive three-dimensional morphological data on developed new UHPC material in comparison with regular conventional concrete. A systematic micro-CT-based image processing method was established for mathematically quantifying the morphological structure of pore network. A significant lower porosity as well as pore connectivity can be found in UHPC, which gives a fundamental explanation with respect to the high strength and robust durability properties of UHPC compared with conventional concrete. A scanning electron microscope was also used for microstructure study by capturing images of the raw material constituents of UHPC and comparing microstructural topography of UHPC with conventional mortar. A proof of stronger hydration products was observed on UHPC material accompanied with a larger amount and more solid structure of C-S-H layers compared to conventional mortar.

3. DURABILITY CHARACTERIZATION OF UHPC

The durability of concrete is a highly desired characteristic especially for nuclear infrastructure applications in addition to strength, toughness and workability. Durability is the ability to exist for a long time without significant deterioration [57]. Durable structures generally have a longer life span expectancy, and contribute to less environmental waste due to minimal reconstruction and repair works from higher resistance to deterioration. The durability of concrete may be defined as the ability of concrete to resist weathering actions, chemical attacks, and physical abrasions while maintaining its desired engineered properties [58]. Since durability is an extended time property, material durability studies generally require a long time period. In this project, various tests have been devised to measure durability, such as the transport properties of concrete materials; each of these tests is performed over a long period of time. UHPC as a new class of material has been expected to show better performance in transport properties, as well as improved mechanical capacity due to its low porosity that is obtained from very low water-to-cement ratios and outstanding packing density. The results of the various UHPC durability tests are reported below.

3.1. Transport properties of UHPC

The durability of concrete materials is closely related with its transport properties. Deterioration in concrete structures is caused by many phenomena that involve the migration of substances into and out from concrete materials, or through concrete into the reinforcement inside concrete members. Therefore, transport properties are one of the main concerns in durability issues. Permeability, diffusion and electromigration are some of the common transport properties. Permeability is defined as the property of concrete which measures how fast a fluid will flow through it when pressure is applied. Diffusion is a process by which an ion can pass through saturated concrete without any flow of water. Electromigration occurs when an electric field is applied across a concrete sample, causing negative ions to migrate to the positive electrode, and vice versa, and can be measured from the electrical resistance of the concrete [59].

3.1.1. Chloride diffusivity

Chloride diffusivity is a common and serious issue that can lead to deterioration of material and corrosion of the reinforcement, thus affecting the durability of the structure. It is widely accepted that the ability of concrete to resist ingress of chloride ions can result in a significantly more durable concrete. Chloride penetrates into concrete mainly by diffusion, and to a lesser extent, by capillary absorption and hydrostatic pressure. In order to study chloride penetration in concrete, a clear understanding of the role of the porous matrix, as well as the reaction between chloride ions and concrete is vital. The diffusion of chloride through the solid portion of a concrete matrix is negligible when compared to the rate of diffusion through the pore structure. Since concrete is non-homogeneous, the rate of diffusion is controlled not only by the diffusion coefficient through the pores but also by the capillary pore structures, which are directly influenced by the water-to-cement ratio of the concrete, the involvement of cementitious admixtures that subdivide the pore structure and the degree of hydration of concrete. Furthermore, concrete is not inert to chlorides. Chloride ions may react with the concrete matrix and become chemically or physically bound, which reduces further rate of diffusion. The chloride binding capacity can be controlled by the cementitious materials used in the concrete [60].

Chloride diffusivity in concrete is conventionally determined by immersion as standardized in ASTM C1543 (comparable to AASHTO T259) [61, 62]. This requires at least 90 days of ponding of a concrete slab with 3% sodium chloride, coring of the slab and pulverizing parts of the specimen on at least four different depths. The powder is then further processed through a series of chemical procedures for the measurement of chloride content in each of the samples according to ASTM C1152 [63]. Due to the long duration required and tedious steps to perform this conventional method, it does not meet the engineering requirements to rapidly evaluate existing structures and new materials [64, 65].

Developed by D. Whiting, an alternative approach that is standardized as ASTM 1202 is to use electromigration [66]. This method of using electrical indication to approach concrete permeability is known as the Rapid Chloride Permeability Test (RCPT) or Coulomb Test, due to the rapid obtainment of the result compared with the chloride solution ponding method. Concrete conductivity and its variation over time are related to material porosity and permeability [67], and the comparison between the results of RCPT and the 90-day ponding test gives a linear correlation between the two methods with a 95% confidence limit [68]. In RCPT, the electrical conductivity of concrete is used as an index to represent its diffusivity. The 6-hour test yields the total charge passed through the concrete sample, which is an indirect indication of the chloride ion penetrability. The permeability of concrete is highly dependent on the pore structure that is related to the degree of hydration of the material. A study done on pore structure and charge passed from RCPT in mineral-free cement-based materials demonstrated an exponential increase in charge passed as coarse capillary pore volume increased [69].

A measurement on several bridge deck concrete mixes investigated at AMEC shows current passed between 100-1000 Coulombs after 90 days. Conventional concrete with charge passed in this range falls into the category of very low chloride ion penetrability according to classification based on ASTM C1202 that is shown in Table 9. In general, there is no significant difference found in chloride permeability among specimens at 90 days and later [70]. Another study done on UHPC material with various steam curing at 28 days and 56 days resulted in charge passed being classified as very low to negligible chloride ion penetrability [71]. Many types of UHPC that require special compaction and curing such as pressure and heat treatments, were found to be impermeable due to their low capillary porosity [72].

Table 9. Chloride ion penetrability based on charge passed according to ASTM 1202

Charge Passed (Coulombs)	Chloride Ion Penetrability
>4000	High
2000-4000	Moderate
1000-2000	Low
100-1000	Very Low
<100	Negligible

1.1.1.1 *Specimen and test setup*

UHPC specimens were prepared from 4-inch diameter cylinders with an 8-inch height that were casted according to ASTM C192 [73] without tamping. These specimens were cut using a wet masonry saw to the thickness of 2±0.04-inch tolerance (Figure 53 and Figure 54).

Prior to the RCPT measurement, specimens were conditioned in a vacuum desiccator using a vacuum pump for three hours, introducing negative pressure to >0.95 bar into the chamber. Distilled water was then instilled into the vacuum system until the entire specimen was immersed in water, and then the pumping was continued for another hour. The vacuum was vented and the specimens remained immersed in distilled water for another 18 hours. After conditioning, concrete samples were installed in between measuring cells. Distilled water from the specimen conditioning was poured into the measuring cells to confirm that no leakage occurred on the cells before they were filled with proper solutions.

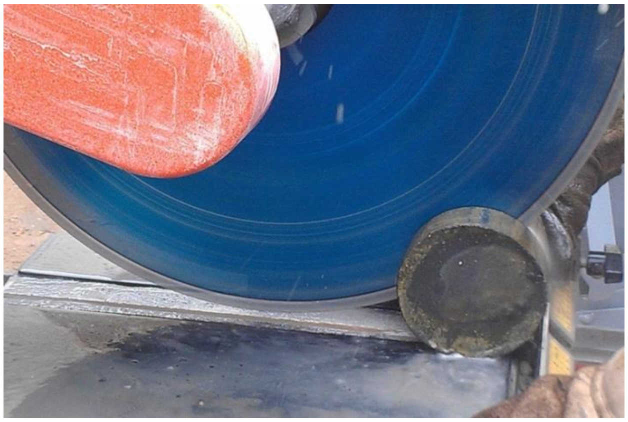

Figure 53. Cutting of cylindrical specimens using wet masonry saw

Figure 54. Cylinder specimens for rapid chloride penetration test

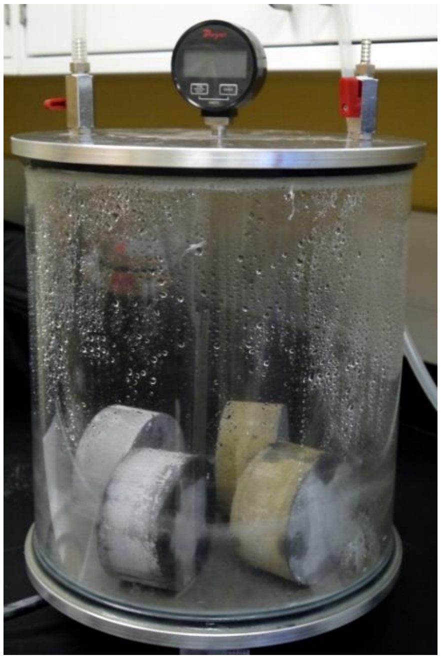

Figure 55. Conditioning of specimens with a vacuum desiccator

Approximately 250mL of solution was poured into respective measuring cells with 3% sodium chloride solution on the anode and 0.3M sodium hydroxide solution on the cathode. These two measuring cells were connected to a power supply through the electrodes. With the flow of electric current that was maintained under 60V DC potential for a six-hour period, anionic chloride was repelled from the anodic side into the specimen. In the case of a higher penetrability specimen, a larger number of ions were transported into the material, which created a higher conductivity between the anode and cathode, indicated by a larger current reading.

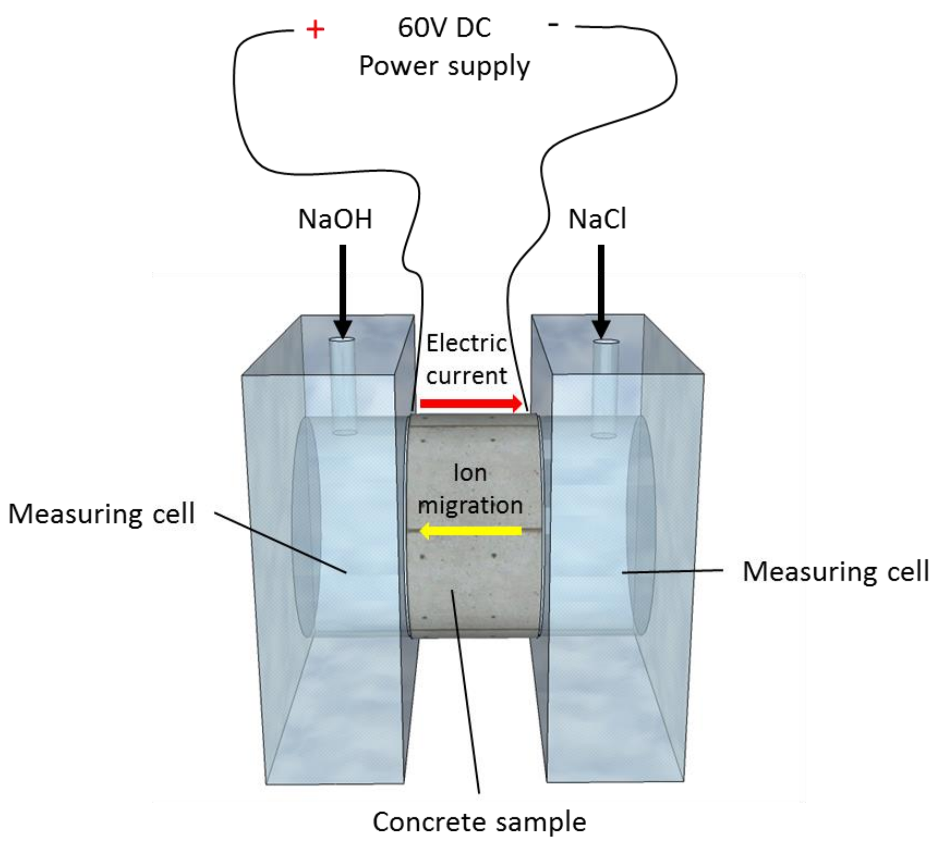

Figure 56. Test setup for RCPT

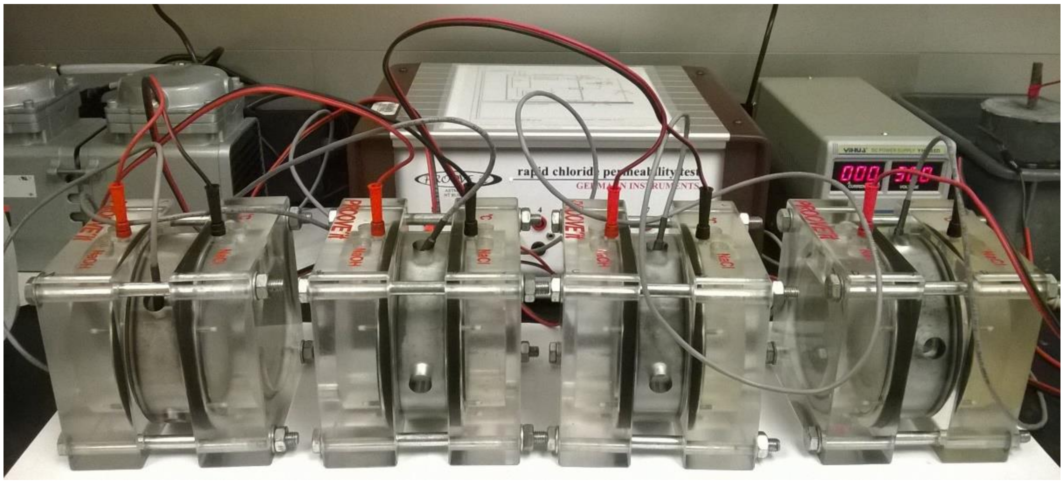

Figure 57. Rapid chloride permeability test measurement in progress

1.1.1.2 *Conductivity and charge measurements*

The rapid chloride permeability test was performed on UHPC and conventional concrete specimens at 28 days and 90 days. Measurement of the current through the distilled water-saturated concrete sample was obtained every five minutes for a total of six hours. The total charge passed through the sample can be obtained by an integration of the current over time, as expressed in the equation below:

$$Q = \int_0^T I(t)\, dt \tag{4}$$

where

Q = charge passed (Coulombs)

I = electrical current (A)

t = current testing time (s)

T = total testing period (6 hours)

Since the measurement was performed in 72 steps at five minute intervals yielding a total of six hours, integration could be done in a simplified calculation shown in Equation (5):

$$Q = 150^{(sec)} \frac{(I_5 + 2I_{10} + 2I_{15} + \ldots + 2\, I_{350} + 2\, I_{355} + I_{360})^{(mA)}}{1000} \quad (5)$$

The UHPC rapid chloride permeability measurement resulted in an average of 48.87 Coulombs of charge passed at 90 days, which is categorized as negligible; 203.52 Coulombs at 28 days, which is categorized as very low; while conventional concrete samples resulted in an average of 4748.16 Coulombs and 3207.89 Coulombs at 28 days and 90 days, respectively. The difference of nearly two orders of magnitudes can be explained by the small number of pores existing in the UHPC cementitious matrix due to the low water-to-cement ratio and high packing density. The conductivity is also an indirect indication of chloride penetration, which depends upon the same porosity properties. The results are shown in Figure 58 and Figure 59.

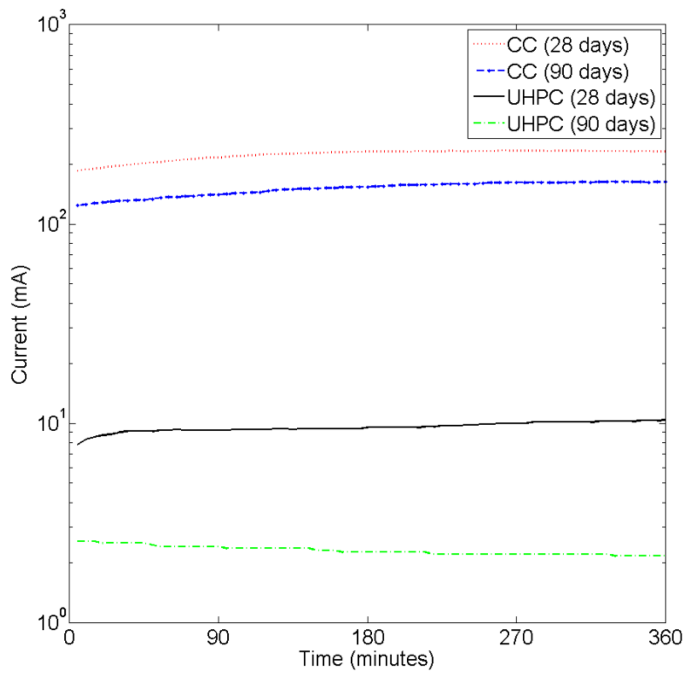

Figure 58. Current measurement of UHPC and conventional concrete specimens under 6V DC within 6 hours period

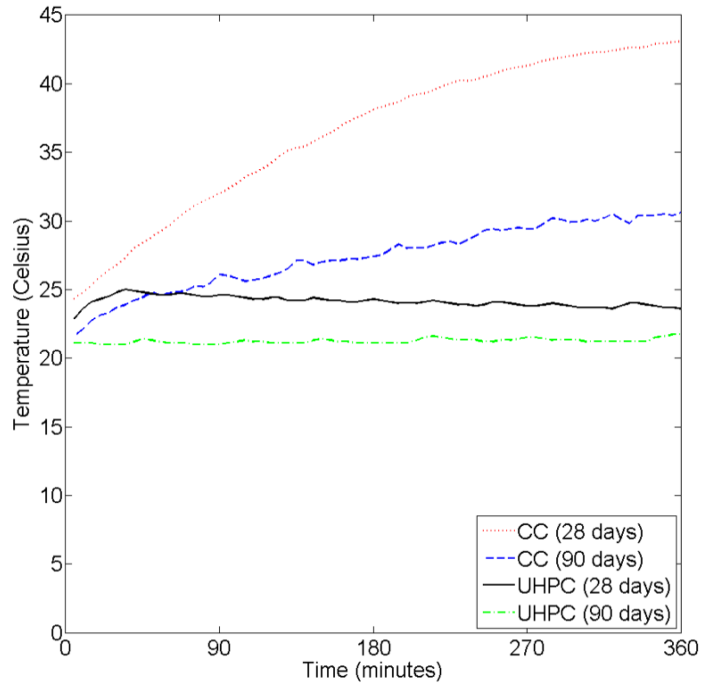

Figure 59. Temperature within specimen during RCPT measurement

Conductivity of the concrete is calculated by Equation (6)

$$\sigma = \frac{Q}{V\,t}\frac{L}{A} \tag{6}$$

where

σ = bulk conductivity (Siemens/meter)

V = applied voltage (V)

L = length of the specimen (m)

A = specimen cross sectional area (m^2)

t = total measurement period (s)

As the experiment proceeds, more ions migrate into the concrete causing an increase in the conductivity of the specimen. However, the net change in conductivity during the test also depends on the amount of chloride ions binding to the concrete matrix which decreases conductivity and a possible increase in the temperature (due to the application of high voltage), which decreases the conductivity according to Equation (7):

$$\rho(T) = \rho_0[1 + \alpha(T - T_0)] \tag{7}$$

where

ρ = resistivity at temperature T (Ω)

ρ_0 = resistivity at temperature T_0 (Ω)

α = temperature coefficient of resistivity

T = temperature (ºC)

T_0 = fixed ambient temperature (ºC)

The net conductivity is observed to decrease slightly for UHPC, and increase slightly for conventional concrete due to the net interaction of the aforementioned reasons. The calculated bulk conductivity is 22.96mS/m and 15.51mS/m for control concrete at 28 and 90 days, and 0.98mS/m and 0.24mS/m for UHPC at 28 and 90 days, respectively.

Table 10. Total charge passed and conductivity in rapid chloride permeability test

		UHPC	Control Concrete
Charge passed (Coulombs)	28 days	203.52	4748.16
	90 days	48.48	3207.89
Conductivity (millisiemens/meter)	28 days	0.98	22.96
	90 days	0.24	15.51

3.1.2. Water permeability

Most processes that cause deterioration in a concrete structure are related to water movement in concrete. Ions that cause corrosion on reinforcement can move through water or move with the water. Both the movement of water and ionic movement in the water may cause damage to concrete. Thus, water permeability is closely related to durability. Permeability in concrete is defined as the property that measures the flow rate of liquid under pressure application [59].

Concrete degradation on the surface layer alters its porous structure. Pores and cracks on the surface layer can be represented by its permeability [74]. The Germann water permeability test (GWT) measures the flow of water on a designated surface over a period of time under a defined pressure [75]. The GWT water chamber is firmly attached to a selected surface through a 15mm gasket with two pliers that are anchored into the concrete. Water is filled into the water chamber and a defined pressure is applied into the concrete surface. The pressure decreases as water permeates into the concrete. A 10mm steel pin is inserted into the water chamber to maintain the defined pressure over a specified time. The length of the steel pin insertion measured with a micrometer gauge is recorded, and calculation can be done for some variables that are selected to represent water permeability as written below:

$$h_t = \left(\frac{d}{D}\right)^2 (g_0 - g_t) \tag{8}$$

where h_t = water penetration depth at time t (mm)

d = diameter of steel pin (10mm)

D = inside diameter of water chamber gasket (62mm)

g_0 = micrometer gauge reading at the beginning of measurement (mm)

g_t = micrometer gauge reading at time t (mm)

A section of a non-cracked flat vertical surface of a UHPC beam was selected as an area of interest as well as a 3600psi concrete slab as the control specimen. Full hydration in both specimens are ensured by using samples that are over 90 days. Two anchoring holes were drilled with a distance of 25cm across the area. Paint was removed from the surface to ensure direct contact of the water to the specimen surface. The water permeability test setup is demonstrated in Figure 60. Teflon tape was used on all the threaded parts of the GWT instrument. The system was inspected for water leakage upon test setup and application of 1 bar pressure on the water chamber. High vacuum grease was used to seal the leakage on the water chamber.

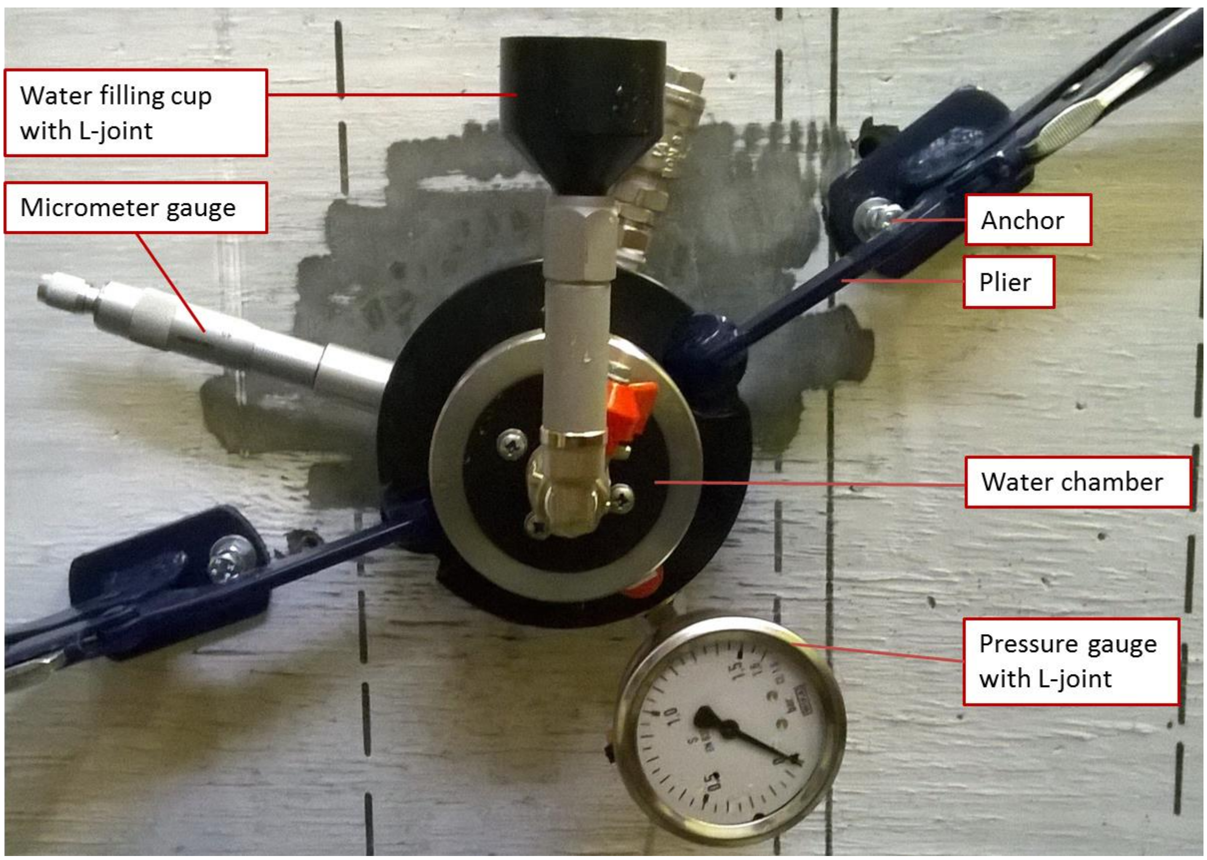

Figure 60. Water permeability test setup with GWT-4000

Depth of water penetration that is dependent on time can be fitted to a curve with function:

$$h_t = a + s\sqrt{t} \tag{9}$$

where

a = intercept

s = sorptivity index (mm/s$^{0.5}$)

The water migration rate signified by sorptivity is susceptible to the microstructure of the material. A lower sorptivity value is desired for higher expected durability [76]. Water permeability test results on UHPC and the control specimen are shown in Figure 61. The maximum limit of the micrometer gauge (20mm) was reached after a 200-second measurement on the concrete specimen; however on UHPC specimens it was not reached even after a 15-minute measurement. The sorptivity index was found to be 0.01386mm/s$^{0.5}$ on UHPC and 0.05554mm/s$^{0.5}$ on the control concrete specimen, once again confirming the lower permeability of UHPC compared to the control concrete specimen due to the lower number of pores and the discontinuity of the pore structures in UHPC.

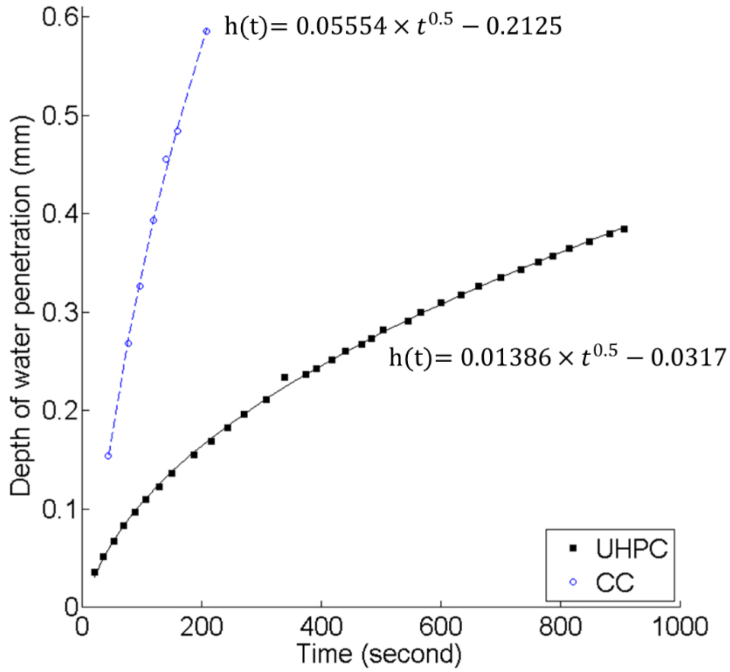

Figure 61. Water permeability measurement

3.2.Free shrinkage and restrained shrinkage

A major durability issue is related to the shrinkage of the material, which can often cause shrinkage-induced cracking in concrete. Cracking will subsequently compromise the transport properties of concrete, providing an easy path for the penetration of moisture, chloride and other hostile chemicals to cause further deterioration. Reduction of length occurs in unloaded concrete that is exposed to ambient humidity and temperature, known as drying shrinkage. Drying shrinkage is a common phenomenon that occurs when concrete is exposed to a lower relative humidity in the environment. This occurrence is also highly influenced by the pore structure of the material [77]. Shrinkage strain can be harmful because once it is constrained, it will induce tensile stress that causes cracks in concrete members due to the low tensile capacity of normal concrete.

Ultra-high performance material with high packing density may cause less concern eeith relation to drying shrinkage. However, chemical and autogenous shrinkage become a larger concern in material with a low water to cement ratio. Chemical shrinkage is also known as hardening shrinkage and is a term used for the phenomenon in which the volume of the hydrate produced by the reaction between unhydrated cement and water is smaller than the total volume of the cement and water; while autogenous shrinkage is a macroscopic reduction in length under a constant temperature without any moisture migration to or from the concrete. Autogenous shrinkage consists of a very small part of chemical shrinkage [78].

3.2.1. Free shrinkage

The shrinkage test for unrestrained UHPC was performed by measuring the length change of prism specimens according to ASTM C157 [79], as shown in Figure 62. Sixty four prism specimens with a cross sectional area of 1 square inch and a length of 11.25 inches for a gage length of 10 inches were cast for UHPC and conventional concrete in eight different environments. Gage studs were cast into the end of each prism according to the mold design specified in ASTM C490 [80]. The prism specimens were cast and demolded after 24 hours and cured in a moist chamber for three days to reach hygral equilibrium.

Figure 62. Test setup for free shrinkage measurement

Figure 63. Controlled humidity desiccator for shrinkage at different RH

Two sets of specimens were measured periodically for shrinkage under exposure to an ambient environment with temperatures between 20 to 24 ºC and a relative humidity between 40 to 70%. Other specimens were stored in different relative humidities (0%, 15%, 35%, 65%, 75%, 85%, 93%) for 28 days prior to length change measurement inside a desiccator as shown in Figure 63. Saturated salt solutions and nitrogen gas flow was used to control the relative humidity of the desiccators. Salt solutions were selected based on the required humidity and the consideration of its insensitivity to temperature variation [81-83]. Humidity control methods are described in Table 11 with consideration that the ambient temperature is 20±2°C.

Table 11. Environment control for unrestrained shrinkage specimens

Relative humidity	Environment control method
0%	Heating in oven at 105°C until consistent mass is achieved followed by cooling down to negate thermal expansion
15%	Dehumidifying by nitrogen gas flow followed by exposure to saturated lithium chloride solution (81.9g / 100mL)
35%	Dehumidifying by nitrogen gas flow followed by exposure to saturated magnesium chloride hexahydrate solution (167g / 100mL)
65%	Exposure to saturated sodium nitrite solution (51.8g / 100mL)
75%	Exposure to saturated sodium chloride solution (36g / 100mL)
85%	Exposure to saturated potassium chloride solution (34.4g / 100mL)
93%	Exposure to saturated potassium nitrate solution (31.5g / 100mL)

Initial length measurement was performed after moist curing as specified in ACI R209-92 [84]. Calculation of length change is according to Equation (10):

$$L = \frac{(L_x - L_i)}{G} \times 100 \qquad (10)$$

where

L_x = comparator reading of specimen at x age minus comparator reading of reference bar at x age

Li = initial comparator reading of specimen minus comparator reading of reference bar at that same time

G = nominal gauge length, 10 inches

ACI R209-92 provides a unified approach for predicting time-dependent concrete volume changes with simplified methods, according to the following equation [85, 86]:

$$(\varepsilon_{sh})_t = \frac{t^e}{f + t^e} (\varepsilon_{sh})_u \tag{11}$$

where $(\varepsilon_{sh})_u$ = ultimate shrinkage strain

t = time

e and f = constants

The power of t has been found to be unity for shrinkage of normal concrete in the standard condition, and the general constant f to be 30. However, for more than 200 days of length change measurement of UHPC, interpolation was performed to obtain the constants that give the best prediction equation, as shown in Figure 64. The best fit equation was chosen by the coefficient of determination, a common statistic indicator used to analyze the regression line and data point relation. The calculation for the coefficient of determination follows the equation below:

$$R^2 = 1 - \frac{\sum_i (y_i - f_i)^2}{\sum_i (y_i - \bar{y})^2} \tag{12}$$

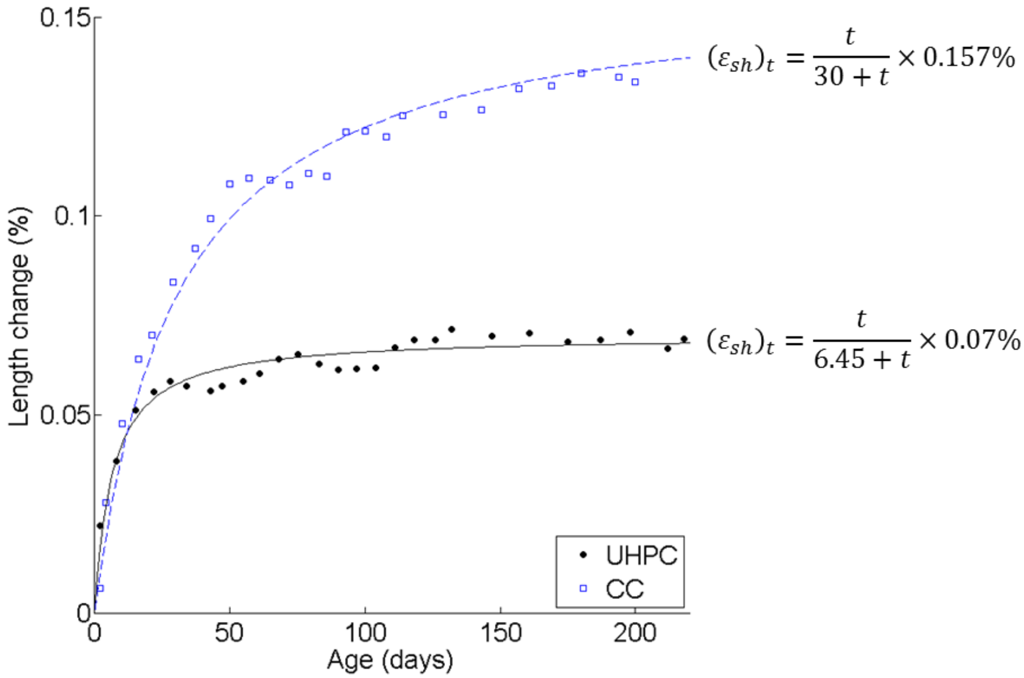

Figure 64. Length-change measurement under ambient humidity

Figure 64 shows that UHPC initially experienced a more rapid increase in length change compared to the control concrete up to 10 days of age; however it reached the shrinkage plateau soon and displayed a significantly lower shrinkage than conventional concrete at a later age. Length change measurement for over a 200-day comparison of UHPC and conventional concrete under ambient humidity shows that UHPC has significantly lower predicted ultimate length change compared to control concrete specimens. The difference gets more significant with the decrease of relative humidity as shown in Figure 65. This shows that the drying shrinkage in conventional concrete is more prominent than autogenous shrinkage that caused concern in UHPC.

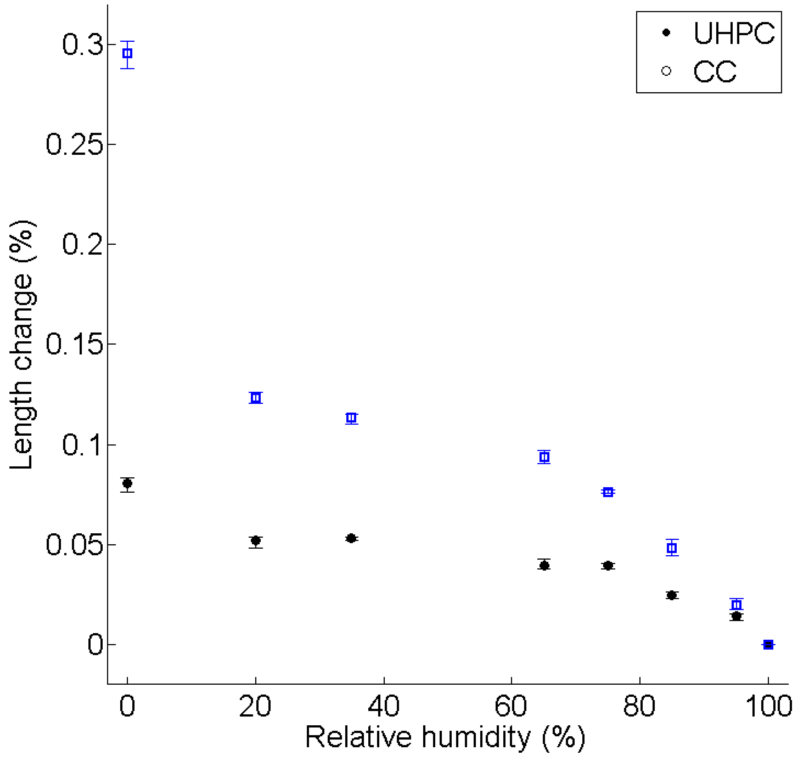

Figure 65. Measurement of length change in different relative humidity

3.2.2. Restrained shrinkage

As previously discussed, shrinkage strain can cause damage to concrete as it is manifested by tensile stress, which, upon restraint in structural application, might result in cracks. Shrinkage cracking is a major concern and can be a critical problem in concrete structures. To investigate the shrinkage cracking tendency on UHPC and conventional concrete, a test setup that follows AASHTO T334-08 [87] was adopted. The test setup and dimensions are shown in Figure 66 and Figure 67.

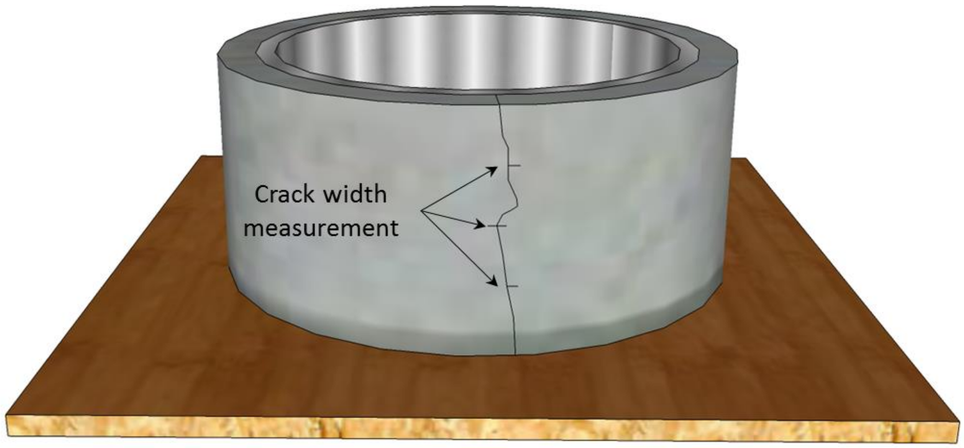

Figure 66. Test setup for crack width measurement of restrained shrinkage test

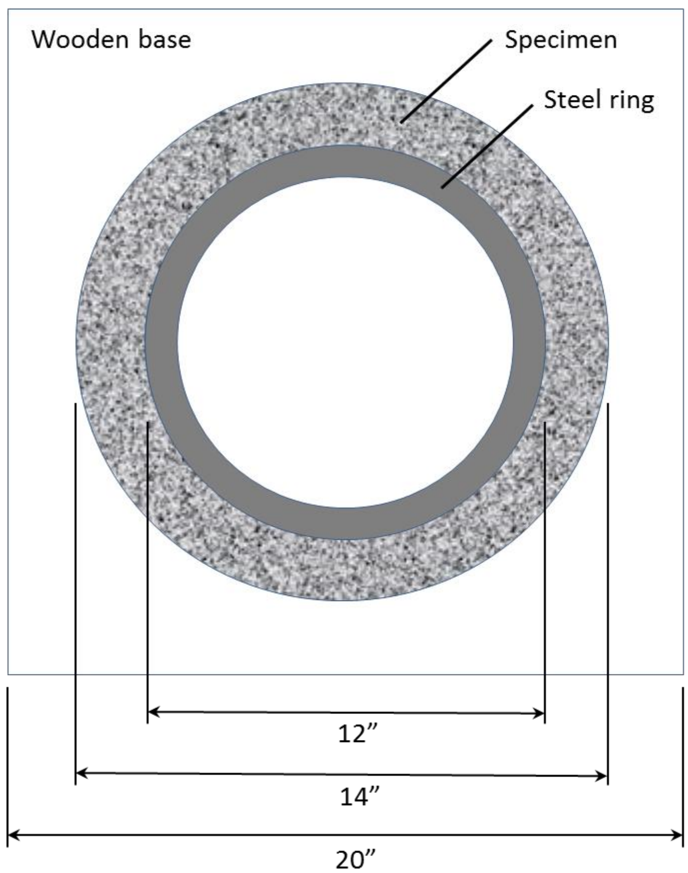

Figure 67. Specimen dimension for restrained shrinkage test

Standard steel rings with an outer diameter of 12 inches and a wall thickness of 0.5 inch were used as the inner mold. Inner and outer faces were machined smooth, round and true, and polished to minimize friction between the specimen and the steel ring as specified in AASHTO (Figure 68). The specimen is expected to experience only tensile stress and uniform constraint along the circumference.

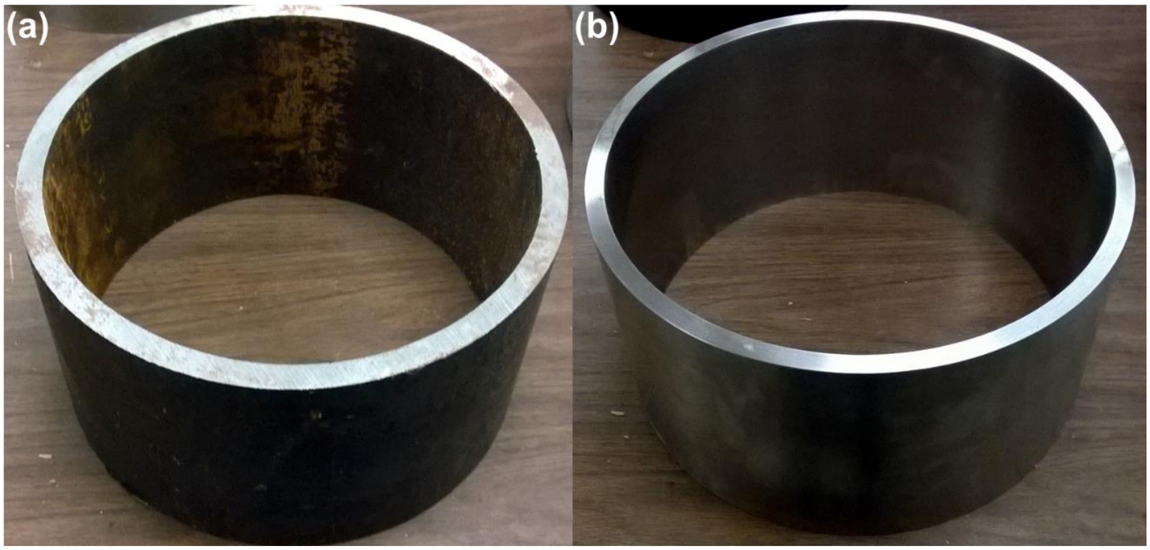

Figure 68. Steel rings for restrained shrinkage test (a) before polishing and (b) after polishing

Medium density fiber board with a thickness of 0.5 inch was used as the mold base layered with a 0.188-inch thick white melamine coated plywood as an unabsorbent layer. Both layers were cut to 20×20 inches and were attached to each other using water resistant high strength adhesives. Standard polycarbonate sheets with a width of 6 inches and a thickness of 1/8 inch were connected by rivets and formed into a 15-inch inside diameter ring as the outer mold. Both outer and inner molds were secured with 3/8 inch wooden dowels, and all connection to the wooden base was sealed with waterproof silicone sealant.

A force-based mixer with a 30 quart capacity was used for material mixing. Following casting, the specimens were covered with waterproof corrugated plastic board. They were demolded one day after casting. Top surfaces of the specimens were lined with silicone sealant to prevent water from evaporating from the top surface. Figure 69 shows the specimens after casting. Curing with wet burlap was done right after the specimen hardened to mimic the condition on site, and the burlap was kept wet for three days prior to its removal (Figure 70). While the specimen was exposed to an ambient temperature between 21ºC to 24ºC and a humidity of 40% to 60%, crack formation and development in the rings was visually monitored periodically using a crack ruler and a polymer microscope lens. For crack width surpassing 2mm, measurement was done using a caliper.

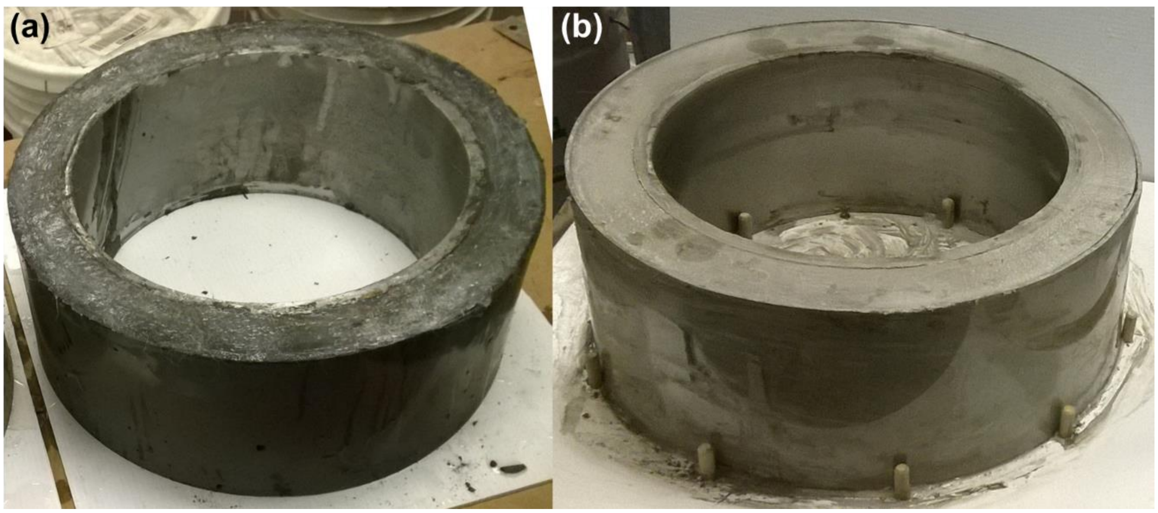

Figure 69. Cast restrained shrinkage specimens of (a) UHPC and (b) conventional concrete

Figure 70. Three days wet curing to simulate field condition

A crack of 0.85mm was found on the conventional concrete specimen on day five, while the crack on the UHPC specimen began at 0.55mm on day eight (Figure 71). Further crack developments were shown in Figure 72 and were monitored for more than 60 days. Only one crack developed on each of the specimens. Measurement results show that the shrinkage crack in the UHPC specimen was developed later with a significantly smaller crack width due to lower shrinkage high tensile strength of the material.

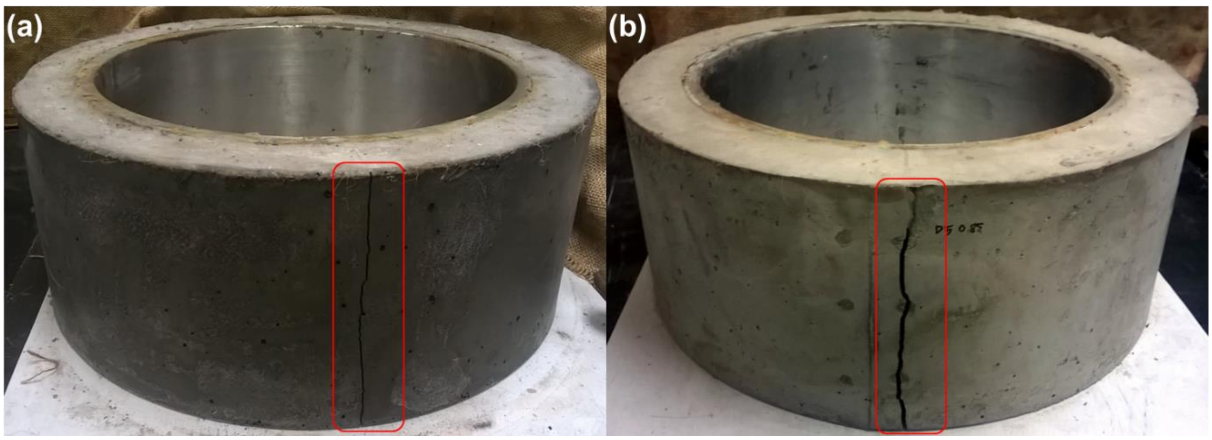

Figure 71. Cracked specimens after restrained shrinkage

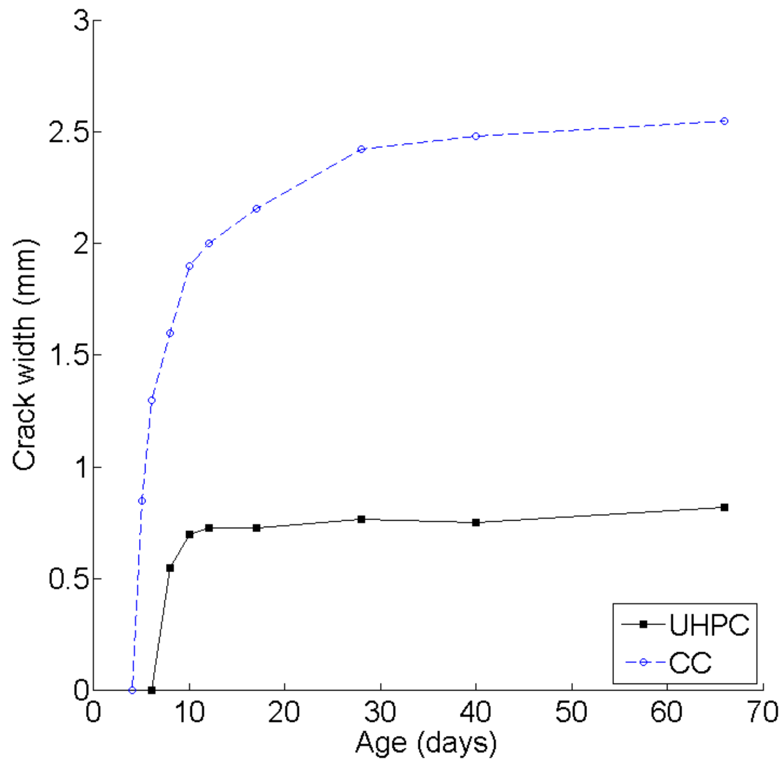

Figure 72. Measurement result of restrained shrinkage test

3.3.Alkali-Silica Reaction

Alkali-silica reaction is one of the durability problems that can cause early deterioration of concrete. This phenomenon will occur only if there are simultaneous existences of reactive silica from reactive aggregates, sufficient alkalies (from Portland cement, mineral admixtures, chemical additives, aggregates and external sources) and sufficient moisture (>80% RH, from the environment) [88]:

Portland cement is known as the main contributor of alkalies in the form of potassium oxide and sodium oxide. ASTM C150 [89] limits the quantity of equivalent alkalies in low-alkali Portland cement type I to 0.6% that can be calculated as follows:

$Na_2O_e = Na_2O + 0.658\ K_2O$

where

Na_2O_e = total sodium equivalent, in percent by mass

Na_2O = sodium oxide content, in percent

K_2O = potassium oxide content, in percent

Hydroxyl ions in a concrete pore solution react with the acidic silanol in poorly crystalline hydrous silica in amorphous aggregates, forming alkali-silicate gels. Absorption of water into these gels causes hydraulic pressure that may result in expansion and cracking around the effected aggregates in concrete. Alkali-silica reaction is more severe with the existence of calcium hydroxide [90]. $Ca(OH)_2$ that results from the reaction between lime and water provides additional hydroxyl ions that sustain the alkalinity of the material.

An ASR test of UHPC and conventional concrete specimens was performed following ASTM C1260 [91] that measures the potential for the aggregates used to undergo alkali-silica reaction. Preparation of the aggregate by crushing and grading was not required due to the absence of coarse aggregate in UHPC. Concrete control specimens were cast using regular river sand and were tested in the same manner as the UHPC specimens. Four specimens for each of both UHPC and regular concrete were prepared in a controlled room with temperature in the range of 20-27.5°C and a relative humidity >50%. The specimens prepared had a cross section of 1 square inch, a length of 10 inches and were equipped with gage studs in accordance to equipment specifications in ASTM C490 [80].

Specimens were put inside a closed container after casting for 24±2 hours before being demolded and measured for initial length reading. Curing of specimens was done by immersing in regular tap water and immediately heating the system by placing the container inside an oven at

80 ±2°C for another 24 hours. Upon removing UHPC specimens from water, another length measurement was done. Specimens were then placed in 1N sodium hydroxide solution that is obtained by mixing 40 grams of a NaOH pellet into one liter of distilled water. The system was again placed inside a 80±2°C oven for another 14 days, while length measurement was done periodically.

The Portland cement used in our UHPC experiment is low alkali cement manufactured in Texas that has a total sodium equivalent of 5.5%. Mineral admixtures used are undensified silica fume with sodium oxide and potassium oxide content each below 2%, and fly ash with a total sodium equivalent 5.6%. Well-crystalized quartz sand both in ungrounded and grounded form are used as aggregates in UHPC, thus lower alkali-silica reaction is expected. ASR potential measurement results of UHPC and control concrete specimen with compressive strength 10ksi is shown in Figure 73. Classification according to the appendix of ASTM C1260 is also shown in the figure. Measurement on UHPC gives harmless behavior, while expansion of the concrete specimen at 14 days falls between 0.1 and 0.2%, which can be harmless or harmful in the field performance [91]. Measurement on the control specimen was extended to 28 days conforming to the suggestion in ASTM 1260. It can be seen from the result that control specimens containing typical river sand had reactive behavior and fell into potentially deleterious category, while UHPC with quartz sand displays no expansion at all upon exposure to an alkali environment.

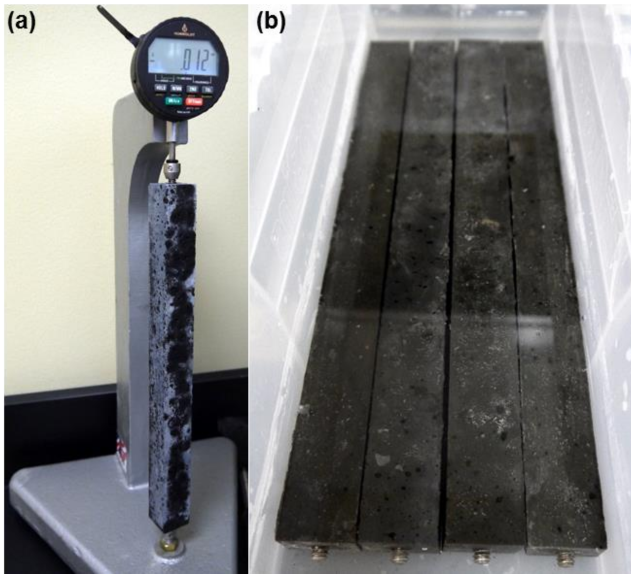

Figure 73. (a) Measurement of accelerated specimen expansion under alkali environment (b) immersion of specimens in 1M NaOH

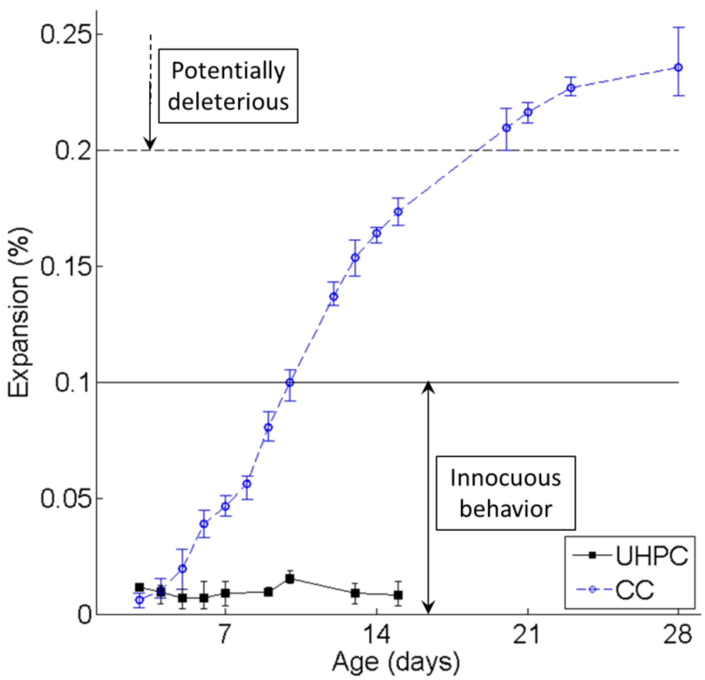

Figure 74. Expansion of control concrete specimens under alkali environment

3.4.Accelerated corrosion

Steel rebars are used in concrete structures as reinforcements to deal with tensile loads, since it is well known that concrete is weak in tension. Upon exposure to chloride environment, however, chloride ions may seep through concrete material and cause corrosion on these rebars. Corrosion causes the metal to expand and induce tensile stress on concrete that leads to concrete cracking. This phenomenon is one of the leading causes of deterioration in concrete structures that requires a lot of maintenance and repair cost. An accelerated corrosion test was designed to study specimen behavior upon exposure to chloride environment in a reduced time.

The accelerated corrosion test is performed using a standard procedure with a 30V DC capacity potentiostat (constant voltage source). Electromigration of chloride ions from the solution into concrete specimen hastens the corrosion and expansion of steel rebar. Localized expansion of rebar generates tensile stress on the concrete specimen that results in cracking. A crack in the concrete allows exposure of the steel bar to the solution and provides a shorter electrical path. This phenomenon results in a current increase that can be a failure indicator even without the appearance of a visible crack on the concrete specimen. The experimental setup is adopted from the Florida DOT standard for accelerated corrosion test [92].

The theory of the accelerated corrosion test relies on the basic theory of electrolysis in electrochemistry. When two different metals are connected to a power supply and immersed in an aqueous electrolyte, the more reactive electrode loses electrons and corrode, as shown in Figure 75. In this case, the iron electrode is more reactive than the copper electrode, and elemental iron readily loses its electrons to become aqueous iron ions.

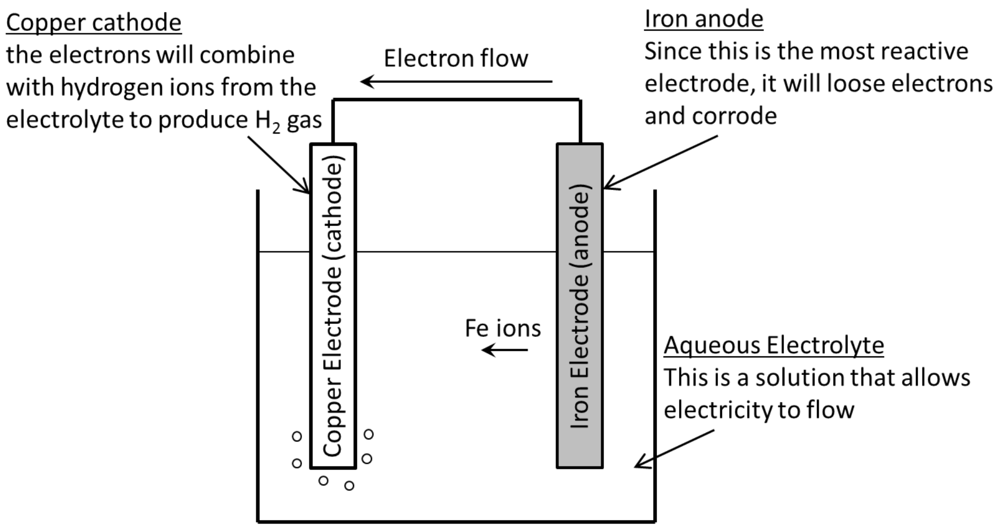

Figure 75. Electrochemical cell of copper and iron

The chloride ions migration from the solution to the rebar through the porous concrete specimen causes oxidation in the steel that manifests in volume expansion thus creating a tensile stress in the embedded rebar, leading up to cracks in the concrete. In order to accelerate the corrosion process, an electrochemical process is used to enhance the efficiency of chloride ions to attach themselves onto the steel bar. Since sodium chloride dissociates into positive sodium ions and negative chloride ions when dissolved in water, the negative charge of chloride is used by attaching the steel bar to a positive voltage source. The higher the voltage of the steel bar, the faster and larger are the amount of chloride ions that are attracted and react to the steel bar.

The standardized procedure for the accelerated corrosion test is to embed a bar through the center of a concrete cylinder with a diameter of 4 inches and a height of 5.75 inches, and suspended at a 1.75-inch height from the cylinder base. The test setup is shown in Figure 76. In this experiment, the specimen was moist cured for 14 days upon demolding, and partially submersed in a 5% sodium chloride solution with a 6V DC applied electric field to facilitate the initiation of corrosion. The steel bar concrete complex using rebar with a diameter of 0.375 inch similar to the ties used in the SC-UHPC beam was electrically connected to the cathode, and a 2-inch wide, 0.063-inch thick stainless steel strip was selected as anode due to its stable behavior compared to the rebar electrode (Figure 77).

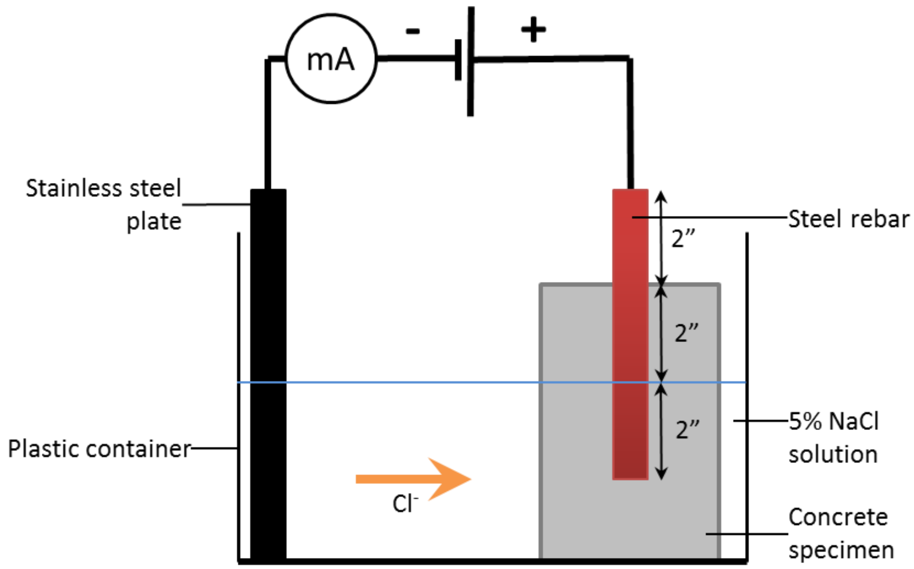

Figure 76. Accelerated corrosion test setup

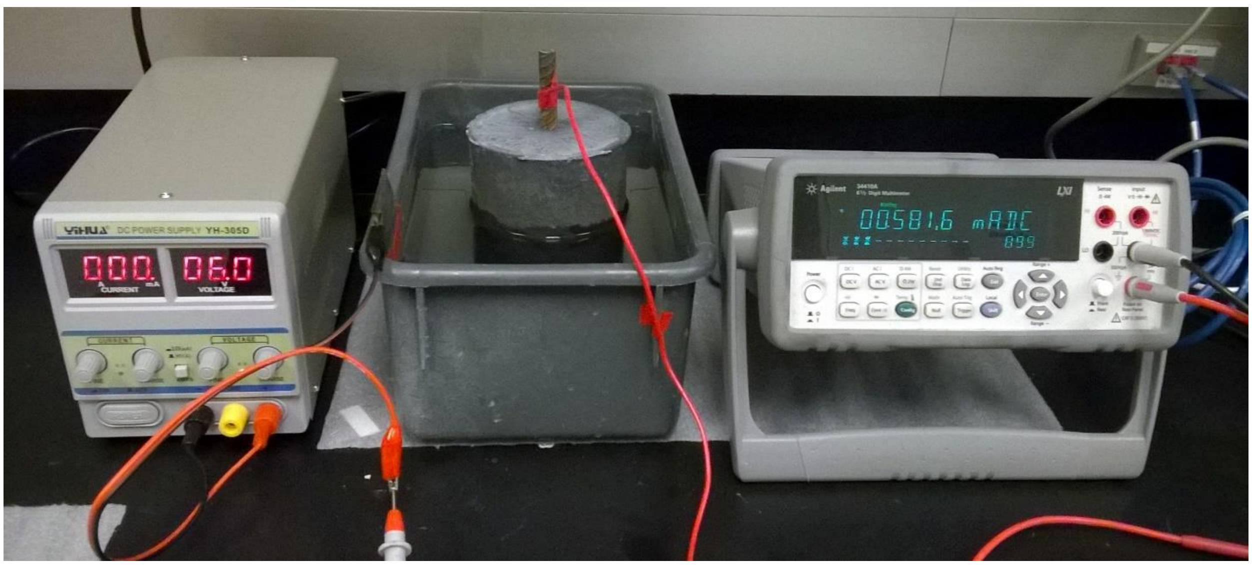

Figure 77. Accelerated corrosion test on a UHPC

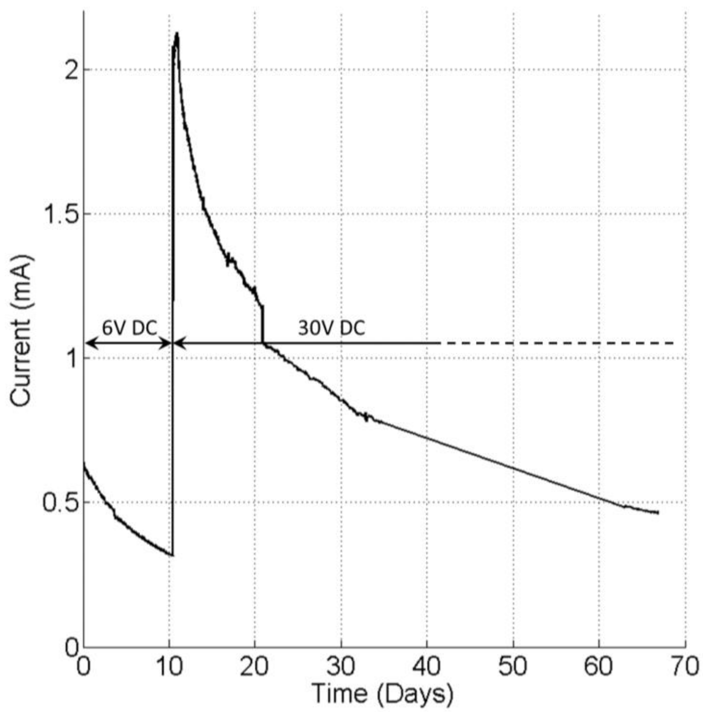

Figure 78. Accelerated corrosion current measurement on UHPC specimen

The system current was continuously monitored and logged at 5-minutes intervals. A similar setup used in other researches agrees that the occurrence of a crack is associated with a sudden current increase [92-94]. After 250 hours of observation on the accelerated corrosion test of UHPC with no sign of any crack occurrence, voltage was increased to 30V DC (Figure 78). There was still no visible crack observed after an additional 60 days on higher voltage. Neither was there any sudden increase in current that would signify the occurrence of a crack. However, gradual reduction on the current reading was detected, which is a feasible sign of internal corrosion that increases the resistivity of the steel rebar. It was suspected that the steel expansion from corrosion was not enough to cause a crack on the 2-inch UHPC cover, thus the monitoring of the system current was discontinued after 60 days.

` New systems were setup using a 3-inch diameter cylinder for both the UHPC and the control concrete, as shown in Figure 79. Cracks on concrete specimens occurred after 35 hours and 32.5 hours of exposure to high DC voltage, inferred by the start of increase on the system current. The UHPC specimens did not develop any cracks for several months of measurement. However, an increase in resistivity signified by current decrease recorded on the ammeter indicates that corrosion was progressing on the steel rebar embedded in the concrete. Finally cracks on UHPC were observed after 3756 hours (156 days) and 4252 hours (177 days).

Figure 79. Corrosion test setup of UHPC and control concrete specimens

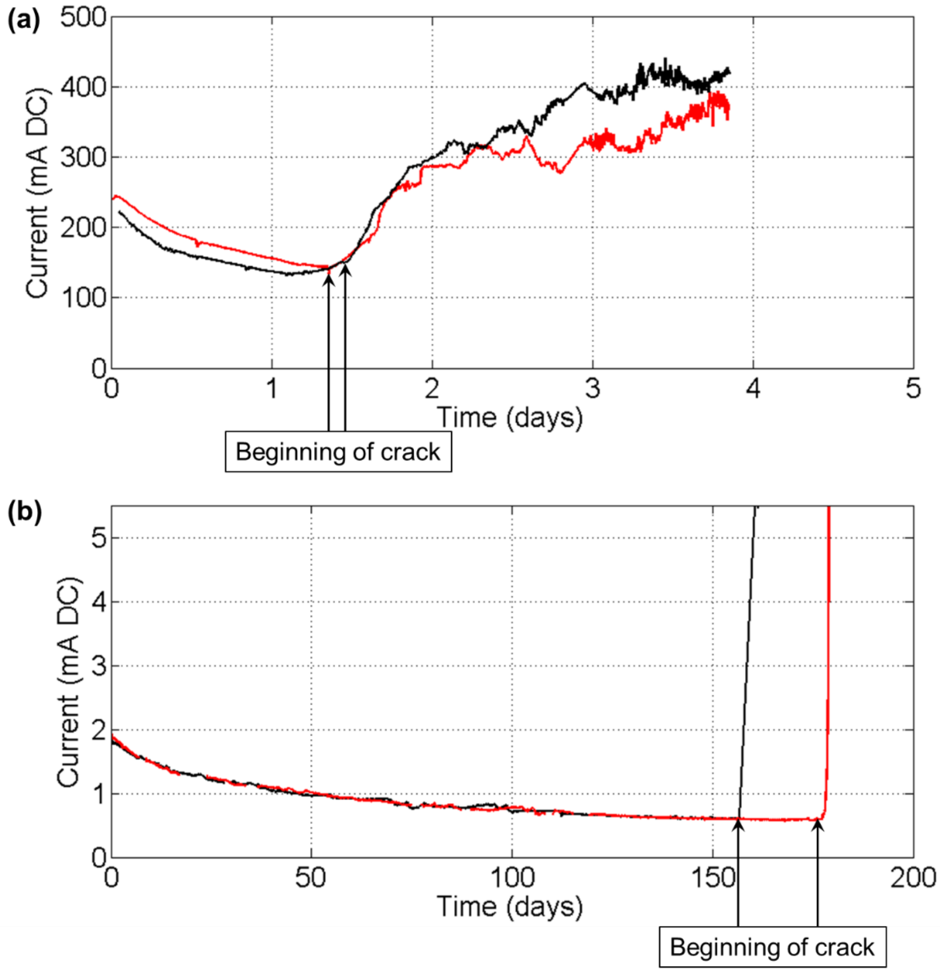

Figure 80. Accelerated corrosion current measurement on 3 inches diameter (a) UHPC and (b) control concrete specimens

The record of the measurement result is given in Figure 80. The appearance of the failed specimens in the accelerated corrosion test and the cracked concrete specimen after the test is shown in Figure 81 and Figure 82. The test result indicates that the high packing density resulting in low porosity and permeability of the UHPC delayed the chloride migration into the rebar embedded in the specimen. Higher tensile stress in the UHPC then contributes in delaying the occurrence of cracks when corrosion is slowly progressing under exposure to the chloride containing environment.

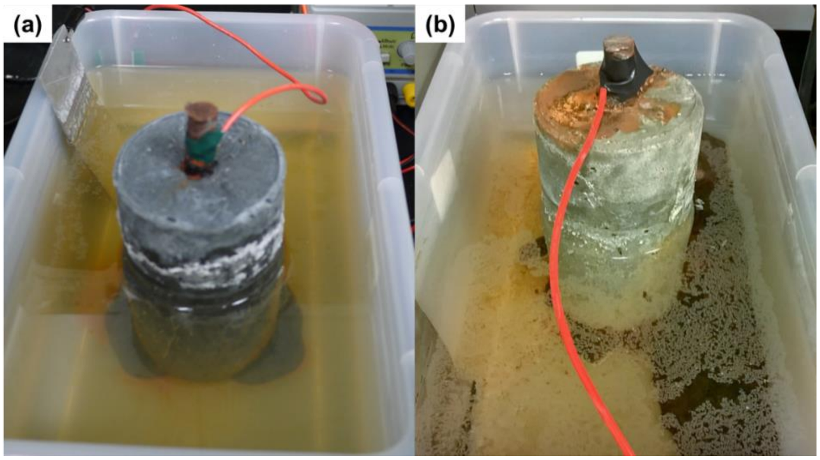

Figure 81. Appearance of (a) UHPC and (b) control concrete specimens, after crack occurrence in accelerated corrosion test

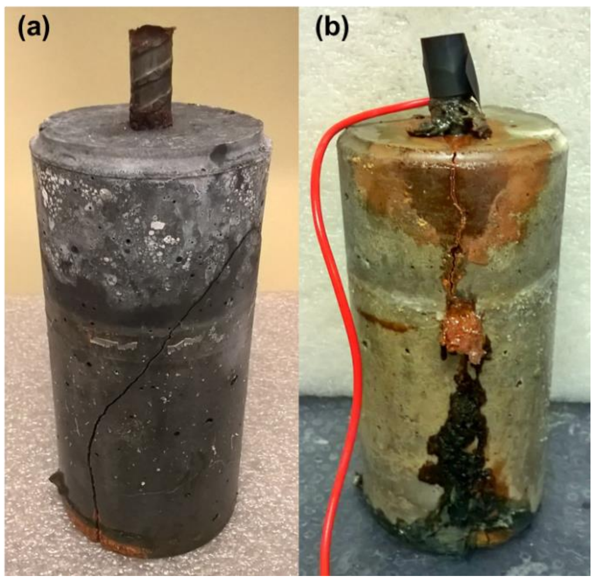

Figure 82. Corrosion crack on (a) UHPC and (b) control concrete specimen

3.5.Elevated temperature

Heat resistance in an elevated temperature environment is one of the durability characteristics of concrete that is highly desired especially for nuclear infrastructure applications, in addition to strength, toughness and workability. Concrete has sufficient strength and radiation resistance to allow its uses in nuclear power plants. However, these preferred properties may experience a downturn when the material is exposed to a detrimental environment such as radiation and high temperatures. Therefore, investigation is required to confirm the safety of the material used in structural members of a nuclear facility.

Upon interaction with radioactive elements, concrete properties were suspected to experience nocuous changes. Radiation energy also causes localized heating that causes damage to concrete [95]. However, the effect of temperature increase on moisture loss is much more significant compared to the radiation effect on the shielding properties of concrete [96]. Exposure of high temperatures causes mechanical and physical changes on concrete material, leading to concrete deterioration that can be seen in the form of strength loss, deformation or spalling [97].

Concrete is a composite material consisting of cement paste and aggregate that have decomposing components when heated [98]. However, evaporation of large amounts and various types of water needs to take place before the decomposing of the solids occurs, resulting in moisture loss. Evaporable waters are free water that exists in voids larger than 50nm, capillary water that is held by capillary tension in small capillaries between 5 to 50nm, adsorbed water and interlayer water between the layers of calcium silicate hydrates (C-S-H) that are physically held by hydrogen bonding. These phenomena cause strength loss in concrete. In a low permeable concrete, water vapor faces a dense barrier on its way to be released into the atmosphere, thus creating a pressure buildup that may lead to spalling [5, 99].

Many studies done on conventional concrete behavior at high temperatures showed that original strength, water-cement ratio, type of cement and rate of heating barely affect concrete strength at elevated temperature; strength reduction is lower on concrete with less aggregate content; and compressive strength on concrete with lightweight aggregate occurs at a higher temperature compared to normal strength aggregate [100, 101]. However, to fulfill the quality requirement of nuclear-safety related structures, high-performance concrete is preferred to conventional concrete, and it may behave differently from conventional concrete in elevated temperatures. As a type of high performance concrete, self-compacting concrete has a denser microscructure compared to conventional concrete, with smaller and less connected pores, resulting in about 80-90% residual compressive strength at 200°C and 60-80% residual compressive strength at 400°C [102, 103].

Another study of high performance concrete reveals that the changes of compressive strength under elevated temperatures is not linear; rather it decreases until the temperature reaches 200°C, then increases until the temperature is 400°C [104]. A study on fiber reinforced reactive powder concrete, which is a type of ultra-high performance concrete (UHPC), shows that there is strength increase during exposure to temperatures of up to 300°C; however at temperatures above 400°C, explosive spalling occurred [105, 106]. In contrast, strain hardening cementitious composites and lightweight strain hardening cementitious composites could withstand temperatures higher than 600°C [107, 108]. The explosive spalling of high strength concrete is due to its brittle nature and the accumulated vapor pressure within the low porosity material due to the presence of silica fume. Also, thermal conductivity and thermal expansions siliceous aggregate used in high strength concrete is generally higher than carbonate aggregate used in normal concrete, while fiber addition does not significantly alter the material thermal properties [109, 110].

Heat treatment is commonly used as a special curing to increase the strength of ultra-high performance concrete. A study reported that pozzolanic reactivity of silica fume was increased with heat treatment at temperatureS up to 250°C. It also allows material to produce longer C-S-H chains in UHPC [111, 112]. The temperature limit used for design in all possible environmental conditions for concrete containment building in A nuclear power plant is 20°C to 200°C [113], and radiation may cause a temperature increase in the concrete up to 250°C. This can be the trigger for UHPC strength increase at elevated temperature, while normal strength concrete starts depreciating at 95°C as it losses its strength along with the increasing temperature and time exposure [95].

The particular UHPC used in this study has not yet experienced moisture loss prior to its exposure to elevated temperature, when the removal of its evaporable water initiates. Besides UHPC as the target material, conventional mortar was used as control material and fiber UHPC was used as an alternative material. Since UHPC is a very low permeable material due to its fine constituents, it was suspected that in such a dense microstructure of UHPC, there is no pathway for water vapor to vent out from the specimen, thus high pressure from the vapor buildup may break the UHPC specimen and cause it to spall in a violent manner. Polyvinyl alcohol (PVA) fiber is involved in this study to see whether or not there will be some pathway created from the evaporated fiber when the environment temperature is higher than the melting point of the fiber. Fiber-UHPC uses the same proportion as UHPC, except that PVA-fiber was gradually added into the mixture by 1% volume at the end of the mixing process, after the paste reached homogenous appearance. Three specimens were prepared for each material under each respective temperature condition.

Fresh mixture was cast into a 2×4-inch cylindrical plastic mold and covered for one day. After demolding, the specimens were water cured for 28 days and then air dried for at least another day. All specimens were weighed before and after heating. An insulated electric furnace with a temperature control system was used to heat the specimens for six hours at 100°C, 200°C, 230°C (that is known as melting point of PVA fiber), 300°C, 350°C and 400°C. The inner dimension of the furnace is 6×6×20 inches The heating follows the general practice of concrete at elevated temperature without specimen sealing to enable stable moisture loss, which is the primary cause of concrete deterioration at high temperatures. Another set of specimens at room temperature was tested as control specimens. Mass loss in the concrete cylinders is calculated as the percentage change in mass after exposure to the heating. Residual strength was measured with a compression test on all specimens that did not spall, after they returned to room temperature. A compression test was performed on a 500kips capacity Tinius Olsen universal testing machine. The physical condition of the specimens was observed using a polymer smartphone microscope lens with 15 times magnification [114] and a smartphone camera with 8 megapixels resolution.

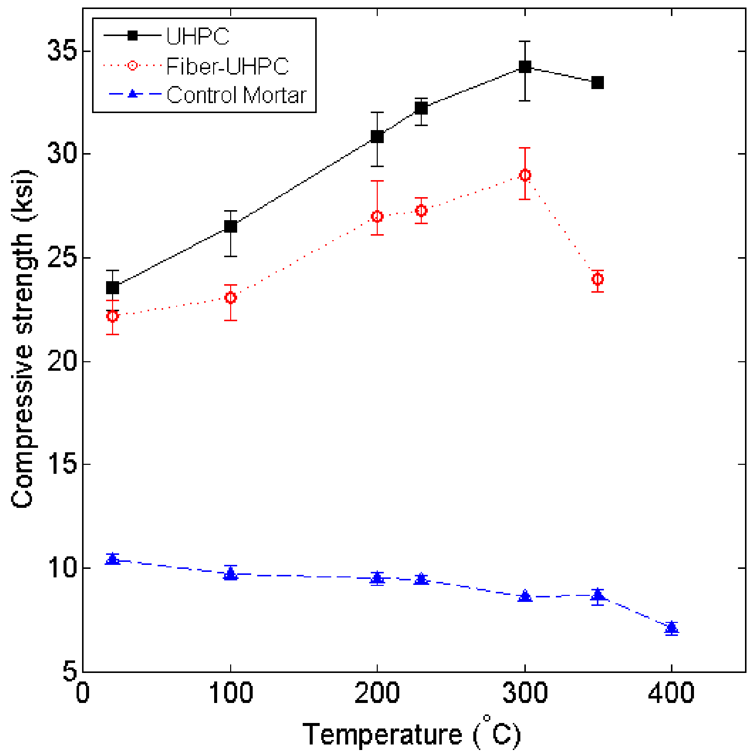

Figure 83. The effect of 6 hours of elevated temperature to compressive strength

Even though there was no spalling observed on conventional mortar specimens, only 70% of residual compressive strength remained after six hours of exposure to a temperature of 400°C. The baseline compressive strength of the unheated control mortar was 10.4ksi. The high water content of the control mortar may have caused the material to retain more evaporable water, thus the strength decreases along with moisture loss. The average compressive strength for the control mortar specimen was 9.7ksi at 100°C, 9.5ksi at 200°C, 9.4ksi at 230°C, 8.6ksi at 300°C, 8.7ksi at 350°C and 7.1ksi at 400°C (Figure 83). However, the large number of pores provided an outlet for the vapor pressure so that no spalling occurred.

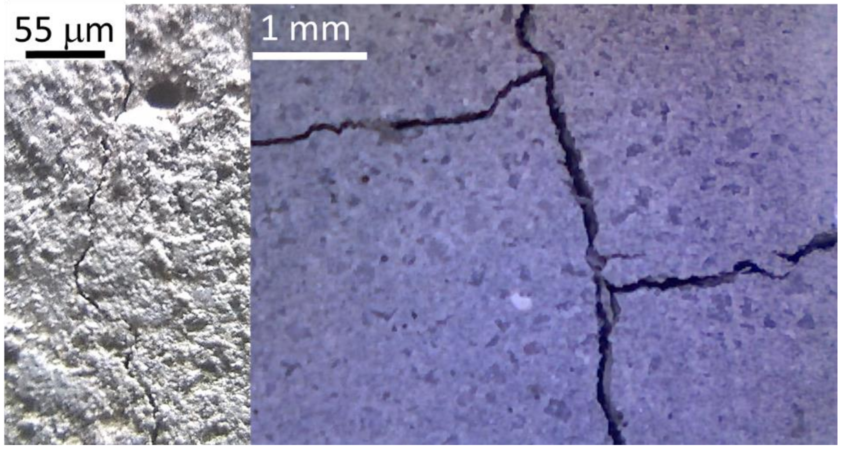

Figure 84. Cracks observed on control mortar specimens at 400 ℃

Figure 85 and Figure 86 show that the moisture loss on control mortar specimens came to almost a stagnant phase after 200°C and may signify that most of the capillary water has evaporated. Removal of adsorbed water and interlayer water requires stronger drying and occurs at a much slower rate. However, this does not change the rate of strength decrease in control mortar. Other than the various thickness of visible cracks that were observed on control mortar specimens at 400°C (Figure 84) that may be caused by severe drying shrinkage or thermal stress, there is no other significant visible deterioration or deformation from the appearance of the specimens, as shown in Figure 87.

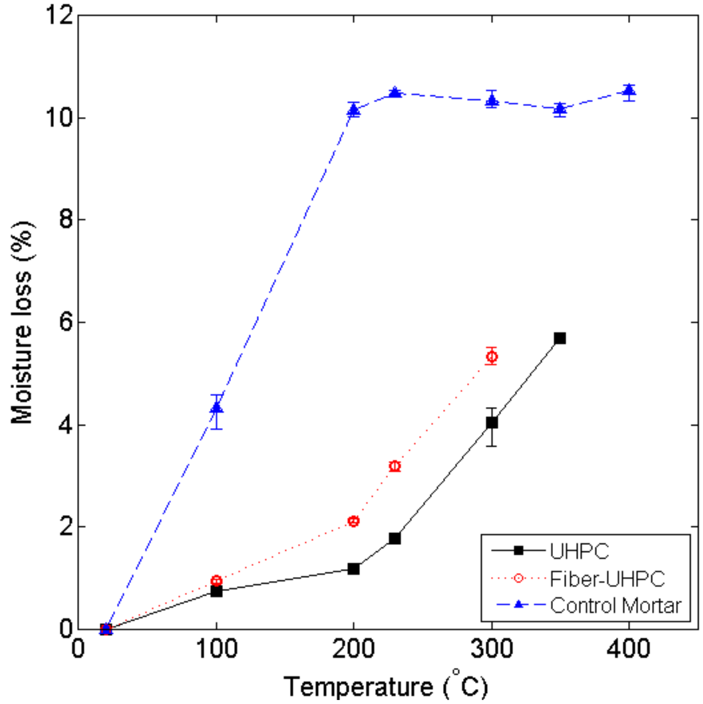

Figure 85. The effect of 6 hours of elevated temperature to moisture loss

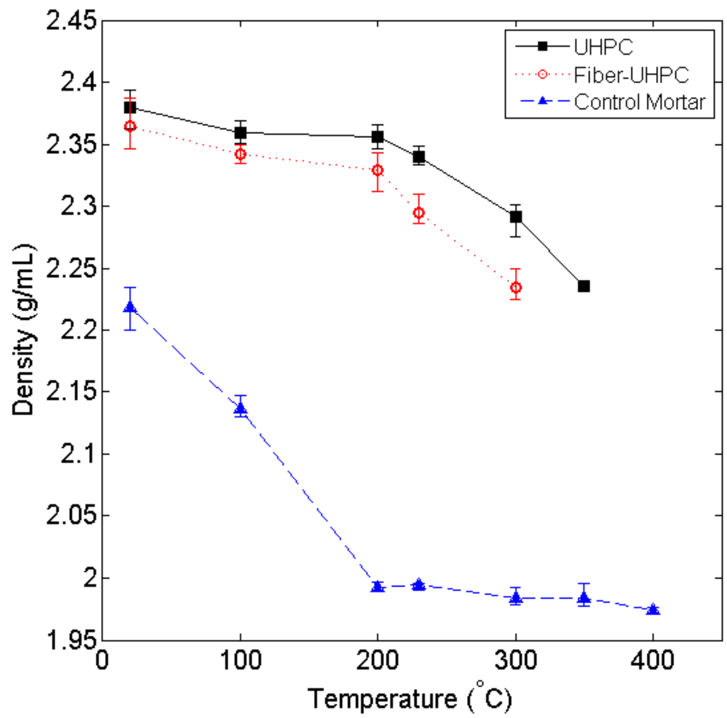

Figure 86. The effect of 6 hours of elevated temperature to specimen density

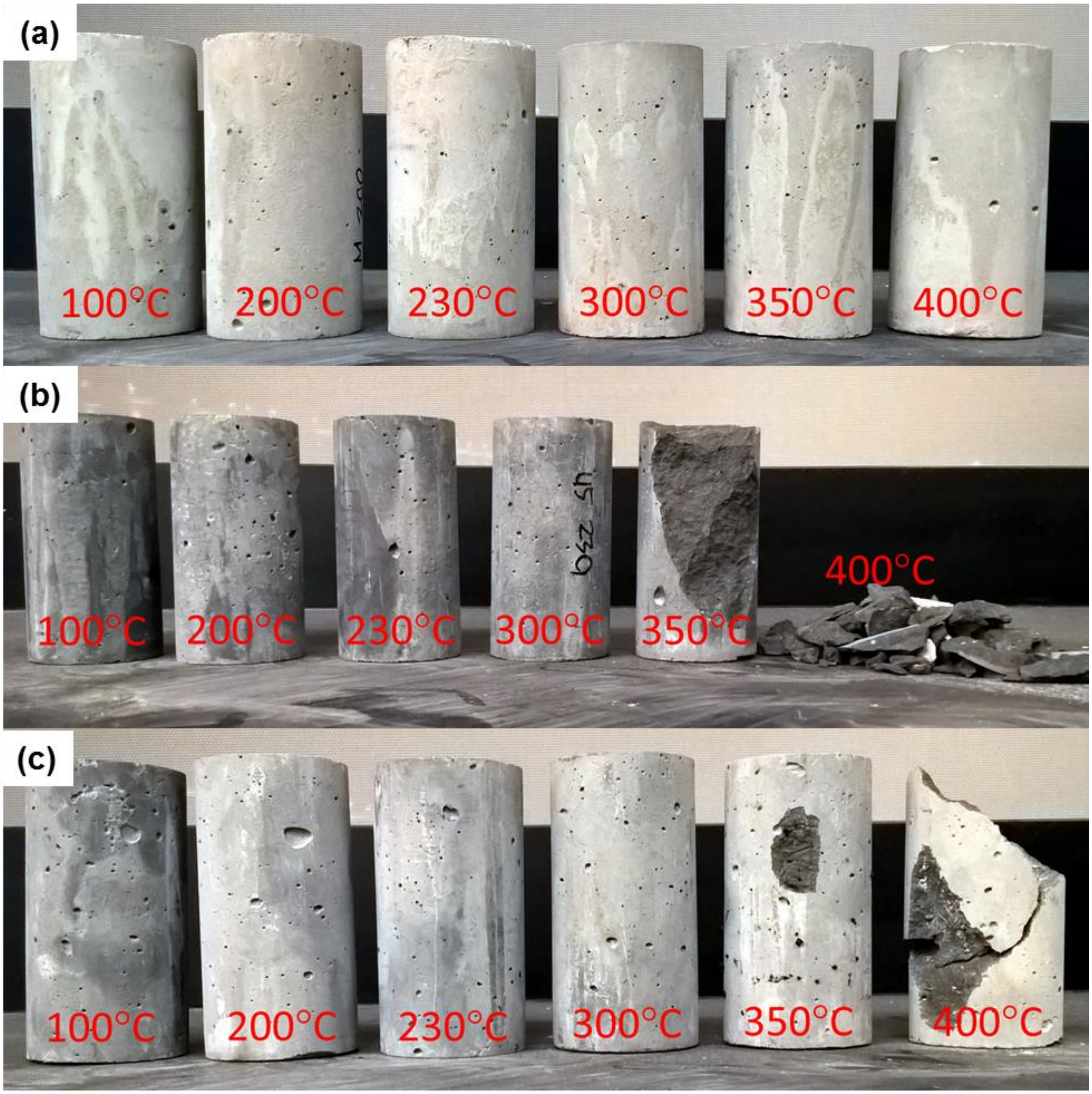

Figure 87. Appearance of (a) mortar specimens, (b) UHPC, and (c) fiber UHPC specimens after 6 hours exposure to elevated temperatures

UHPC specimens at room temperature obtain an average compressive strength of 23.5ksi. The strength increased as the material was exposed to an elevated temperature of 100°C to 300°C for six hours. The average residual compressive strength obtained for each temperature was 26.5ksi at 100°C, 30.9ksi at 200°C, 32.2ksi at 230°C and 34.2ksi at 300°C where the maximum strength obtained was 35.4ksi which was 150% its original strength and four times as high as the residual strength of the control mortar exposed to the same condition. At 350°C local spalling occurred on two of three specimens while all specimens at 400°C experienced explosive spalling, as shown in Figure 87. The condition of the furnace upon the occurrence of spalling at 400°C is given in Figure 88. Residual compressive strength of one specimen that survived spalling at 350°C was found to be 33.4ksi, lower than its value at 300°C. However, there is no visible difference in microscopic observation between the cracked surface of UHPC at 20°C and 350°C (Figure 89).

Figure 88. Furnace condition after heating at 400 °C

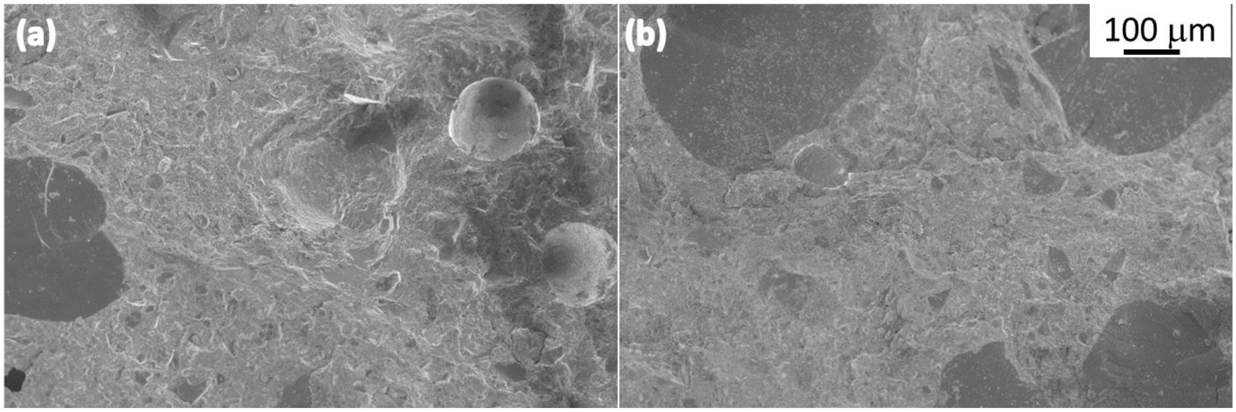

Figure 89. Cracked surface of UHPC (a) at 20 ℃ and (b) at 350 ℃

Moisture loss of both UHPC and fiber-UHPC increased more rapidly after the temperature reached 200°C. While the rate of increase in moisture loss from 20°C to 200°C was 0.006%/°C, it was 0.030%/°C from 200°C to 350°C. That is five times faster than the initial stage, as seen in Figure 85. In fiber-UHPC, the mass loss at the initial state (20°C–200°C) increased by 0.012%/°C and at a later state (200 °C to 300°C) it increased by 0.032%/°C. The mass loss in fiber-UHPC past the melting point of PVA-fibers includes the decomposition (partial or total) of the PVA-fiber. However, since the mass loss from water loss and fiber decomposition cannot be separated, it was all considered as moisture loss. The high rate of moisture loss increase in UHPC specimens signifies that the amount of interlayer water between C-S-H layers in UHPC, which requires extreme drying conditions to evaporate, is higher than the easily removed free water and capillary water within the voids of the specimens. Due to the low porosity and low permeability of the material, steam pressure from the evaporation of interlayer water at the high temperature was building up faster than the releasing of the vapor out of the specimen, thus causing severe spalling. Complete removal of evaporable water in the specimens by prolonged pre-exposure to elevated temperatures between 100-300°C may reduce the risk of explosion, while it also increases the tensile strength of the material.

Fiber-UHPC specimens possess similar behavior with UHPC specimens under the compression test, with lower compressive strength. The average compression strength was increasing with the increase of temperature, from 22.1ksi at 20°C, 23.0ksi at 100°C, 27.0ksi at 200°C, 27.3ksi at 230°C, to the highest value of 29.0ksi at 300°C despite minor spalling that occurred on all specimens. Specimen breaking by spalling was observed on specimens at 400°C, even though it was not as explosive as the UHPC without fiber, and one of the specimens only experienced local spalling (Figure 90). This spalling may be triggered by additional voids near the specimen surface due to the decomposition of the fiber (Figure 91). Figure 92 shows the gradual decomposition of fiber: normal fiber appearance at 20°C, fiber was turning to a yellowish color at 100°C, further change of fiber color to dark brown and some fiber disappearance at its melting point of 230°C and some footprints of fiber existence after six hours exposure to an elevated temperature of 300°C.

Figure 90. Locally spalled fiber-UHPC specimen at 350 ℃

Figure 91. Appearance of decomposed fiber at 400 ℃

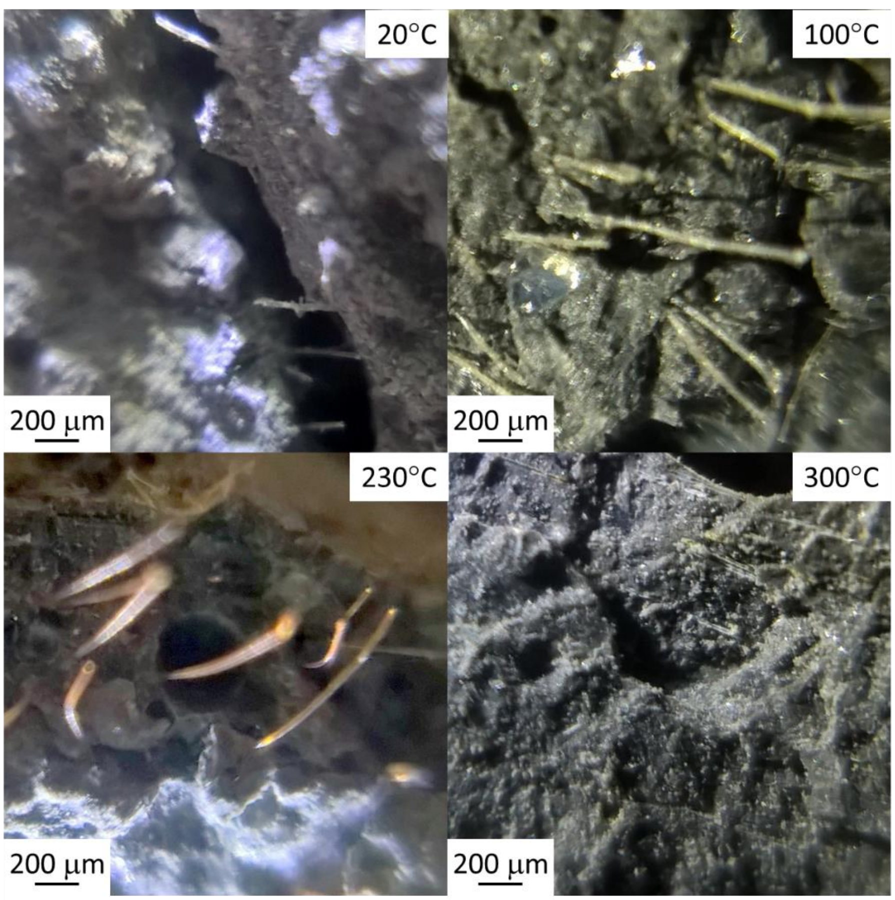

Figure 92. Fiber condition after specimen exposure to 6 hours of different temperatures

3.6.Summary

Durability tests to evaluate the transport properties and dimension stability were performed on UHPC and normal concrete control specimens. These standardized tests include measurements on chloride diffusivity, water permeability, free and restrained shrinkage, alkali-silica reaction, accelerated corrosion and elevated temperature. Based on the results obtained, UHPC possesses higher durability compared to conventional concrete in every experimental test, which include significant lower chloride permeability and thermal conductivity, lower shrinkage and inactivity under exposure to an alkaline environment. The improved durability is expected due to a significant amount of pore reduction and high packing density of the material compared to normal concrete control specimens.

The charge passed measured through the rapid chloride permeability test on UHPC falls into a category very low at 28 days and negligible at 90 days according to ASTM C1202 chloride penetrability classification, while that of conventional concrete is categorized into a high level. The GWT-4000 water permeability test on both specimens also confirmed the higher permeability resistance of UHPC. The high resistance of UHPC to chloride penetration and its low water permeability can be attributed to its denser microstructure, lower porosity and pore connectivity.

The free shrinkage and restrained shrinkage test on UHPC and conventional concrete was performed with a long-term measurement for the purpose of measuring length change due to water loss and hydration reaction, as well as crack tendency of the developed UHPC material and control concrete. The measurement results exhibit more rapid length change at an early age for the developed UHPC specimen; however with significantly lower later-age length change compared with the conventional concrete specimen under normal ambient temperature and humidity. Length change measurement was also performed in an ASR test to determine the reactivity of UHPC material under alkaline environment in comparison with conventional concrete. The result showed zero expansion on UHPC material due to the inert aggregate used, compared with the control concrete specimen that was categorized as potentially deleterious. An accelerated corrosion test was performed on UHPC and control concrete specimens, resulting in cracking on concrete specimens at 32.5 and 35 hours, while cracking in UHPC specimens occurred at 156 and 177 days, signifying low permeability and high tensile strength of UHPC material.

The effect of elevated temperature to compressive behavior of UHPC was studied, with conventional mortar as the control material and PVA fiber-UHPC as the alternative material. A compressive strength up to 35ksi was obtained for UHPC specimens that were subjected to elevated temperatures for extended periods of time. When individual UHPC samples were placed under conditions simulating normal nuclear power plant operations within an electric furnace at 300 °C for six hours, the compressive strength was observed to increase by 1.5 times as high as its original strength.

When UHPC was exposed to a high temperature of 400°C for six hours (such as during the event of a fire), UHPC specimens experienced severe spalling. Measurement of moisture loss at respective temperatures showed that there is more water in between C-S-H layers (interlayer water) of UHPC compared to the easily removable capillary water within the voids of the specimen. Extreme drying conditions are needed for removal of interlayer water. Prolonged pre-exposure to elevated temperatures between 100-300°C may reduce the risk of explosion by allowing complete desiccation that eliminates evaporable water within the micropores of the UHPC material, while increasing the tensile strength of the material.

4. PERFORMANCE OF SC and S-UHPC BEAMS with CROSS TIES

4.1. Introduction

Steel-plate Concrete (SC) has been used for the shield building in nuclear power plants AP1000 recently. However, the minimum cross tie ratio for SC beams is unknown.

For a SC module to behave efficiently, a good bond between the concrete and steel plates is necessary. There are different forms of construction of a SC beam module such as the adhesive bonded form, the overlapping shear studs, J-Hook and cross ties. The adhesive bonded form may result in shear failure due to the predominant bond slip between the concrete and the steel plates. The overlapping shear studs may prevent the progress of bond slip and resist shear failure. However, the compression plate between the shear studs may buckle due to lack of a continuous bond between steel plates and concrete. The cross ties method is considered to be one of the most efficient forms to construct SC modules in terms of construction time, quality and cost. Furthermore as the key for the integrity of the SC module is efficient shear transfer between the steel plates and concrete, cross ties can also act as shear reinforcement and increase the shear carrying capacity of SC modules [115, 116].

When a Steel-plate Concrete (S-UHPC) module with cross ties is subjected to both flexure and out-of-plane shear, the cross ties connecting the two steel faceplates with concrete filled in between the faceplates need to be designed to ensure the integrity of the SC module. Unfortunately, no design codes and tests are available for the cross tie design. For the first time, we will experimentally identify the amount of cross ties for SC and S-UHPC beams. The bond between steel plates and concrete is crucial. However, it is a challenge to develop reliable debonding monitoring and detection techniques for SC modules because of the inaccessibility of the interface.

This research employs a novel sensing technology to monitor the bonding behavior between the steel plates and the infill concrete or UHPC, to ensure quality control for robust production of SC modules.

A thorough understanding of the flexural and shear behavior of the SC modules is critical to the success of the modular construction. When SC modules are designed, their ductile behavior needs to be ensured. When a SC module is governed by flexure or shear, the amount of cross ties needs to be critically examined through experiments to ensure that the designed SC beam is in an integrated unit, i.e. not separated into three components due to loading. Therefore, the minimum cross tie ratios in SC modules need to be identified, especially since no research or standards are currently available.

ACI 349 [117] has been used for the design of SC structures. ACI 349 adopts the considerations of ACI 318. ACI 318 [118] has been developed for the design of Reinforced Concrete (RC) structures. In section 11.1.1 of the ACI 318, the nominal shear force (Vn) is given as the summation of shear strength provided by concrete (Vc) and the shear strength provided by the shear reinforcement (Vs). Minimum shear reinforcement is essential to prevent sudden shear failure. The ACI 318 has specified this in section 11.4.6. According to the code, the minimum shear reinforcement area and ratio are given by:

$$A_{v,min} = 0.75\sqrt{f_c^{'}}\frac{b_w s}{f_{yt}} \geq 50\frac{b_w s}{f_{yt}} \tag{13}$$

$$\rho_{t,ACI} = 0.75\frac{\sqrt{f_c^{'}}}{f_{yt}} \geq 50\frac{1}{f_{yt}} \tag{14}$$

where $A_{v,min}$ is the minimum area of shear reinforcement, ρ is the shear reinforcement ratio, s is the spacing of cross ties in a member of width b_w. F_{yt} is the yield strength of rebars and fc' is the 28 days compressive strength of concrete[118].

As a reference, six Steel-plate Concrete (SC) beams were tested under out-of-plane shear. From the test results, the effect of concrete strength and the critical a/d ratio was evaluated. Subsequently two S-UHPC beams were designed and tested to determine the minimum shear reinforcement ratio ($\rho_{t,min}$) for S-UHPC modules under out-of-plane shear. Nonlinear finite element models for SC and S-UHPC beams were then developed for simulation purposes. The developed nonlinear finite element model is an extension of the previous model developed at the University of Houston, the CSMM (Cyclic Softened Membrane Model). The CSMM model which was developed for predicting the nonlinear behavior of reinforced concrete has been extended to predict the behavior of SC and S-UHPC beams.

4.2. Experimental Program for SC Beams with Normal Strength Concrete

A strip of nuclear containment (Figure 93) is taken out as the studied specimen and it is scaled down by a factor of 4/9[119]. Figure 94 shows the geometric properties of the SC beams. The length, width and depth of each SC beam are 15.0 feet (4572 mm), 12.0 inches (305 mm) and 16.0 inches (406 mm), respectively.

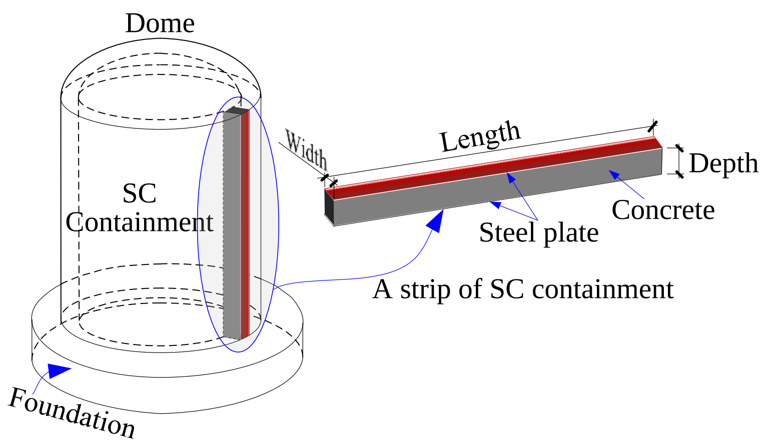

Figure 93. SC nuclear containment and a cut strip

Table 12 shows the experimental matrix for SC beams cast with normal strength concrete. The shear span-to-depth (a/d) ratio and cross tie ratio ($\rho_{t,test}$) are the main test parameters. Reinforced Concrete (RC) members subjected to concentrated load exhibit minimum shear strength when the shear span-to-depth (a/d) ratio is about 2.5[120]. This phenomenon was captured in tests on Prestressed Concrete (PC) beams. Based on the test results, a minimum amount of shear reinforcement for the PC member was proposed. The proposed amount was double the value specified in the ACI 349 provisions for a/d between 2.0 to 4.0[121, 122]. Therefore, three a/d values, 1.5, 2.5 and 5.2, were selected, and $\rho_{t,test}$ varied from 0.102% to 0.205%. The shear span a, as shown in Figure 94(a), is defined as the distance from the center line of the support to the center line of the actuator, and the depth d, as shown in Figure 94(b), is defined as the distance from the extreme top fiber to the center line of the bottom steel plate. Design of cross ties in Specimen SC1 was based on ACI 349 provisions (Eq. 13) to verify the applicability of the current ACI 349 code [117] to SC beams. Specimens SC2 and SC3 were designed and prepared based on test results of Specimen SC1. The cross tie ratios of Specimens SC2 and SC3 were increased in order to identify the minimum cross tie ratio ($\rho_{t,min}$) for SC beams. Specimens SC4, SC5 and SC6 were designed and prepared based on test results of Specimens SC2 and SC3. Specimen SC4, which had higher shear reinforcement ratio than Specimen SC3, was tested to further verify the minimum cross tie ratio ($\rho_{t,min}$). Moreover, Specimens SC5 and SC6 were tested to investigate the behavior of SC beams under different a/d.

Deformed No. 2 reinforcing bars were used as shear reinforcement, and high-strength low-alloy structural steel (ASTM A572-50 [123]) was used as top and bottom steel plates. The yield strength of No. 2 rebars ($f_{y,tie}$) and yield strength ($f_{y,sp}$) of the steel plate were 60.8 ksi (419 MPa) and 55.0 ksi (379 MPa), respectively. Specimens SC1 to SC6 were cast in three different times, and concrete compression strength (f_c') varied from 5.82 to 8.13 ksi (40.1 to 56.0 MPa).

To fully secure the connections between steel plates and shear reinforcement, penetration welding was applied, as shown in Figure 95. The holes on the top and bottom plates were drilled at the desired spacing, then the shear reinforcement was placed. The welding was applied on both the outside and inside surface of steel plates.

Table 12. Experimental matrix, ultimate strength, and failure mode

Specimen	a/d	S_{tie} # (in.)	f_c' * (ksi)	$\rho_{t,ACI}$ (%)	$\rho_{t,test}$ (%)	$\rho_{t,test}/\rho_{t,ACI}$	$F_{ult.}$ ** (kips)	Ductility δ †	Failure Mode
SC1 north	2.5	8.00	8.13	0.111	0.102	0.92	27.4	——	Brittle
SC1 south	2.5	8.00	8.13	0.111	0.102	0.92	26.1	——	Brittle

SC2 south	2.5	7.00	5.80	0.094	0.117	1.25	26.9	0.730	Brittle
SC3 north	2.5	6.00	5.82	0.094	0.137	1.45	31.7	1.17	Ductile
SC3 south	2.5	6.00	5.82	0.094	0.137	1.45	34.9	1.79	Ductile
SC4 north	2.5	5.00	7.37	0.106	0.164	1.54	42.7	1.58	Ductile
SC4 south	2.5	4.00	7.37	0.106	0.205	1.93	53.0	1.65	Ductile
SC5 south	1.5	6.00	8.00	0.110	0.137	1.25	55.9	1.43	Ductile
SC5 north	1.5	5.00	8.00	0.110	0.164	1.49	64.7	1.48	Ductile
SC6	5.2	6.00	8.00	0.110	0.137	1.25	29.3	1.99	Ductile

S_{tie} is the spacing of cross ties

* f_c' = the concrete compression strength from concrete cylinder (6.00″×12.0″), tested on the testing day (over 28 days)

** $F_{ult.}$ = the ultimate shear force

† δ = deflection at the peak /deflection when cross ties yielded

1.0 in. =25.4 mm, 1.00 kips= 4.40 kN, 1.00 ksi = 6.89 MPa

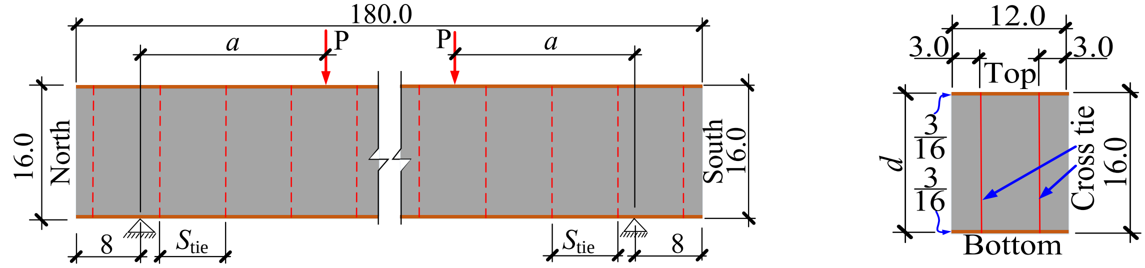

(a) Elevation view of SC beam specimens (b) Cross setion dimensions

Figure 94. Dimensions of SC beam specimens (unit: inch)

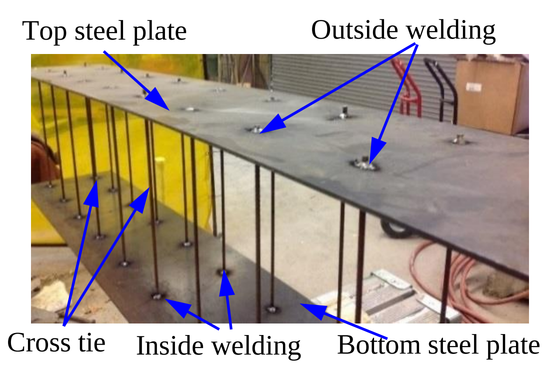

Figure 95. Penetration welding of shear reinforcement

4.2.1. Loading protocol and test setup

The specimens were subjected to vertical loading provided by north and/or south actuators with a capacity of 600 kips (2670 kN) each, as depicted in Figure 96(a). The loads and displacements of the actuators were controlled by the MTS Flex system. The loading protocol was comprised of several loading steps. Every loading step had a constant loading rate of 0.10 inch (2.54 mm) per 15.0 minutes. During each loading step, the loading might be put on hold and resumed to check and mark the cracks. Each test lasted three to five hours. The displacement control feature was essential in capturing the post peak behavior of SC beams.

Specimens SC1 and SC3 were loaded simultaneously at both north and south ends. Due to an unexpected problem of the loading control system during symmetrical loading on SC2, SC2 north failed when the north actuator was out of control, while SC2 south was intact and not loaded. Therefore, specimen SC2 was only loaded at the south end. Specimens SC4 and SC5 were tested one end at a time. The end with lesser shear reinforcement (Specimen SC4 north/SC5 south) was tested first and the support at the failure end was moved to the uncracked section for the test on the other end (Specimen SC4 south/SC5 north). Moreover, Specimen SC6 was loaded in the middle span using one actuator.

4.2.2. Instrumentation

Load cells installed under supports, as shown in Figure 96(a) were used to measure shear forces in the specimens. Linear Variable Differential Transformers (LVDTs) were placed vertically at the two supports and under the loading point to measure settlements of the supports and total deflection of each specimen, respectively. The net deflection of the specimen can be obtained by subtracting the support settlement from the total deflection. Six LVDTs forming a rosette were installed on the side faces of the specimens to get the smeared strains within the critical zone (Figure 96(b)).

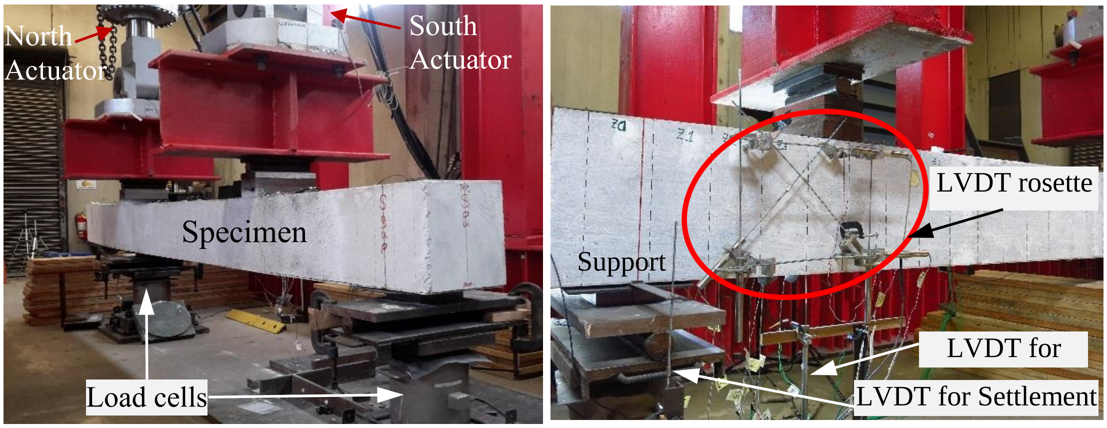

(a) Loading arrangement (b) Setup of LVDT

Figure 96. Test setup of specimen

Strain gauges were pasted on the surface of cross ties to measure the local strains of cross ties embedded in the concrete. The cracks were expected to occur close to the loading section. Thus, several strain gauges were pasted on the cross ties close to the loading section. Strain gauges were also pasted on the surface of the bottom steel plate under the actuator to measure the maximum tensile strain in the bottom steel plate. Figure 97 shows the arrangement and labels of strain gauges in Specimen SC1, and Figure 98 shows the typical arrangement and labels of strain gauges in Specimens SC2 to SC6. The label of each strain gauge in Specimens SC2 to SC6 contains two letters and one number. The first letter indicates the north or south end of a specimen, the second letter represents the elevation or position of the strain gauge, i.e. top, middle or bottom, and the number denotes the horizontal distance from the center line of loading to the strain gauge, i.e. the smaller the integer the closer to the loading point. NSP and SSP are the labels of strain gauges to measure maximum tensile strain in the bottom steel plate at the north and south end, respectively.

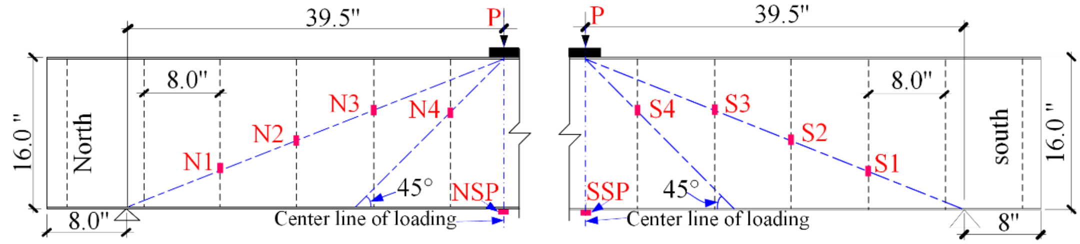

(a) North end (b) South end

Figure 97 Strain gauges arrangement and labels of Specimen SC1 (unit: inch)

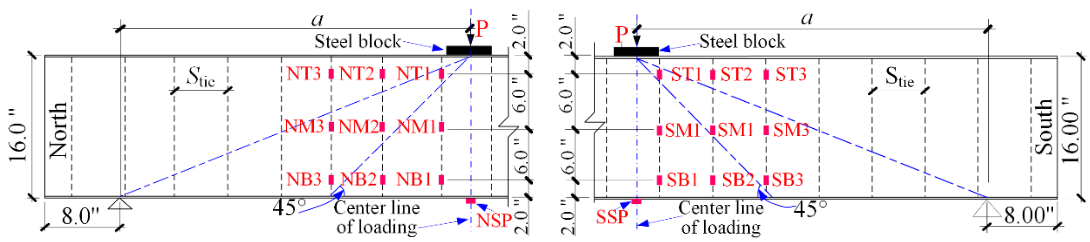

(a) North end (b) South end

Figure 98. Typical strain gauges arrangement and labels of Specimens SC2 to SC6 (unit: inch)

Data from load cells, LVDTs and strain gauges were collected, plotted and stored by the HBM Spider 8 data acquisition system. This system is capable of parallel and dynamic measurements, with a sampling frequency of 0.20 Hz. A real-time plot of the shear force vs. deflection was used to control the actuator during the tests. In addition, real-time plots of strains in concrete, cross ties and steel plate were used to examine the structural behavior of each specimen during the test.

4.2.3. Test Results

Details about the test results of each specimen, namely the shear force-deflection curves, crack patterns and shear force-strain curves of cross ties and steel plate, are discussed below. The data is used to critically evaluate the structural behavior and identify the minimum shear reinforcement ratio ($\rho_{t,min}$) of SC beams.

Specimen SC1

SC1, with a minimum shear reinforcement ratio per ACI 349 Code (Eq. 1), was tested under four-point bending. Shear force-deflection curves of SC1 north and south are given in Figure 99(a) and Figure 99(b), respectively. Each occurrence of a new crack resulted in stiffness reduction and load reduction. As a result of flexural crack, north shear force (F_{north}) dropped from 8.60 kips (38.3 kN) to 7.80 kips (34.7 kN), and south shear force (F_{south}) dropped from 7.40 kips (32.9 kN) to 5.60 kips (24.9 kN). An inclined crack in the south shear span (Figure 100(a)) occurred when F_{south} reached 9.50 kips (42.3 kN). In the north shear span, the inclined crack was observed when F_{north} reached 11.6 kips (51.6 kN). Bond slip, in the interface between bottom steel plate and concrete, was initiated as the inclined crack formed in the shear span.

Shear force in the SC1 south end (F_{south}) reached the ultimate at 26.1 kips (116 kN) and the corresponding deflection (Δ_{south}) was 0.290 inch (7.37 mm). In the post ultimate loading stage of SC1 south, the inclined crack propagated up to 0.50 in. (12.7 mm) away from the top steel plate (Figure 100(b)), and the bond slip became more pronounced. F_{north} reached ultimate at 27.4 kips (122 kN) and the corresponding deflection (Δ_{north}) was 0.400 inch (10.2 mm), as shown in Figure 99(a). Neither cross ties nor bottom steel plate yielded, and the concrete was not crushed. SC1 failed in a brittle way with no ductility due to the lack of sufficient shear reinforcement and debonding between the bottom steel plate and concrete.

.

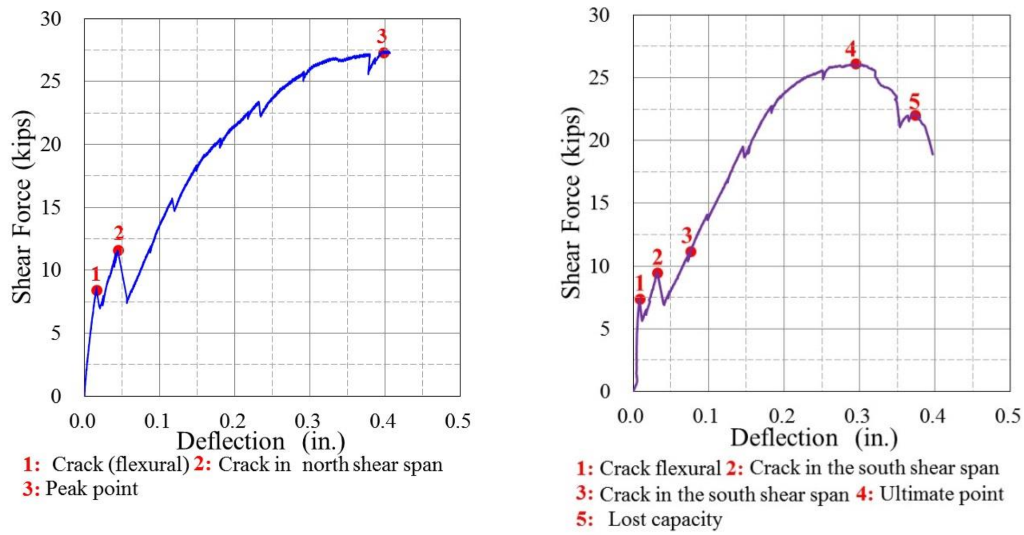

(a) North side (b) South side

Figure 99. Shear force-deflection curves of SC1

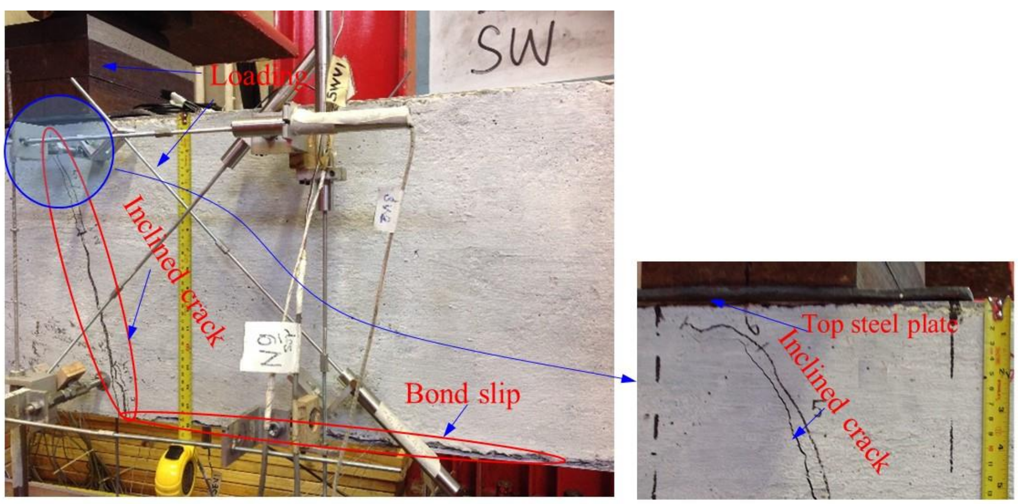

(a) Crack pattern and debond (b)Crack close to top steel plate

Figure 100. Inclined shear crack and bond slip of SC1 south in post ultimate stage

Specimen SC2 south

The shear reinforcement ratio of SC2 was 25% more than the minimum required by ACI 349 Code (Equation 13). The shear force-deflection curve of the south end is given in Figure 101. A flexural crack appeared when F_{south} reached 8.90 kips (39.6 kN), and the corresponding deflection Δ_{south} was 0.03 in. (0.760 mm). The inclined crack (Figure 102[a]) appeared when F_{south}

reached 22.6 kips (101 kN), and corresponding Δ_{south} was 0.09 in. (2.29 mm). As the cracks developed, the stiffness of SC2 south was reduced. F_{south} reached the peak at 26.9 kips (120 kN) with a corresponding deflection Δ_{south} of 0.22 in. (5.58 mm). Specimen SC2 south lost bearing capacity abruptly, when the inclined crack was 2.0 in. (50.8 mm) below the top steel plate (Figure 102[b]) and the bond slip in the bottom interface developed (Figure 102[c]). According to recordings from strain gauge SM1, the cross tie was yielded in the post peak stage, as shown in Figure 101. Concrete was not crushed at the peak load stage or in the post peak loading stage, as shown in Figure 102(b). Therefore, SC2 south still had a brittle failure with no ductility.

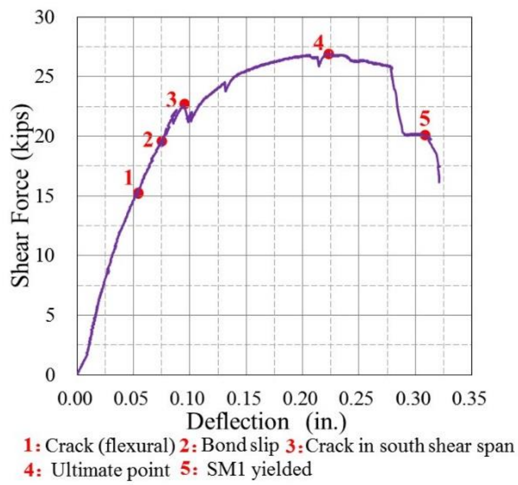

Figure 101. Shear force-deflection curve of SC2 south

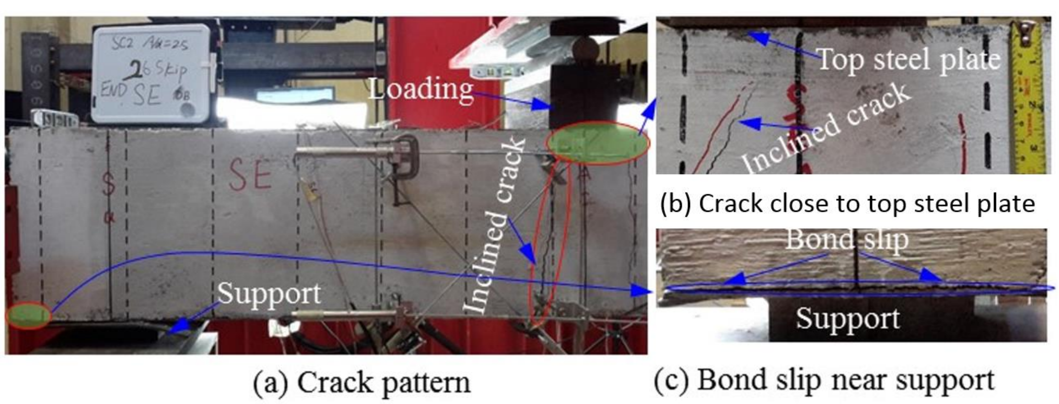

Figure 102. Crack pattern and bond slip of SC2 south after test

Specimen SC3

The shear reinforcement ratio of SC3 was 45.0% more than the minimum required by ACI 349 Code (Equation 13). SC3 was tested under four-point bending. The shear force-deflection curves of SC3 north and south ends are given in Figure 103(a) and (b), respectively.

In the north shear span, the concrete cracked when F_{north} reached 7.57 kips (33.7 kN), and the corresponding deflection Δ_{north} was 0.02 in. (0.510 mm). As shown in Figure 103(a), cracks led to stiffness reduction on the north side of SC3. When F_{north} reached 32.3 kips (143 kN), a shear crack occurred, as shown in Figure 104(b), which led to a sudden drop of F_{north}, see Figure 103(a). However, F_{north} continued to take some load and cross ties were yielded when F_{north} reached 30.5 kips (136 kN), as shown in Figure 105(a). Right before it failed completely, F_{north} reached 31.69 kips (141 kN), and the corresponding deflection Δ_{north} was 0.48 in. (12.2 mm). The shear crack width increased to 0.35 in. (9.0 mm), and the bottom steel plate slipped 0.16 in. (4.0 mm), as shown in Figure 104 (c). No concrete crushing was observed in Specimen SC3 north during and after the test.

In the south shear span, the concrete cracked when F_{south} reached 10.7 kips (47.5 kN), and the corresponding deflection Δ_{south} was 0.05 in. (1.27 mm). As shown in Figure 103(b), cracks reduced the stiffness. After the concrete cracked in SC3 south, the strains of cross ties close to the crack increased considerably and cross ties were yielded before F_{south} reached ultimate at 34.9 kips (155 kN), as shown in Figure 105(b). Concrete was not crushed in SC3 south during and after the test.

To quantify the behavior of the SC beam, the ductility (δ) is defined as the ratio of defection at the ultimate load to deflection corresponding to the first yielding of cross ties. Specimen SC3 exhibited a ductile behavior, and the ductility of SC3 north and south were 1.17 and 1.79, respectively.

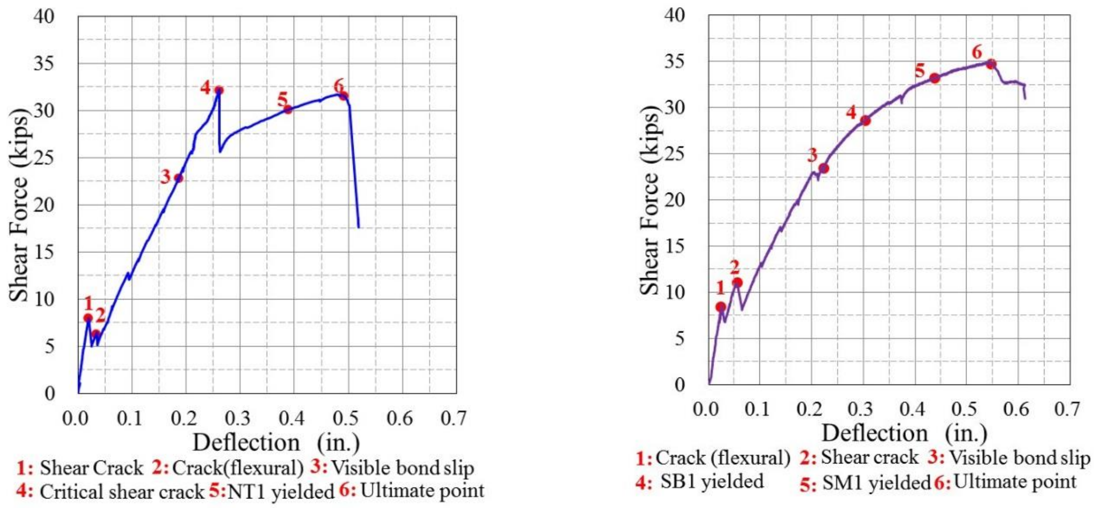

(a) SC3 north (b) SC3 south

Figure 103. Shear force-deflection curves of SC3

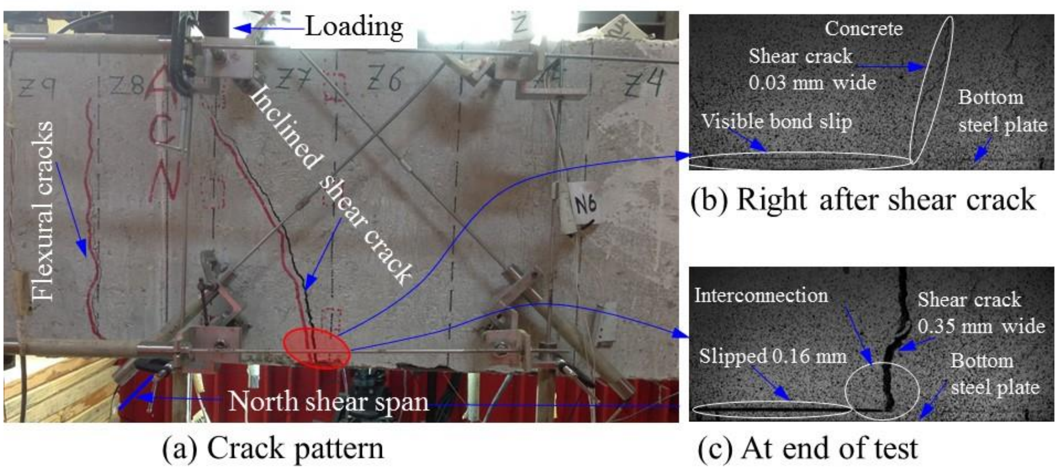

Figure 104. Crack pattern and bond slip of SC3 north in post peak stage

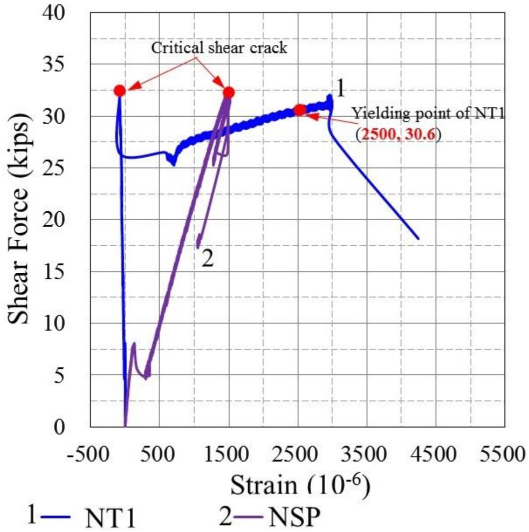

(a) SC3 north

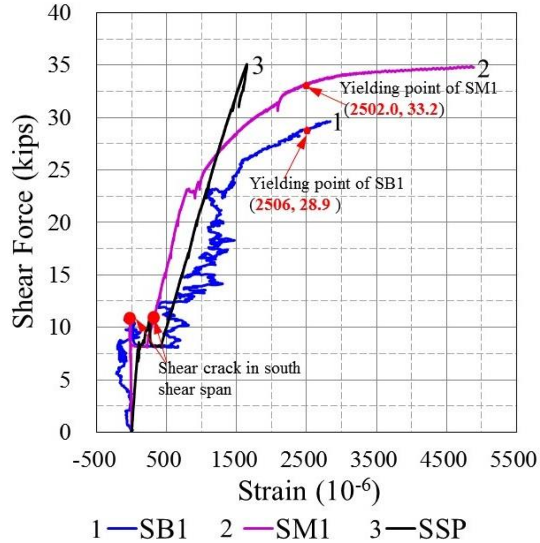

(b) SC3 south

Figure 105. Strains in cross ties and bottom steel plate of SC3

Specimen SC4

The shear reinforcement ratios of SC4 north and south were 54% and 93% more than the minimum required by ACI 349 Code (Equation 13), respectively. SC4 north and south were tested one end at a time. SC4 north was tested first. As shown in Figure 106, SC4 north exhibited several new structural states compared with SC1 to SC3:

More flexural cracks developed before shear crack appeared. Both cross ties close to shear crack and bottom steel plate were yielded before shear force F_{north} reached the peak. The peak shear force increased up to 42.7 kips (190 kN), and corresponding deflection Δ_{south} was 0.47 in. (11.9 mm).

After the yielding of cross ties and steel plate in SC4 north, stiffness of SC4 north was reduced significantly, as shown in Figure 106(a). The width of the shear crack kept increasing and propagating towards the top steel plate, and the bond slip between the bottom steel plate and concrete was observed. The inclined shear crack was approximately in the 45-degree direction, as shown in Figure 107(a). When F_{north} reached the peak point, the maximum crack width was 0.35

in. (9.00 mm) and the crack propagated up to 2.00 in. (50.8 mm) below the top steel plate (Figure 107[a]). At the post peak load stage, the bottom steel plate slipped 0.75 in. (19.1 mm), as shown in Figure 107(b). Concrete was not crushed in the north end.

The south end was tested after the north end was unloaded. To eliminate the influence of damage at the north end, the north support was moved toward the uncracked section, in this case 45.0 in. (1140 mm) southward from its' original position. The position of the south support and south actuator remained the same.

The shear force-deflection curve of the south end is given in Figure 106(b). When F_{south} reached 14.5 kips (64.6 kN) corresponding to Δ_{south} of 0.04 inch (1.02 mm), the concrete cracked and stiffness was reduced. As the shear force increased, cross ties close to the shear crack (SB2) yielded after the occurrences of the inclined crack and visible bond slip. Furthermore, the bottom steel plate under the actuator and cross ties near the top steel plate were yielded in succession. The beam end reached a plateau region right after yielding of the bottom steel plate. This phenomenon showed that the SC beam subjected to out-of-plane shear could exhibit a ductile behavior if a proper amount of cross ties was provided. Near the end of the plateau region, the inclined shear crack, with a crack width up to 0.08 inch (2.00 mm), propagated towards top fiber, as shown in Figure 108(a). Before the test, the positions of cross ties embedded in concrete were marked with dashed lines on the concrete surface and black dots on the side of the bottom steel plate. At the post peak stage, the cross ties were sheared off and the bottom steel plate slipped up to 0.50 inch (12.7 mm), as shown in Figure 108(b). No concrete crushing was observed in the south end.

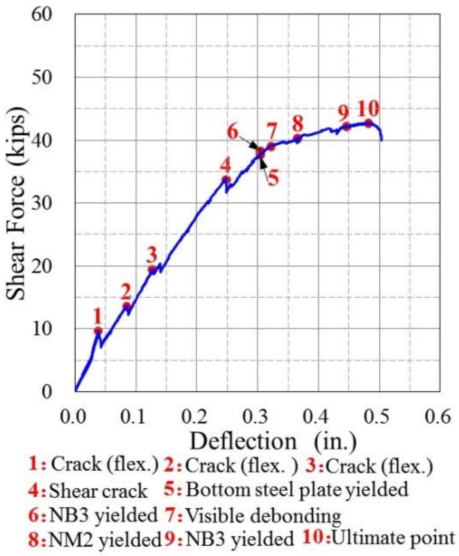

(a) SC4 north of cross ties spacing at 5 in.

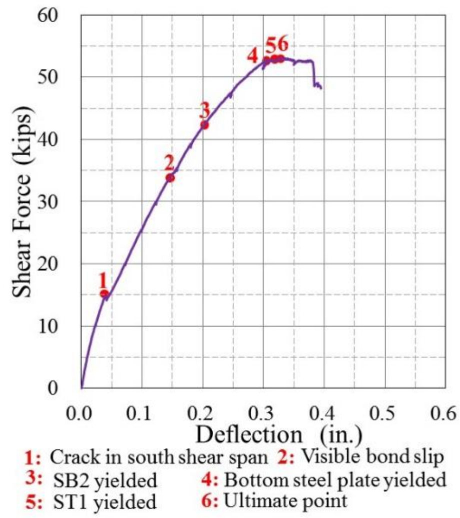

(b) SC4 south of cross ties spacing at 4 in.

Figure 106. Shear force-deflection curves of SC4

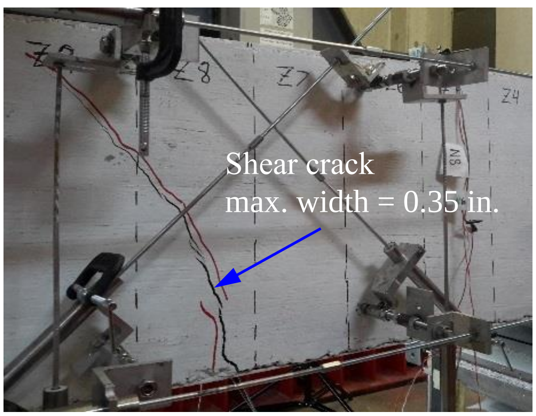

(a) North critical shear crack at ultimate loading stage

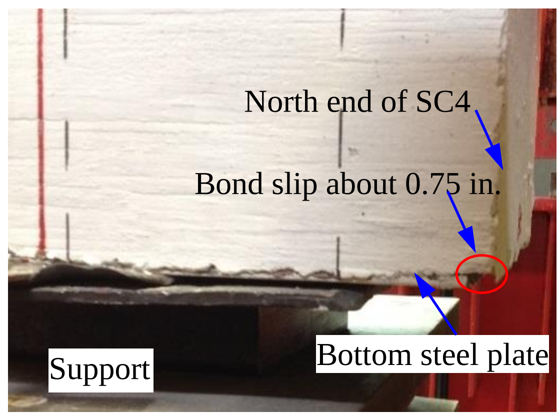

(b) Bond slip at the north end at end of test

Figure 107. Critical shear crack and bond slip of SC4 north

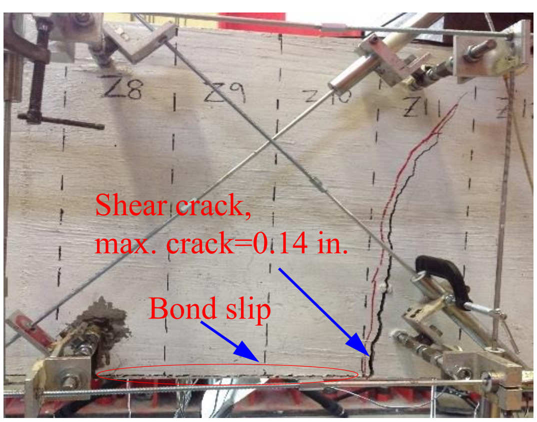

(a) South critical shear crack

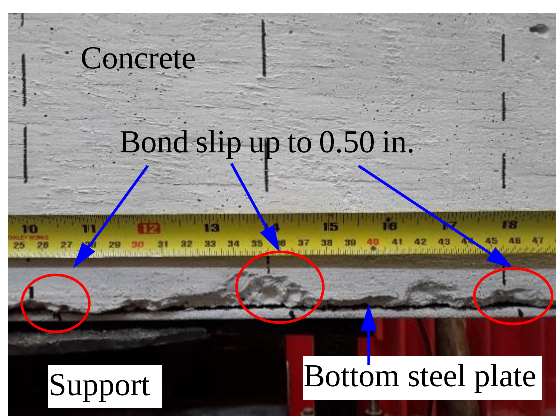

(b) Bond slip at the north end

Figure 108. Critical shear crack and bond slip of SC4 south before failure

Specimen SC5

The SC5 north and south were tested one end at a time under the shear span-to-depth ratio (a/d) of 1.5. The shear reinforcement ratios of SC5 north and south were 25% and 49% more than the minimum required by ACI 318 Code (Equation 13), respectively.

The SC5 south end was tested first. A crack occurred when F_{south} reached 11.0 kips (49.1 kN) and the corresponding deflection Δ_{south} was 0.004 in. (0.100 mm). After the SC5 south crack, the stiffness reduced quite significantly, as shown in Figure 109(a). When the bond slip became visible and cross ties were yielded, F_{south} entered into a plateau region with a magnitude of 55.0 kips (245 kN) and Δ_{south} increased to 0.10 in. (2.54 mm) in the plateau. In the plateau region, the bond slip was about 0.125 inch (3.17 mm), and the maximum crack width was about 0.100 inch (2.50 mm), as shown in Figure 110(a). Near the end of the plateau region, F_{south} reached the peak at 55.9 kips (249 kN), and the corresponding deflection Δ_{south} was 0.241 inch (6.12 mm). Concrete was not crushed in the south end, steel plate was not yielded and the south end had a ductility of 1.43.

The SC5 north end was tested after the south end was unloaded. To eliminate the influence of the damage at the south end, the south support was moved toward the uncracked section, in this case 37.0 inches (939 mm) northward from its origin position. The position of the north support and north actuator remained the same.

The north end cracked when F_{north} reached 16.7 kips (74.3 kN), and the corresponding deflection was 0.005 inch (0.127 mm). The stiffness reduced as the north end cracked, as shown in Figure 109(b). After the crack extended and the bond slip became visible, cross ties close to the bottom steel plate were yielded (NB2). As the cross ties were yielded, F_{north} entered into a plateau stage with a shear force of 64.0 kips (285 kN). Within the plateau stage, more cross ties were yielded, and the north deflection increased around 0.100 inch (2.54 mm). F_{north} reached the peak at 64.7 kips (288 kN), and the corresponding deflection Δ_{north} was 0.250 inch (6.35 mm). Concrete was not crushed in the north end, the bottom steel plate was not yielded and the north end had a ductility of 1.48.

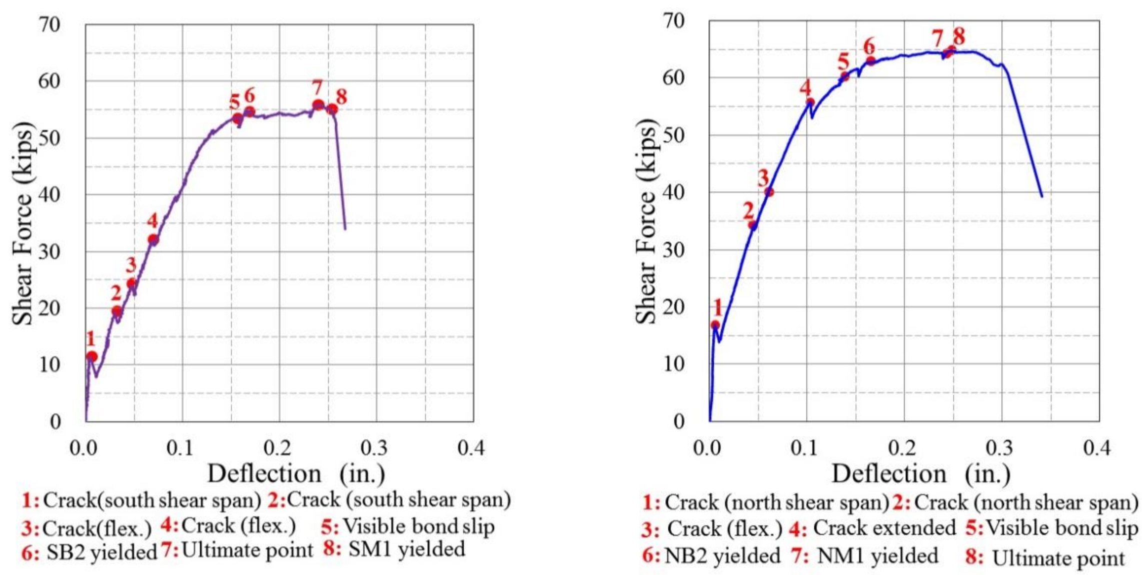

(a) SC5 south of cross ties spacing at 6 in. (b) SC5 north of cross ties spacing at 5 in.

Figure 109. Shear force-deflection curves of SC5

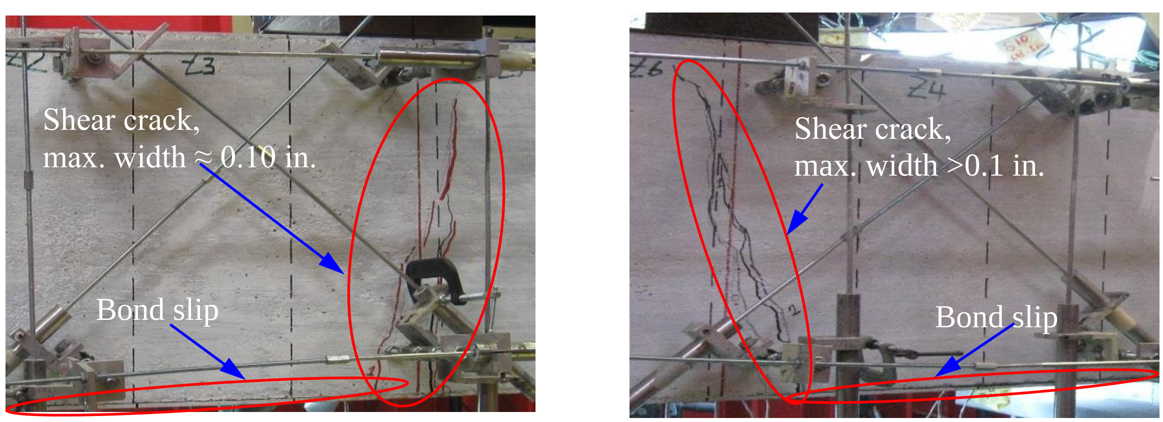

(a) SC5 south before failure (b) SC5 north before failure

Figure 110. Shear crack and bond slip of SC5 north and south

Specimen SC6

Specimen SC6 was tested under a shear span-depth ratio (a/d) of 5.15. Cross ties in specimen SC6 were spaced at 6.00 inches (152.4 mm), giving a shear reinforcement ratio of 25% more than the minimum required by ACI 349 Code (Equation 13).

Compared with SC1 to SC5, more flexural cracks were developed in SC6, which reduced the stiffness significantly, as shown in Figure 111. The cross ties yielded a moment after the yielding of the bottom steel plate. SC6 reached its ultimate at 29.3 kips (130 kN) and the corresponding deflection Δ_{north} was 1.17 inches (29.7 mm). Specimen SC6 was the most ductile among all tested beams, and the ductility of SC6 was 1.99. Concrete was not crushed during and after the test.

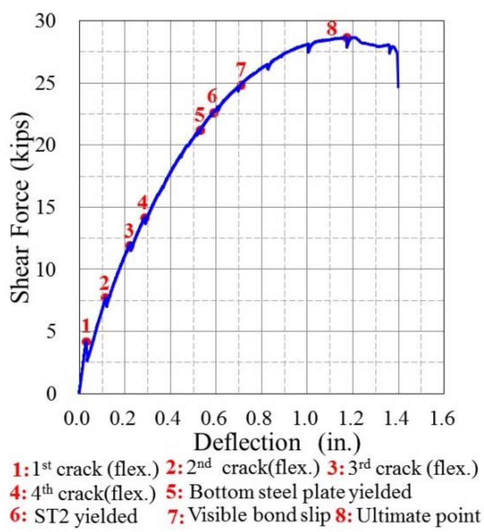

Figure 111. Shear force-deflection curve of SC6

4.2.4. Minimum cross tie ratio of SC structures under out-of-plane shear

In this section, a minimum cross tie ratio of SC structures subjected to out-of-plane shear is proposed after the analysis on test results of specimens SC1 to SC6. Specimens SC1 and SC2 failed prematurely due to insufficient of cross ties. Specimens SC4 north and south ends, which were tested one end at a time, and specimen SC3 were tested under the same shear span-to-depth ratio (a/d) 2.5 with different shear reinforcement ratio ($\rho_{t,test}$), as shown in Table 12. To compare test results of these specimens, normalized shear force-deflection curves are plotted in Figure 112. The shear force was normalized with $\sqrt{f_c'}b_w d$, and deflection was normalized with $\Delta_{peak.}$ (deflection corresponding to peak shear force).

Figure 112 shows that capacity and ductility increase as more cross ties are provided. Specimen SC3 had 45% more shear reinforcement than the minimum required by ACI 349 Code. Both the north and south ends were tested simultaneously, and they exhibited different behaviors. Specimen SC3 north had a sudden load drop right after it reached its peak due to the shear crack. The north end, however, was able to resist the load, but its stiffness reduced significantly. Cross ties in specimen SC3 north were yielded before F_{north} reached the second peak value, and the ductility of SC3 north was 1.17. On the other hand, specimen SC3 south behaved in a ductile manner. After yielding of cross ties in specimen SC3 south, the stiffness reduced gradually as loading continued. The ductility of specimen SC3 south was 1.79. Specimen SC3, north and south ends, just had adequate shear reinforcement ratio for SC beams to preserve a certain ductile behavior. Shear reinforcement ratios of Specimens SC4 north and south were 54% and 93% more than the minimum required by ACI 349 Code, respectively. Specimen SC4, both north and south ends, showed ductile behavior and higher ultimate shear strength than those of specimen SC3. The ductility of Specimens SC4 north and south was 1.58 and 1.65, respectively. The peak shear strength of each of specimens SC4 south and north was 35% and 67% more than the peak shear strength of specimen SC3 north, respectively. This trend further confirms that SC beams can have ductile behavior if the sufficient shear reinforcement is provided.

Specimens SC3, SC5 south and SC6 had the same shear reinforcement ratio of 0.137%, and were tested under three different shear-span-depth ratios (a/d). The shear force-deflection curves of these specimens are presented in Figure 113. It is obvious that the capacity and stiffness increases as a/d decreases. For instance, specimen SC5 South, with the smallest a/d of 1.5, had the highest capacity and stiffness. It is also obvious that the deflection increases as a/d increases. For instance, specimen SC6, with the largest a/d of 5.2, had the largest deflection. Specimens SC3 south, SC3 north, SC5 south and SC6 had a ductility of 1.17, 1.79, 1.43 and 1.99, respectively. Compared to the minimum shear reinforcement ratio specified by ACI 349 Code in Equation 13, the shear reinforcement ratio ($\rho_{t,test}$) of specimens SC3 south and north was 45% more, and the shear reinforcement ratio ($\rho_{t,test}$) of specimens SC5 south and SC6 was 25% more.

An interesting phenomenon can be found from the tests: more shear reinforcement (relative to the minimum required by the ACI 349 Code) is required for SC beams tested under a/d 2.5 than for SC beams tested under a/d 1.5 or 5.2. A similar trend can also be found in reinforced concrete members (Kuo et al., 2014[124]) and prestressed concrete members (Laskar et al., 2010[122]). Thus, the proposed minimum shear reinforcement ratio ($\rho_{t,min}$) for SC beams is

$$\rho_{t,min} = 1.45 \times \rho_{t,ACI} \quad \text{for } 2.0 < a/d < 4.0, \text{ or} \qquad (15)$$

$$\rho_{t,min} = 1.25 \times \rho_{t,ACI} \quad \text{for } a/d \leq 2.0 \text{ and } a/d \geq 4.0. \qquad (16)$$

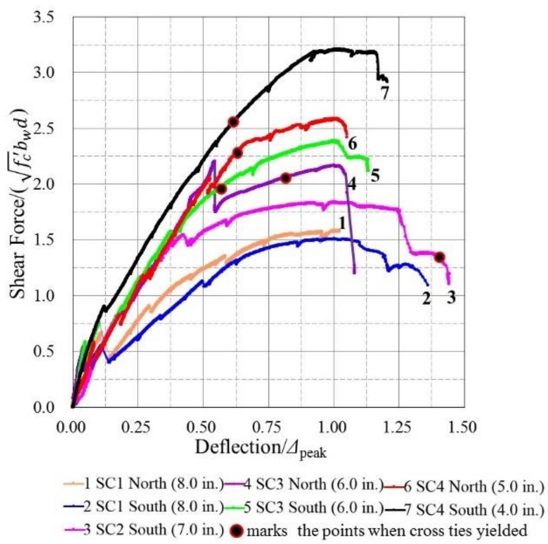

Figure 112. Specimens with the same shear span-to-depth ratio of 2.5

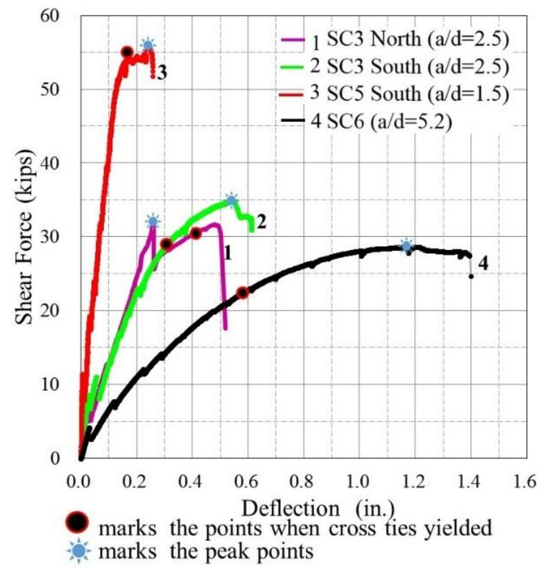

Figure 113 Specimens with cross tie spacing of 6.00 in

4.3.Bond slip detection between steel plate and concrete in SC beams using smart aggregates

4.3.1. Introduction

Bond-slip detection between steel plate and concrete is of great importance in providing early warnings of potential brittle failure and ensuring the safety of SC structures. In this report, an active sensing approach using Smart Aggregates (SAs) was developed to detect and monitor the initiation and development of bond-slip. A smart aggregate, designed by sandwiching a fragile piezoceramic patch between protection materials, can be utilized as both actuator and sensor by taking advantage of the piezoelectricity of piezoceramic material. Two SC beams with distinct shear reinforcement ratios (ρ_t) were experimentally investigated under loading tests. Based on the wavelet packet decomposition of the received signals from the SAs, the initiation of bond-slip was detected, and the development of bond-slip was quantitatively monitored. The bond-slip severities of the two SC beams were compared in order to study the improvement of the bond-slip condition rendered by providing more shear reinforcement.

Due to the inaccessibility and invisibility of the interface, the interfacial performance monitoring and debonding detection has proved challenging[125]. The development of reliable monitoring techniques for interface debonding has received extensive attention. For detecting damage as voids and debonding in glass fiber reinforced polymer (GFRP)-wrapped concrete structures, Feng et al. developed an electromagnetic (EM) imaging technique based on the reflection analysis of a continuous EM wave sent toward and reflected back from the layered GFRP-adhesive concrete medium[126]. Unfortunately, as EM waves cannot penetrate steel casing, this approach cannot be applied to SC beams. Based on velocity dispersion analysis of laser ultrasonic waves, the laser ultrasonics was demonstrated to detect delamination between concrete and steel plate[127]. However, this technology still requires application expertise for continuous improvement. A far-field airborne radar technique was proposed by Yu et al. to assess the condition of GFRP-retrofitted concrete structures[128]. This method detected near-surface defects and delaminations located in the vicinity of GFRP-concrete interface. Finite-element analyses by Cheng et al. proved that Lamb waves could be used to evaluate the bond condition of steel plate strengthened concrete[129].

In this report, piezoceramic-based Smart aggregates (SAs), which have been proved applicable to health monitoring and damage detection of various civil structure members, are extended to detect and monitor bond-slip between the concrete and the steel plates in SC members. Piezoceramic-based Smart aggregates (SAs) are widely applicable in the structural health monitoring due to advantages such as low cost, quick response, high reliability and the wide frequency range of excitation, etc.[130, 131]. Using a pitch-catch mode, piezoelectric sensors and actuators, embedded in Reinforced Concrete (RC), detected debonding between concrete and rebar and yielding of rebars[132]. With a combination of accelerometers and piezoceramic sensors, a vibration-impedance-based monitoring method was proposed by Kim et al. to predict the loss of prestressing forces in prestressed concrete (PC) girder bridges[133]. In an experimental study conducted by Xu et al., SAs were used to detect debonding of concrete filled steel tube (CFST) columns, and wavelet packet analysis was used to evaluate the debonding[125]. Based on the time reversal technology, the smart aggregate-based approach proposed by Yan et al. could effectively detect the compactness of concrete in CFST columns[134].

A series of tests on SC beams was conducted for this project. This series of tests was designed to find out the minimum shear reinforcement ratio ($\rho_{t,min}$) of SC beams. Shear reinforcement (cross ties) in the tests played a significant role in transferring shear force between the steel plate and the concrete at interface. These SC beams were prone to bond slip between the steel plates and concrete. Specimens SC1 and SC4 were selected to investigate the development of bond slip and cracks for conventional concrete and Specimens S-UHPC-1(only south) and S-UHPC-2 were selected for Ultra-High Performance Concrete. The smart-aggregate based active sensing system was used to detect and monitor the bond slip of SC and S-UHPC beams under loading.

4.3.2. Detection principles

A smart aggregate-based active sensing approach was developed to detect the bond slip between steel plate and concrete/UHPC of the SC/S-UHPC beam, as shown in Figure 114. One smart aggregate (marked in red) embedded in the concrete was utilized as an actuator, which could generate a repeated swept sine wave. The other smart aggregate deployed on the steel plate was utilized as a sensor to detect the swept sine wave, as shown in Figure 114(a). In the initial condition when bond slip did not occur, the received signal $\boldsymbol{S}_0$ from the sensor was used as the baseline signal which represented the health state of the SC beam, as shown in Figure 114(a). When bond slip occurred, the compactness between the steel plate and the concrete was decreased. Therefore, the energy of the received signal $\boldsymbol{S}_i$ attenuated corresponding to the severity of the bond slip condition, as shown in Figure 114(b). The energy attenuation of the signal $\boldsymbol{S}_i$ can be characterized by a wavelet packet-based structural damage index. The distinct severity of the bond slip in different locations can be detected by distributed sensors on the steel plate.

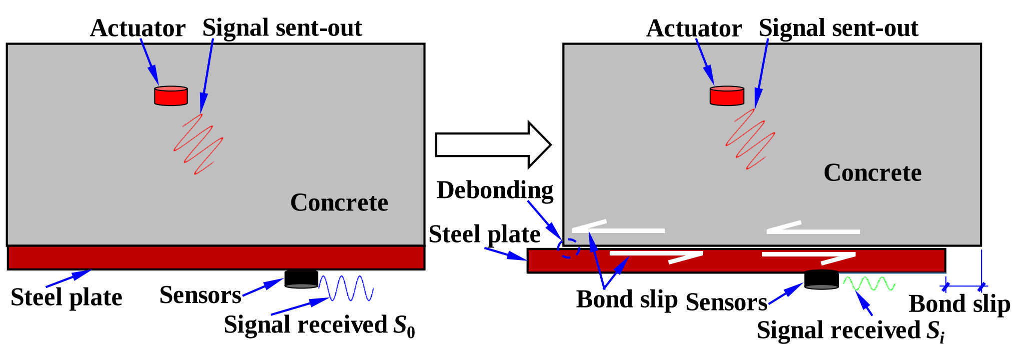

(a) Health state before bond slip (b) Damaged state after bond slip

Figure 114. A developed smart aggregate based active sensing approach to detect bond slip between steel plate and concrete

Wavelet packet analysis is widely used in mathematics, signal processing, image processing, quantum mechanics and theoretical physics, etc. Compared to the traditional Fourier Transform, the wavelet packet technique is a localized analysis in time-frequency of signals[135]. The signal can be specifically characterized based on wavelet packet analysis. Based on wavelet packet analysis, Samuel and Pines utilized a normalized energy vector for the fault classification of helicopter gearboxes[136]. Song et al. proposed a wavelet packet-based structural damage index by direct application of energy vector, and experimental results showed that the structural damage index can capture cracks in a reinforced concrete bridge bent-cap[137].

In this report, the damage index was adopted to identify the initiation and the severity of the bond slip. Based on an n-level wavelet packet decomposition, the sensor signal $\boldsymbol{S}_i$ was decomposed into 2^n signal sets $\{\boldsymbol{S}_{i,1},\ \boldsymbol{S}_{i,2},\ \cdots,\boldsymbol{S}_{i,j},\cdots,\boldsymbol{S}_{i,2^n}\}$, where $\boldsymbol{S}_{i,j}$ is specified in Equation 16. The energy $E_{i,j}$ of the decomposed signal $\boldsymbol{S}_{i,j}$ is defined by Equation 17, and the energy vector $\boldsymbol{E}_i$ of the sensor signal $\boldsymbol{S}_i$ is given by Equation 18[137].

$$\boldsymbol{S}_{i,j} = [x_{i,j,1},\ x_{i,j,2},\ \cdots,\ x_{i,j,m}] \tag{17}$$

$$E_{i,j} = \|\boldsymbol{S}_{i,j}\|_2^2 = {x_{i,j,1}}^2 + {x_{i,j,2}}^2 + \cdots + {x_{i,j,m}}^2 \tag{18}$$

$$\boldsymbol{E}_i = [E_{i,1},\ E_{i,2},\ \cdots,\ E_{i,2^n}] \tag{19}$$

where j is the frequency band ($j = 1,\cdots,2^n$), m is the number of the sampling data, and i is the serial number of the measured sensor signal.

The energy vector of the initial signal $\boldsymbol{S}_0$, which represented a healthy state, was $\boldsymbol{E}_0 = [E_{0,1},\ E_{0,2},\cdots,\ E_{0,2^n}]$. The energy vector of signal $\boldsymbol{S}_i$ was $\boldsymbol{E}_i = [E_{i,1},\ E_{i,2},\cdots,\ E_{i,2^n}]$. The Damage Index (DI) was defined using Root-mean-square Deviation (RMSD), as shown in Equation 20 [137].

$$DI = \sqrt{\frac{\sum_{j=1}^{2^n}(E_{i,j}-E_{0,j})^2}{\sum_{j=1}^{2^n}E_{0,j}^2}} \tag{20}$$

The Damage Index (DI) represents the transmission of energy loss caused by structural damage such as cracks, debonding and bond-slip, etc. When the Damage Index (DI) is close to zero, it means the structure is in a healthy state. When the value of the Damage Index (DI) increases, the structure is considered under damage condition. The damage index has been successfully used to detect cracks in reinforced concrete (RC) bent-cap [137], and has been proven effective in assessing damage severity of the concrete shear wall [131].

4.3.3. Installation and location of SAs

SA actuators were placed inside the beam before casting of the concrete, as shown in Figure 115(a). SA sensors were attached on the outside surface of steel plates using epoxy, as shown in Figure 115(b).

The arrangements of SAs for SC beams (SC1 and SC4) are shown in Figure 116 and Figure 117, respectively. For SC beams with conventional concrete, the signal actuators in the north and south ends were labeled as SA1 and SA2, respectively. Receiver sensors SA3 and SA5 were attached on the bottom steel plate in the north and south ends, respectively. Furthermore, sensors SA4 and SA6 were attached on the top steel plate in the north and south ends, respectively. SA3 and SA5 were used for bond slip detection, and SA4 and SA6 were used as reference for comparison.

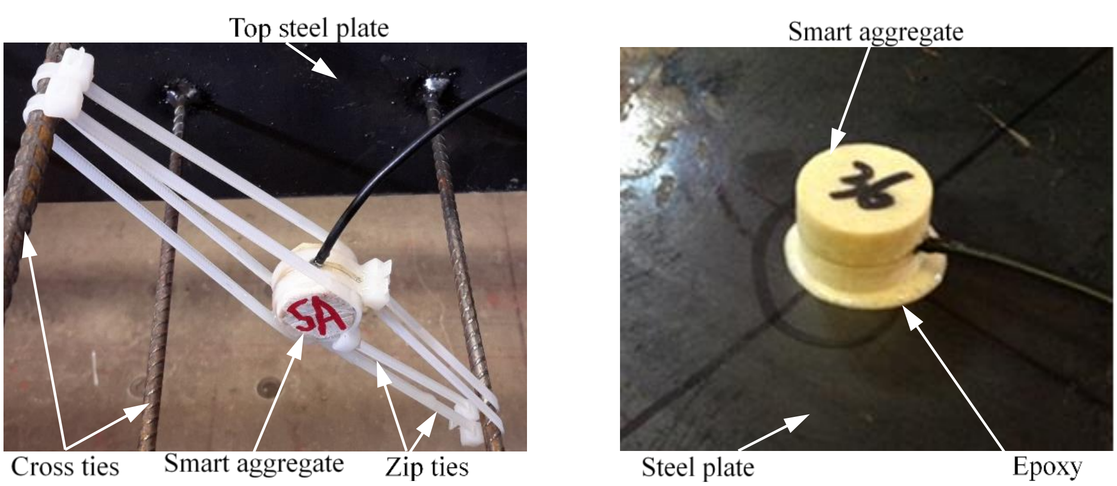

(a) SA as actuator (b) SA as sensor

Figure 115. Installation of Smart Aggregates (SAs) as actuator and sensor

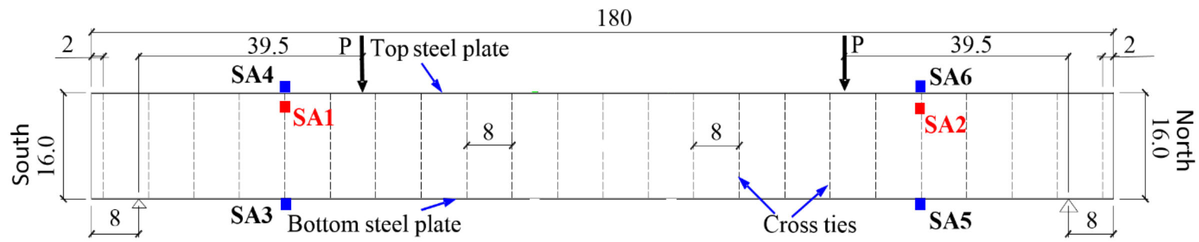

Figure 116. Arrangement of SAs in Specimen SC1 (unit: inch)

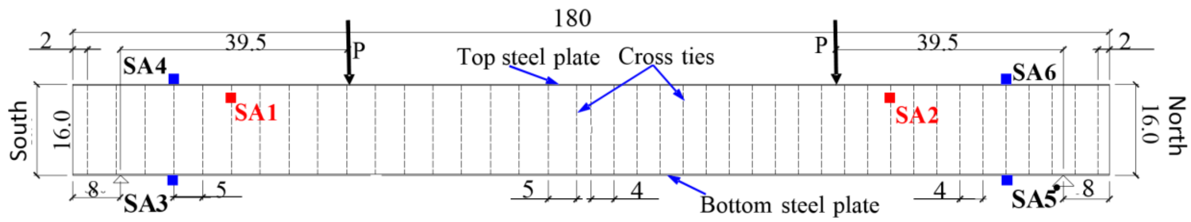

Figure 117. Arrangement of SAs in Specimen SC4 (unit: inch)

4.3.4. Instrumental setup

The schematic of the instrumental setup is shown in Figure 118, which includes a function generator (Agilent 33120A), a power amplifier (Trek 2100HF), a data acquisition board (NI USB6363) and a laptop with supporting software. A repeated swept sine wave is generated and then amplified using the function generator and power amplifier, respectively. The details of the swept sine wave are shown in Table 13. SA actuators connected to the power amplifier generate a guided stress wave which will be detected by SA sensors. The detected wave signals are recorded by the data acquisition board associated with the laptop. The sampling frequency of the data acquisition board is 1.00 MS/s. The instrumental setup for the test on SC1 is shown in Figure 119(a).

Load cells were setup under north and south supports, as shown in Figure 119(b), to measure shear force in the SC beams. Data from load cells were collected, plotted and stored by the HBM Spider 8 data acquisition system. The system was capable of parallel and dynamic measurement, with a sampling frequency of 0.20 Hz.

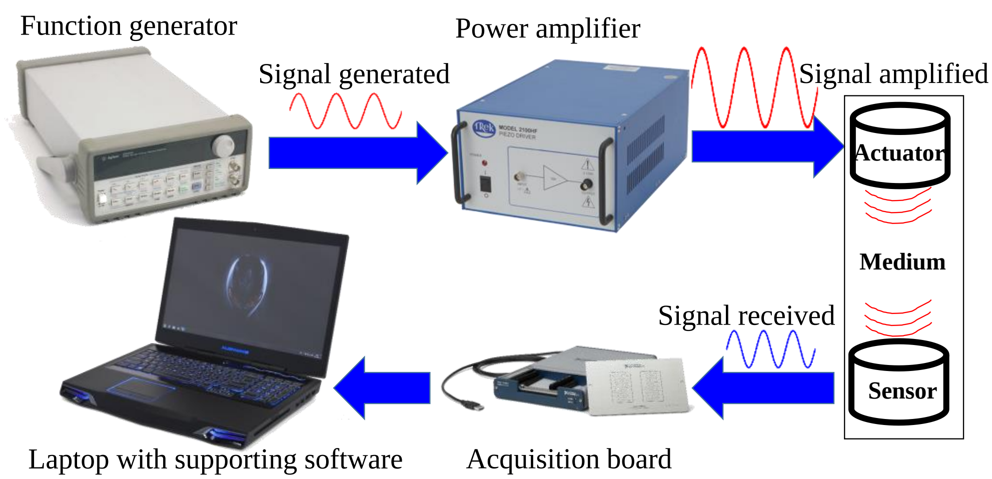

Figure 118. Schematic of experiment instrumentation

Table 13. Parameters of sine wave signal sent out by SA actuator

Amplitude (v)	Start frequency (Hz)	Stop frequency (kHz)	Period (s)
10.0	100	150	0.50

4.3.5. Test procedure

The specimens were subjected to vertical loading provided by north and/or south actuators with a capacity of 600 kips (2669 kN) each. SC1 north and south were loaded simultaneously, and the arrangement of supports and actuators is shown in Figure 119 (b). For Specimen SC4, the end (SC4 north) with lesser shear reinforcement was tested first, as shown in Figure 120(a). Before the test on SC4 south was conducted, the support at the failure end had been moved to the uncrack-section. The north support was moved 45.0 inches (1143 mm) southward from the original position, as shown in Figure 120(b).

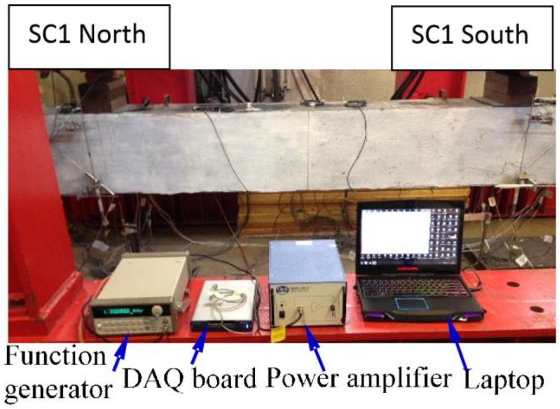

(a) Experiment setup of instrumentation

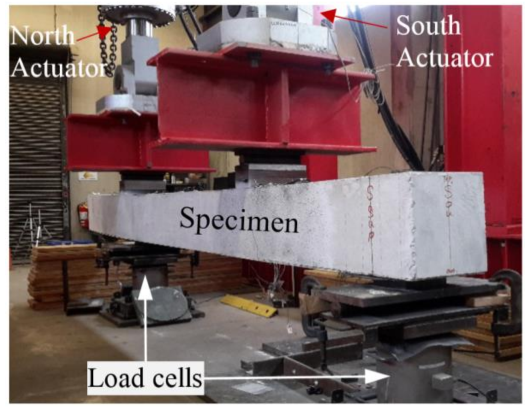

(b) Setup of supports and actuators

Figure 119. Test setup of SC1

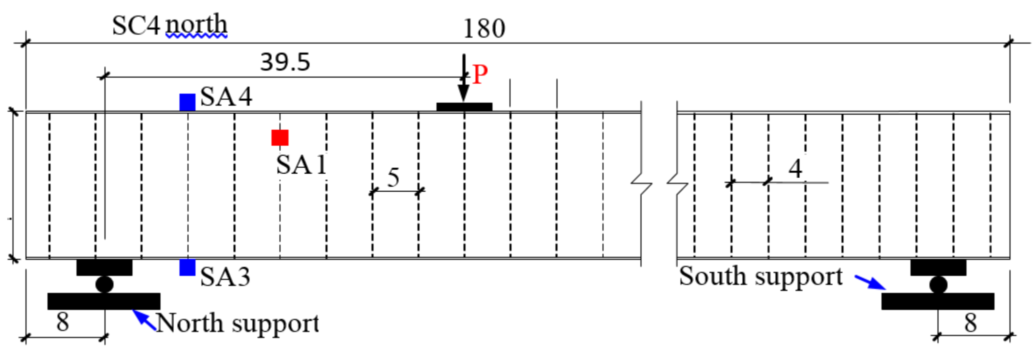

(a) Test setup of SC1 north

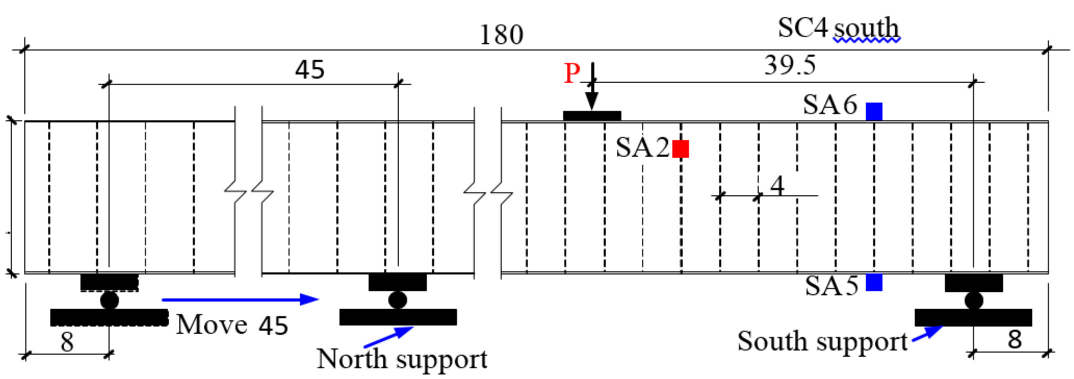

(b) Test setup of SC2 south

Figure 120. Test setup of Specimens SC4 (unit: in.)

Loads and displacements of the actuators were controlled by the MTS Flex system. The loading protocol was comprised of several loading steps. Each loading step had a constant loading rate of 2.54 mm (0.10 inch) per 15.0 minutes. During each loading step, the loading might be put on hold before resuming for the inspection of cracks and bond slip. Each test lasted three to five hours. The initial sensor signal S_0 before loading was measured as the baseline representing health state. During the test, the sensor signal was measured every five to ten minutes.

4.3.6. Tests results

Loading history

Loading histories of Specimens SC1 and SC4 are given in Figure 121 and Figure 122, respectively. In these figures, points corresponding to the occurrences of cracks, visible bond slip, ultimate points and failure are marked. The occurrences of cracks led to an instant drop of shear force in SC1 south and north and SC4 north, as shown in Figure 121(a), Figure 121(b) and Figure 122(a), respectively. However, the occurrences of cracks barely resulted in any drop of shear force in SC4 south, as shown in Figure 122(b). The shear force in SC4 south increased steadily until it reached the plateau stage shown in Figure 122 (b). The plateau stage started from 6255 s and ended at 9305 s, during which the shear force fluctuated around 234 kN (52.5 kips). According to these curves and the observation during the tests, information about time of important events, such as the occurrences of cracks, visible bond slip, ultimate point and failure is given in Table 14.

A test on Specimen SC1 was stopped when SC1 south lost capacity abruptly, as shown in Figure 121 (b). The maximum shear capacity of SC1 was 122 kN (27.4 kips) as shown in Figure 121 (a). The shear capacities of SC4 north and south were 190 kN (42.7 kips) and 236 kN (53.0 kips), respectively. Despite the lower concrete strength of SC4 compared to the concrete strength of SC1 as shown in Table 12, the shear capacities of SC4 north and south were 1.55 and 1.93 times the maximum shear capacity of SC1, respectively. This reveals that cross ties act as an effective shear transfer mechanism and increase the shear capacity of SC beams.

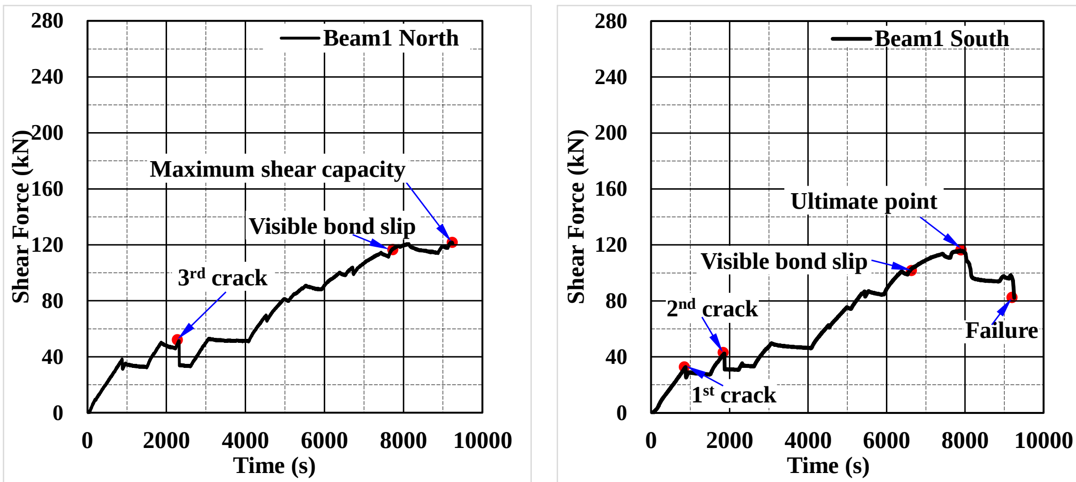

(a) SC1 north (b) SC1 south

Figure 121. Shear force-time curves of SC1 north and south

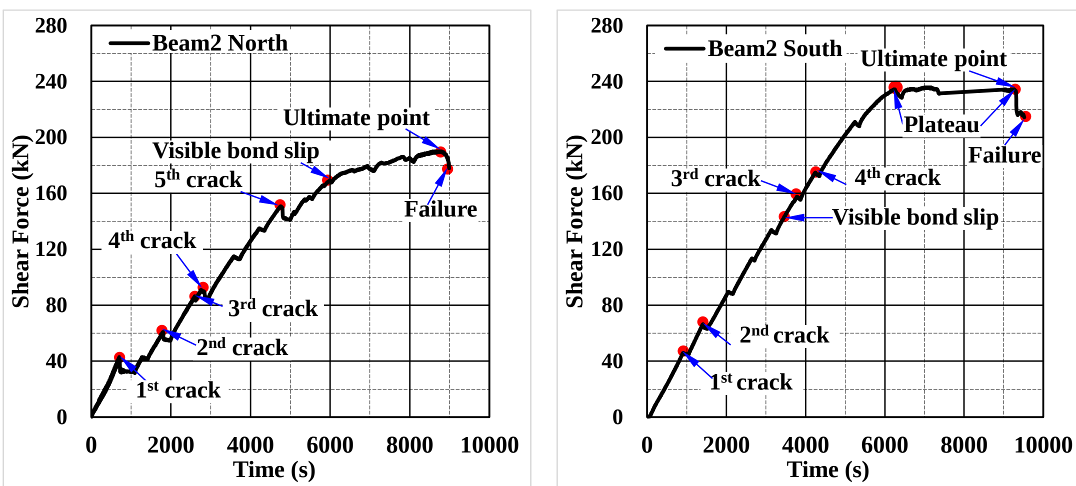

(a) SC4 north (b) SC4 south

Figure 122. Shear force-time curves of SC4 north and south

Table 14. Time information about important events during tests (unit: s)

	1st crack	2nd crack	3rd crack	4th crack	5th crack	Visible bond slip	Ultimate point	Failure
SC1 North	—	—	2320	—	—	7690	—	—
SC1 South	880	1870	—	—	—	6615	7800	9245
SC4 North	715	1810	2610	2849	4804	6200	8860	8990
SC4 South	1045	1410	3960	4295	—	3535	9170	9550

Specimen SC1

The test on Specimen SC1 lasted around 2.64 h (9500 s). Bond slip and three major cracks were observed, as shown in Figure 123 and Figure 124 for SC1 north and south, respectively. These cracks were labeled as the 1st, 2nd and 3rd cracks according to the time of occurrences given in Table 14. The first and second cracks were in the SC1 south, as shown in Figure 124(a). The third crack was in SC1 north, as shown in Figure 123(a). The second and third cracks were inclined shear cracks. All cracks started from the bottom and propagated upwards as the loading increased. According to the observation during the test, bond slip occurred along the bottom interface within the shear span to the end of the beam, as shown in Figure 123 and Figure 124 for SC1 north and south, respectively.

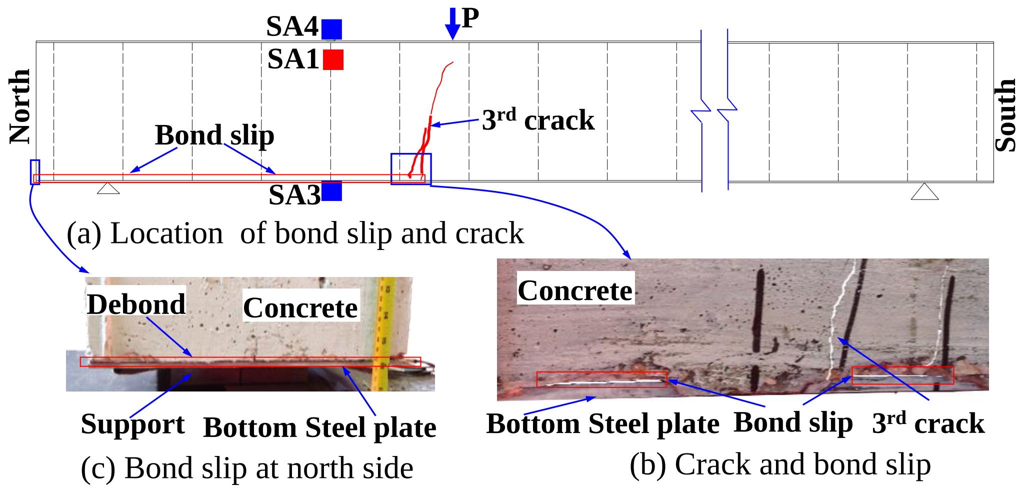

Figure 123. Bond slip and crack patterns in SC1 north after test

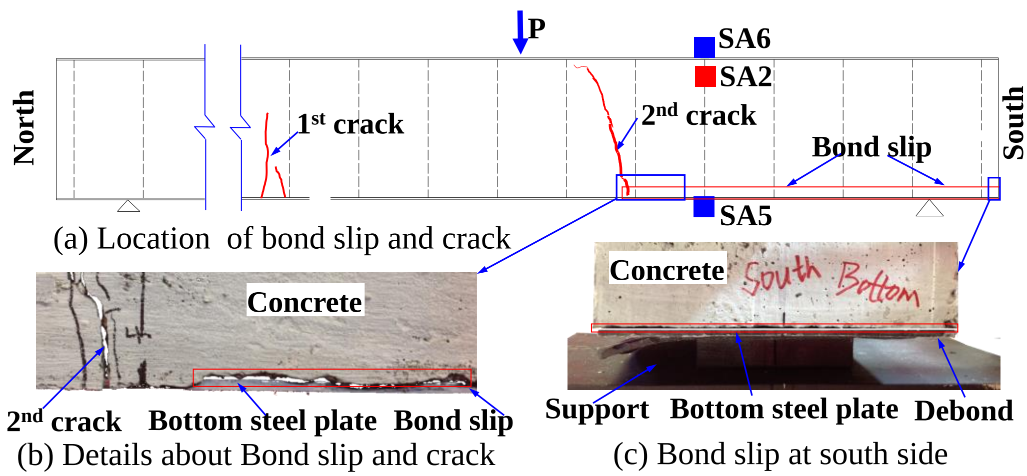

Figure 124. Bond slip and crack patterns in SC1 south after test

In SC4 south, no crack or bond slip occurred between actuator SA2 and sensor SA6 (on the top of the beam within the shear span). The only bond slip was on the stress wave path between sensor SA2 and sensor SA5 (on the bottom within the shear span). A similar case can be found in the SC1 north. Therefore, sensors SA4 and SA6 can be used as reference for comparative study; sensors SA3 and SA5 were used to capture bond slip at the interface between the bottom steel plate and the concrete.

Damage indexes of sensors of SC1 north and south are shown in Figure 125 and Figure 126, respectively, which were measured after the occurrences of important events, as marked in these figures.

The damage index of each sensor was obtained at certain increments from 0 s to 834 s. However, during this period in the test no crack occurred, and the shear forces applied on SC1 south and north had been increased monotonically. A possible reason for the increase of all the damage indexes at 834 s could be that increasing shear force led to boundary adjustment and altered concrete compactness and interfacial conditions of SC1.

Despite the increase of shear force at 834 s, damage indexes of SA4 and SA6 were trivial and almost unchanged throughout the test, as shown in Figure 125 and Figure 126, respectively. This agreed well with the observation that no crack or bond slip occurred near SA4 and SA6. Before the occurrence of the second crack, the bond slip in SC1 south had already developed. Meanwhile, the damage index of SA5 in Figure 126 had a small increase between 834 s and 1645 s, which captured the initial development of the bond slip in SC1 south. The second crack started from the interface between the bottom steel plate and the concrete, as shown in Figure 125, leading to deterioration of the bond slip. Consequently, the damage index of SA5 increased dramatically from 0.28 to 0.90. Before the occurrence of the third crack, shown in Figure 123, the damage index of SA3 increased to 0.88, as shown in Figure 125, which captured the development of the bond slip in SC1 north. Damage indexes of SA5 and SA3 indicated severely damaged bond conditions in the bottom interface of SC1 south and north, respectively, which provided warning in advance of the structural failure.

Under continued loading, the bond condition in the bottom interface of SC1 south kept deteriorating. When F_{south} reached the peak value (F_{peak}) 116 kN (26.1 kips) at 7875 s, as shown in Figure 121(b), the damage index of SA5 increased to 0.98, as shown in Figure 126. When the bottom steel plate debonded from the concrete, SC1 south failed and F_{south} dropped to 72.5% of F_{peak}, as shown in Figure 121(b). On the contrary, the damage index of SA3 did not yield a considerable increase after the occurrence of the third crack and was below 0.9. Due to the residual bond in the bottom interface of SC1 north, shear force (F_{north}) applied on SC1 north could increase, as shown in Figure 121(a). Therefore, it is apparent that SC1 south and north behaved differently during the test, although they had the same shear reinforcement ratio and were tested simultaneously. This different behavior between SC1 south and north indicates that bond condition is of great importance to structural performance of SC beams.

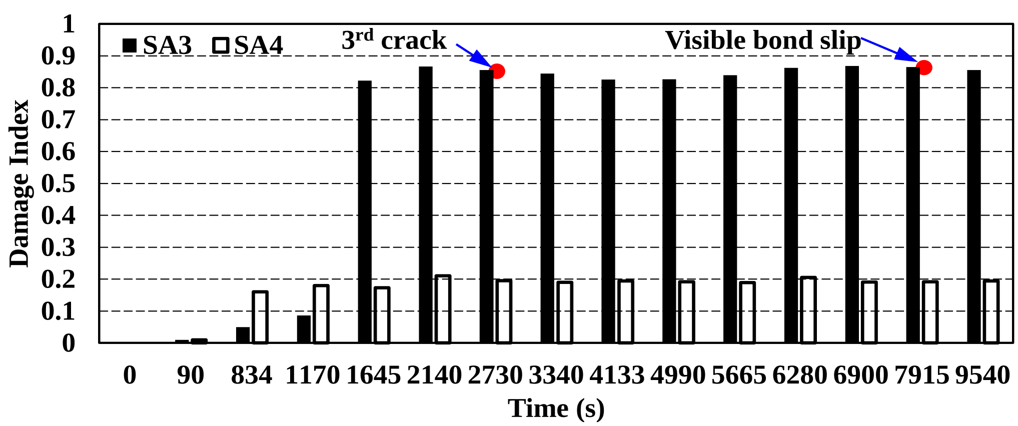

Figure 125. Damage indexes of sensors installed on SC1 north

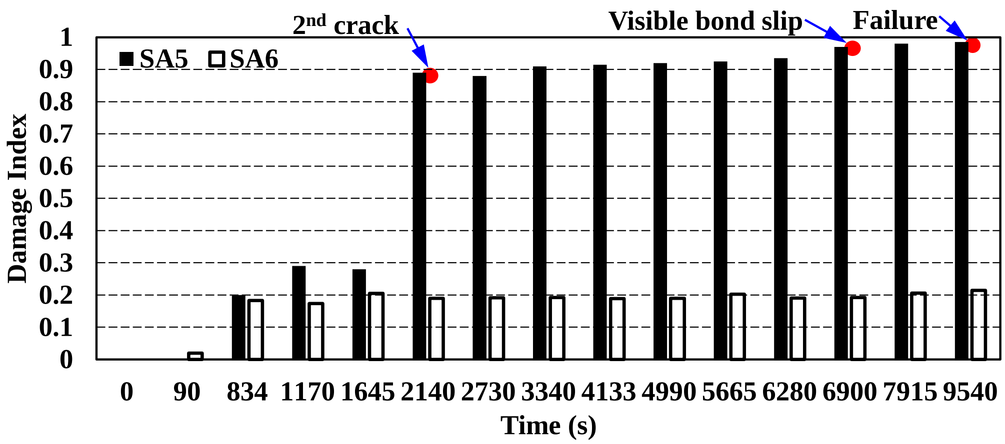

Figure 126. Damage indexes of sensors installed on SC1 south

SC4 north

Major cracks and bond slip in the SC4 north are shown in Figure 127. Five major cracks were observed and labeled as the first to the fifth cracks according to the time of occurrences given in Table 14. The first to the fourth cracks were flexural cracks, and the fifth crack was the only shear crack. Bond slip existed along the bottom interface, as shown in Figure 127(a). After the test, the bottom steel plate slipped 0.75 inch (19.0 mm), as shown in Figure 127(c).

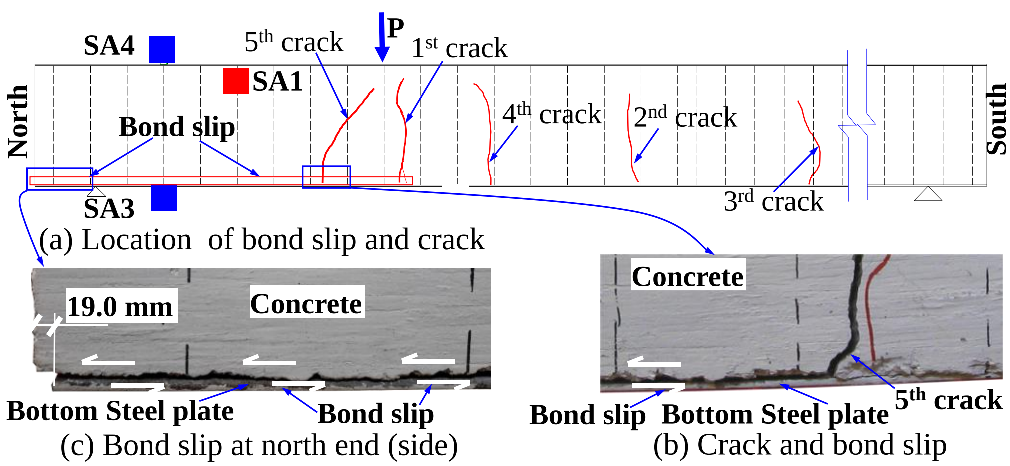

Figure 127. Bond slip and cracks in SC4 south after test

Similar to the case in SC1, sensor SA3 was used to capture the bond slip, and SA4 was used as reference for comparative study. Damage indexes of sensors SA3 and SA4 are given in

Figure 128. Damage indexes measured after the occurrences of important events, such as cracks, visible bond slip and failure are marked in the figure.

The damage index of SA4 was irrelevant to the bond slip and cracks, as shown in Figure 128, and was negligible compared to the damage index of SA3. This agreed well with the observation that no crack or bond slip occurred near SA4. Before the first crack occurred, the damage index of SA3 (Figure 128) had been increasing steadily, which captured the initial development of the bond slip at the bottom interface. Right after the occurrence of the first crack (715 s), the damage index of SA3 yielded a considerable increase from 0.17 to 0.37. This damage index increase of SA3 was due to the weakening of the bond slip triggered by the first crack, as shown in Figure 127. The second to the fourth cracks did not show any influence on the damage index of SA3, as shown in Figure 128.

The occurrence of the fifth crack signified the beginning of the further deterioration of the bond slip, as shown in Figure 128. The bond slip became more severe as loading continued, and the damage index of SA3 was 1.00 when the bond slip became visible, as shown in Figure 128. According to the definition of damage index, as expressed in Equation 20, damage index equal to 1.00 means that the bottom steel plate was separated from the concrete. Therefore, in advance of the failure of SC4 north, the damage index of SA3 provided early warning about the debonding of the bottom steel plate from the concrete. At the moment of failure during the test, several cross ties at the debonded interface were sheared off, and the maximum width of the fifth crack increased from 4.50 mm to 7.00 mm.

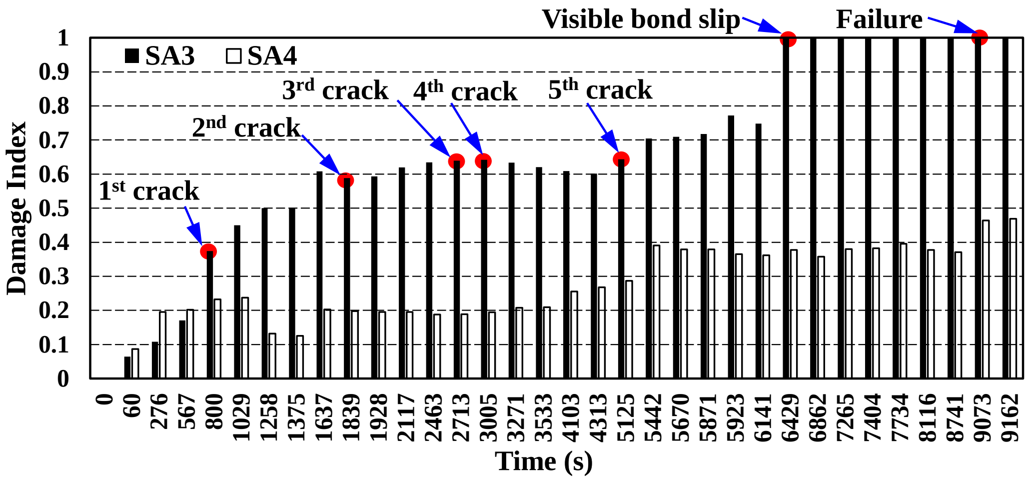

Figure 128. Damage indexes of sensors installed on SC4 north

SC4 south

The bond slip and major cracks in the SC4 south are shown in Figure 129, where the four major cracks were labeled as the first to the fourth cracks according to the time of occurrences given in Table 14. Only the second crack was an inclined shear crack, and all the other cracks were flexural cracks. The bond slip was along the bottom interface within the shear span, as shown in Figure 129.

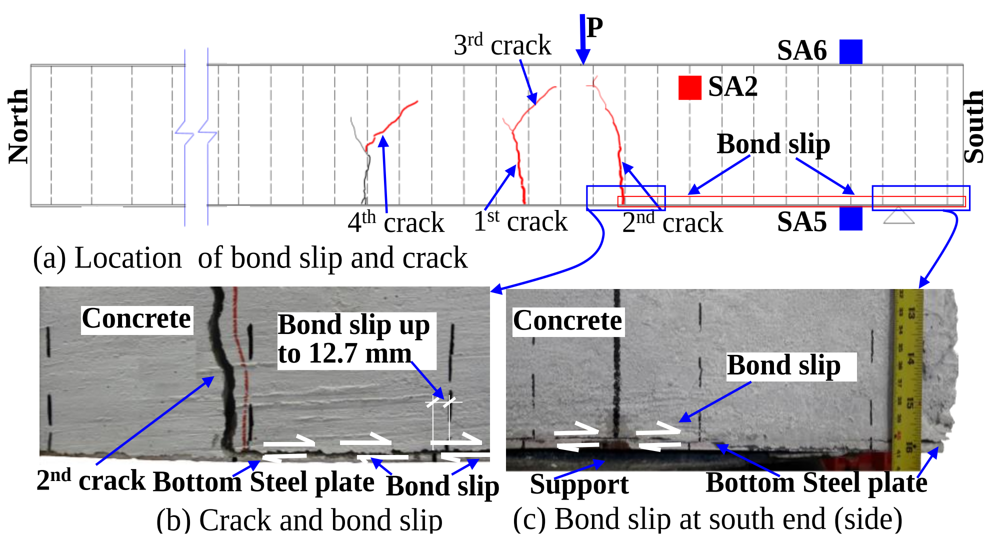

Figure 129. Bond slip and cracks in SC4 south

During the test, SA6 lost communication with the DAQ system, and the damage index of SA5 is presented in Figure 130. The damage index measured after the occurrences of important events, such as cracks, visible bond slip and failure is marked in Figure 130. Similar to the cases in SC1 and SC4 north, SA5 was used to detect the bond slip.

Just as no major drop of shear force happened due to the occurrences of cracks, as shown in Figure 122(b), no immediate increase in the damage index happened due to the occurrences of cracks, as shown in Figure 130, which was different from the cases of SC1 and SC4 north. Before the secpmd crack occurred, the damage index of SA5 had increased to 0.19, which captured the initial development of the bond slip. The second crack triggered the bond slip, which could be demonstrated by the evident increase of the damage index of SA5 following the occurrence of the second crack, as shown in Figure 130. During the unique plateau stage of the shear force-time curve marked in Figure 122(b), the loading continued and the damage index of SA5 fluctuated around 0.60. When the shear force-time curve reached into the descending branch after the plateau stage, as shown in Figure 122(b), the damage index of SA5 increased to 0.81, as shown in Figure 130, which provided early warning about the bond condition of the interface before the failure. When the bottom steel plate was debonded from the concrete and several cross ties at the debonded interface were sheared off, SC4 south failed, and the damage index of SA5 was 0.89 after the failure.

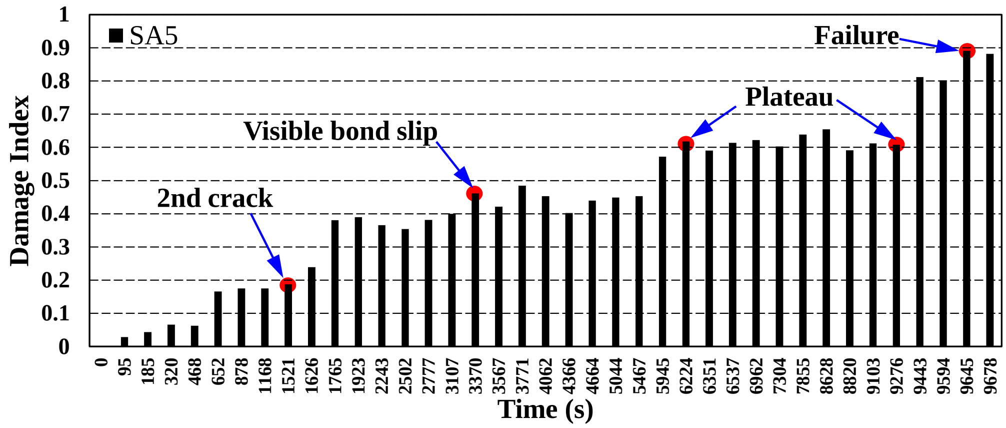

Figure 130. Damage index of sensors installed on SC4 north

4.3.7. Effect of shear reinforcement ratio on bond-slip severity

As test results and analysis indicated, sensors SA3 and SA5 in Specimens SC1 and SC4 captured initial development of the bond slip successfully. Figure 131 gives the shear force-damage index curves of SA3 and SA5 for SC1 and SC4, respectively. From SC1 to SC4 north and south, an increasingly higher shear reinforcement ratio ($\rho_{t,test}$) was provided, as given in Table 12. As shown in Figure 131, when more shear reinforcement was provided, the SC beam could resist a larger shear force with significantly lesser damage caused by the bond slip. This was especially true when shear force was larger than 10.0 kips, as shown in Figure 131. SC4 south equipped with the highest shear reinforcement ratio had the evident symbol of ductile behavior. In the unique plateau stage of SC4 south, the damage index fluctuated around 0.60 and shear force was around 52.5 kips (234 kN), despite the fact that loading continued at the same time. Therefore, it is clear that cross ties can effectively improve the bond condition at the interface of SC beams. Meanwhile, cross ties as shear reinforcement can significantly improve ductility and shear strength of SC beams.

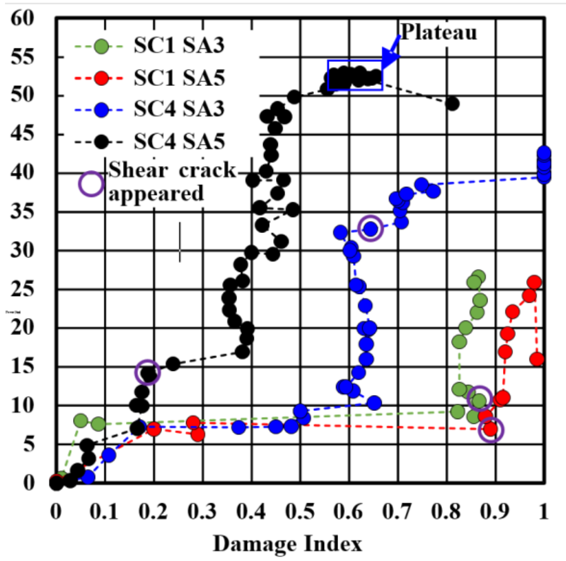

Figure 131. Shear force-damage index curves of SC1 and SC4

4.4. Experimental Program for SC Beams with UHPC

The main test parameter in this study is only the cross ties ratio ($\rho_{t,test}$). The cross ties ratio of the beams varied from 0.184% to 0.321% in order to find the minimum cross ties ratio for the SC beam to exhibit a ductile behavior. The cross ties ratio of 0.184% is calculated based on the minimum shear reinforcement ratio recommendations of ACI 318. The design of the south side of S-UHPC-1 was based on Equation 13 to verify the applicability of ACI 318 to S-UHPC structures. The cross tie ratio was further increased by 25%, 50% and 75% to identify the minimum cross tie ratio ($\rho_{t,min}$) for S-UHPC beams. The shear span-to-depth ratio (a/d), also known as shear span ratio, has been kept constant in the design of the beams. Shear span (a), as shown in Figure 132, is defined as the distance between the loading point and the center line of the support. Shear at failure depends on the shear span-to-depth ratio (a/d). For Reinforced Concrete (RC), the shear stress at failure increases by 225% when the a/d ratio changes from 2.35 to 1.17[138]. It was found that the load carrying capacity of beams reached a minimum at a/d=2.5[120]. Furthermore, based on the test results of SC beams with normal strength concrete, an a/d of 2.5 resulted in the most critical loading condition (Section 4.2.3). Therefore, an a/d ratio of 2.5 was selected as the most critical loading condition for the purpose of this study. The elevation and the cross section of the S-UHPC beam are shown in Figure 132 and Figure 133, respectively.

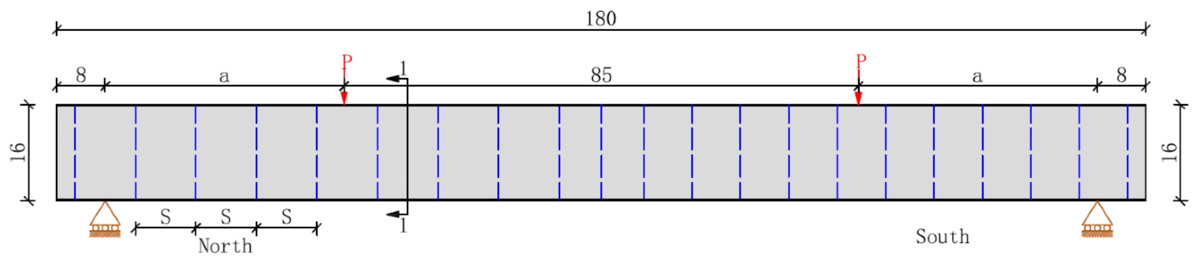

Figure 132. Elevation of S-UHPC beam. Unit: Inch

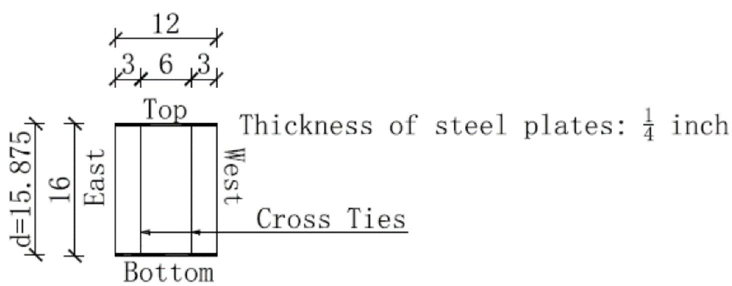

Figure 133. Section 1-1

The diameter of the rebars and the spacing (S) of the cross ties were calculated based on the designed shear reinforcement ratio. No. 3 rebars were used as the shear reinforcement and grade 70 high-strength steel conforming to ASTM/ASME SA 516-2010 grade 70 was used as the top and bottom steel plates. The details of the preliminary design of S-UHPC beams can be found in Table 15.

Table 15. S-UHPC beam preliminary design

Specimen	a/d	$\rho_{t,ACI}$ (%)	$\rho_{t,test}$ (%)	S (in)	$\rho_{t,test}/\rho_{t,ACI}$
S-UHPC-1 South	2.5	0.184	0.184	10	1
S-UHPC-1 North	2.5	0.184	0.230	8	1.25
S-UHPC-2 South	2.5	0.184	0.274	6.75	1.49

S-UHPC-2 North	2.5	0.184	0.321	5.75	1.75

Notes: a/d= Shear span-to-depth ratio, $\rho_{t,ACI}$ (%) = The minimum cross ties ratio based on ACI 319-05 recommendations, $\rho_{t,test}$ (%) = The designed cross ties ratio for S-UHPC beams, S = Spacing of cross ties.

4.4.1. Instrumentation

The instrumentation included pasting of strain gauges on the surface of cross ties for measuring local strains, installing smart aggregates for crack and bond monitoring and six LVDTs forming a rosette for measuring the smeared strain within the critical zone. The location and arrangement of strain gauges, smart aggregates and LVDT rosette are shown in Figure 134.

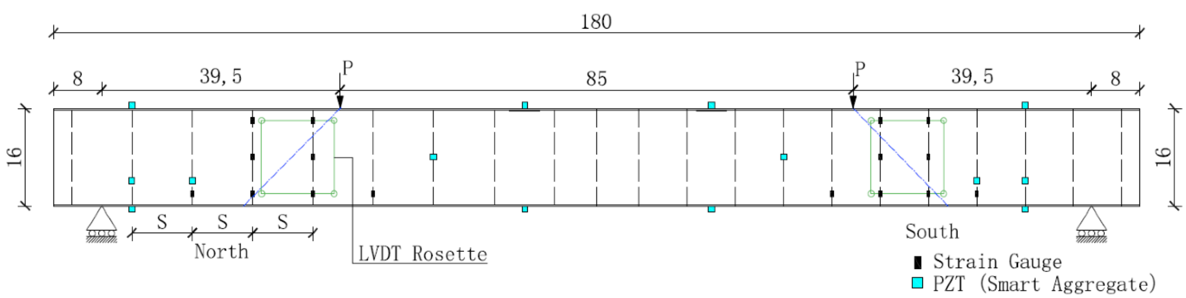

Figure 134. Arrangement of strain gauges, smart aggregates and LVDT rosette

Strain gauges were strategically placed and labeled as per their location on the cross ties and the side of the beam on which they are located. The labeling of strain gauges is as per Figure 135.

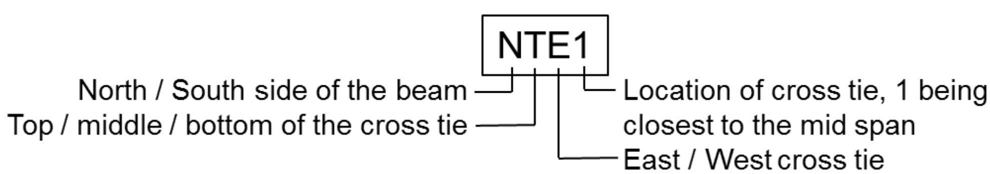

Figure 135. Labeling of strain gauges

The arrangement of the cross ties and the location of strain gauges for S-UHPC-1 and S-UHPC-2 are shown in Figure 136 and Figure 137, respectively. NSS (north steel-plate strain-gauge) and SSS (south steel-plate strain-gauge) are the labels of the strain gauges that are used to measure the tensile stresses at the bottom steel plate in the north end and south end, respectively.

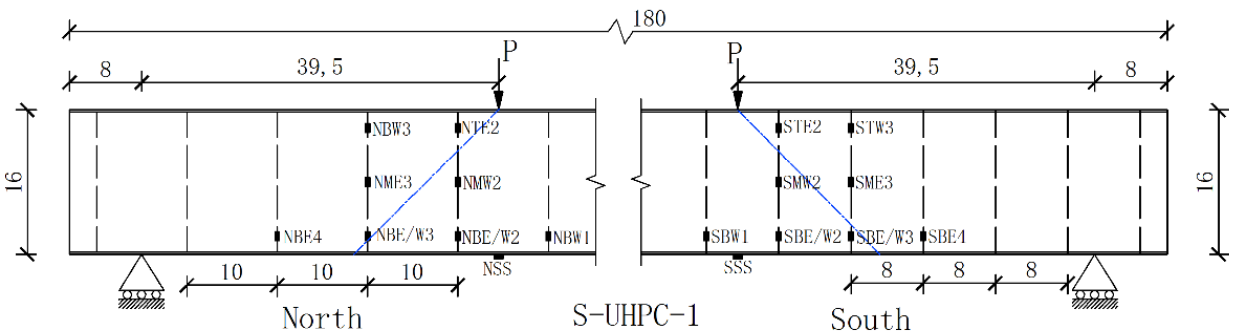

Figure 136. Arrangement of strain gauges for S-UHPC-1

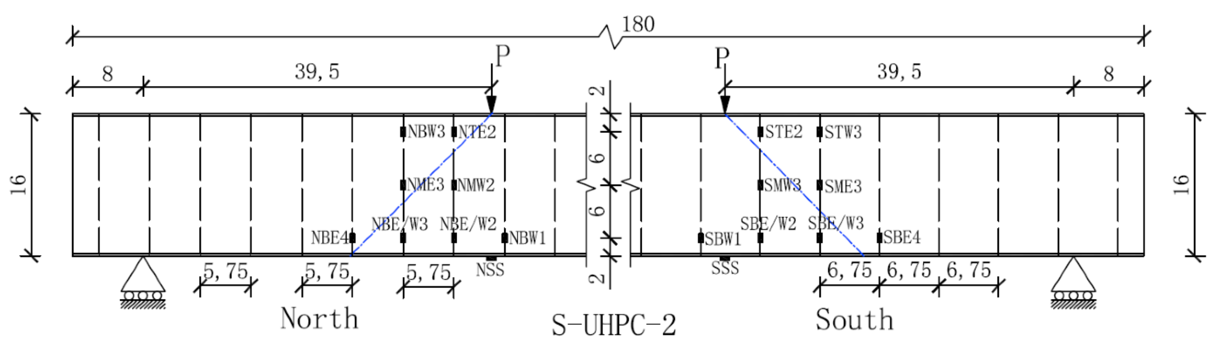

Figure 137. Arrangement of strain gauges for S-UHPC-2

After the location of the strain gauges, the LVDT rosette and smart aggregates were decided and they were installed in the framework of the S-UHPC beam as shown in Figure 138.

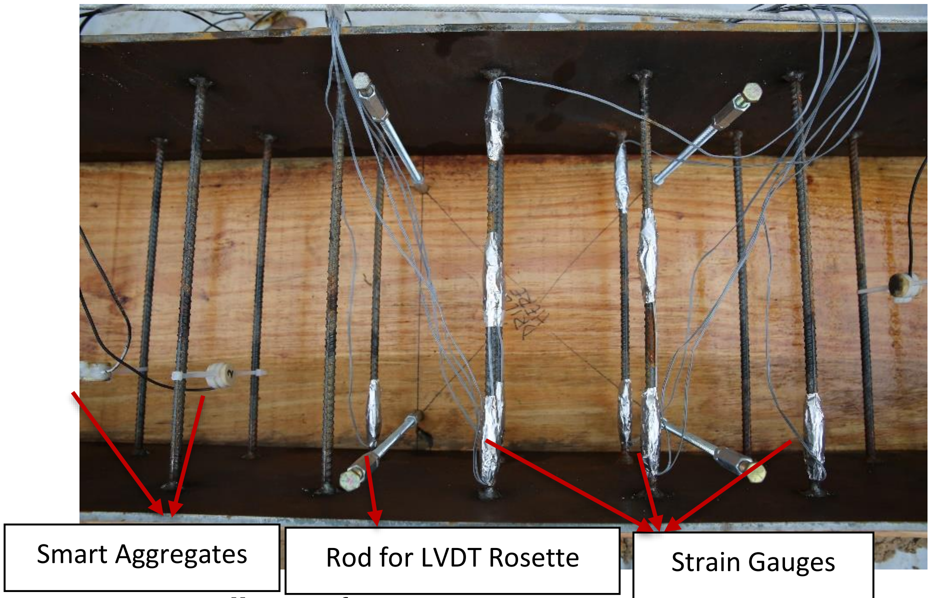

Figure 138. Installation of smart aggregates, LVDT rosette and strain gauges

4.4.2. Casting and test setup

The beams were cast using the UHPC developed in this project (Figure 139). The UHPC was mixed using an 11 cubic-feet concrete gravity mixer. S-UHPC-1 and S-UHPC-2 were cast on different days. Since enough room should be kept in the mixer for efficient mixing, six cubic feet of UHPC were cast at a time. It took about four batches of six cubic feet of UHPC to fully cast one beam. At least three cylinder specimens were prepared from each batch to measure the compressive strength after 28 days of curing.

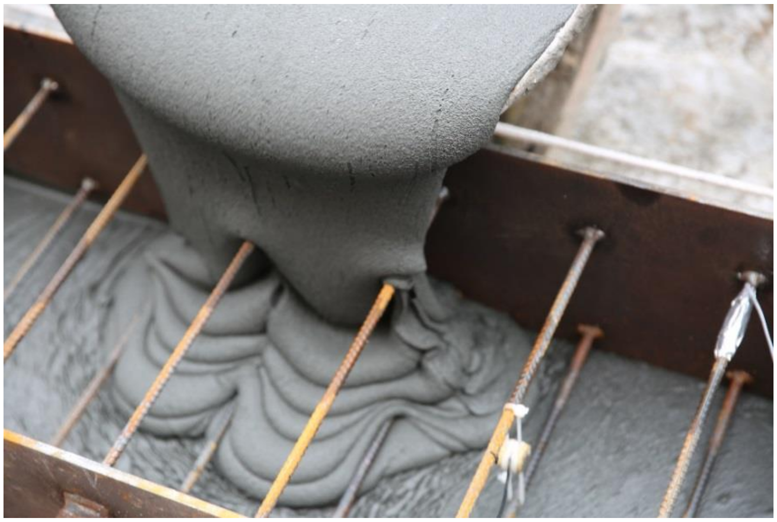

Figure 139. Casting of S-UHPC beam

Since the developed UHPC is self-consolidating, no vibration was performed. After completion of the casting, the S-UHPC beams were cured by sprinkling water and covering them with burlap and plastic sheeting for 28 days (Figure 140).

Figure 140. Curing arrangement for S-UHPC beams

The supports, each containing a load cell to measure the shear force in the specimen, was set up according to the layout of the beam with respect to the location of the actuators as shown in Figure 141. The actuators were set based on the a/d ratio and the dimensions of the beam.

Figure 141. Support setup

The beam was then moved to the test frame location by using an overhead crane. Lasers were used to precisely center the beam on the supports. The loading arrangement and test setup are shown in Figure 142.

Figure 142. Loading arrangement and setup

The beams were subjected to vertical loading provided by the North and South actuators with a capacity of 600 kips (2670 kN) each. The MTS Flex system was used to control the loads and displacements of the actuators. The displacement control feature was essential in capturing the post peak behavior of the SC beams. The loading protocol had several loading steps. Every loading step was planned to have a constant loading rate of 0.10 inch (2.54 mm) per 15.0 minutes. The cracks and the bond between the steel plates and the UHPC were continuously monitored and recorded during the tests. Each end of the beams was tested individually. The side with a higher cross tie ratio (North) was tested first. Each test lasted 3 to 7.5 hours.

The HBM Spider 8 data acquisition system (Figure 143) was used to continuously record the data from the load cells, LVDTs and strain gauges. This system is capable of parallel and dynamic measurements, with a sampling frequency of 0.20 Hz. A real-time plot of the shear force vs. deflection was used to observe and control the actuator during the tests. In addition, the real-time plots of strains in concrete, cross ties and steel plates were used to observe and monitor the structural behavior of the specimen during the tests.

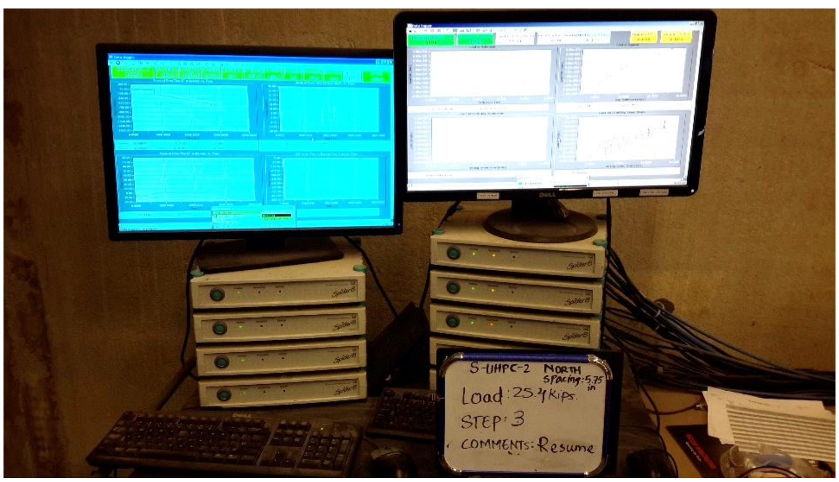

Figure 143. HBM Spider 8 data acquisition system

4.4.3. Experimental Results

The test results for two full scale Steel plate-UHPC (S-UHPC) beams are presented in this section. The details about the properties of the materials, shear force-deflection curves and crack patterns are discussed and used in order to understand the behavior of S-UHPC beams and to identify the minimum amount of cross tie ratio for SC structures subjected to out-of-plane shear.

The materials used for the fabrication of the beams were tested and their specifications are arranged in Table 16.

Table 16. Mechanical properties of the materials

Specimen	f_y (ksi)	f_u (ksi)	E_s (ksi)	*Elongation (%)*	*Yield Strain*
No.3 Rebars	66.5	87.4	27,359	24.5	0.243%
Grade 70 Steel plate	74	87.95	33,505	-	0.221%

Notes: fy = Yield stress, fu = Maximum tensile stress, Es = Modulus of Elasticity

The values of $\rho_{t,ACI}$ were re-calculated as per the material test results and the final experimental matrix was prepared as shown in Table 17.

Table 17. Experimental Matrix

Specimen	s_{tie}# (in.)	$f_c'^*$ (ksi)	$\rho_{t,ACI}$ (%)	$\rho_{t,test}$ (%)	$\rho_{t,test}/\rho_{t,ACI}$
S-UHPC-1 South	10.00	22.34	0.170	0.184	1.08
S-UHPC-1 North	8.00	22.34	0.170	0.231	1.35
S-UHPC-2 South	6.75	22.32	0.170	0.277	1.63
S-UHPC-2 North	5.75	22.32	0.170	0.323	1.90

Notes:
s_{tie} = spacing of cross ties
* f_c' = concrete compressive strength from concrete cylinder (4.00″×8.00″), tested on the 28th day.
1.0 in. =25.4 mm, 1.00 kips= 4.40 kN, 1.00 ksi = 6.89 MPa

Specimen S-UHPC-1 (North)

The north side of specimen S-UHPC-1 has a cross tie ratio of 1.35 times the minimum amount of cross ties recommended by ACI. In other words, the shear reinforcement ratio provided is 0.231% as compared to 0.170%, which is the minimum requirement of the ACI code. The north side of S-UHPC-1 was tested first under three-point bending. Figure 144 shows the shear force deflection curve of the north end of S-UHPC-1. The loading protocol was set under displacement control at a rate of 0.1 inch every 15 minutes. Two flexural cracks appeared during the first loading step at 11 kips. The location of crack 1 (Figure 145) was in the shear span (a) between the loading point and the reaction support and crack 2 (Figure 146) was at a location close to the mid-span region. The test was paused at the occurrence of the cracks and crack width measurements were taken. At the end of the first loading step (11 kips), the widths of cracks 1 and 2 were measured to be 0.15 inch and 0.25 inch, respectively. As a result of the occurrence of the flexure crack, the north end shear force (F_{north}) dropped from 11.16 kips to 9.18 kips. At the end of the second loading step (16 kips), crack 1 widened to 0.25 in. while crack 2 remained the same. In addition, two new flexure cracks appeared in the mid-span region during the second loading step. During the fourth loading step, crack 1 propagated in an inclined fashion towards the top of the beam near the loading point as shown in Figure 145. Three new flexural cracks appeared in the mid-span region during the loading steps 3, 4 and 5 as shown in Figure 146.

The cracks further widened as the test progressed. There were a total number of six loading steps operated under displacement control. The details of all the cracks and their corresponding widths are shown in Table 18.

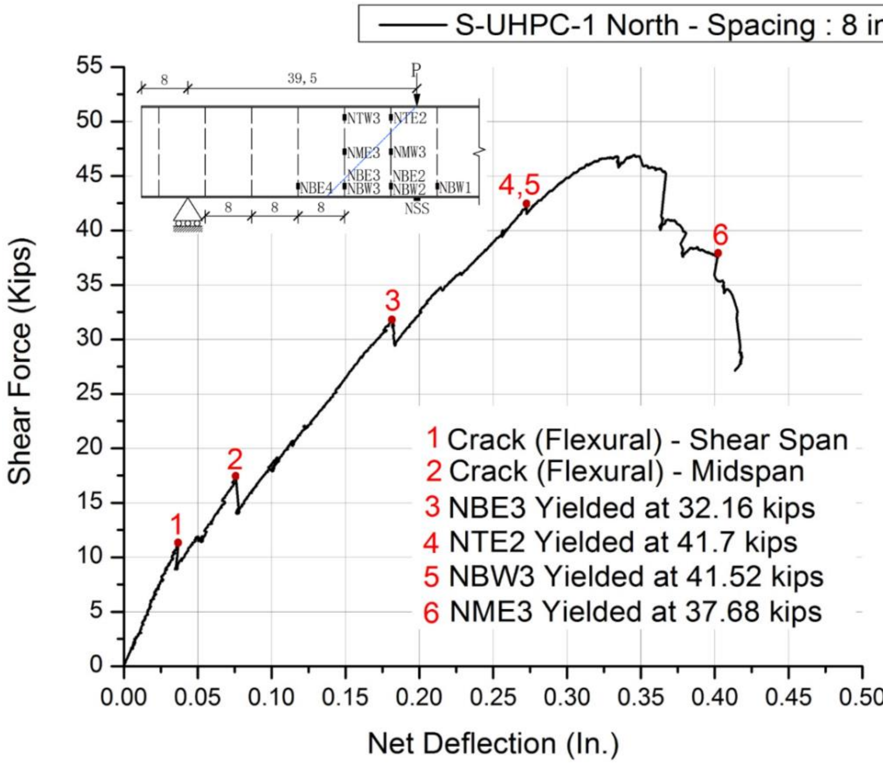

Figure 144. Shear-force deflection curve for S-UHPC-1 (North)

The shear force in the north end (F_{north}) reached a maximum of 46.92 kips. The corresponding net deflection at this stage was 0.345 in.

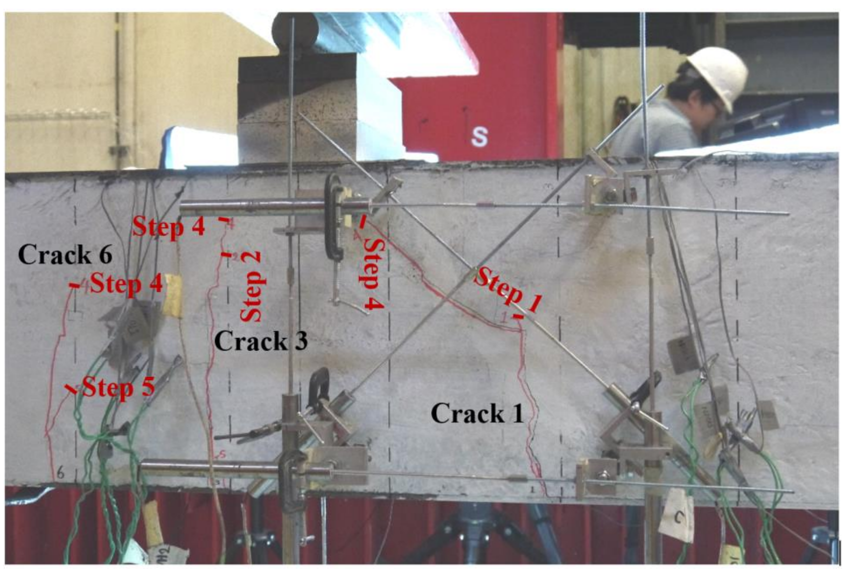

Figure 145. Crack pattern (Shear span)

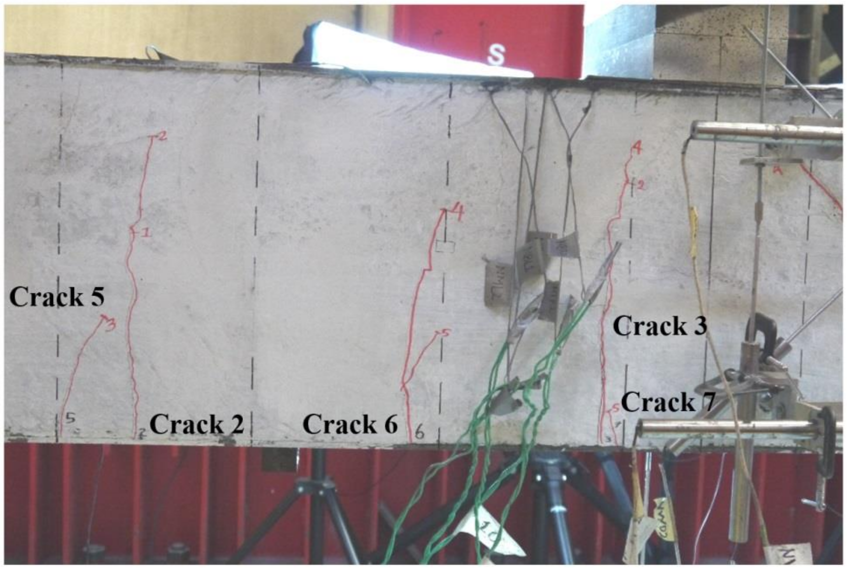

Figure 146. Crack pattern (Mid-span)

Although some of the cross ties yielded, the bottom steel plate didn't yield and the concrete wasn't crushed. Specimen S-UHPC-1 (North) failed with a certain amount of shear ductility. The shear ductility was found to be 1.72. The amount of cross ties was sufficient to prevent premature failure of the beam due to bond slip. The final crack pattern and beam failure mode are shown in Figure 147.

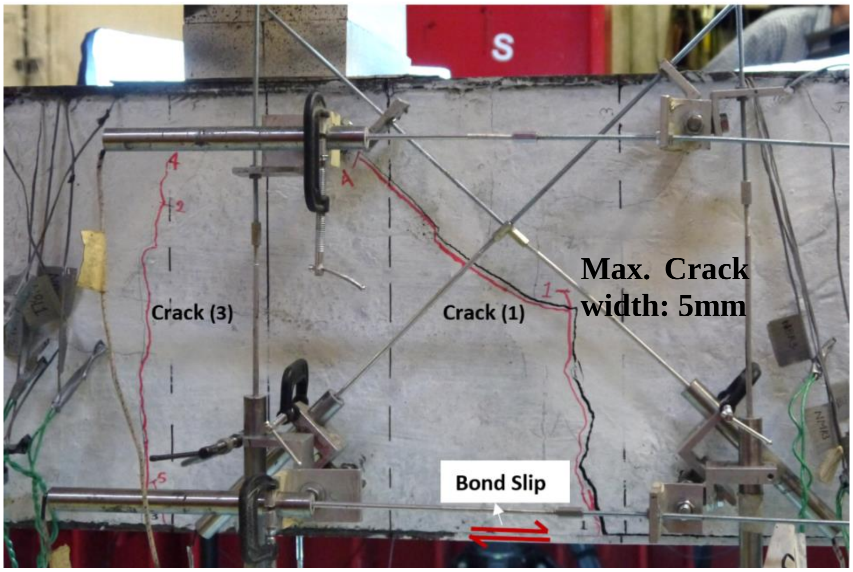

Figure 147. Crack Pattern at Failure Mode (S-UHPC-1 North)

Table 18. Crack Record for S-UHPC-1 North – Spacing : 8 in.

Step #	Load (Kips)	Crack Width (mm)							Comments
		Crack 1	Crack 2	Crack 3	Crack 4	Crack 5	Crack 6	Crack 7	
1	11	0.15	0.25						
2	16	0.25	0.25	0.45	0.10				
2	18.75	0.25	0.30	0.50	0.10				
2	20.16	0.25	0.30	0.50	0.25				
3	30.9	0.30	0.30	0.60	0.30	0.25			
4	39.6	0.65	0.30	0.65	0.30	0.30	0.25		Visible bond slip
5	46.0	1.20	0.30	0.70	0.30	0.30	0.30	0.15	
6	45.0	2.0	0.30	0.70	0.30	0.30	0.35	0.15	
6	37.0	2.50	0.30	0.70	0.30	0.30	0.35	0.15	
6	34.4	5.0	0.30	0.70	0.30	0.30	0.35	0.15	End of test

Specimen S-UHPC-1 South

S-UHPC-1 South, designed as per the minimum cross ties ratio criteria of ACI 349 code (Equation 13), was tested under three-point bending. The loading protocol was set under displacement control at a rate of 0.1 inch every 15 minutes. To reduce the effect of damage due to testing of the north end of the beam, the support on the north side was moved to the nearest un-cracked section. An initial flexure crack in the shear span had occurred during the testing of the north end of the specimen. This initial flexure crack may have reduced the initial stiffness of the beam. The shear force-deflection curve is shown in Figure 148.

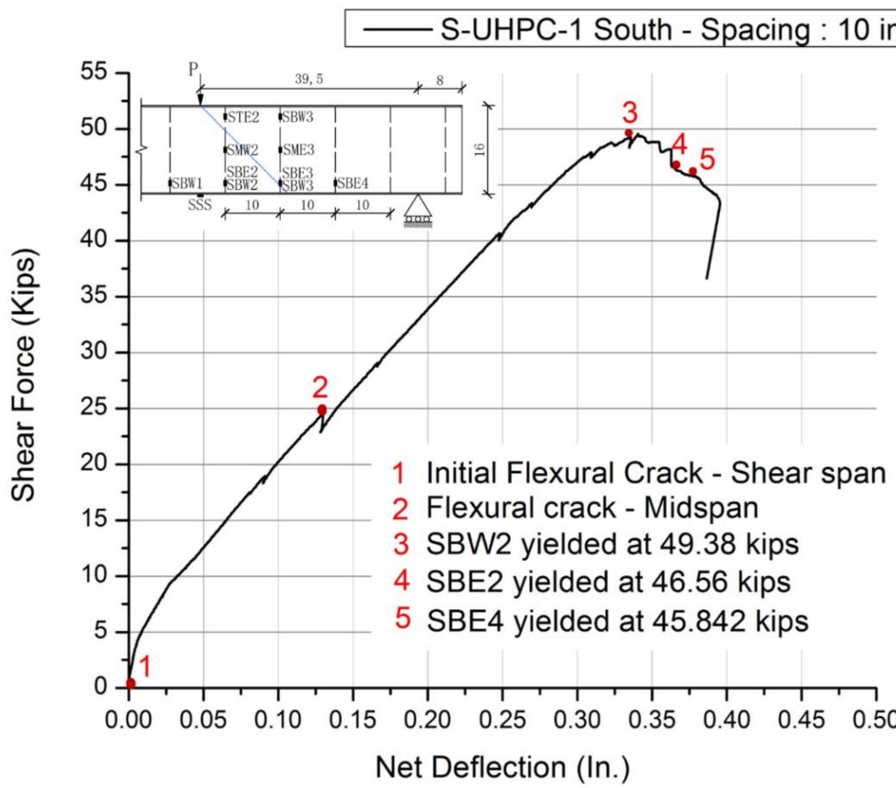

Figure 148. Shear-force deflection curve for S-UHPC-1 (South)

The second flexure crack occurred during the second loading step at the mid-span region. The shear force in the south end dropped from 24.54 kips to 23.10 kips due to crack 2. The corresponding deflection at this stage was 0.130 inch. The first cross tie yielded at 49.32 kips at which time the corresponding deflection was 0.339 inch. The specimen reached a peak load of 49.56 kips at a net deflection of 0.3405 inch right after the first cross tie yielded. Two cross ties yielded in the descending branch at 46. 6 kips and 45.8 kips. The steel plate didn't yield and concrete was not crushed at the peak. The maximum crack width was 2.50 mm. The details of the cracks and their corresponding widths are shown in Table 19.

Yielding of the cross tie before the peak delineates the role of the cross tie in transferring the shear forces between the concrete and steel plates effectively. The shear ductility was found to be 1.0035 for the south end. If the amount of cross ties was less than the amount provided, the beam would have failed in a brittle fashion due to premature debonding, as observed in the SC beam tests cast with normal strength concrete (Section 4.2.3). The amount of cross ties in S-UHPC-1 (South) was found to be just sufficient enough to prevent a premature sudden failure due to debonding between the UHPC and steel plate. The final crack pattern and beam failure mode are shown in Figure 149.

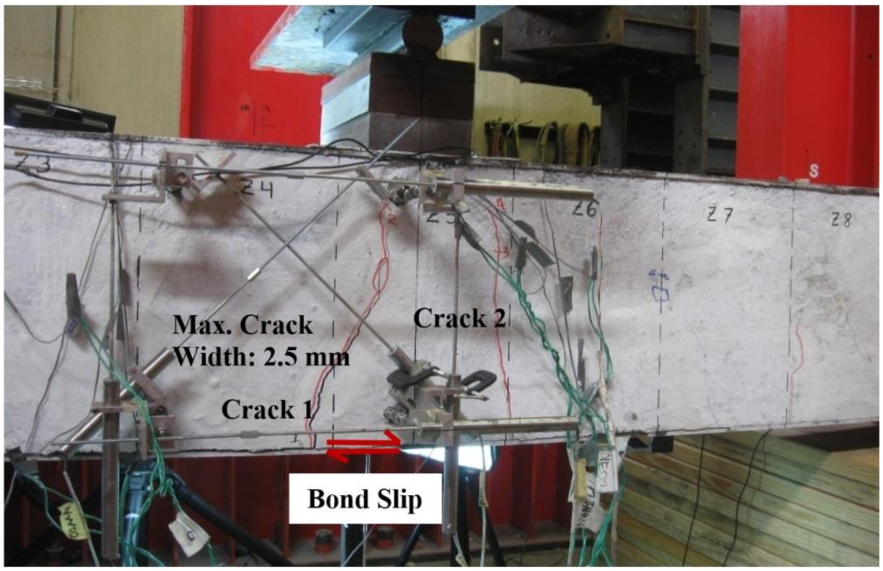

Figure 149. Crack Pattern for S-UHPC-1 South

Table 19. Crack Record for S-UHPC-1 (South) – Spacing : 10 in.

Step #	Load (Kips)	Crack Width (mm)			Comments
		Zone (4)	Zone (6)	Zone (2)	
		Crack 1	Crack 2	Crack 3	
2	18.6	0.50			
3	22.7	0.50	0.15		
4	40.2	0.85	0.50		Visible Bond Slip
4	48.9	1.40	0.60	0.15	
5	44.4	2.50	0.60	0.15	End of test

Specimen S-UHPC-2 (North)

The north end of S-UHPC-2 (North) has 90% more cross ties than the minimum amount recommended by the ACI code. The north side of specimen S-UHPC-2 was tested first. The beam was tested under three-point bending. The shear span-to-depth ratio was kept similar to that of S-UHPC-1 as 2.5. The loading protocol was set under displacement control at a rate of 0.1inch every 15 minutes. The shear force-deflection curve shown in Figure 21 was obtained from the tests.

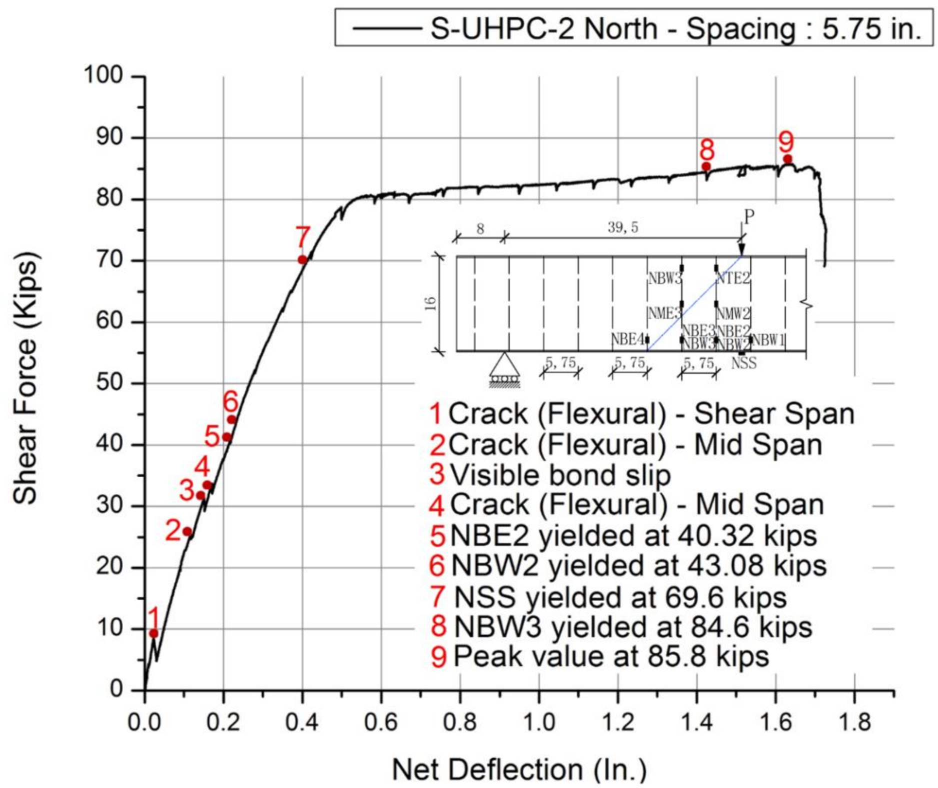

Figure 150. Shear-force deflection curve for S-UHPC-2 (North)

Note: (NSS=North steel-plate strain-gauge)

The test started with all the readings from strain gauges, LVDTs and load cells equal to zero. A total number of 22 loading steps were completed and the test lasted 7.5 hours. The shear forces, strains and deflections were continuously measured by the Spider 8 data acquisition system. In addition, at every occurrence of a crack and at the end of a loading step, crack measurements were taken.

As the test progressed and the specimen was subjected to an increasing load, a flexural crack occurred at the shear span region near the loading point as shown in Figure 151. This crack caused the load to drop from 8.8 kips to 5.04 kips. Likewise, flexural cracks 2, 3, 4, 5 and 6 occurred as the test progressed. The details of the cracks with their corresponding widths are shown in Table 20.

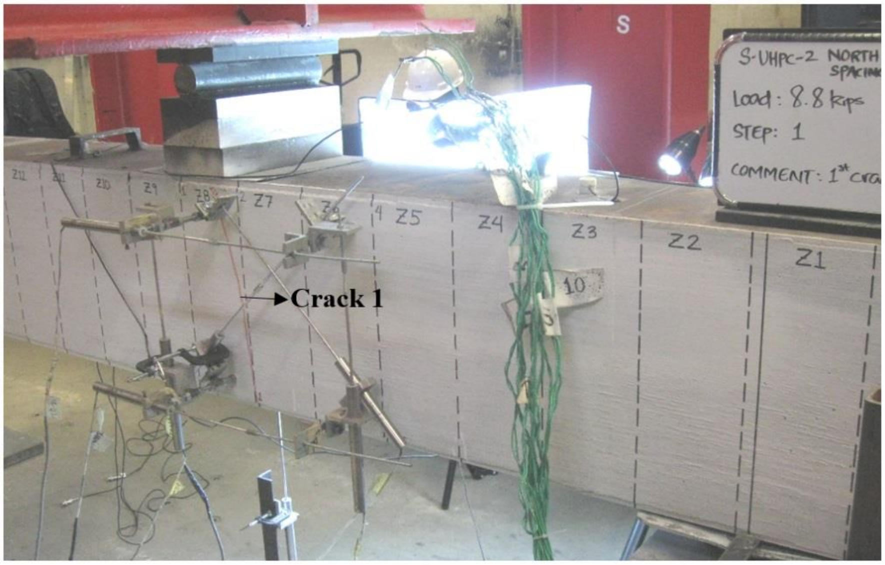

Figure 151. Crack 1 - Shear span

The cross ties at NBE2 and NBW2 yielded at 40.32 kips and 43.08 kips, respectively. As it can be seen from the shear-force deflection curve, the stiffness of the specimen didn't reduce after the cross ties yielded. This may be due to the shear strength contribution of the UHPC being much higher than the cross ties at this stage. As it can also be seen from the crack pattern shown in Figure 152, the cracks did not pass through the location of the cross ties; thus the contribution of the cross ties at this stage didn't dictate the strength of the specimen. The north steel-plate strain-gauge (NSS) yielded at 69.6 kips which corresponds to the deflection of 0.409 in. The yielding of the steel plate was followed by the plateau region in which the deflection increased considerably with a small increase of load. The peak value reached 85.8 kips, which corresponded to a deflection of 1.642 inches. The flexural ductility was found to be 4.01. The shear force-deflection curve (Figure 150) shows that the increased amount of cross ties prevented premature failure of the beam due to bond slip and increased its total shear carrying capacity. The increased amount of cross ties delayed the debonding of the bottom steel plate and the UHPC and provided an efficient shear transfer mechanism, which led to the stresses in the steel plate to develop to yield point and beyond.

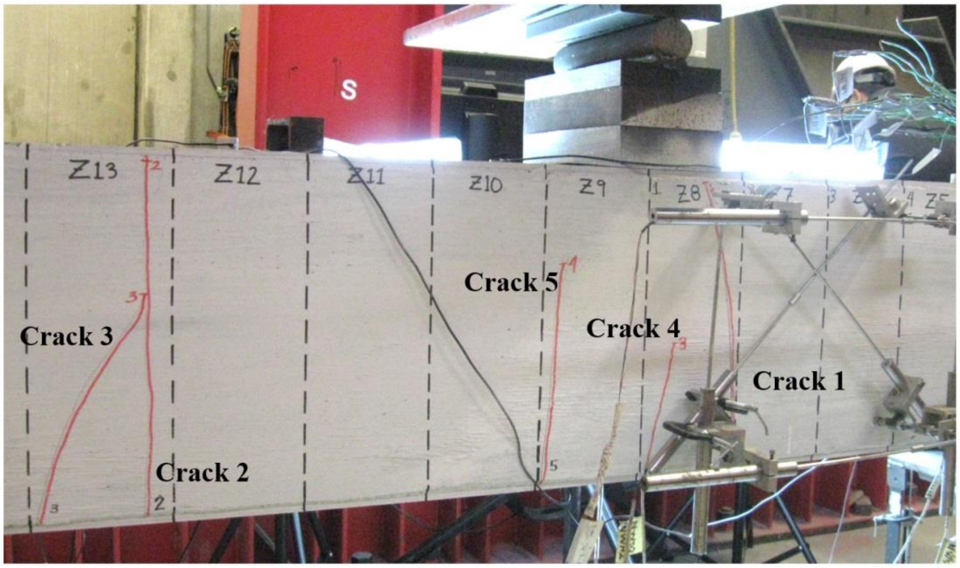

Figure 152. Crack pattern at yielding of NBE2 and NBW2

The concrete was locally spalled at the north end of the beam. The spalling of the concrete opened the surface of the cross ties for further observations. From Figure 154, it can be visually understood that the cross ties were effective in delaying the debonding and provided an effective shear transfer mechanism for the SC beam. The final crack pattern and beam failure mode are shown in Figure 153.

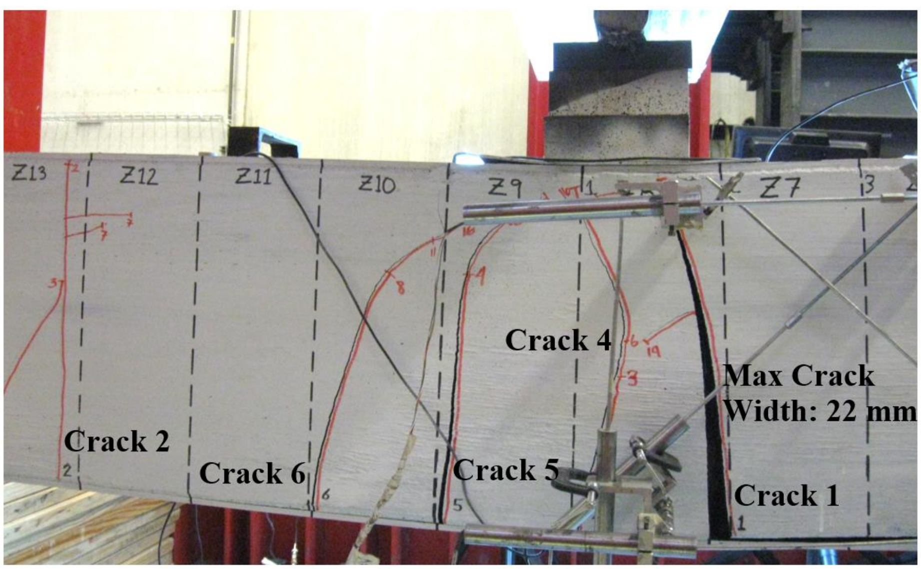

Figure 153. Crack pattern at failure (S-UHPC-2 North)

Figure 154. Spalling of concrete (S-UHPC-2 North)

Table 20. Crack Record for S-UHPC-2 (North)

Step	Load (Kips)	Width of Cracks (mm)						Comments
		Zone 8	Zone 13	Zone 13	Zone 8	Zone 9	Zone 10	
		Crack 1	Crack 2	Crack 3	Crack 4	Crack 5	Crack 6	
1	8.80	0.25						Crack
1	7.70	0.25						End
2	19.90	0.45	0.15					End
3	25.20	0.50	0.15	0.15	0.10			Pause
3	31.40	0.60	0.15	025	0.15			Visible slip
4	33.80	0.65	0.15	0.25	0.15	0.15		Pause
4	40.70	0.75	0.15	0.30	0.15	0.25		End
5	52.08	0.90	0.15	0.35	0.15	0.40		End
6	62.34	1.40	0.15	0.35	0.15	0.55		End
7	70.86	1.50	0.15	0.40	0.15	0.70		End
8	78.20	2.00	0.15	0.45	0.15	0.90	0.25	End
9	80.20	2.50	0.15	0.55	0.15	1.40	0.40	End
10	80.28	2.50	0.15	0.60	0.15	2.50	0.45	End
11	81.12	3.5	0.15	0.60	0.15	3.5	0.45	End
12	82.14	3.5	0.15	0.60	0.15	4.0	0.45	End
13	82.38	4.0	0.15	0.60	0.15	4.5	0.50	End
14	82.68	5.0	0.15	0.60	0.15	5.0	0.60	End
15	83.16	6.0	0.15	0.60	0.15	5.5	0.60	End
16	83.34	6.0	0.15	0.60	0.15	5.5	0.75	End
17	83.82	6.0	0.15	0.60	0.15	5.5	1.30	End
18	84.54	6.5	0.15	0.70	1.40	6.0	1.50	End
19	85.38	6.5	0.15	0.70	1.40	6.5	2.00	End
20	84.24	7.0	0.15	0.70	2.00	6.5	2.50	End
21	84.96	7.5	0.15	0.70	2.00	7.0	2.50	End
22	69.20	2	0.10	0.25	2.00	5.5	2.50	Fail

Specimen S-UHPC-2 (South)

The south side of S-UHPC-2 was tested under the shear span-to-depth (a/d) ratio of 2.5. The shear reinforcement ratio of the south end of S-UHPC-2 is 63% more than the minimum required by the ACI code. The spacing for the south end of S-UHPC-2 was considered to be 6.75 inches. To reduce the effect of damage due to testing of the north end of the beam, the support on the north side was moved to the nearest un-cracked section. The loading protocol was set under displacement control at a rate of 0.1 inch per 15 minutes. The test lasted for 2.5 hours and a total of eight loading steps was completed. The data from the actuators, load cells, LVDTs and strain gauges were continuously recorded by the Spider 8 data acquisition system.

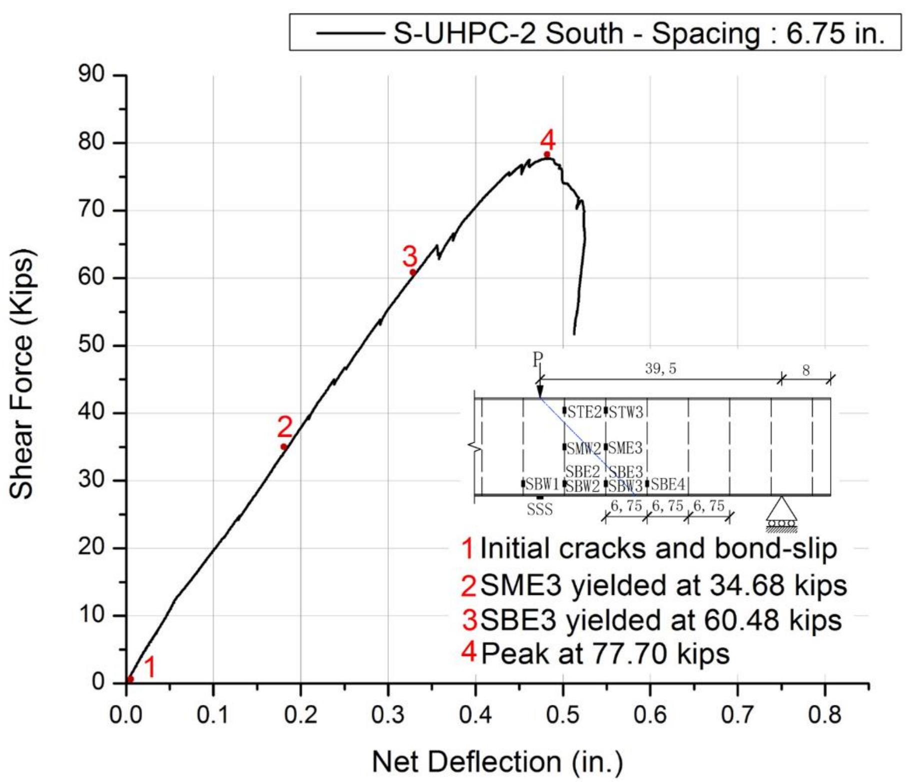

Figure 155. Shear-force deflection curve of S-UHPC-2 South

The shear-force deflection curve is shown in Figure 155. During the testing of the north end of the specimen, four cracks appeared at the south end of the specimen in the shear span and the mid-span region. These cracks may have reduced the initial stiffness of the specimen.

Cross ties at SME3 and SBE3 yielded at 34.68 kips and 60.48 kips with a corresponding deflection of 0.183 inch and 0.330 inch, respectively. The peak reached 77.70 kips at a net deflection of 0.486 inch. The ductility was found to be 2.65. The steel plate didn't yield and concrete was not crushed at peak load. The details of the cracks with their corresponding widths are shown in Table 21. The final crack pattern and beam failure mode are shown in Figure 156.

It can be concluded that the shear reinforcement ratio provided was sufficient to prevent premature bond failure and increase the shear carrying capacity of the SC beam. However, the cross ties weren't sufficient to maintain the bond until yielding of the bottom steel plate.

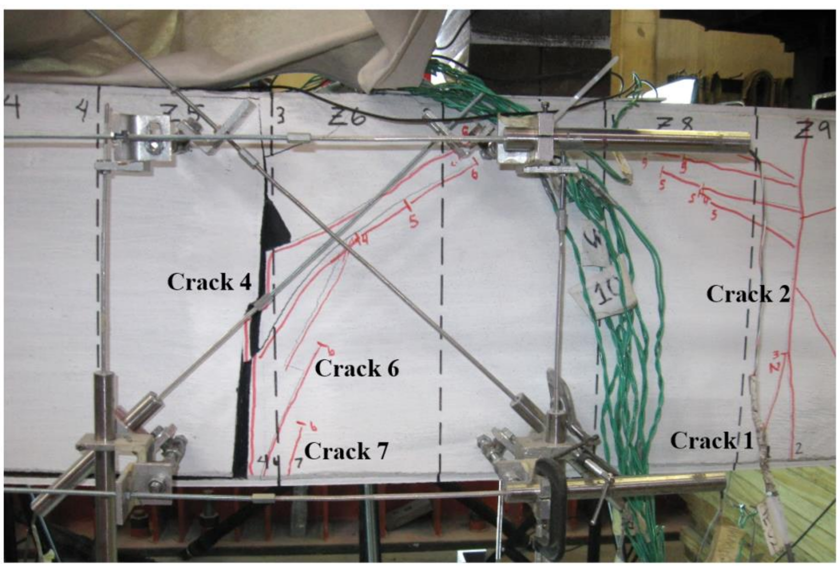

Figure 156. Crack pattern at failure (S-UHPC-2 South)

Table 21. Crack Record for S-UHPC-2 (South)

Step #	Load (Kips)	Width of Cracks (mm)							Comments
		Zone(5)	Zone(9)	Zone(9)	Zone(13)	Zone(9)	Zone(6)	Zone(6)	
		Crack 4	Crack 1	Crack 2	Crack 3	Crack 5	Crack 6	Crack 7	
Initial	0	0.05	0.10	0.05	0.15				
1	11.0	0.10	0.10	0.05	0.15				End
2	24.18	0.15	0.15	0.10	0.15				End
3	39.66	0.60	0.30	0.45	0.35				Visible Bond Slip
4	53.88	0.80	0.30	0.60	0.40				End
5	63.6	1.40	0.40	0.60	0.45	0.25			Pause
5	66.5	1.40	0.40	0.60	0.45	0.30			End
6	76.7	2.0	0.45	0.60	0.45	0.60	0.10	0.10	End
7	71.0	3.7	0.45	0.60	0.45	0.60	0.10	0.10	End
8	56.0	18	0.15	0.25	0.15	0.10	0.35	0.10	Test End

Two S-UHPC beams were tested under out-of-plane shear with various cross tie ratios and a shear span-to-depth ratio of 2.5. The tests were conducted to understand the structural performance of the modules and to find the minimum cross tie ratio required for the SC beam to exhibit a ductile behavior. Table 22 shows the experimental matrix and the summary of the results for the two S-UHPC beams.

Table 22. Experimental matrix and results

Specimen	s_{tie}# (in.)	f_c'* (ksi)	$\rho_{t,ACI}$ (%)	$\rho_{t,test}$ (%)	$\rho_{t,test}/\rho_{t,ACI}$	$F_{peak.}$** (kips)	Ductility δ†	Failure Mode
S-UHPC-1 South	10.00	22.34	0.170	0.184	1.08	49.56	1.003	Ductile
S-UHPC-1 North	8.00	22.34	0.170	0.231	1.35	46.56	1.706	Ductile
S-UHPC-2 South	6.75	22.32	0.170	0.277	1.63	77.70	2.650	Ductile
S-UHPC-2 North	5.75	22.32	0.170	0.323	1.90	85.80	4.010¥	Ductile

Notes:
s_{tie} = spacing of cross ties
* f_c' = concrete compressive strength from concrete cylinder (4.00″×8.00″), tested on the 28th day
** $F_{peak.}$ = peak shear capacity
† δ = Shear ductility (deflection at the peak /deflection when cross ties yielded)
¥ = Flexural ductility
1 in. =25.4 mm, 1.00 kips= 4.40 kN, 1.00 ksi = 6.89 MPa

4.5. Finite Element Simulation of SC and S-UHPC Beams

4.5.1. Introduction

Many of the SC structures such as the shield building of AP1000 and SC shear walls can be visualized as assemblies of membrane elements. If the behavior of an element is known, the behavior of the entire structure can be predicted using the finite element method.

To apply nonlinear finite element analysis to SC structures, two points are of importance: establishment of nonlinear constitutive models and development of nonlinear finite element methods. In this research program, the constitutive models of RC elements are extended and used in the finite element analysis of SC structures[139]. Different models have been developed in the past to predict the behavior of RC elements such as truss models, orthotropic models, nonlinear elastic models, plastic models, micro models, etc. Among these, the orthotropic model is better in terms of accuracy and efficiency as compared to other models. Many researchers in the past three decades have used this model for predicting the shear behavior of reinforced concrete elements. Furthermore, over the past three decades, a series of four analytical models were established at the University of Houston (UH)[140]. The models are the RA-STM ([140-142]), FA-STM ([143, 144]), SMM[145] and CSMM ([146, 147]). These models are developed based on rational principles and they satisfy Navier's three principles of mechanics of materials which are stress equilibrium, strain compatibility and the constitutive laws of materials. Among these models, CSMM is the most accurate and versatile. It is used for predicting the cyclic shear behavior of the reinforced concrete membrane element. It can predict various parameters such as stiffness, ultimate strength, descending branch, ductility and energy dissipation.

Finite element analysis of SC structures is a highly nonlinear problem because of the nonlinear constitutive relationships of concrete and steel. The nonlinear problem can be solved by using a solution algorithm. One of the solution algorithms is the iterative solution algorithm which is used to solve nonlinear problems until a convergence is achieved with acceptable accuracy. Advanced solution algorithms such as the quasi-newton method with acceleration, line searches, arc-length, automatic increments and restart methods have been previously developed for nonlinear analysis. By applying these advanced solution algorithms, fast and stable convergence could be achieved [139].

General finite element programs which include finite element models of nodes, elements, materials and loads have already been developed in the past and are being used by many researchers. Some of these programs are FEAP, ABAQUS and OpenSees. These softwares allow the user to implement their own elements and constitutive laws. These finite element programs are either written using function-oriented languages (such as FORTRAN) or object-oriented languages (Such as C++). The use of object-oriented language has improved the usability of the software as compared to function-oriented language. OpenSees [148], which applies object-oriented language (C++) to finite element analysis, is one of the most noted nonlinear finite element programs. Key features of OpenSees are the ability to interchange components and integrate existing libraries and new components into the framework without the need to change the existing code. This makes it possible to implement new classes of materials, elements and other components [148]. Many of the finite element techniques suitable for nonlinear analysis have already been implemented in OpenSees. However, OpenSees was not applicable to RC plane stress structures because no analytical models of RC structures were included. Zhong implemented CSMM into the framework of OpenSees to perform nonlinear finite element analysis of RC plane stress structures [139].

4.5.2. Previous Analytical Models Developed by Research Group at UH

Four analytical models have been developed in the past for predicting the nonlinear shear behavior of reinforced concrete membrane elements. These models are the Rotating-Angle Softened Truss Model (RA-STM) [140-142], Fixed-Angle Softened Truss Model (FA-STM) [143, 144], the Softened Membrane Model (SMM)[149] and the Cyclic Softened Membrane Model (CSMM) [146, 147]. They all satisfy Navier's three principles of mechanics of materials and thus are rational.

The first model developed was the Rotating-Angle Softened Truss Model (RA-STM) [140, 141, 150], which was a rotating crack model. The RA-STM had two improvements over the previous model developed in Toronto, the Compression Field Theory (CFT) [151, 152]: (1) The tensile stress of concrete was taken into account so that the deformations could be correctly predicted, and (2) the average stress-strain curve of steel bars embedded in concrete was derived on the "smeared crack level" so that it could be correctly used in the equilibrium and compatibility equations, which are based on continuous materials.

By 1996 the UH group [143, 144] reported the Fixed-Angle Softened Truss Model (FA-STM), which assumed the cracks to be oriented in the direction perpendicular to the applied principal tensile stress. A complicated constitutive relationship of concrete in shear was used to account for the shear stresses in the concrete struts along the cracks. The FA-STM, although more complex than RA-STM, was capable of predicting the "concrete contribution" (V_C). Zhu, Hsu and Lee [153] derived a rational shear modulus and produced a new solution algorithm of FA-STM that was simple as compared to that of RA-STM.

Both RA-STM and FA-STM were able to satisfactorily predict the pre-peak behavior (ascending branches) of reinforced concrete elements under shear. However, the post-peak behavior (descending branches) of the load-deformation curves could not be correctly predicted using these two models. This was because the stresses and strains of cracked reinforced concrete due to the Poisson effect were neglected and Poisson ratios were taken as zero in these models.

The SMM model was developed by Hsu and Zhu [149] to predict the shear behavior of reinforced concrete membrane elements. The SMM model could predict the post-peak branches of the shear stress versus shear strain curves by considering the Poisson effect. Twelve panels were tested to quantify the Poisson effect [154, 155]. It was found that the Poisson effect could be characterized by two Hsu/Zhu ratios, defined as "the Poisson ratios of cracked reinforced concrete based on the smeared crack concept." The Hsu/Zhu ratio ν_{12} (tensile strain caused by perpendicular compressive strain) in the post-yield range was found to be a constant of 1.9, and the Hsu/Zhu ratio ν_{21} (compressive strain caused by perpendicular tensile strain) was taken to be zero. Similar to FA-STM, the SMM model assumes that the cracks are oriented in the direction perpendicular to the applied principal tensile stress. This would result in concrete contribution V_C. Zhu, Hsu and Lee [153] greatly simplified the SMM model by developing a simple and rational shear modulus instead of the empirical constitutive relationships of concrete in shear.

Furthermore, CSMM (Cyclic Softened Membrane Model) was developed by Mansour and Hsu ([146, 147]) to predict the reversed cyclic response of RC membrane elements, including the unloading and reloading of stress-strain curves. The CSMM is an extension of SMM that incorporates the cyclic constitutive laws of concrete and steel bars in membrane elements[156]. In CSMM, it was assumed that the Hsu/Zhu ratio ν_{12} (tensile strain caused by perpendicular compressive strain) in the post-yield range was a constant of 1.0 under cyclic loading based on the comparative studies of shear stress-strain curves of panels[157]. The Hsu/Zhu ratio ν_{21} (compressive strain caused by perpendicular tensile strain) was taken to be zero. CSMM is a smeared crack model in which the cracked reinforced concrete is treated as continuous material. To relate the stresses and strains in equilibrium and compatibility equations, the material laws for concrete and steel should be developed based on smeared stresses and strains. The smeared models of concrete and mild steel bars have been established for monotonic and cyclic loading at the University of Houston ([141, 156, 158]). The constitutive laws in the CSMM were found to accurately predict the hysteretic loops, the shear stiffness, the shear ductility and the energy dissipation capacities of RC panels under cyclic shear.

These models are advantageous because they determine the overall behavior of reinforced concrete elements without dealing with variables such as crack width and spacing and interface bond slip. The smeared crack models account for these variables indirectly in the formulation of the smeared stress-strain curve for embedded steel bars. These models consider the effect of the Poisson ratio using the Hsu/Zhu ratios. The Hsu/Zhu ratios are considered the same for both steel and concrete since SMM and CSMM treats cracked reinforced concrete as a continuous material.

SMM and CSMM assume that the cracks in the reinforced concrete element are oriented in the direction of applied principal compressive stress of the element and not the principal compressive stress of the concrete.

For the purpose of this research, CSMM model will be extended to be used in the nonlinear finite element analysis of SC structures. The program will be validated with the results obtained from the experimental test results.

4.5.3. Cyclic Softened Membrane Model (CSMM)

In this study, the scope of the CSMM model will be expanded to take into account the force transfer mechanism between concrete and steel plate in SC structures. In order to develop the CSMM model for SC structures, the basic principles of the CSMM model for RC is summarized first.

Coordinate Systems in CSMM

Three Cartesian coordinates, x-y, 1-2 and x_{si}-y_{si}, are defined in the reinforced concrete elements, as demonstrated in Figure 157. Coordinate x-y defines the local coordinate of the elements. Coordinate 1-2 represents the principal stress directions of the applied stresses that have an angle θ_1 with respect to the x-axis. Steel bars can be oriented in different directions in the elements. Coordinate x_{si}-y_{si} indicates the direction of the 'i_{th}' group of rebars, where the 'i_{th}' group of rebars is located in the direction of x_{si} axis with an angle θ_{si} to the x-axis. The stress and strain vectors in x-y coordinates and 1-2 coordinates are denoted as $[\sigma_x, \sigma_y, \tau_{xy}]^T$, $[\varepsilon_x, \varepsilon_y, 0.5\gamma_{xy}]^T$, $[\sigma_1, \sigma_2, \tau_{12}]^T$ and $[\varepsilon_1, \varepsilon_2, 0.5\gamma_{12}]^T$, respectively.

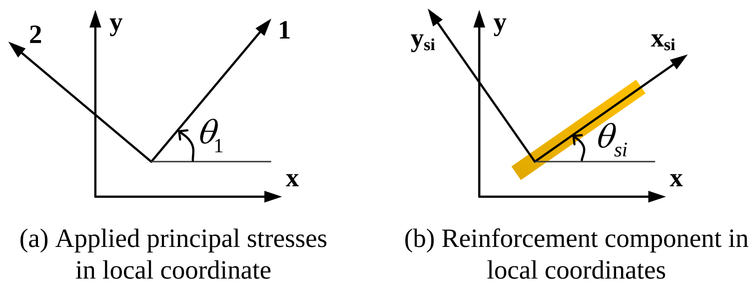

Figure 157. Coordinate systems for reinforced concrete elements: (a) applied principal stresses in local coordinate (b) reinforcement component in local coordinate

The stress and strain vectors in x-y coordinates and 1-2 coordinates are denoted as $\{\sigma_x \quad \sigma_y \quad \tau_{xy}\}^T$, $\left\{\varepsilon_x \quad \varepsilon_y \quad \frac{1}{2}\gamma_{xy}\right\}^T$, $\{\sigma_1 \quad \sigma_2 \quad \tau_{12}\}^T$ and $\left\{\varepsilon_1 \quad \varepsilon_2 \quad \frac{1}{2}\gamma_{12}\right\}^T$, respectively. Here $\tau_{12} = 0$ because the 1-2 coordinate represents the principal stress directions.

By using the transformation matrix $[T(\alpha)]$, the stresses and strains can be transformed between different coordinates. $[T(\alpha)]$ is given by,

$$[T(\alpha)] = \begin{bmatrix} c^2 & s^2 & 2sc \\ s^2 & c^2 & -2sc \\ -sc & sc & c^2 - s^2 \end{bmatrix} \tag{21}$$

where $c = \cos(\alpha)$ and $s = \sin(\alpha)$, and the angle α is the angle between the two coordinates.

The stresses and strains transformed from the x-y coordinate to the 1-2 coordinate using the transformation matrix are expressed as follows:

$$\begin{Bmatrix} \sigma_1 \\ \sigma_2 \\ 0 \end{Bmatrix} = [T(\theta_1)] \begin{Bmatrix} \sigma_x \\ \sigma_y \\ \tau_{xy} \end{Bmatrix}, \tag{22}$$

$$\begin{Bmatrix} \varepsilon_1 \\ \varepsilon_2 \\ \frac{1}{2}\gamma_{12} \end{Bmatrix} = [T(\theta_1)] \begin{Bmatrix} \varepsilon_x \\ \varepsilon_y \\ \frac{1}{2}\gamma_{xy} \end{Bmatrix}. \tag{23}$$

The equilibrium equation that relates the applied stresses in the x-y coordinate (σ_x, σ_y and τ_{xy}) to the internal stresses (σ_1^c, σ_2^c and τ_{12}^c) in the principal stress directions, and the stress in the reinforcing bars (f_{si}) in the rebar directions is given by:

$$\begin{Bmatrix} \sigma_x \\ \sigma_y \\ \tau_{xy} \end{Bmatrix} = [T(-\theta_1)] \begin{Bmatrix} \sigma_1^c \\ \sigma_2^c \\ \tau_{12}^c \end{Bmatrix} + \sum_i [T(-\theta_{si})] \begin{Bmatrix} \rho_{si} f_{si} \\ 0 \\ 0 \end{Bmatrix}, \; i = 1, 2, 3\ldots, \tag{24}$$

where ρ_{si} is the rebar ratio in the "i^{th}" direction; and $[T(-\theta_1)]$ and $[T(-\theta_{si})]$ are the transformation matrices from the 1-2 coordinate and the x_{si}-y_{si} coordinate to the x-y coordinate, respectively.

Equilibrium and Compatibility Equation

The equilibrium equation that relates the applied stresses in the x-y coordinate (σ_x, σ_y and τ_{xy}) to the internal stresses (σ_1^c, σ_2^c and τ_{12}^c) in the principal stress directions, and the stress in the reinforcing bars (f_{si}) in the rebar directions is given by:

$$\begin{Bmatrix} \sigma_x \\ \sigma_y \\ \tau_{xy} \end{Bmatrix} = [T(-\theta_1)] \begin{Bmatrix} \sigma_1^c \\ \sigma_2^c \\ \tau_{12}^c \end{Bmatrix} + \sum_i [T(-\theta_{si})] \begin{Bmatrix} \rho_{si} f_{si} \\ 0 \\ 0 \end{Bmatrix}, \; i = 1, 2, 3\ldots, \tag{25}$$

where ρ_{si} is the rebar ratio in the "i^{th}" direction; and $[T(-\theta_1)]$ and $[T(-\theta_{si})]$ are the transformation matrices from the 1-2 coordinate and the x_{si}-y_{si} coordinate to the x-y coordinate, respectively.

The compatibility equation defines the relationship between the steel strain (ε_{si}) in the x_{si}-y_{si} coordinate and the concrete strain ($\varepsilon_1, \varepsilon_2$ and $\frac{1}{2}\gamma_{12}$) in the 1-2 coordinate, which is expressed in Equation 26.

$$\begin{Bmatrix} \varepsilon_{si} \\ \varepsilon_{si'} \\ \frac{1}{2}\gamma_{si} \end{Bmatrix} = \left[T(\theta_{si} - \theta_1)\right] \begin{Bmatrix} \varepsilon_1 \\ \varepsilon_2 \\ \frac{1}{2}\gamma_{12} \end{Bmatrix}. \tag{26}$$

It is noted that the steel strains (ε_{si}) and concrete strains ($\varepsilon_1, \varepsilon_2$) in Equation 26 are biaxial strains.

Uniaxial Strain and Biaxial Strain

In reality, uniaxial tests are usually performed in the laboratory to determine material properties. There is no such experimental biaxial constitutive material model for the biaxial strains in Equation 25. In order to solve problems in the 2-D dimension, the biaxial strains need to be converted to uniaxial strains so that the unixial constitutive material model tested in laboratory could be used. The uniaxial strains are related to the biaxial strains by the Poisson Ratios of cracked concrete:

$$\begin{Bmatrix} \bar{\varepsilon}_1 \\ \bar{\varepsilon}_2 \\ 0.5\gamma_{12} \end{Bmatrix} = [V] \begin{Bmatrix} \varepsilon_1 \\ \varepsilon_2 \\ 0.5\gamma_{12} \end{Bmatrix}; [V] = \begin{bmatrix} \frac{1}{1-\nu_{12}\nu_{21}} & \frac{\nu_{12}}{1-\nu_{12}\nu_{21}} & 0 \\ \frac{\nu_{21}}{1-\nu_{12}\nu_{21}} & \frac{1}{1-\nu_{12}\nu_{21}} & 0 \\ 0 & 0 & 1 \end{bmatrix} \tag{27}$$

In Equation 27, ν_{12} is the ratio of the resulting tensile strain increment in the principal 1-direction to the source compressive strain increment in the principal 2-direction, and ν_{21} is the ratio of the resulting compressive strain increment in the principal 2-direction to the source tensile strain increment in the principal 1-direction. Values for ν_{12} and ν_{21} for reinforced concrete elements were derived from the panel tests [149].

Uniaxial Constitutive Model for Concrete and Embedded Steel

The cyclic uniaxial constitutive relationships of concrete with embedded mild steel bars were proposed by Mansour and Hsu [156]. The characteristics of these concrete constitutive laws include: (1) the softening effect on the concrete's compressive stress and strain due to the tensile strain in the perpendicular direction; (2) the softening effect on the concrete in compression under reversed cyclic loading; and (3) the opening and closing of cracks, which are taken into account in the unloading and reloading stages, as shown in Figure 158(a). As illustrated in Figure 158(b), the smeared yield stress of embedded mild steel bars is lower than the yield stress of bare steel bars and the hardening ratio of steel bars after yielding is calculated from the steel ratio, steel strength and concrete strength. The unloading and reloading stress-strain curves of embedded steel bars take into account the Bauschinger effect.

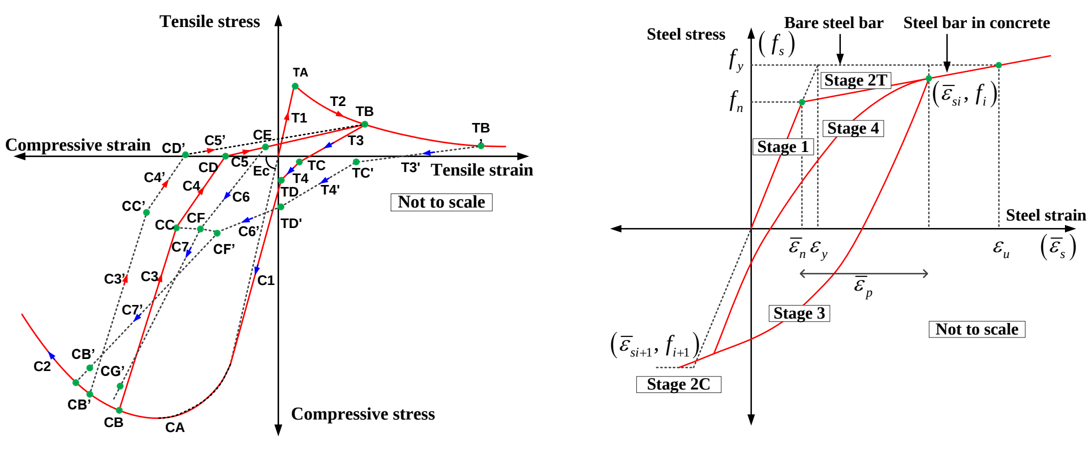

(a) Concrete

(b) Steel

Figure 158. Cyclic stress-strain relationships of materials

Uniaxial Material Models

Uniaxial concrete model ConcreteZ01 and uniaxial steel model SteelZ01 were created based on the uniaxial constitutive model for concrete and embedded steel discussed earlier. The concrete model ConcreteZ01 will be used in the development of nonlinear finite element analysis of SC and S-UHPC beams. Steel model SteelZ01 will be modified to account for the bond slip between concrete and steel plate and will be used in the development of the finite element program.

SteelZ01

The first steel model incorporated in the OpenSees framework was Steel01 which was based on a uniaxial bilinear material model as shown in Figure 159. Before yielding, it has an elastic part followed by a strain hardening part. The unloading and reloading part follows a bilinear pattern in which the slopes of the paths are the same as the elastic modulus before yielding and hardening modulus after yielding.

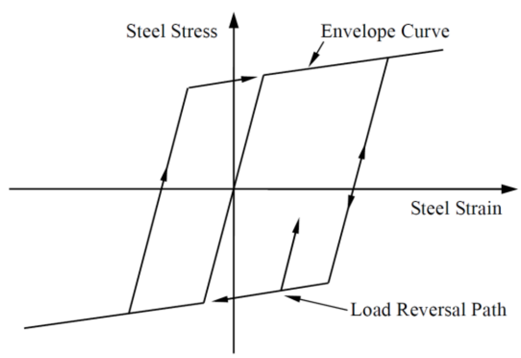

Figure 159. Steel01 material model

Steel01 does not consider the smeared yield stress and strain of embedded steel. Furthermore, the unloading and reloading paths do not take into account the Bauschinger effect. In reinforced concrete structures, reinforcement is embedded inside concrete and therefore the smeared yield strain and stress of embedded steel should be considered in the finite element model.

SteelZ01 was developed to consider the same. It incorporates both the envelope and the unloading/reloading pattern of uniaxial material laws of embedded mild steel in the CSMM model. Iteration was needed to calculate stress at a point based on a given strain. The iteration method was avoided by approximating the nonlinear curves using straight line segments. As shown in Figure 160, the dotted lines show the unloading and reloading paths defined by CSMM. However, the unloading and reloading paths are simplified in the SteelZ01 material model by linearizing them as shown in Figure 160.

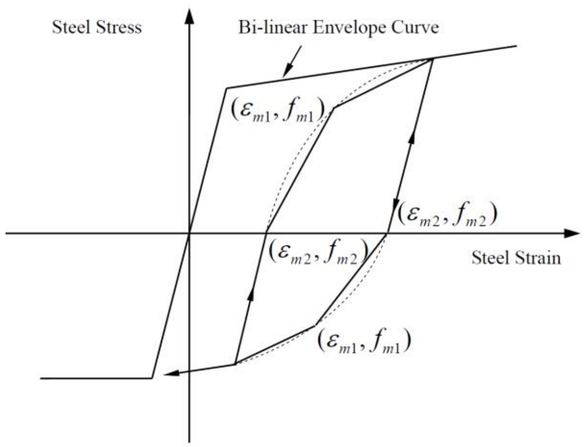

Figure 160. SteelZ01material model

Since the focus of this study is only static loading and not cyclic loading, only the bilinear envelope curve will be further discussed.

Two turning points (ε_{m1}, f_{m1}) and (ε_{m2}, f_{m2}) are chosen so that $f_{m1}=\pm 0.65f_y$ and $f_{m2}=0$. ε_{m1} and ε_{m2} are calculated by substituting f_{m1} and f_{m2} into the following equation.

$$f_s = E_s\bar{\varepsilon}_s, \quad (\bar{\varepsilon}_s \le \bar{\varepsilon}_n),$$

$$f_s = f_y\left[\left(0.91-2B\right)+\left(0.02+0.25B\frac{\bar{\varepsilon}_s}{\varepsilon_y}\right)\right], \quad (\bar{\varepsilon}_s > \bar{\varepsilon}_n),$$

$$\text{where} \quad B = \frac{1}{\rho}\left(\frac{f_{cr}}{f_y}\right)^{1.5} \quad \text{and} \quad \rho \ge 0.5\%,$$

$$\bar{\varepsilon}_n = \varepsilon_y(0.93-2B),$$

To avoid iteration, the turning points need to be determined. After determining the turning points, the stresses of any point will be linear function of strains and stresses of the turning points and can be calculated from a given strain.

This model will be modified to create a new model to account for bond slip in Steel-plate concrete structures.

Slip-Steel Model

SteelZ01 was modified and extended to steel-plate concrete structures and incorporated into the CSMM model. In steel-plate concrete structures, the bond between steel plate and concrete is crucial for the structure to not fail prematurely due to bond slip between concrete and steel plate. The minimum amount of shear reinforcement was investigated to prevent premature failure due to bond-slip and was reported in the previous quarterly reports. The shear transfer in the case of steel-plate concrete structures happened across a plane at the interface of steel plate and concrete.

A shear-friction model should be used to find the relationship between shear-transfer strength and the reinforcement crossing the shear plane. ACI 318-11 [118] provides a provision to estimate the shear-transfer strength when the shear-friction reinforcement is perpendicular to the shear plane. The nominal shear strength V_n as per 11.6.3 of ACI 318-11 is given by

$$V_n = 0.8A_{vf} f_y + A_c K_1 \quad (28)$$

where A_c is the area of concrete section resisting shear transfer (in^2), A_{vf} is the shear reinforcement area and f_y is the yield strength of the shear reinforcement.

In the right side of Equation 27, the first term represents the contribution of cross ties to shear transfer resistance. The coefficient 0.8 represents the coefficient of friction. The second term characterizes the sum of the resistance provided by friction between the rough surfaces of concrete and steel plate and the dowel action of the cross ties.

Consider the free body diagram of all the forces on the beam between the point of application of the load and the end of the beam, as shown in Figure 161.

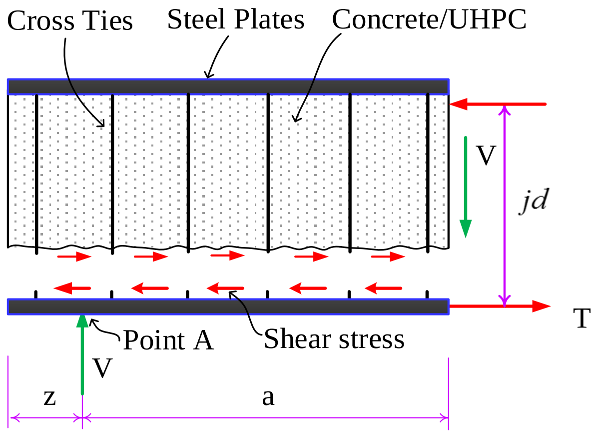

Figure 161. Free body diagram of SC/S-UHPC beam

By equilibrium equation:

$$V_{max} \cdot a = jd \ \cdot T_{max} \tag{29}$$

From ACI 318 – 11[19]:

$$T_{max} = (K_1 + 0.8\rho_{sv} f_{yv}) b(z + a) \tag{30}$$

From Equations 28 and 29:

$$K_1 = \frac{V_{max} \cdot a}{jd \ \cdot b(z+a)} - 0.8\rho_{sv} f_{yv} \tag{31}$$

where K_1 is the maximum bond strength between concrete and steel plate, V_{max} is the peak shear force, "a" is the shear span, "jd" is the effective depth of beam, "T_{max}" is the maximum tensile force in the steel plate, "ρ_{sv}" is the shear reinforcement ratio and "f_{yv}" is the yield strength of the shear reinforcement.

The value of K_1 which depends on the a/d ratio and the bond strength between the two distinct materials (concrete and steel) is calibrated for both SC and S-UHPC beams by using Equation 30. Table 23 shows the calculation results for finding K_1 for SC beams with conventional concrete.

Table 23. Calibration of K1 for SC beams

Specimen	b (in.)	t (in.)	a/d	ρ (%)	fy (ksi)	fc (ksi)	jd (in.)	Vmax (kips)	0.8ρfy (ksi)	T (kips)	K1 (ksi)
SC1 North	12.00	0.188	2.5	0.102	60	8.12	15.81	27.36	0.0489	76.00	0.08
SC1 South	12.00	0.188	2.5	0.102	60	8.12	15.81	26.16	0.0489	72.67	0.08
SC3 North	12.00	0.188	2.5	0.137	60	5.80	15.81	34.92	0.0657	97.01	0.10
SC3 South	12.00	0.188	2.5	0.137	60	5.80	15.81	32.25	0.0657	89.58	0.09
SC4 North	12.00	0.188	2.5	0.164	60	7.40	15.81	42.72	0.0786	118.67	0.13
SC4 South	12.00	0.188	2.5	0.205	60	7.40	15.81	52.99	0.0982	147.18	0.16
SC5 South	12.00	0.188	1.5	0.137	60	7.98	15.81	55.93	0.0657	93.21	0.18
SC5 North	12.00	0.188	1.5	0.164	60	7.98	15.81	64.74	0.0786	107.90	0.21
SC6	12.00	0.188	5.2	0.137	60	7.98	15.81	28.68	0.0657	165.71	0.09

The procedure for finding an expression for K1 is simplified in a flowchart shown in Figure 162.

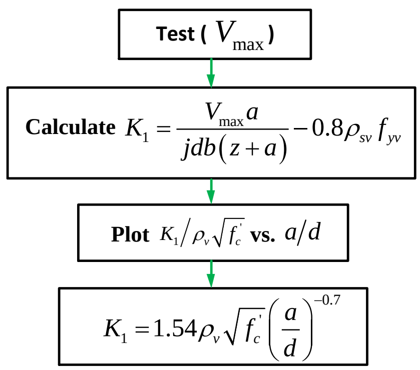

Figure 162. Flowchart for K1 calibration

K_1 is normalized with the percentage of shear reinforcement and concrete strength and plotted against a/d ratio in order to perform regression analysis to find the relationship between K1 and the a/d ratio as illustrated in Figure 163.

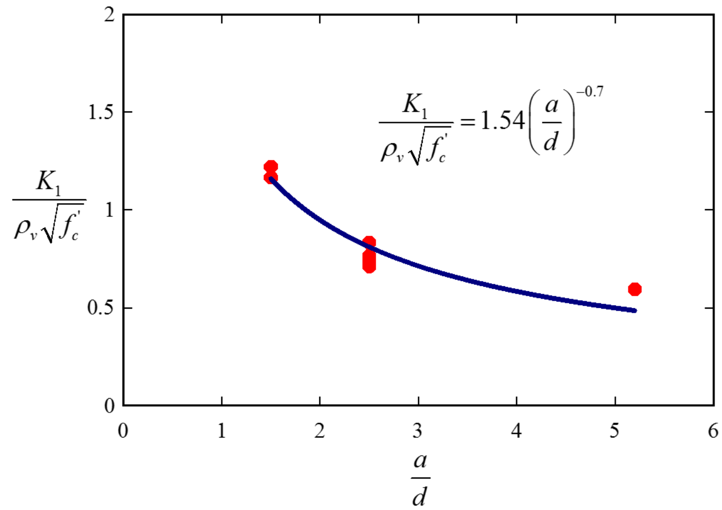

Figure 163. Normalized K1 Vs. a/d

After performing regression analysis, the expression for K_1 for SC beams with conventional concrete is found to be:

$$K_1 = 1.54\rho_v\sqrt{f_c{}'}(\frac{a}{d})^{-0.7}. \quad (32)$$

A similar procedure was carried out for the calibration of K_1 for S-UHPC beams. The calculation details for S-UHPC beams is shown in Table 24.

Table 24. Calibration of K1 for S-UHPC beams

Specimen	b (in.)	t (in.)	a/d	ρ (%)	fy (ksi)	fc (ksi)	jd (in.)	Vmax (kips)	0.8ρfy (ksi)	T (kips)	K1 (ksi)
S-UHPC1 South	12.00	0.25	2.5	0.184	60	22.34	15.81	49.56	0.088	137.68	0.15
S-UHPC2 South	12.00	0.25	2.5	0.274	60	22.34	15.81	77.71	0.132	215.85	0.25
S-UHPC2 North	12.00	0.25	2.5	0.321	60	22.34	15.81	85.92	0.154	238.68	0.27

The results for S-UHPC2 North are not included because of the possible instrumentation error. This discrepancy was confirmed by calculating the value of K_1 for S-UHPC2 North and noticing the inconsistency of the value of K_1 as compared to other specimens.

To find an expression for K_1, K_1 is normalized with concrete strength and plotted against the percentage of shear reinforcement as shown in Figure 164.

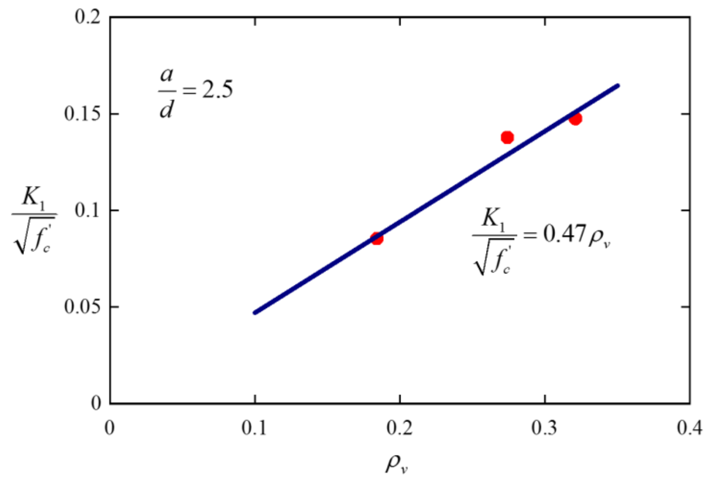

Figure 164. Normalized K1 Vs. $\boldsymbol{\rho_v}$

After performing regression analysis, the expression for K1 for S-UHPC beams was found out to be:

$$K_1 = 0.89\rho_v\sqrt{f_c{}'}\left(\frac{a}{d}\right)^{-0.7}. \tag{33}$$

The calibrated constitutive model for Slip-Steel model is shown in Figure 165.

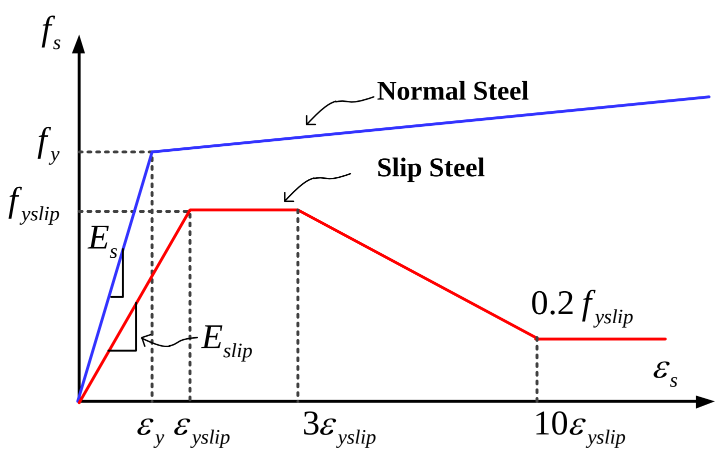

Figure 165. Slip-Steel material model

The stress strain curve for the Slip-Steel model is comprised of three parts: (1) The linear elastic part up to f_{yslip}, (2) the plastic part at which the steel plate continues to deform under constant load up to a strain of three times the strain at yielding and (3) the bond slip region at which the bond between the steel plate and concrete has been weakened and on any further loading the member would fail. However, to capture the descending portion of the load-deflection curve of SC structures, it is assumed that the stress would drop to 20% of the peak. This would avoid any convergence problems in the finite element model.

F_{yslip} is the yield strength of the slip steel and is given by Equation 33. Furthermore, the modulus of elasticity for slip steel was calibrated to account for the reduced stiffness due to bond slip and is given by Equation 34.

$$f_{yslip} = \frac{(z+a)}{t}\left(0.8\rho_{sv} f_{yv} + K_1\right) \tag{34}$$

$$E_{slip} = E_s\left(0.89 - 0.073\frac{a}{d}\right) \tag{35}$$

ConcreteZ01

The first concrete model incorporated in Opensees is Concrete01. Concrete01 incorporates the modified Kent and Park material model (Kent and Park 1982). The tensile strength of concrete has not been considered in this model. The stress–strain curve for the model is illustrated in Figure 166.

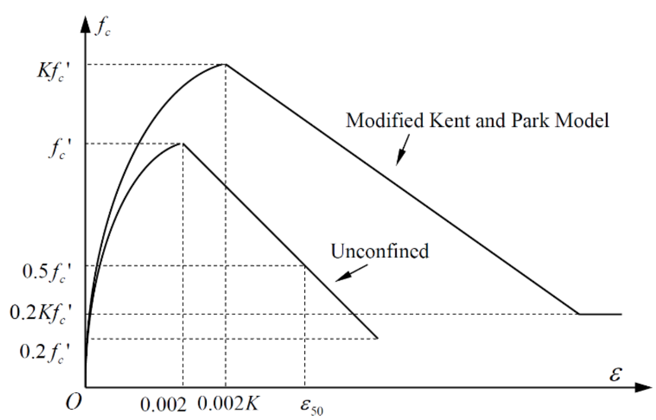

Figure 166. Modified Kent and Park model for monotonic stress-strain relationship of confined concrete

Concrete01 does not consider the effect of softening on the compressive stress and strain due to tensile strain in the perpendicular direction. Since no appropriate uniaxial material model for concrete was available, Zhong developed a new concrete model ConcreteZ01 which has the following improvements over Concrete01: (1) Tensile stress of concrete is taken into account so that deformation could be accurately predicted, and (2) The effect of softening was considered on the compressive stress and strain due to perpendicular tensile strain[139].

The envelopes of the ConcreteZ01 model (Figure 167) in compression and tension are the same as those of concrete constitutive relationships in CSMM. The equations defining the envelopes are expressed below. The unloading and reloading paths in the ConcreteZ01 model will not be discussed here since the type of loading in this study is only static loading.

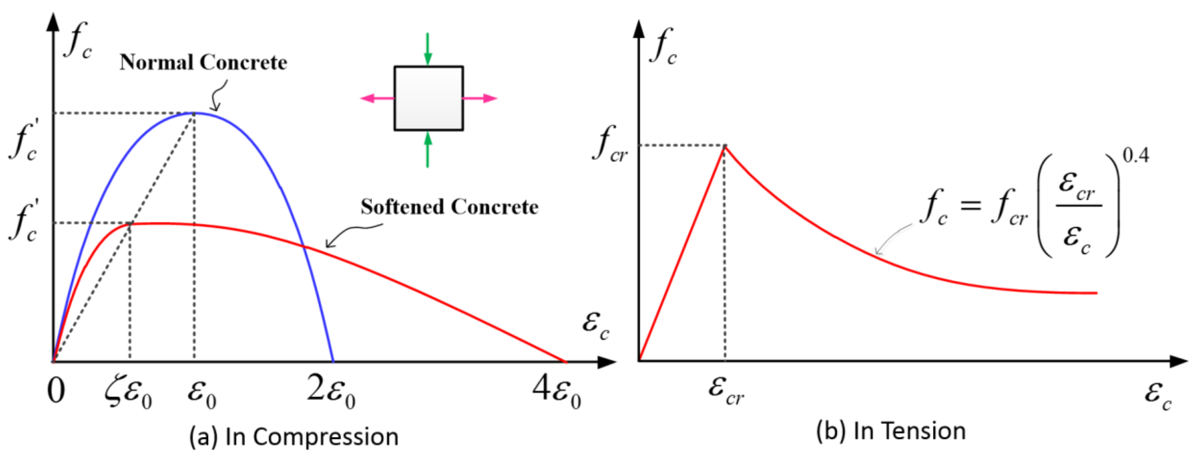

Figure 167. ConcreteZ01 material model

The equations defining the compression and tension envelopes for concrete in ConcretZ01 model is expressed as follows:

Compression:

(Stage 1) $$\sigma^c = D\zeta f_c' \left[2\left(\frac{\bar{\varepsilon}}{\zeta\varepsilon_o}\right) - \left(\frac{\bar{\varepsilon}}{\zeta\varepsilon_o}\right)^2 \right], \quad 0 \le |\bar{\varepsilon}| \le |\zeta\varepsilon_o|, \tag{36}$$

(Stage 2) $\sigma^c = D\zeta f_c^{'}\left[1-\left(\frac{\bar{\varepsilon}/\varepsilon_o - 1}{4/\zeta - 1}\right)^2\right], \quad |\bar{\varepsilon}| > |\zeta\varepsilon_o|,$ (37)

where

$$\zeta = \frac{5.8}{\sqrt{f_c^{'}(MPa)}}\frac{1}{\sqrt{1+400\bar{\varepsilon}_T^{'}/\eta^{'}}} \le 0.9, \tag{38}$$

$$D = 1 - 0.4\frac{\varepsilon_c^{'}}{\varepsilon_o} \le 1.0. \tag{39}$$

It was defined that $\eta^{'} = \dfrac{\rho_t f_{ty} - \sigma_t}{\rho_\ell f_{\ell y} - \sigma_\ell} \le 1.0$ in the original concrete constitutive model in CSMM. For simplification, here the effect of steel ratio $\eta^{'}$ on ς is neglected by taking $\eta^{'} = 1.0$.

Tension:

(Stage 1) $\sigma^c = E_c\bar{\varepsilon}$, if $0 \le \bar{\varepsilon} < \varepsilon_{cr}$, (40)

(Stage 2) $\sigma^c = f_{cr}\left(\frac{\varepsilon_{cr}}{\bar{\varepsilon}}\right)^{0.4}$, if $\bar{\varepsilon} > \varepsilon_{cr}$. (41)

Finite Element Implementation

The constitutive laws discussed before are combined with the equilibrium and compatibility equations to form a tangent stiffness matrix [*D*] for the element. The detail of the derivation of the matrix [*D*] is presented in Zhong's PhD dissertation[139]. The formulation to determine [*D*] is given as follows:

$$[D] = \partial\begin{Bmatrix}\sigma_x\\ \sigma_y\\ \tau_{xy}\end{Bmatrix} / \partial\begin{Bmatrix}\varepsilon_x\\ \varepsilon_y\\ 0.5\gamma_{xy}\end{Bmatrix} \tag{42}$$

[*D*] is evaluated by:

$$[D] = \left[T(-\theta_1)\right][D_c][V]\left[T(\theta_1)\right] + \sum_i\left[T(-\theta_{si})\right][D_{si}]\left[T(\theta_{si}-\theta_1)\right][V]\left[T(\theta_1)\right] \tag{43}$$

In Equation 42, [V] is the matrix defined in Equation 26 which translates the biaxial strains into uniaxial strains using the Hsu/Zhu ratios. [D_c] and [D_{si}] are the uniaxial tangential constitutive matrix of concrete and the uniaxial tangential constitutive matrix of steel, respectively. [D_c] and [D_{si}] are defined as follows:

$$\left[D_c\right] = \begin{bmatrix} \bar{E}_1^c & \dfrac{\partial \sigma_1^c}{\partial \bar{\varepsilon}_2} & 0 \\ \dfrac{\partial \sigma_2^c}{\partial \bar{\varepsilon}_1} & \bar{E}_2^c & 0 \\ 0 & 0 & G_{12}^c \end{bmatrix}; \ \left[D_{si}\right] = \begin{bmatrix} \rho_{si}\bar{E}_{si} & 0 & 0 \\ 0 & 0 & 0 \\ 0 & 0 & 0 \end{bmatrix} \tag{44}$$

In Equation 43, $\bar{E}_1^c$, $\bar{E}_2^c$ and $\bar{E}_{si}$ are the tangential stiffness of uniaxial moduli of concrete and reinforcement which are computed at a stress/strain state. The derivatives of stress over strain $\partial\sigma_1^c/\partial\varepsilon_2$ and $\partial\sigma_2^c/\partial\varepsilon_1$ can be obtained by using the uniaxial constitutive relationships and taking into account the states of the concrete stresses and uniaxial strains in the 1-2 directions[139]. G_{12}^c is the shear modulus of concrete and is evaluated by the following equation.

$$G_{12}^c = \frac{\sigma_1^c - \sigma_2^c}{\varepsilon_1 - \varepsilon_2} \tag{45}$$

Finite Element Framework

For the purpose of this study, OpenSees, an object-oriented framework for simulation applications in earthquake engineering using finite element is chosen as the finite element framework for developing the analysis program. OpenSees stands for Open System for Earthquake Engineering Simulation[148]. OpenSees has been developed in the Pacific Earthquake Engineering Center (PEER). An object-oriented framework is a set of cooperating classes that can be used to generate software for a specific class of problems, such as finite element analysis. The framework dictates overall program structure by defining the abstract classes, their responsibilities and how these classes interact. OpenSees is a communication mechanism for exchanging and building upon research accomplishments, and has the potential for a community code for earthquake engineering because it is an open source.

Using the OpenSees as the finite element framework, a nonlinear finite element program titled Simulation of Concrete Structures (SCS) was developed for the simulation of reinforced concrete structures subjected to monotonic and reversed cyclic loading[159]. To create an SCS program for SC/S-UHPC structures, the CSMM was implemented into OpenSees. Two material modules, namely ConcreteZ01 and RCPlaneStress and a new material model Slip-Steel has been incorporated into the SCS program to perform nonlinear finite element analysis of the SC and S-UHPC beams. Slip-Steel and ConcreteZ01 are the uniaxial material modules, in which the uniaxial constitutive relationships of steel and concrete specified in the CSMM are defined. The RCPlaneStress is implemented with the quadrilateral element to represent the four-node reinforced concrete membrane elements. The uniaxial materials of Slip-Steel and ConcreteZ01 are related with material RCPlaneStress to determine the material stiffness matrix of membrane Steel-plate Concrete in RCPlaneStress.

4.5.4. Validation

The developed finite element program will be used for the analysis of SC and S-UHPC structures. The program will be verified by the experimental data reported in the previous quarterly reports. The modeling, meshing and the boundary condition of the beam are shown in Figure 168. The steel plates were modeled as Slip-Steel truss elements and the concrete was simulated by RCPlaneStress quadrilateral elements.

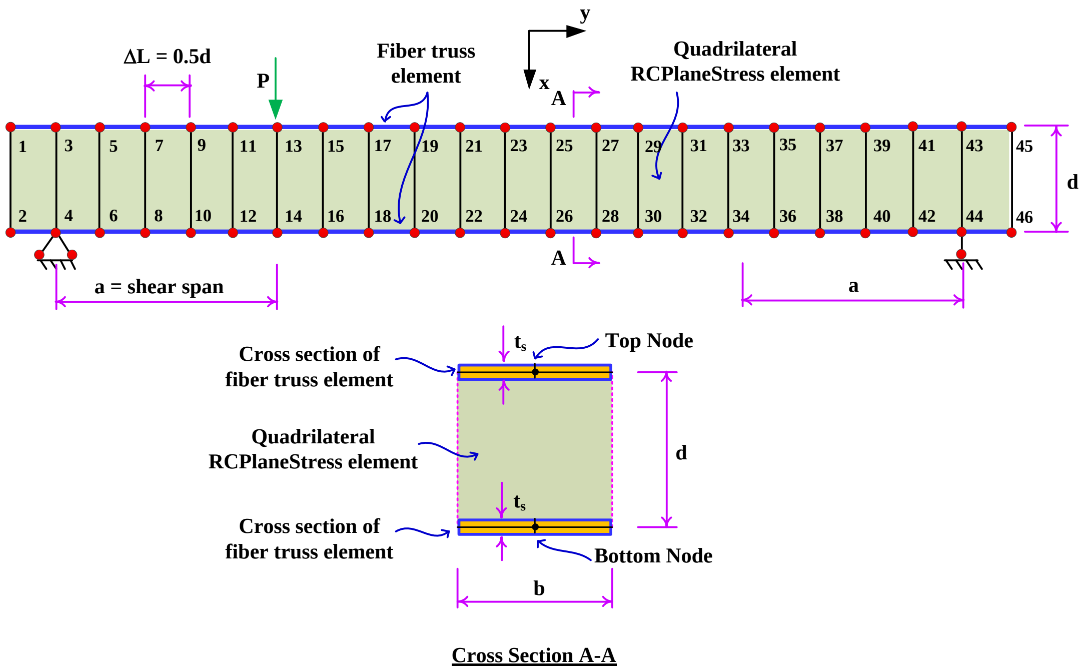

Figure 168. Finite element mesh

The dimensions and the properties of the specimens are summarized in Table *25*.

Table 25. Experimental matrix, strength, and failure mode

Specimen	a/d	$s_{tie}^{\#}$ (in.)	f_c' * (ksi)	$\rho_{t,ACI}$ (%)	$\rho_{t,test}$ (%)	$\rho_{t,test}$ / $\rho_{t,ACI}$	F_{peak} ** (kips)	Ductility $\delta^{\dagger}$	Failure Mode
SC1 north	2.5	8.00	8.13	0.111	0.102	0.92	27.4	——	Brittle
SC1 south	2.5	8.00	8.13	0.111	0.102	0.92	26.1	——	Brittle
SC3 north	2.5	6.00	5.82	0.094	0.137	1.45	31.7	1.17	Ductile
SC3 south	2.5	6.00	5.82	0.094	0.137	1.45	34.9	1.79	Ductile
SC4 north	2.5	5.00	7.37	0.106	0.164	1.54	42.7	1.58	Ductile
SC4 south	2.5	4.00	7.37	0.106	0.205	1.93	53.0	1.65	Ductile
SC5 south	1.5	6.00	8.00	0.110	0.137	1.25	55.9	1.43	Ductile
SC5 north	1.5	5.00	8.00	0.110	0.164	1.49	64.7	1.48	Ductile
SC6	5.2	6.00	8.00	0.110	0.137	1.25	29.3	1.99	Ductile
S-UHPC-1 (South)	2.5	10.00	22.34	0.170	0.184	1.08	49.56	1.003	Ductile
S-UHPC-2 (South)	2.5	6.75	22.32	0.170	0.277	1.63	77.70	2.650	Ductile
S-UHPC-2 (North)	2.5	5.75	22.32	0.170	0.323	1.90	85.80	4.010¥	Ductile

Note:
stie = spacing of cross ties
* $f_c^{'}$ = concrete compressive strength from concrete cylinder
** F_{peak} = peak shear capacity
† δ = deflection at the peak /deflection when cross ties yielded
¥ = Flexural ductility = deflection at the peak / deflection when the steel plate yielded

The experimental and analytical results are compared and shown in Figure 169 (a-g) and Figure 170 (a-c) for all the specimens mentioned in Table 25.

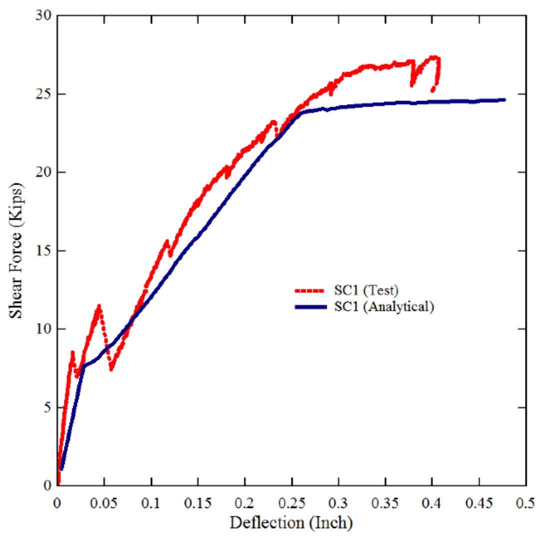

(a) SC1

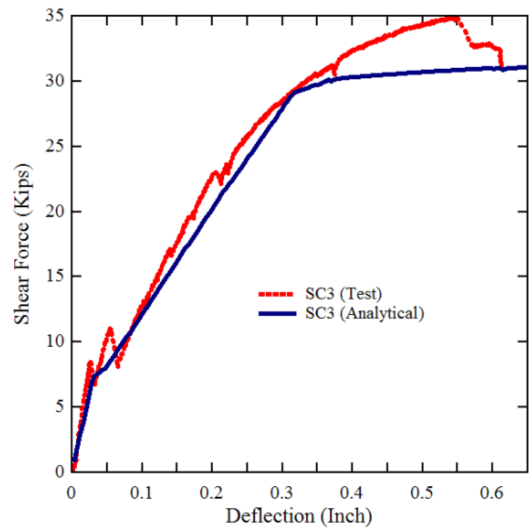

(b) SC3

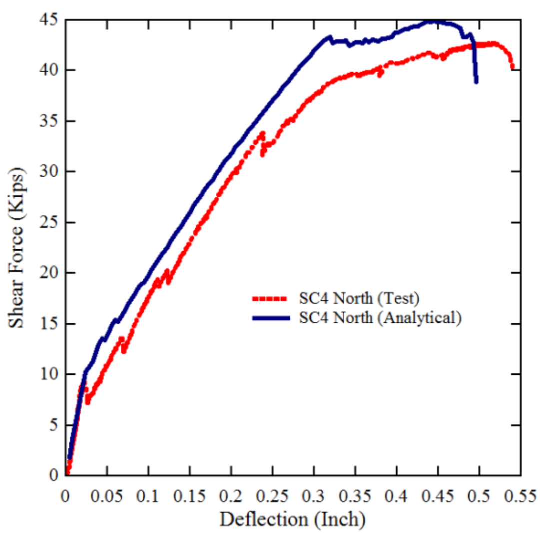

(c) SC4 North

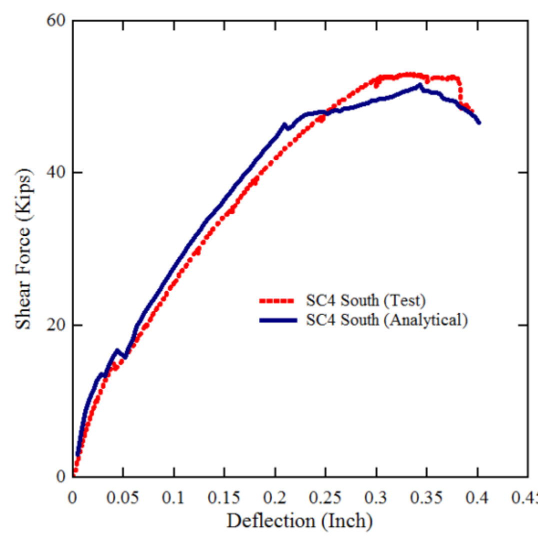

(d) SC4 South

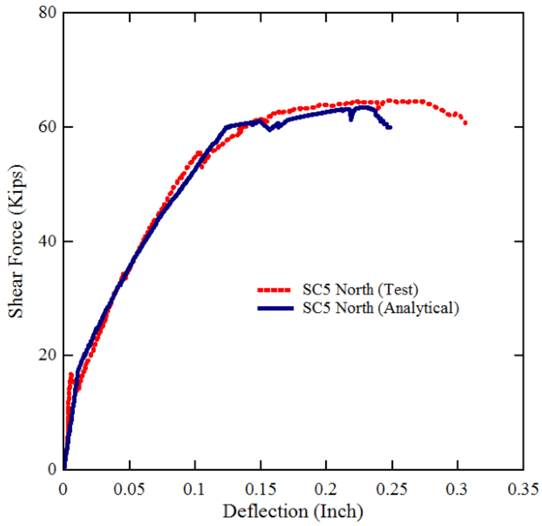

(e) SC5 North

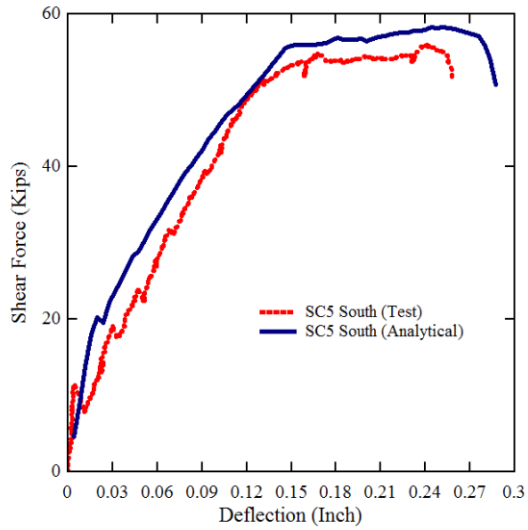

(f) SC5 South

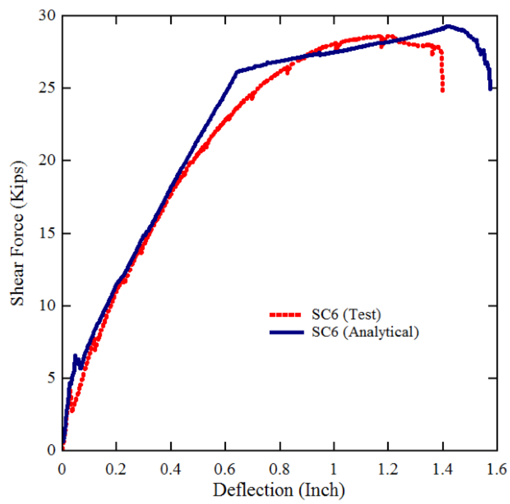

(g) SC6

Figure 169. Analytical vs. Experimental results for SC beams

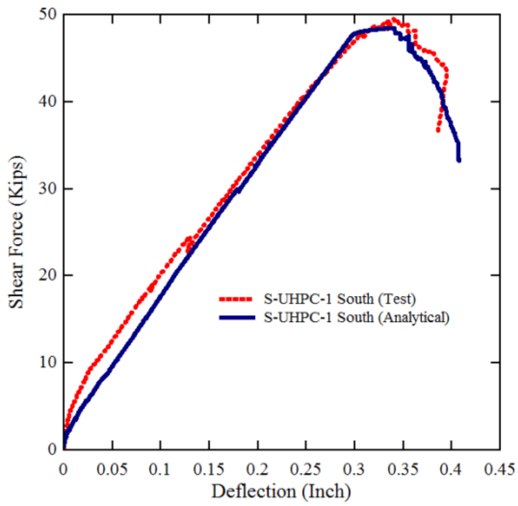

(a) S-UHPC-1 South

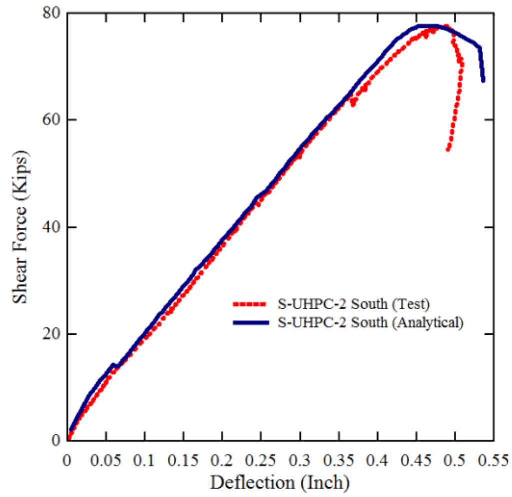

(b) S-UHPC-2 South

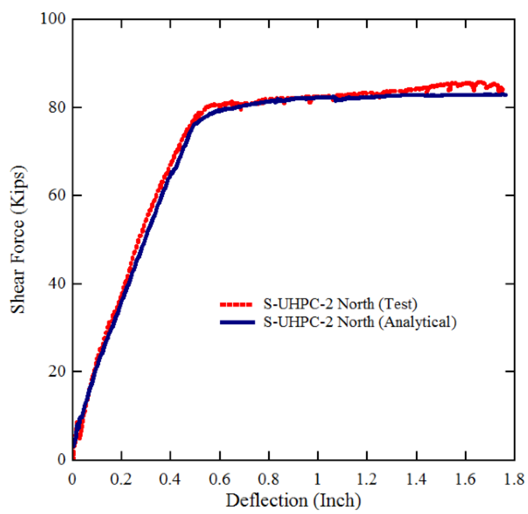

(c) S-UHPC-2 North

Figure 170. Analytical vs. Experimental results for S-UHPC beams

As could be seen from the above results, the SCS program can accurately predict the behavior of SC and S-UHPC beams under out-of-plane shear. This SCS program can now be used to predict the behavior of any SC/S-UHPC beams.

4.6. Summary

The minimum cross tie ratio for SC structures to exhibit a ductile behavior was investigated by subjecting the SC beams to out-of-plane shear. Based on the test results of specimens SC1 to SC6 for normal strength concrete and specimens S-UHPC-1 and S-UHPC-2 for ultra-high performance concrete, a minimum cross tie ratio is proposed. The proposed minimum amount of cross tie ratios for each of normal strength concrete and ultra-high performance concrete is described below.

For SC beams with normal strength concrete: $\boldsymbol{\rho_{t,min}}$=1.45*$\boldsymbol{\rho_{t,ACI}}$ for 2.0 < a/d < 4.0, or

$\boldsymbol{\rho_{t,min}}$=1.25*$\boldsymbol{\rho_{t,ACI}}$ for a/d ≤ 2.0 and a/d ≥ 4.0

For SC beams with Ultra-High Performance Concrete (UHPC): $\boldsymbol{\rho_{t,min}}$=1.10*$\boldsymbol{\rho_{t,ACI}}$ for a/d=2.5.

The contribution of UHPC in resisting shear is more than that of normal strength concrete due to the compressive strength of UHPC being almost four times the strength of normal concrete. Therefore, a higher amount of shear reinforcement is required in the case of SC with normal strength concrete to resist shear, which explains the higher coefficient.

An active sensing approach based on Smart Aggregates (SAs) is proposed to detect and monitor bond slip in SC beams. In this approach, damage index, which is based on wavelet packet decomposition of the received signals from SAs, is utilized to evaluate bond condition quantitatively. The initiation and development of bond slip in SC beams were captured successfully during the tests, which validated the applicability of the active sensing approach. This approach can provide early warning about the debonding of the steel plate and the concrete in SC beams before structural failure happens. Using the damage index, a quantitative study was conducted to compare the interfacial bond condition of SC beams equipped with different shear reinforcement ratios. Results show that cross ties can effectively improve the interfacial bond condition of SC beams, and that cross ties as shear reinforcement can significantly improve ductility and shear strength of SC beams.

A new material model was created to account for the bond-slip between the concrete and steel plate. The material model was incorporated into CSMM and implemented in OpenSees. A nonlinear finite element program was developed for the analysis of SC/S-UHPC structures based on the CSMM model. The developed finite element program was further validated by the experimental results of five SC and two S-UHPC beams. The analytical results show good agreement with the experimental data.

5. PERFORMANCE OF S-UHPC WALL PANEL SUBJECTED TO PURE SHEAR

In recent years, steel plate concrete (SC) has been widely used for building and nuclear containment structures to resist lateral forces induced by severe earthquakes and heavy winds. Compared to the conventional reinforced concrete, SC has higher strength and ductility, enhanced stiffness and large energy dissipation capacity. SC is also advantageous for faster construction and cost-effectiveness due to the fact that steel plates can serve as formwork for concrete during construction. Recently, SC has been proposed in AP1000 (Figure 171) and US-APWR (US-Advanced Pressurized Water Reactor) nuclear power plants to reduce the construction time[160]. In addition, the use of SC offers an additional benefit--it improves the quality control of the nuclear power plant structures because SC modules can be prefabricated at the factory and assembled at the construction site. A Steel-plate Concrete (SC) structure consists of two steel faceplates with cross ties connecting the faceplates and the infilled concrete (Figure 172).

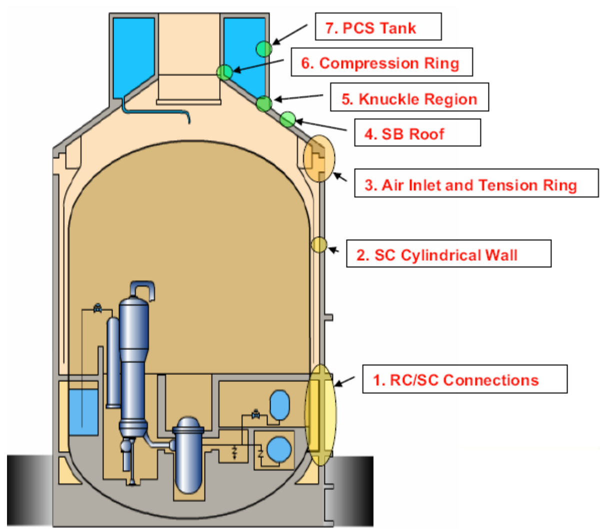

Figure 171. AP 1000 Nuclear Power Plant [160]

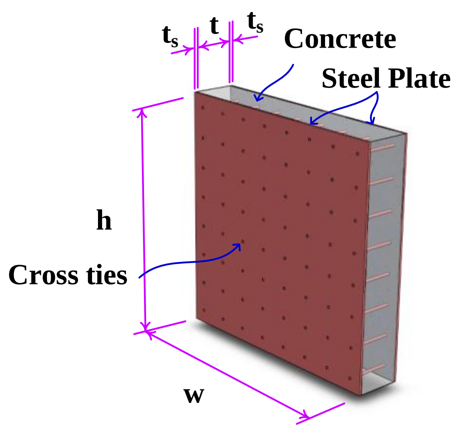

Figure 172. SC wall

Shear behavior of Reinforced Concrete (RC) structures is well understood. Shear in reinforced concrete has been theoretically, experimentally and analytically investigated. Rational models have been developed in the past few decades to accurately predict the shear behavior of RC elements[140]. However, no significant amount of research has been performed for understanding the shear behavior of SC/S-UHPC wall elements and there are no rational computer models available to predict the shear behavior of SC walls.

Shear force in structures is classified as shear in beam, shear in slabs and shear in walls. Shear in beams and walls have the same nature. In both cases, shear force acts in the plane of a structure member. However, shear in slab is different and acts orthogonally to the plane of the slab and is generally referred to as out-of-plane shear or punching shear. SC nuclear containments are also subjected to out-of-plane shear in regions close to the foundation and at connections or interfaces with other structures ([161],[162]). The problem with out-of-plane shear in SC structures has already been dealt with and the results were presented in the previous quarterly reports. Steel-plate Concrete (SC) structures under in-plane shear are always subjected to compression-tension biaxial stresses. The possible failure modes of SC structures in shear could be yielding or buckling of the steel plates, crushing of concrete or debonding of steel-plates from the concrete.

As mentioned before, a minimum amount of cross ties was investigated for SC/S-UHPC beams under out-of-plane shear and reported in the previous quarterly reports. By providing the minimum amount of cross ties, premature brittle failure due to debonding could be prevented. Therefore, to simulate the real nuclear power plant structure, which is subjected to both in-plane and out-of-plane shear, a minimum amount of cross ties will be provided in the testing of SC/S-UHPC wall panels under in-plane shear.

The cylindrical wall in nuclear power plants is effective in resisting lateral loads originating from an earthquake or wind. Because a large portion of the lateral shear forces are often assigned to such structures, it is important to understand their behavior under the predicted loads. If the behavior of an element is known, the behavior of the entire structure could be predicted by finite element methods. An attempt has been successfully made to investigate the behavior of a wall element of the SC/S-UHPC cylindrical wall in shear, both experimentally and analytically.

The behavior of an element subjected to shear is characterized by shear stress vs. shear strain curve. An element subjected to pure shear does not fail immediately at the peak load, but there exists a descending branch which indicates the ductility and energy absorption capacity of the element. Several models have been proposed in the past to predict this behavior. Most of these models were successful in predicting the ascending branch of the curve but failed to predict the descending branch accurately.

The Softened Membrane Model[149] was introduced that accounts for the Poisson's effect for predicting the shear behavior of reinforced concrete structures. This model was able to predict the descending branch of the shear stress vs. shear strain curve. In general, the behavior of a reinforced concrete membrane element could be predicted by a set of governing equations, which are derived based on the fundamentals of mechanics of materials. These equations consists of three equilibrium equations, which are obtained from the transformation of two dimensional stress in concrete and steel, and three compatibility equations obtained from the transformation of two dimensional strain in concrete and steel. The solution of theses six equations requires additional equations to describe the relationships between the stress and strain of concrete in compression and tension as well as steel in tension. These relationships were established by extensive tests on reinforced concrete panels. The tests revealed that the tensile strains in the perpendicular direction softened the strength and strain of concrete in compression[140, 141].

The objective was to verify the applicability of the SMM (softened membrane model) to steel-plate concrete wall panels. In addition, the bond between the steel plate and concrete is one of the most important factors that may influence the behavior of the wall panel. The PZT-based Smart Aggregates (SA) was used to evaluate the bond between the steel plates and the UHPC. When an SA is excited with sweep sinusoidal signals, the responses of the remaining SA are measured. Based on the wavelet packet analysis of the SA measurements, the debonding areas will be detected by using the Fourier spectra and two evaluation indices. This monitoring method will provide an innovative approach to detect the debonding damage of SC modular construction.

The universal panel tester at the University of Houston will be used to accomplish this objective. This machine is capable of simulating any combination of in-plane normal stresses (tension and compression), in-plane and out-of-plane shear and in-plane and out-of-plane bending and torsion.

5.1. The Universal Panel Tester

The developed UHPC in this project was used to cast an S-UHPC wall panel. The fabrication of the wall panel started with creating a new formwork for the designed dimensions of the wall panel. It will be informative if more details about the universal panel tester is given at this stage. The universal panel tester is capable of testing panels of 55 inches by 55 inches with thicknesses of up to 16 inches. They are considered full scale since reinforcing bars of up to 1 inch diameter can be used in the panel. The forces to the panel are applied through 60 jacks, 40 in-plane and 20 out-of-plane hydraulic jacks. The capacity of each in-plane jack is 250 kips and the capacity of each out-of-plane jack is 140 kips. Six reaction forces are required to keep the test panel in equilibrium and to avoid any rigid body movements. To satisfy these criteria, three of the forty in-plane jacks were replaced with rigid links. Furthermore, three of the twenty out-of-plane jacks were replaced with rigid links to avoid any rigid body movements and to serve as reaction supports[163].

Until 1993, the ascending branch of the stress-strain curve could be reliably obtained from the test results. In 1993, a closed-loop servo-control system was installed in the universal panel tester which made it capable of switching to strain-control mode. The universal panel tester became the most versatile testing machine in the world to perform full-size panel tests in displacement-control mode[154]. The schematic diagram of the panel tester is shown in Figure 173.

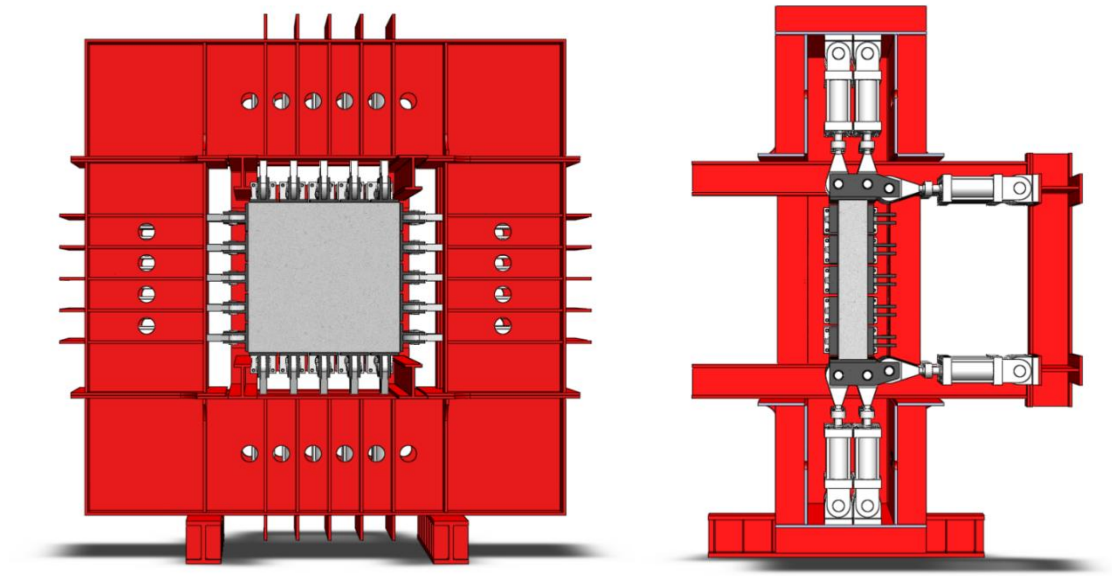

(a) Front View *(b) Side View*

Figure 173. The Universal Panel Tester

The forces are applied along the four edges of the panel at five locations equally spaced from each other on each edge. Two in-plane jacks and one out-of-plane jack act at each of the locations. The loads from the three jacks are transmitted to the panel through a connector yoke.

5.1.1. The Servo-Controlled Hydraulic System

The hydraulic system in the Universal Panel Tester is controlled by two controllers: (1) Manual Controller and (2) Servo Controller. The manual controller is used for installation of the test specimen. This mode will facilitate the jacks to be controlled and moved individually by either contracting or extending them. This control mode allows the rod-eye hole of a jack to line up with the yoke hole of the panel. Once lined up, a 3.54-inch diameter steel pin is inserted through the two holes to connect the jack to the panel. There are 60 manually controlled valves, which can control the jacks to be in tension, compression or holding mode. [164]

The servo controller mode controls the forces applied to the jacks by the servo-control system. The servo-control system has ten channels. Each channel consists of a servo controller and a servo-valve package. The servo-valve package has a servo-valve, a manifold with ten pairs of outlets and a pair of Delta P pressure transducers. A set of jacks on each side and face of the panel can apply different loads to the panel since different oil pressures can be applied to each channel. The oil pressure is applied to the jacks by connecting each jack to the manifold using a pair of flexible hoses with quick-disconnect fittings[164]. Figure 174 shows the hoses connected to the manifold on the south side of the universal panel tester. The manifolds are controlled by the servo-boxes. The servo-box receives its command from the software installed on the computer. Subsequently, it receives a feedback from either the Delta P pressure transducers or the LVDTs installed on the panel, depending upon the control mode.

Figure 174. South side of the Universal Panel Tester [163]

The command and the feedback will be compared in the servo-box and a signal will be sent to the servo valve on the manifold, and the oil pressure will be adjusted accordingly. The schematic diagram of the control system for both manual control and servo control is shown in Figure 175.

The servo-controlled system is a closed loop. This allows the load, displacement, stress or strain to be controlled automatically. The basic principle of the closed-loop servo control system is shown in Figure 176.

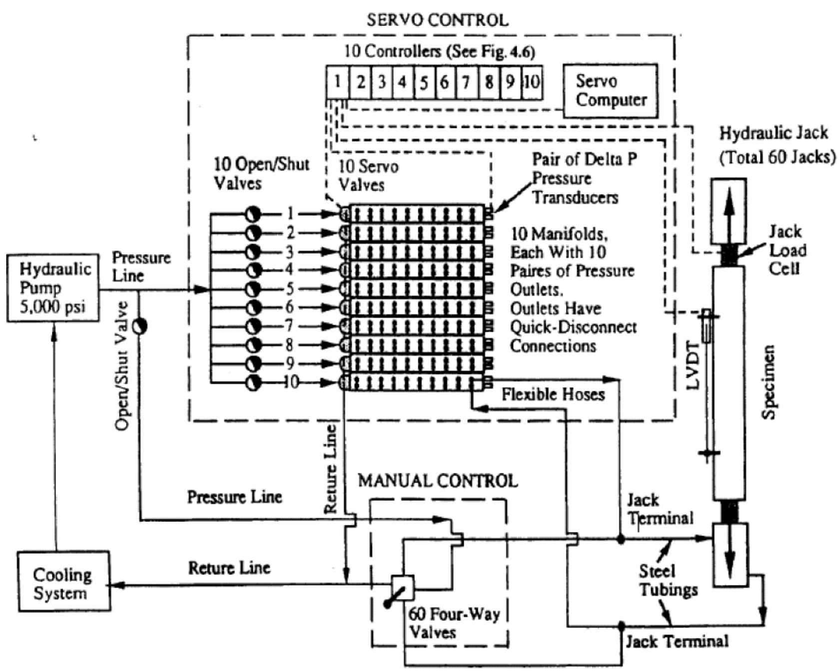

Figure 175. Schematic diagram of hydraulic and control system [164]

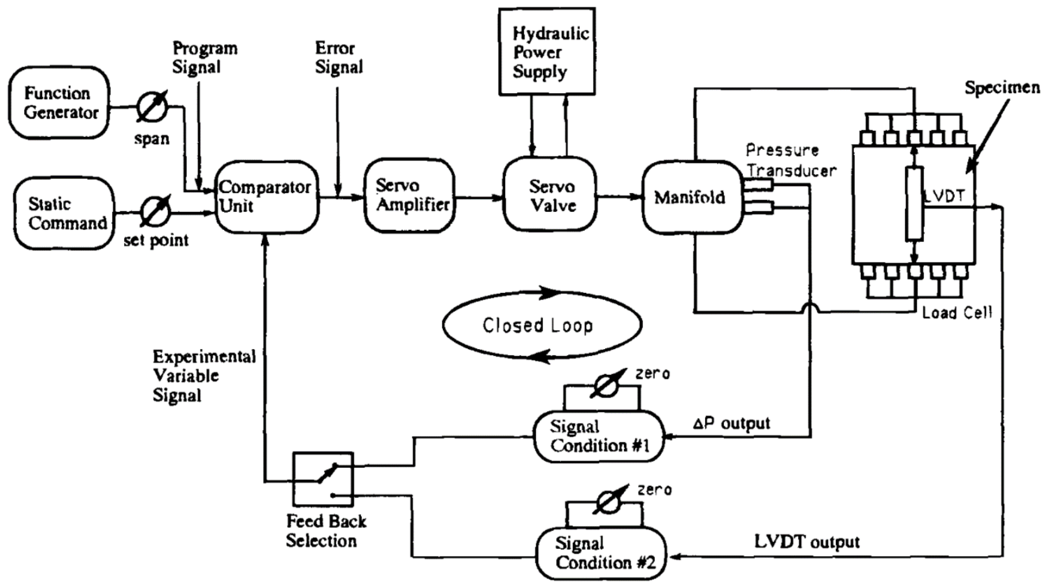

Figure 176. Schematic of the closed-loop servo-control system [165]

Signal Condition #1 is for load control mode. This selection is used for control of loads or stresses. A pair of Delta P pressure transducers which measure the amount of pressure applied to the jacks, serves as the feedback in this case. The second signal condition (#2) which is used for the controlling of displacements or strains uses the LVDTs installed on the test specimen as the feedback[164].

If the control mode is chosen to be load-control, then the experimental feedback from a pair of Delta P pressure transducers is compared with the pre-assigned program signal in a comparator unit. If there exists a voltage difference in the comparator unit, an error signal will be generated and will activate the servo-valve to adjust the oil-pressure in the manifold. The adjusted oil-pressure will change the loading condition in the test panel. The Delta P pressure transducers will measure and send a new feedback voltage based on the adjusted pressure levels in the jack. Once the programmer input voltage and the feedback voltage are equal, the resultant error signal will be zero and the servo-valve will reach a state of equilibrium. The servo control system can conduct the test in load control, strain control or a combination of both.

The servo controllers which controls the servo valves required an upgrade. Their power supplies and internal batteries were renewed and were reset to factory settings. The valves were balanced mechanically and electronically so that the pressure to the jacks are applied stably.

The hydraulic jack connections were checked and fixed for any damage in them. The signal conditioners, which remove noise from the signals received from the jacks, were also checked and fixed. Furthermore, the LVDT power supply boxes were renewed with much more sturdy and reliable ones as shown in Figure 177. The computer software which is used to send command to servo controllers was optimized and upgraded.

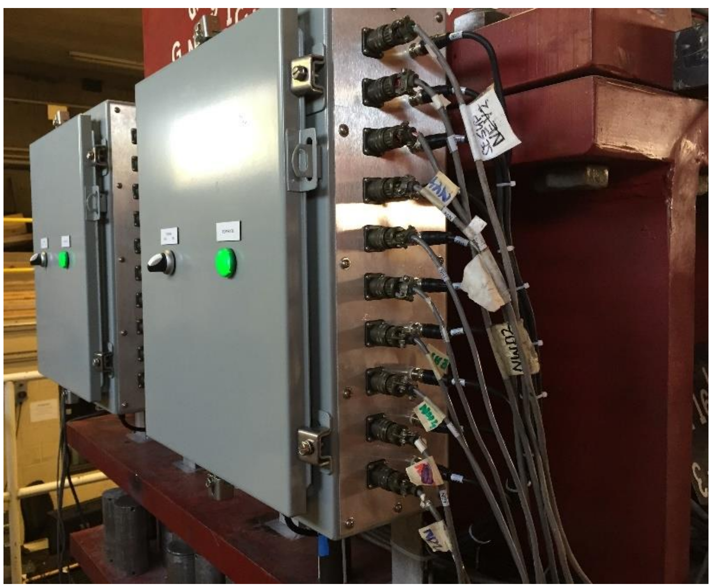

Figure 177. New power supply boxes for LVDTs

In addition, a state of the art tele-participation system was installed in the facility area to capture and telecast the entire test to a potential audience online. The system includes four fixed and two movable high resolution and wide-lens cameras with 360-degree rotation capabilities.

5.2. Experimental Program

The setup for the shear experiment had to be designed to apply tension and compression to the specimen proportionally. This would create a state of pure shear at 45 degrees to the principal stress directions. The specifications of the test specimens are presented in Table 26.

Table 26. SC Wall Panel Test Matrix

No.	Specimen	T_t	T_s	f_y (Steel plate)	fc'	$\rho_{t,test}/\rho_{t,ACI}$
1	SC-45	3 in.	3/16 in.	72.5 ksi	7.112 ksi	1.45
2	S-UHPC-10	3 in.	3/16 in.	72.5 ksi	22.237 ksi	1.10

Note: T_t = Total thickness of specimen, T_s = Steel plate thickness

The forces are applied along the four edges of the panel at five locations equally spaced from each other on each edge. Two in-plane jacks and one out-of-plane jack act at each of the locations. The loads from the three jacks are transmitted to the panel through a connector yoke.

Test panels are 55 inches by 55 inches by 7 inches. for reinforced concrete structures with normal strength concrete. Since the strength of UHPC is much higher than normal concrete, the test panel size was re-designed to meet the capacity of the Universal Panel Tester. The panel size was reduced to 40 inches by 40 inches by 3 inches. A new frame was built for the sides of the test panel to meet the dimensions of the opening of the Universal Panel Tester where the test specimen was mounted on for testing. Furthermore, a steel formwork was constructed for fabrication and casting of the new test panel, as shown in Figure 178.

Figure 178. Steel formwork for test panel

Cross ties were designed based on the minimum amount of shear reinforcement required for the SC module to behave as an integrated unit under out-of-plane shear and to preserve a certain shear ductility. This was done to simulate the actual panel element of an SC structure.

The stresses in the edge regions of the panel may be disturbed locally due to concentrated loads from the jacks. According to St. Venant's principle, this local disturbance diminishes at a distance equal to the thickness of the specimen. A 4.5-inch region was considered in the test panel to avoid the effect of this local disturbance in the measurement of strains and deformation in the specimen. The edges of the panel were strengthened by doubling the steel plate thickness at the edges to avoid local failure due to locally disturbed stresses. The loads were transferred to the panel through the connector yokes to steel inserts. Steel inserts were welded to the faces of the steel plates. The details of the test panel are shown in Figure 179.

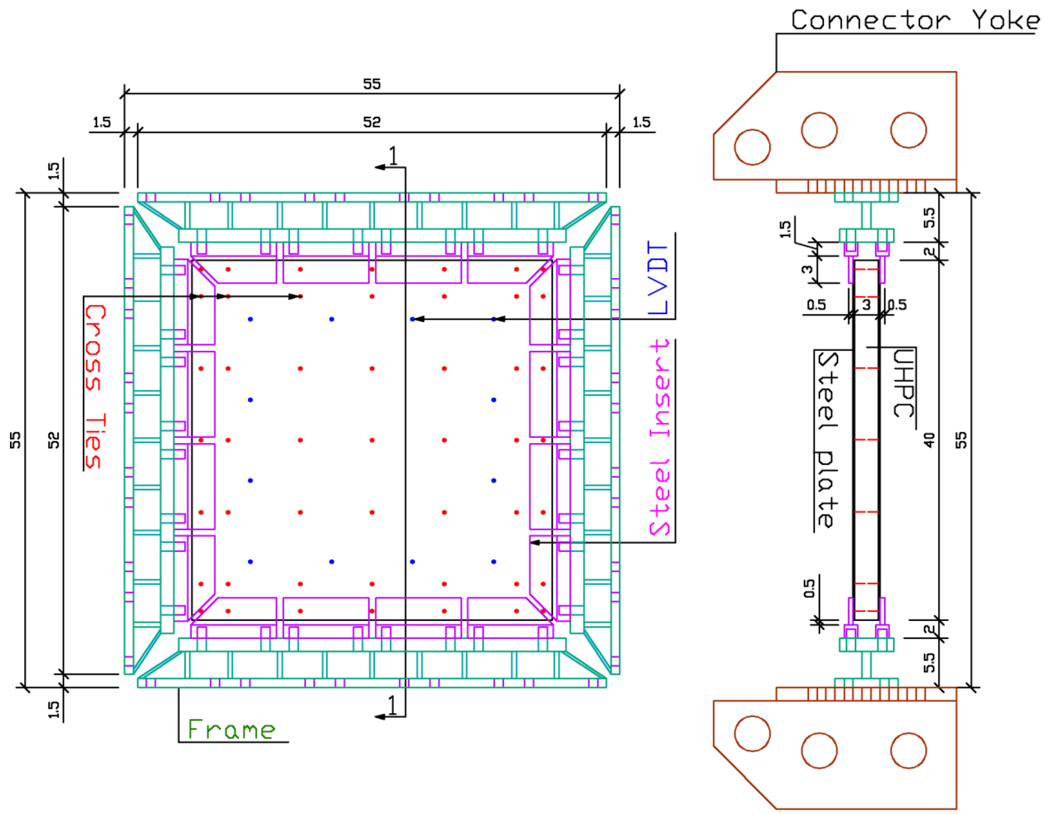

Figure 179. SC wall panel schematic

Two different designs were made for the steel inserts. The first design uses welding to transfer the loads from the steel inserts to the steel plate. The second design uses bolts for transferring the loads from the steel inserts to the steel plate. The schematic figures for specimens SC-45 and S-UHPC-10 are shown in Figure 180 and Figure 181.

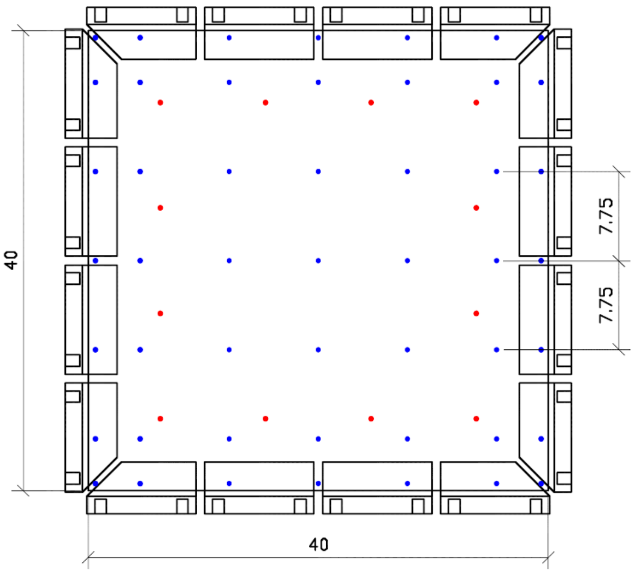

Figure 180. Specimen SC-10 (unit: inch)

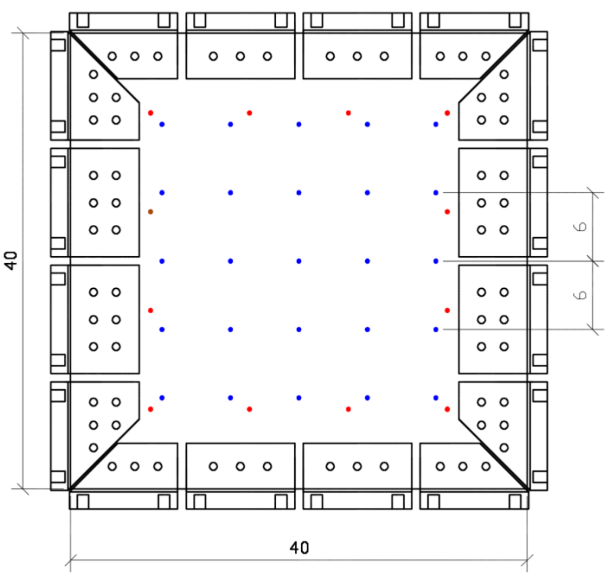

Figure 181. Specimen SC-45 (unit: inch)

5.2.1. Specimen Preparation

Fabrication of the test panel started with the drilling of holes on the steel plates. The holes were drilled using a magnetic drilling machine with a tolerance of 1/16 inch. The drilled holes were then counter-sink drilled on the outside faces of the steel plates to make more surface area for the effective welding. Strips of steel plates of the same thickness were welded on the 4.5-inch edge regions for strengthening purposes. The steel inserts were then fixed to the steel formwork and welded or bolted to the steel plates. Once the steel inserts and the steel plates were welded or bolted together, cross ties were welded on the steel plates as shown in Figure 182(a). The test panel was then ready for casting, as shown in Figure 182(b).

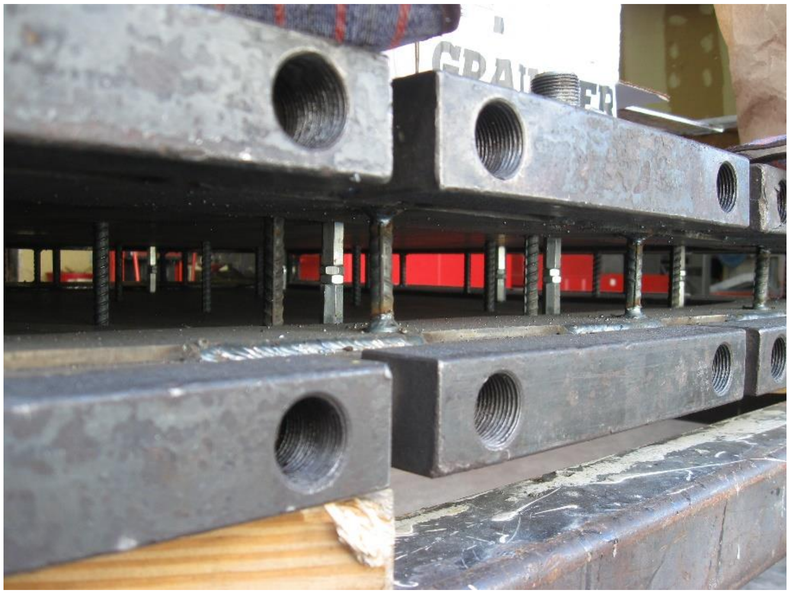

(a)

(b)

Figure 182. Fabrication of SC panel

The test panel was then cast with the concrete or UHPC. Mixing of concrete or UHPC was done using an 11 cubic-foot conventional concrete mixer. Vibration or tamping was not performed due to the self-consolidating capability of concrete or UHPC. The cast SC wall is shown in Figure 183.

Figure 183. SC wall panel cast with UHPC

After the 28 days of curing, the S-UHPC specimen was moved into the main testing laboratory where the Universal Panel Tester is situated. The steel inserts in the S-UHPC wall panel was tapped and cleaned as shown in Figure 184.

Figure 184. Tapping and cleaning the holes of the steel inserts

After tapping and cleaning the holes of the steel inserts, the socket set screw bolts are inserted into the steel inserts as shown in Figure 185.

Figure 185. Inserting socket set screw bolts to the steel inserts

Once the socket set screw bolts were tightened, the beam frame was lowered and slid onto the bolts as shown in Figure 204.

Figure 186. Setting up the steel beam frame onto the specimen

The beam frame was then tightened to the specimen by inserting a 1.5-inch high strength nut to the socket set screw bolts. Subsequently, the wall panel was lifted and put horizontally for the purpose of fixing the yokes onto the frame as shown in Figure 187.

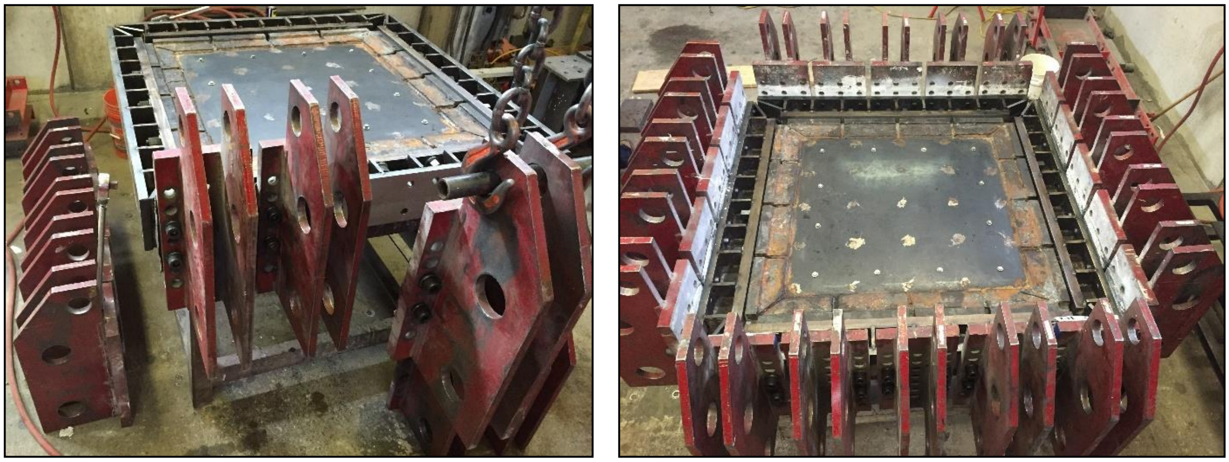

Figure 187. Fixing yokes onto the beam frame

After fixing all the yokes onto the beam frame, the specimen was ready to be moved to the testing frame inside the Universal Panel Tester as shown in Figure 188.

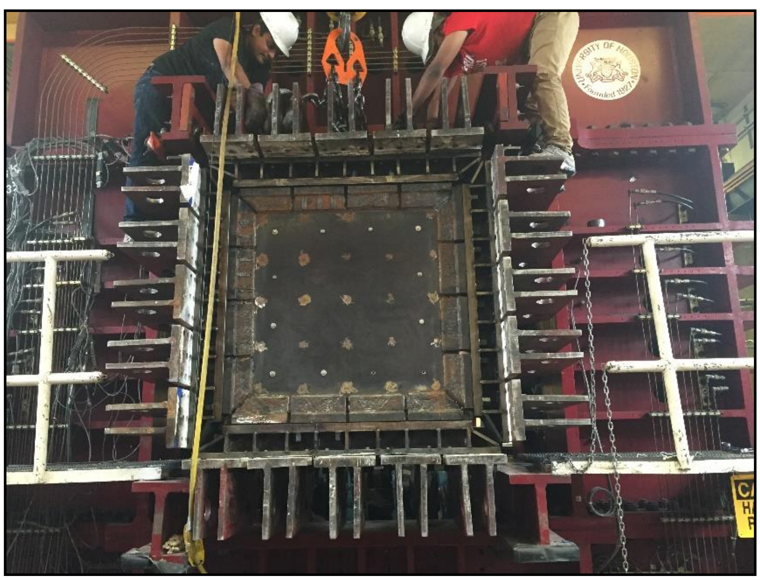

Figure 188. Specimen ready to be moved inside the testing frame

The specimen was lifted up using the overhead 10-ton crane and then fastened onto the two trolleys attached to the two out-of-plane beams of the test frame by threaded bolts. The crane was removed and the specimen was pulled inside the machine. Each jack was then adjusted by using the manual control mode. Forty 4-inch diameter pins were installed to connect the yokes and the heads of the jacks as shown in Figure 189. To ensure the stability of the specimen and the uniformity of the applied forces, two rigid links on the top and one rigid link on the east side were used. Three out-of-plane rigid links were also used to avoid the out-of-plane movement.

Figure 189. Fixing the wall panel inside the testing frame of UPT

5.2.2. Control Arrangement

For the pure shear test in this project, oil pressure in each of the eight servo valve manifolds were controlled by a servo valve which, in turn, was monitored by a controller. On each manifold, up to 10 jacks could be connected by flexible hoses and fixed steel tubing. Two of the eight controllers are called programming controllers, Nos. 4 and 10. These controllers can be directly controlled by the programming computer to achieve the expected load levels. The other six controllers can be controlled by the signals from these two programming controllers or by the signals from the in-plane rigid links. Three in-plane rigid links were installed to supply reactions from the jacks and to fix the test panel in space.

Figure 190 and Figure 191 show the servo control system and the cable arrangement of the pure shear test. In the north side, jacks N11 and N15 are actually the rigid links to fix the test panel in the vertical direction. Jack N8 is the rigid link to fix the test panel in the horizontal direction. During the test, all the unbalanced forces would be taken by the rigid links. The load cell readings in the rigid links is sent as input signals to the controllers. For the panel tests in this research, the 20 jacks in the south side and the 17 jacks in the north side was controlled individually to make the strains on both faces of the panel more uniform. Controllers 4 and 10 are designed to be controlled directly by the programming computer. Controllers 1, 2 and 3 were controlled by controller 4. However, the polarity of the signal was switched for controllers 2 and 3 since the compressive load is designed to be applied through the top and bottom jacks for the pure shear test. Furthermore, controller 8 was controlled by the switched output of controller 10. Controller 7 was controlled by the signal from the rigid link N8; and controller 9 was controlled by the average signal from rigid link N11 and N15.

On the south face, the pressure in the jacks at the bottom, to the west, at the top and to the east were supplied by manifolds 3, 4, 2 and 1, respectively. On the north face, the five jacks at the bottom and to the west were supplied by manifolds 8 and 10, respectively. The four jacks N6, N7, N9 and N10 were controlled by manifold 7; and the three jacks N12, N13 and N14 by manifold 9. After yielding, the strain-control mode was used. The average value of four vertical LVDT signals on both the south and north faces of the panels is designed to be sent to controllers 3 and 8, respectively, as vertical strain feedbacks. In a similar way, the average values of four horizontal LVDT signals on both south and north faces were sent as horizontal strain feedbacks to controller 4 and 10, respectively. The aforementioned control method was achieved by arranging the electric cables at the back of the servo-boxes (Figure 191).

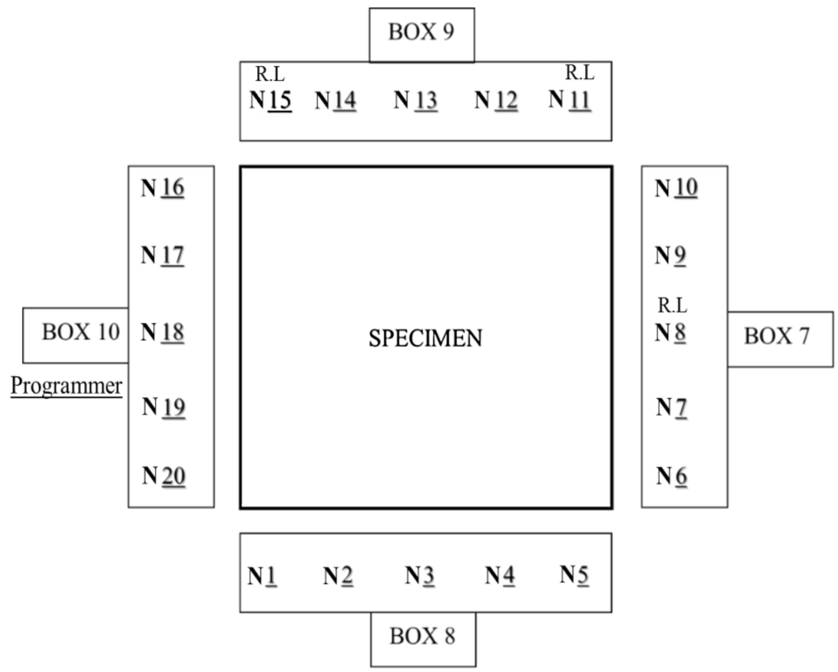

a) North Side

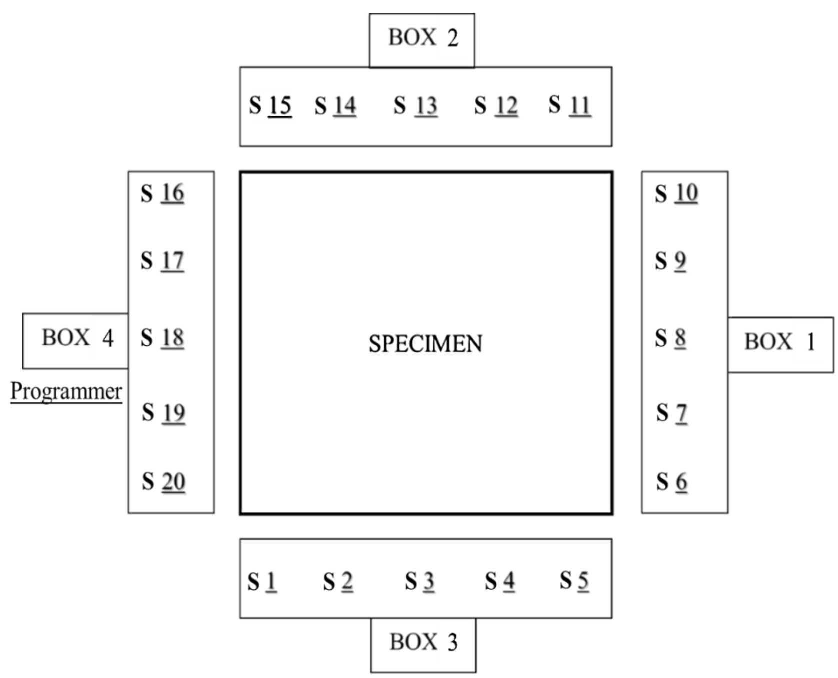

b) South Side

Figure 190. Control arrangement for the shear tests

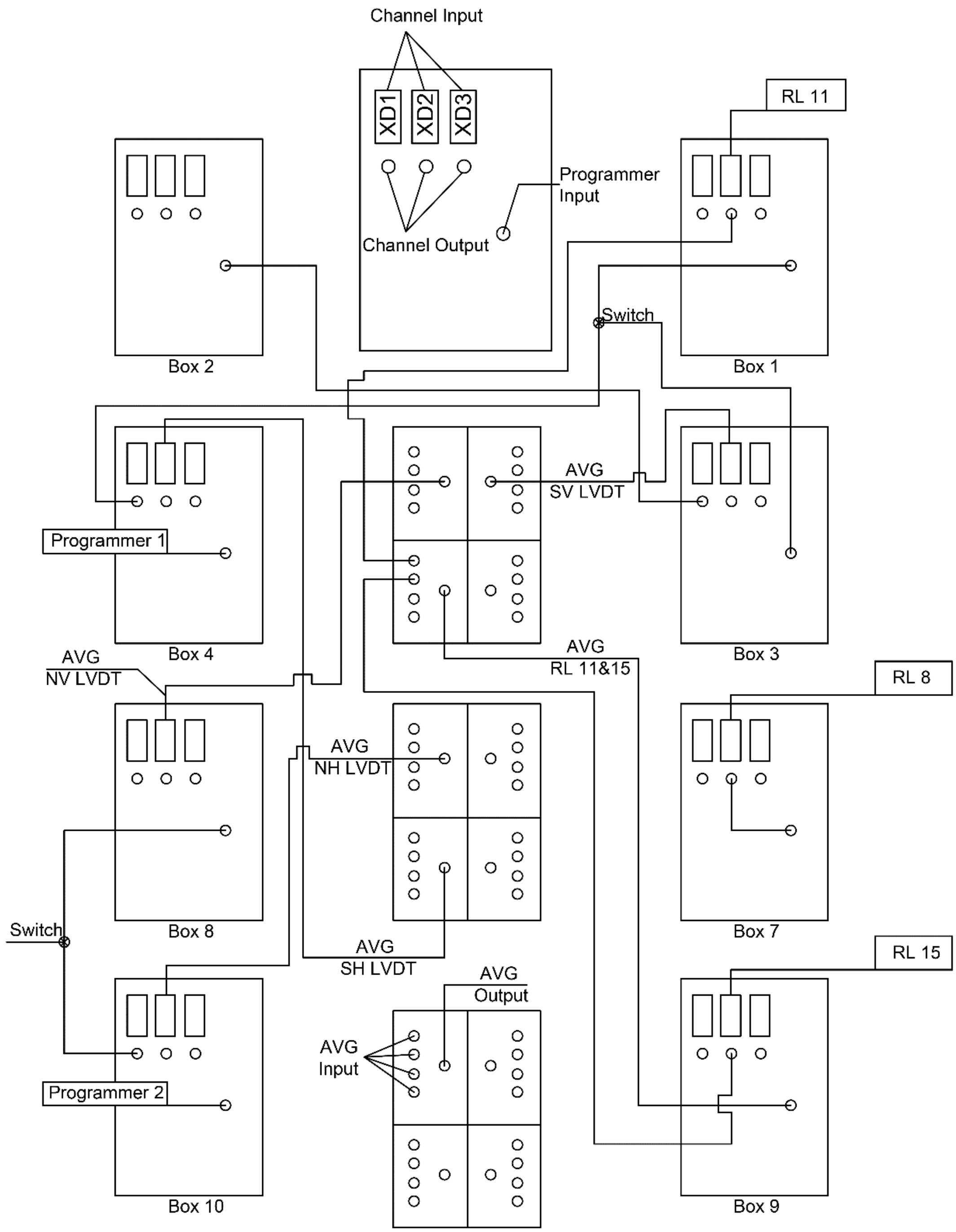

Figure 191. Cable arrangement for the pure shear test

5.2.3. Instrumentation

Strain Measurement

A total of 14 Linear Variable Displacement Transducers (LVDTs) are used to measure the average strain on each side of the test panel. Coupling nuts with 3/8-inch diameter threaded rods were pre-cast in the test panel. This arrangement is used to install the LVDTs on the faces of the test specimen.

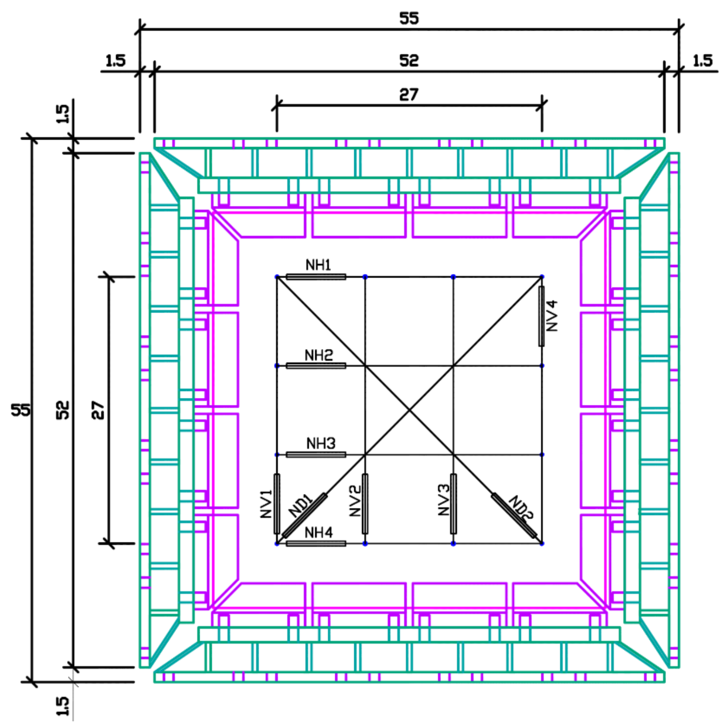

(a) North side

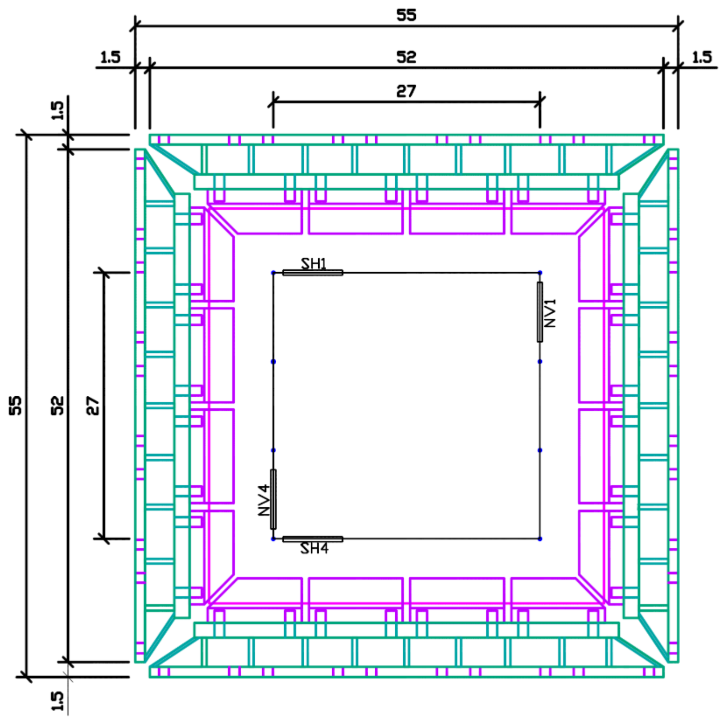

(b) South side

Figure 192. LVDT arrangement for the panel pest

The LVDTs are arranged to measure the strains in four directions: horizontal, vertical and two diagonals as shown in Figure 192 (a) and (b). Six LVDTs with a 1/2-inch range were used to measure the compressive strains in the vertical direction, and six LVDTs with a 2-inch range were used to measure the tensile strains in the horizontal direction. Two LVDTs with a 1-inch range were used for the measurement in the diagonal directions. Four pairs of corner brackets and four pairs of center brackets were specially designed to securely fasten the LVDTs to the test specimen. The brackets were fastened securely to prevent any movement of the measuring points. The LVDTs were then attached to the brackets as shown in Figure 193. The gage length for the horizontal and vertical LVDTs is 27 inches and 38.2 inches for the diagonal LVDTs. The initial values of the LVDTs were zeroed mechanically by adjusting the position of the rods (sensor attached), and was electronically zeroed by the servo-boxes before the start of the test.

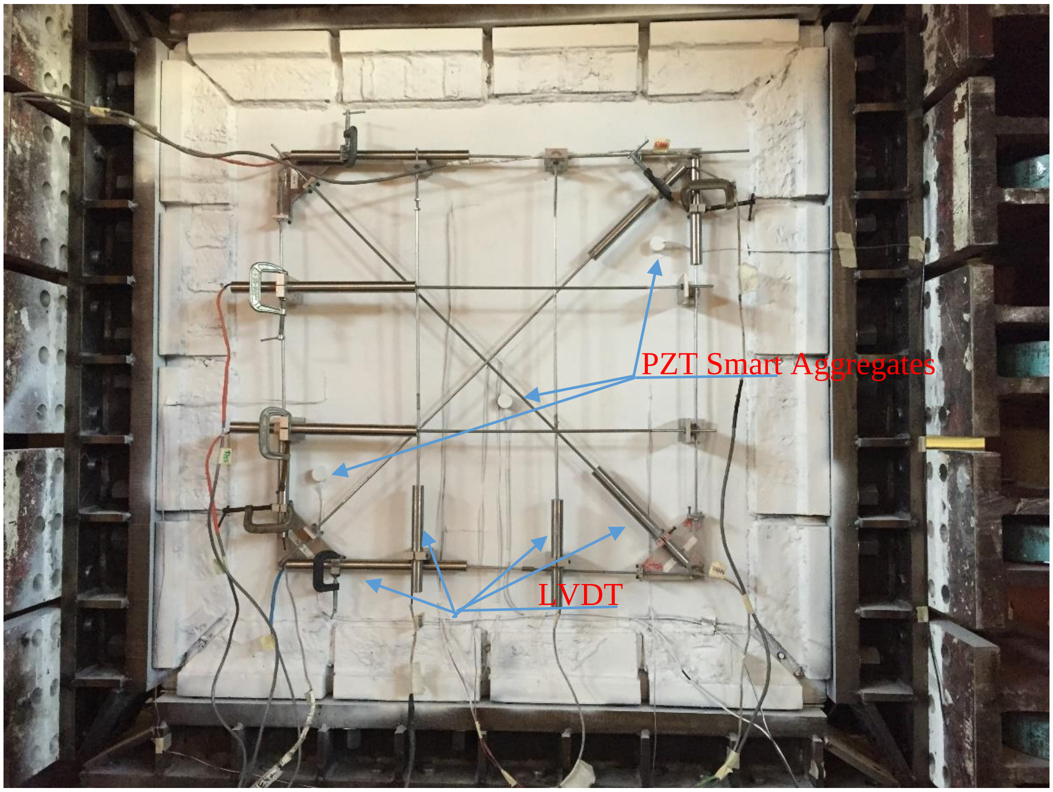

Figure 193. Instrumentation on the north side of specimen

DIC (Digital Image Correlation) system

A Digital Image Correlation (DIC) system was used to obtain the displacement and deformation field on the south side of the specimen. The DIC technique, which is based on non-contact 3D deformation measurement, was used to measure full field 3D deformation of the SC wall panel. The DIC system was also used to measure the local or global buckling that might occur to the steel plates during the application of the loads. The DIC setup for the S-UHPC wall panel is shown in Figure 194.

Figure 194. DIC setup on the south side

Fundamental principle of DIC for 2D measurement

DIC is an optical non–contact 2D and 3D deformation measurement technique. It captures sets of high resolution images before and after deformation of an object to represent different non–deformed and deformed stages. Each stage consists of a set of two or more images of the same object from different prefixed positions[166]. Grayscale digital image is an image in which every single pixel has luminance value, of range 0 (gray) to 1 (no color), regardless of its color. Numerical value of each pixel is a robust tool for image processing and computation. Therefore, captured images from high resolution cameras of the DIC system are digitized to grayscale. A square subset of pixels is chosen from the reference image in the original undeformed configuration. The selected subset is matched in the target image to find its location in the deformed configuration [167-169]. The displacement vector of subset center from reference subset to target subset is determined. The subset displacement can be best evaluated by predefining a correlation function to estimate similarity between the reference subset and target subset. Several cross-correlation and sum-squared difference correlation criteria are available in literature [173-175], among which the zero-normalized cross-correlation and zero-normalized sum of squared differences are extensively used as they are insensitive to linear scale in illumination lighting and provide robust noise-proof correlation [174, 175]. The best match for the subset is carried out by searching the peak position (maxima or minima) of the distribution of correlation coefficients [173, 174, 176-180]. Image speckles should be sampled by at least a 3 by 3 pixel array in order to ensure that subset math accurately [181]. A 2D technique is not accurate enough for out-of-plane measurement and other 3D measurements; therefore the 2D digital image correlation technique and stereo vision technique have been combined together to develop the 3D Digital Image Correlation technique [181-184].

Although the shape of reference subset is transformed to a different shape in the target subset, a set of neighboring points remains common in both subsets. Therefore, shape function or displacement mapping function are used to map the neighbor points of reference subset center in the target subset[185, 186]. First-order shape functions are most commonly used in mapping to depict translation, rotation, strain and their combinations; however more complex deformed targets require higher-order shape functions[187]. The coordinates of the neighbor points of reference subset center in the deformed subset may locate between pixels (i.e. sub-pixels); therefore intensity of the points with sub-pixel locations need to be determined in advance matching reference and deformed subsets. Also, certain sub-pixel interpolation schemes are required. Various sub-pixel interpolation schemes with different orders have been developed, among which higher-order interpolation schemes such as bicubic spline interpolation or biquintic spline interpolation can achieve higher registration accuracy than that of lower-order interpolation schemes[188, 189].

Digital Image Correlation (DIC) Method for Structure Testing

Full field 3D measurement and computation accuracy of specimens using DIC is very sensitive to several factors; therefore the following factors were taken into account to minimize the measurement noise.

- The size and pattern of black speckles on white background of the specimen's surface under measurement have no specific guidelines. Numerous hit and trials of speckle patterns were carried out to minimize noise. Five to ten pixels on every direction of each black speckle may result in minimum measurement noise. The size and distribution of black speckles may also adversely affect the accuracy of measurement. The speckle pattern for the wall panel is shown in Figure 195.

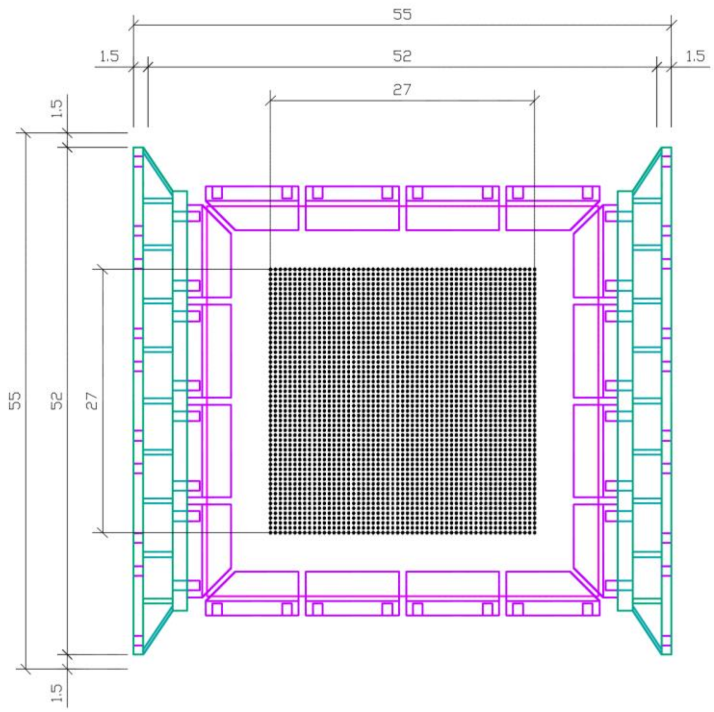

Figure 195. Speckle pattern on the test specimen

- Indoor ambient light and DIC inbuilt light was found to not be sufficient to provide constant adequate illumination; therefore external sources of light was used.
- Based on the speckle pattern, available space for camera setup and desired volume of measurement, different constant focal length lenses of cameras can be adopted; however a 12 megapixel camera of 50 mm focal length has resulted in better images.
- Calibration of a DIC system on the desired volume of measurement was carried out using a standard calibration panel or calibration cross.

DIC is not extremely sensitive to vibration; hence a vibration isolation table is not necessary. However, both the DIC camera and specimen should be stable. DIC cameras need to be mounted on a firm and stable stand and should be intact throughout the test. Large vibration and any further adjustment on the cameras after calibration result in higher noise and unreliable measurements.

Although DIC system is able to capture full filed 3D measurement (displacement) of target object, DIC algorithm is not able to compute cracking, spalling, and localization.

For the DIC setup, uniform random black speckles were sprayed on the white background of a DIC target wall panel surface. A pair of non–perpendicular 12-megapixel charge–coupled device (CCD) cameras with 50 mm was mounted on the cross–bar of a tripod in order to capture high resolution images. The distance between cameras, object distance from cameras and angle between cameras was adjusted based on target size and available space using the DIC system manual. An external source of fluorescent lights were used to maintain constant optimum illumination of the surface.

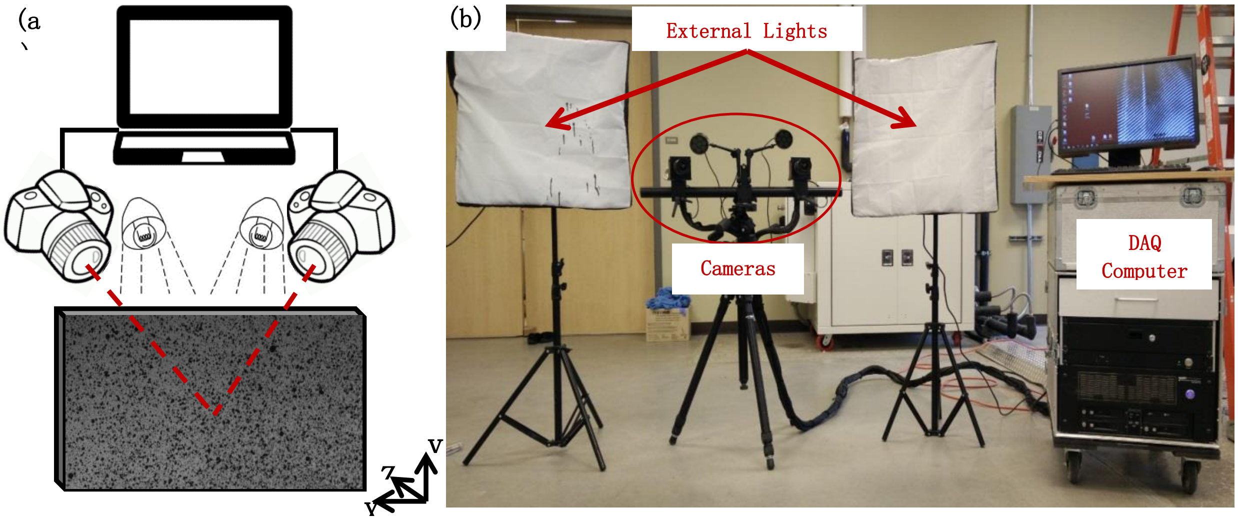

Figure 196. DIC system setup, (a) Schematic illustration, (b) Pictorial illustration

Figure 196(a) shows the schematic setup illustration of digital image correlation system (DIC). White background with black speckled target should be constantly illuminated by white fluorescent light sources. A set of high resolution cameras mounted on specific distance and angle will capture a set of high resolution images. The DIC setup is calibrated by using a very precise calibration panel or calibration cross, and calibration data is captured by the computer. All high resolution images are collected by the computer having a high computing capacity. Images are further computed to obtain 3D deformation of the target using the captured calibration. A set of DIC system setups with external lights, DIC inbuilt lights, pairs of cameras and computer are shown in Figure 196(b).

PZT Smart aggregates

Lead Zirconate Titanate (PZT) smart aggregates were attached to both faces of the test specimen to monitor the bond between the steel plate and concrete/UHPC.

Three smart aggregates were attached on each side of the steel plates. One smart aggregate was utilized as the actuator generating repeated swept sine wave. The other actuators on the other face of the steel plate were utilized as sensors to detect the swept sine wave.

In the initial condition when there is no bond slip, the received signal $\boldsymbol{S_0}$ will be used as the baseline signal representing the perfect condition of the wall panel. The detection principle of PZT smart aggregates is explained in section 4.3.2. The arrangement of smart aggregates is shown in Figure 193.

Strain gages

Strain gages were applied to the steel plates to monitor the local strains along the direction of the applied load. The arrangement of strain gages on the test specimen is shown in Figure 197.

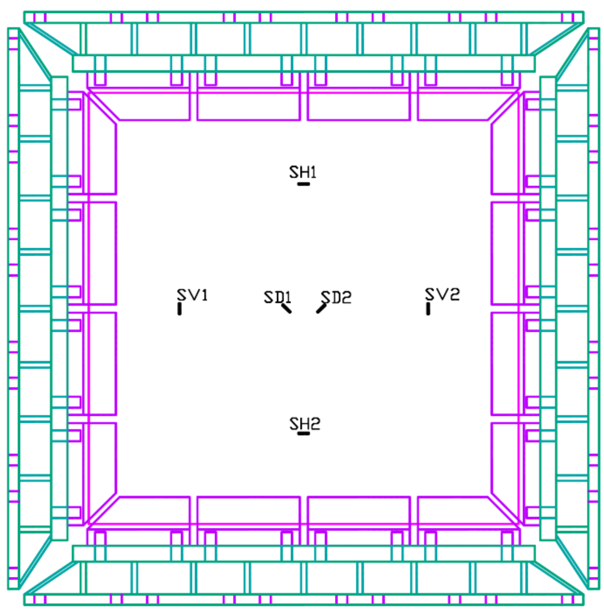

(a) North side

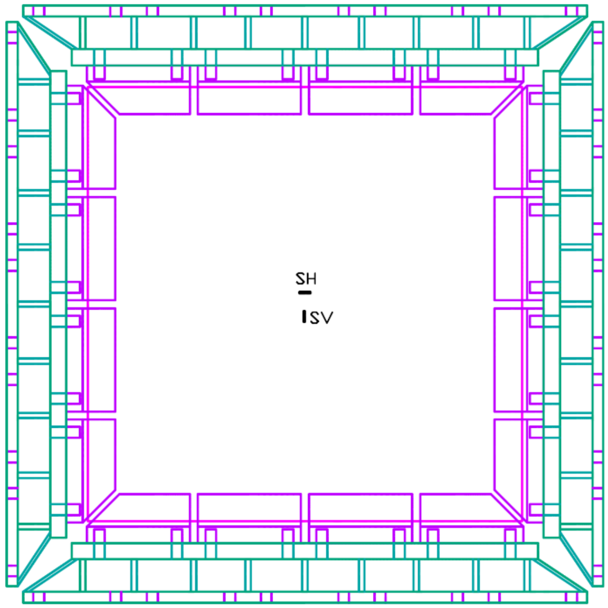

(b) South side

Figure 197. Arrangement of strain gages

5.3. Experimental Results

A proportional loading path was used to simulate pure shear condition in the specimen. In this type of loading path, the tensile and compressive stresses are applied simultaneously. The horizontal tensile stresses and vertical compressive stresses are applied with equal magnitude $\sigma_1 = -\sigma_2$ to simulate a pure shear state in the 45-degree direction as shown in Figure 198.

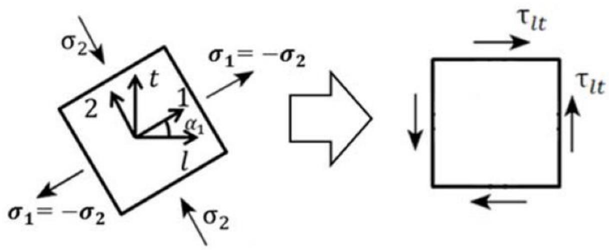

Figure 198. Proportional loading in 1-2 direction

The stress transformation equations of the element in terms of principle applied stresses are given as

$$\sigma_l = \sigma_2 \cos^2 \alpha_1 + \sigma_1 \sin^2 \alpha_1, \tag{46}$$

$$\sigma_t = \sigma_2 \sin^2 \alpha_1 + \sigma_1 \cos^2 \alpha_1, \tag{47}$$

$$\tau_{lt} = (-\sigma_2 + \sigma_1) \sin \alpha_1 \cos \alpha_1 . \tag{48}$$

Substituting α = 45°, the following could be found out

$\sigma_1 = \sigma_1$ and $\sigma_2 = \sigma_2$

Shear stress, $\tau_{lt} = \dfrac{\sigma_1 - \sigma_2}{2}$

The strain is measured along the horizontal, vertical and diagonal directions using LVDTs. The setup and arrangement of LVDTs have been reported in the previous quarterly report. In total there are 14 LVDTs. ε_1, the measured horizontal principal strain, is the average value of four horizontal LVDTs on the north side and two horizontal LVDTs on the south side. Furthermore, the vertical principle strain ε_2, is the average value of four vertical LVDTs on the north side and two vertical LVDTs on the south side. The two diagonal strains are the average values of two diagonal LVDTs on the north side of the panel.

The strain transformation equations in terms of principal strain are given as

$$\varepsilon_l = \varepsilon_2 \cos^2 \alpha_1 + \varepsilon_1 \sin^2 \alpha_1 + \frac{\gamma_{12}}{2} 2 \sin \alpha_1 \cos \alpha_1, \tag{49}$$

$$\varepsilon_t = \varepsilon_2 \sin^2 \alpha_1 + \varepsilon_1 \cos^2 \alpha_1 - \frac{\gamma_{12}}{2} 2 \sin \alpha_1 \cos \alpha_1, \tag{50}$$

$$\frac{\gamma_{lt}}{2} = (-\varepsilon_2 + \varepsilon_1) \sin \alpha_1 \cos \alpha_1 + \frac{\gamma_{12}}{2} \left(\cos^2 \alpha_1 - \sin^2 \alpha_1\right), \tag{51}$$

Substituting α = 45°, the following could be found out

$\varepsilon_1 = \varepsilon_1$ and $\varepsilon_1 = \varepsilon_2$

Shear strain, $\gamma_{lt} = \varepsilon_1 - \varepsilon_2$

From the test results, the shear stress and shear strain were calculated based on the stress and strain transformation equations. The typical shear stress strain for RC panels exhibits five stages as shown in Figure 199: (1) The elastic stage up to concrete cracking, (2) the post-cracking elastic stage up to the first yielding of steel rebars (*l* or *t* direction), (3) the post-cracking stage up to the second yielding of steel rebars, (4) the plastic stage after yielding of transversal and longitudinal rebars up to peak and (5) the post peak deformation softening stage after initiation of concrete crushing up to failure of the panel [140].

However, for the SC panel, the shear stress-strain curve did not show a distinct point for the concrete cracking stage. Furthermore, since the amount of reinforcement is equal in *l and t* directions ($\rho_l = \rho_t$), the steel-plate in both directions will yield simultaneously. The shear stress-strain curve for the specimens tested in this study will be presented in the subsequent subsection.

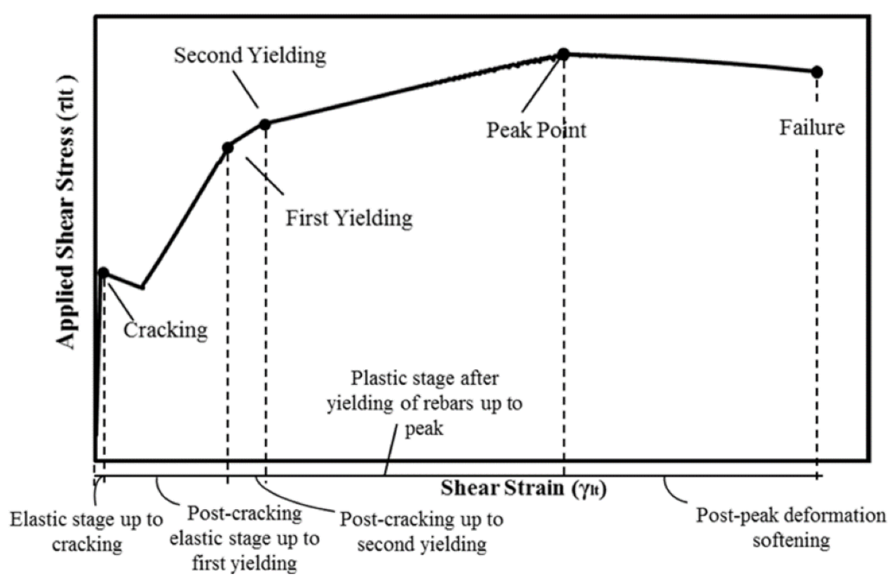

Figure 199. Typical Shear Stress-Strain curve of RC panels [140]

5.3.1. Specimen SC-45

Specimen SC-45 was cast with self-consolidating concrete. The slump flow test was performed in accordance with ASTM 1611 [26]. The spread value was measured to be 31 inches which satisfies the requirements of ACI 237 [23].

Furthermore, to simulate the real nuclear power plant structure, which is subjected to both in-plane and out-of-plane shear, a minimum amount of cross ties was provided in the testing of the SC wall panels under in-plane shear. The minimum amount of cross ties for SC was previously found out to be 45% more than the requirements of ACI.

The specimen preparation is the same as reported in the previous quarterly report. However, the steel insert design has been changed for this specimen. As seen in Figure 200, the specimen is connected to the steel inserts through A325 high-strength bolts.

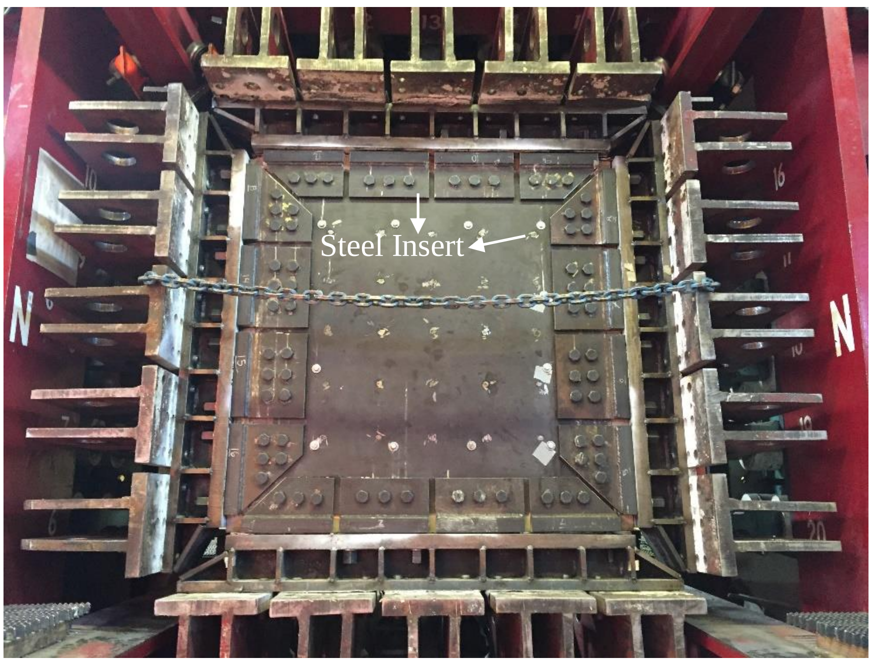

Figure 200. Placement of specimen inside The Universal Panel Tester

After setting up the specimen inside the Universal Panel Tester, instrumentation such as LVDTs, strain gages, smart aggregates and DIC were installed. The details of instrumentation have been presented in the previous quarterly report.

The south side of the specimen is shown in Figure 201. A total number of four LVDTs, two in the horizontal direction and two in the vertical direction, were installed using triangular brackets. Furthermore, strain gages and smart aggregates were also installed to measure local strain and debonding, respectively. A speckle pattern was painted on the surface of the specimen for measuring deformations in 3D using the DIC system.

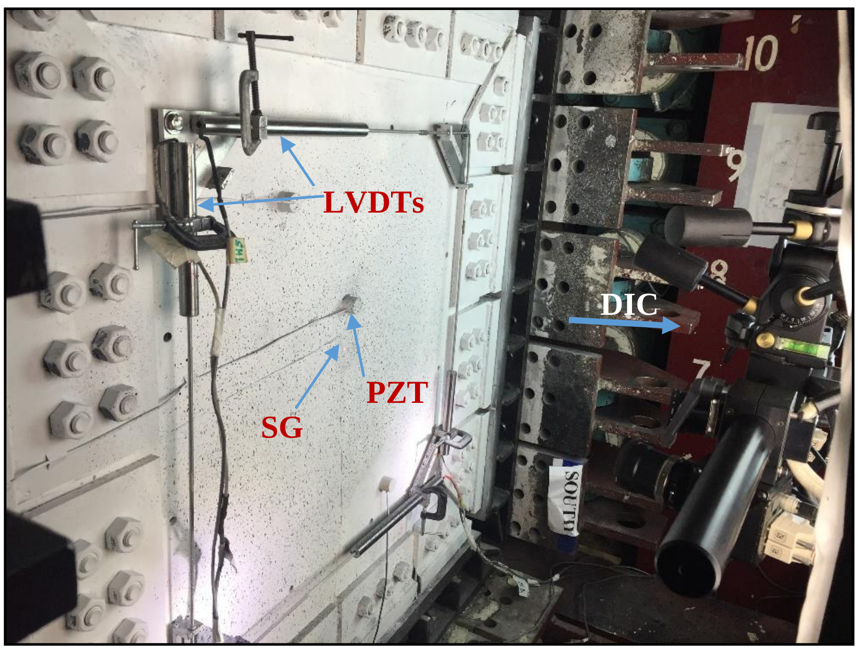

Figure 201. South side of specimen SC-45

Similarly, the north side of the specimen is shown in Figure 202. Four LVDTs are installed in the horizontal direction, four in the vertical direction and two in the diagonal direction. In addition, smart aggregates (PZT) and strain gages are installed for measuring debonding and local strain, respectively.

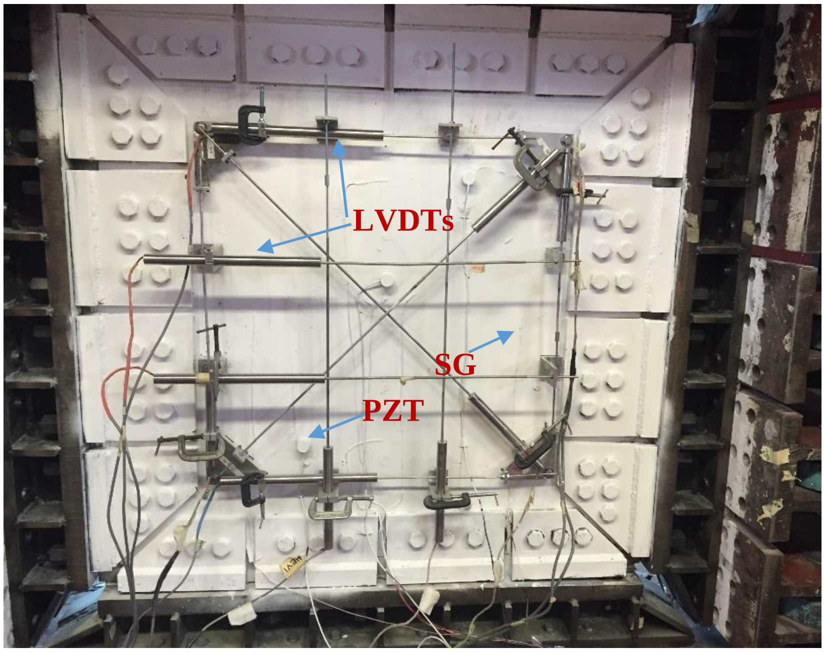

Figure 202. North side of specimen SC-45

The application of loads was controlled by a hydraulic servo-control system. The details of the system and the control arrangements have been presented in the previous quarterly report. The experiment lasted about nine hours. The initial phase of the loading was controlled by a load-control procedure. The tensile and compressive stresses were applied proportionally. The control procedure was switched to strain control before the yielding of steel plates. The data acquisition system recorded the load cell outputs and LVDT measurements at intervals of 10 seconds.

The shear stress-strain curve for specimen SC-45 is shown in Figure 203. As observed from the curve, the peak stress and strain reached 7.26 ksi and 0.634%, respectively. Before yielding of the steel plates, the behavior of the panel is elastic with a constant slope. After yielding of the steel plates, the shear strain increased rapidly with smaller a increase in shear stress.

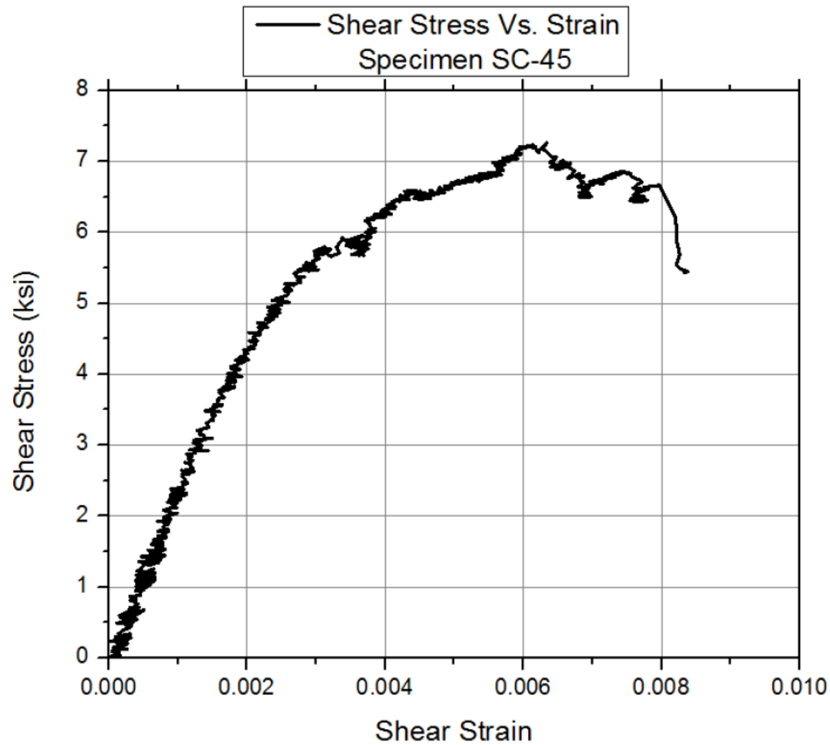

Figure 203. Shear stress-strain curve for SC-45

The compressive stress-strain and tensile stress-strain curves are also plotted and shown in Figure 204 and Figure 205. As seen from the curves, the peak tensile stress and strain reached 7.123 ksi and 0.370%, respectively. The compressive stress for the wall panel reached a peak of 7.44 ksi which corresponds to compressive strain of 0.252%.

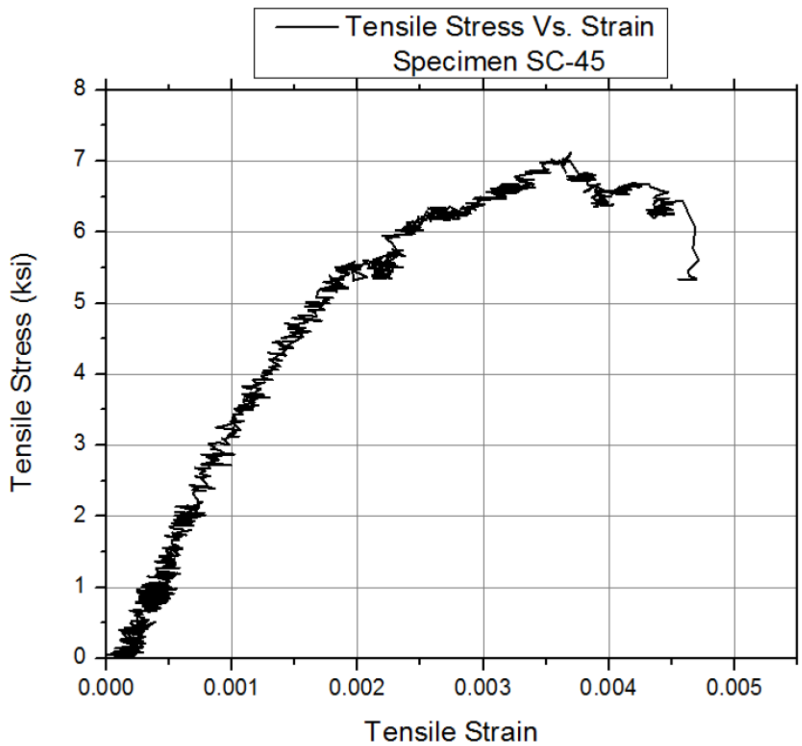

Figure 204. Tensile stress-strain curve for SC-45

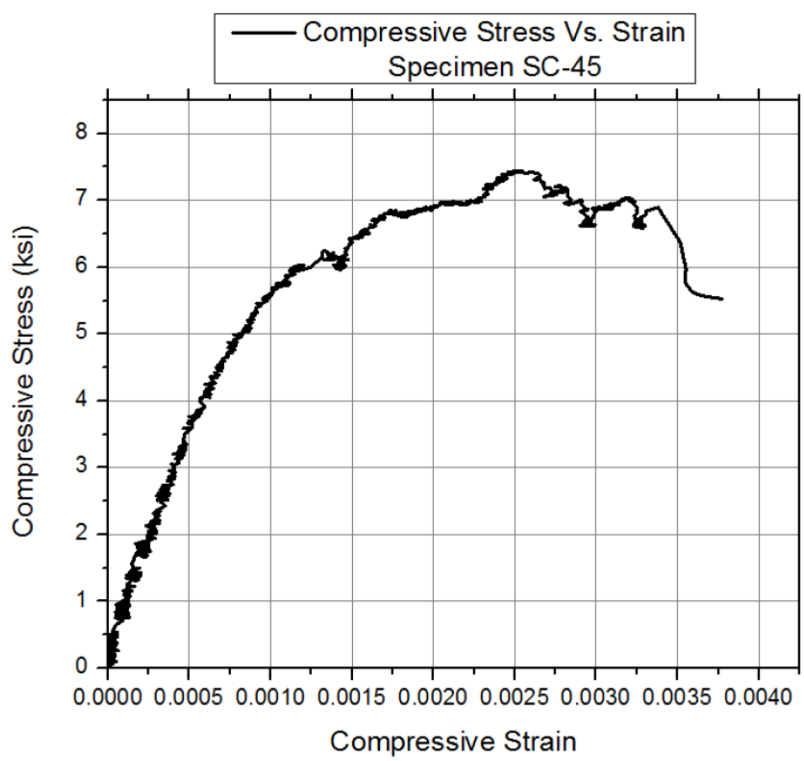

Figure 205. Compressive stress-strain curve for SC-45

Figure 206 shows the arrangement of smart aggregates on the wall panel. The smart aggregates on the south side of the specimen were used as actuator and the ones on the north side were used as the sensor.

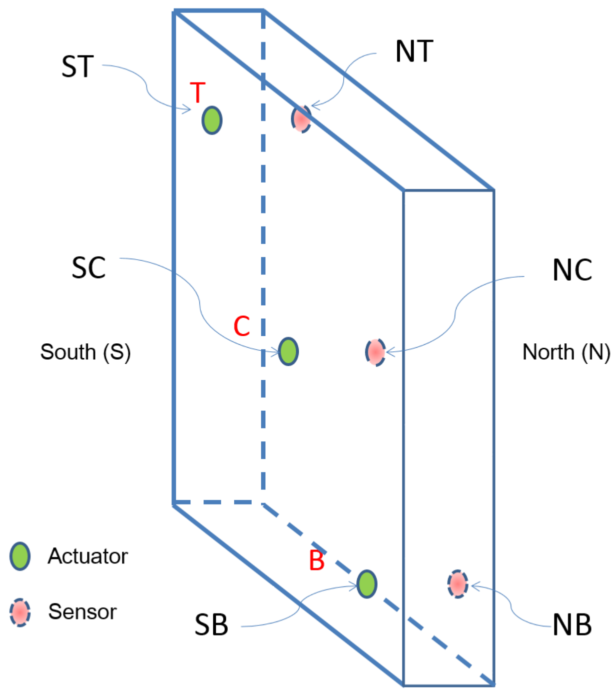

Figure 206. Arrangement of smart aggregates on the wall panel

Several readings were taken during the course of the experiment. From the readings, the Damage Index (DI) was calculated. Damage index relates the healthy state of the wall panel to its damaged state. A damage index of "0" indicates a perfect bond between the steel-plate and concrete, and a damage index of "1" indicates complete debonding between the steel-plate and concrete.

Figure 207 shows the damage index (DI) of the sensor installed on the north center (NC) receiving wave signal from the south center (SC) actuator. It can be observed that as the load increases on the wall panel, bond-slip between the steel-plates and concrete becomes more prominent. However, from the smart aggregates results, debonding doesn't occur at the center of the specimen.

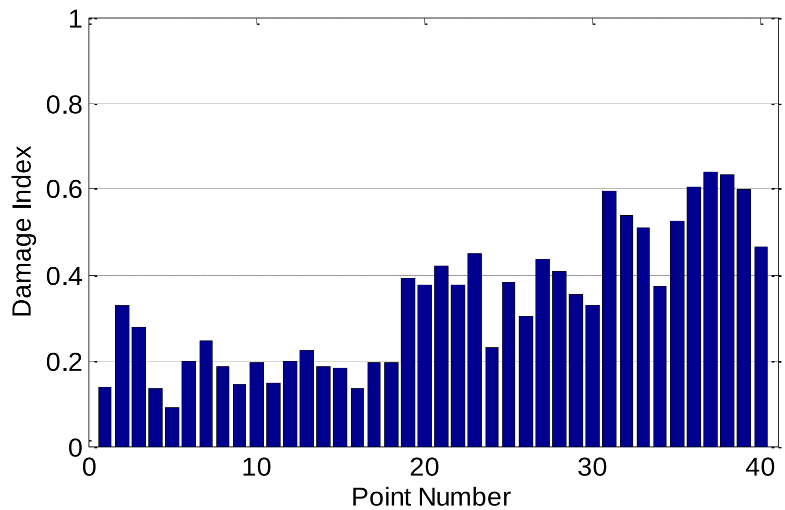

Figure 207. Damage index of sensor installed on north center (NC) receiving the wave from south center (SC)

The damage index from other sensors indicate that the steel-plates debonded completely from the concrete at other locations. For example, as shown in Figure 208, the damage index of sensor installed on the north center (NC) receiving wave from the south bottom (SB) actuator indicates that the steel-plate and concrete have debonded.

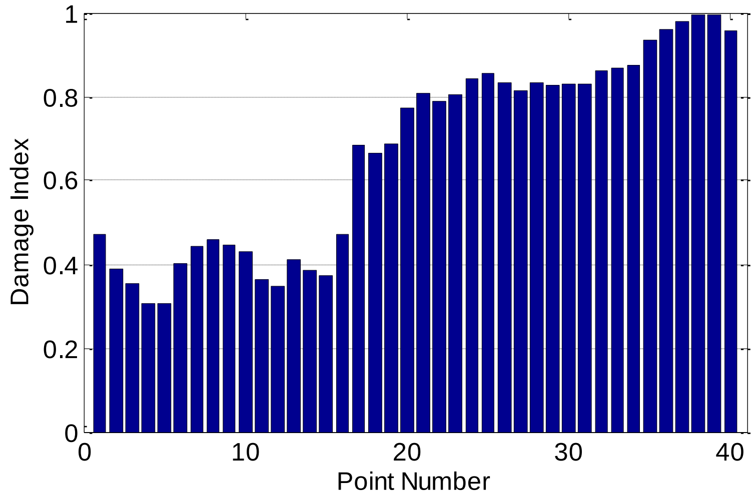

Figure 208. Damage index of sensor installed on north center (NC) receiving wave signal from south bottom (SB)

Furthermore, as shown in Figure 209, the damage index of the sensor installed on the north bottom (NB) receiving wave signal from the south bottom (SB) actuator also indicates that the steel-plates and concrete have debonded.

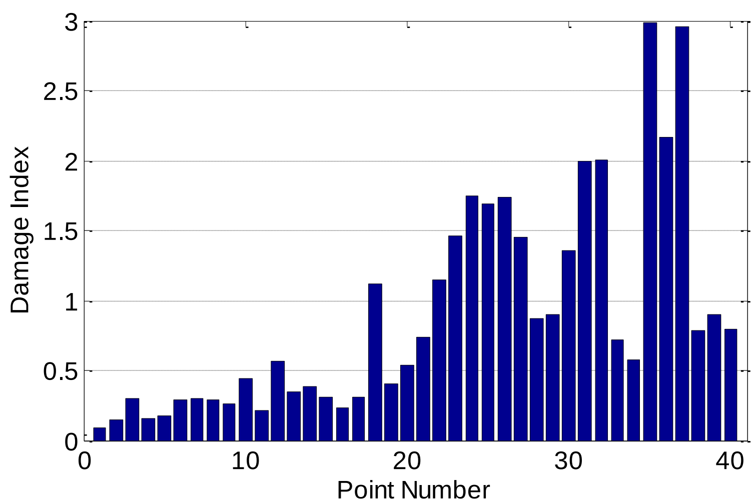

Figure 209. Damage index of sensor installed on north bottom (NB) receiving wave signal from south bottom (SB)

The Digital Image Correlation (DIC) system was used to measure the out-of-plane deformations in the wall panel. As illustrated in Figure 210, the deformations were measured at nine points on the surface of the specimen. By the end of the test, the deformations had reached 17mm (0.67 in.).

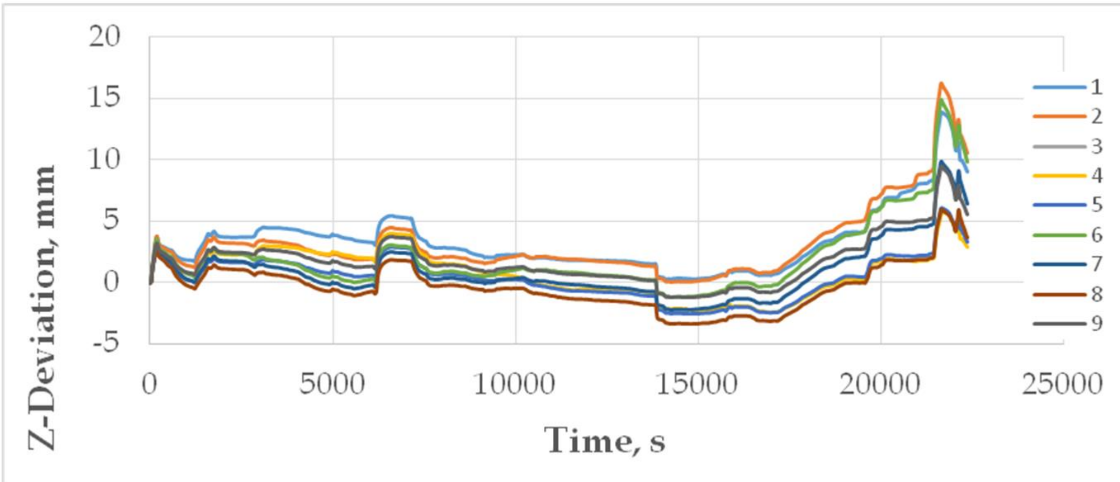

Figure 210. Out-of-plane deformations in the specimen

5.3.2. Specimen S-UHPC-10

Specimen S-UHPC-10 was cast with Ultra-High Performance Concrete (UHPC) developed in this project. The compressive strength of concrete after 28 days of water curing was found out to be 22.237 ksi. Furthermore, to simulate the real nuclear power plant structure, which is subjected to both in-plane and out-of-plane shear, a minimum amount of cross ties was provided in the testing of S-UHPC wall panels under in-plane shear. The minimum amount of cross ties for S-UHPC was previously found to be 10% more than the requirements of the ACI code.

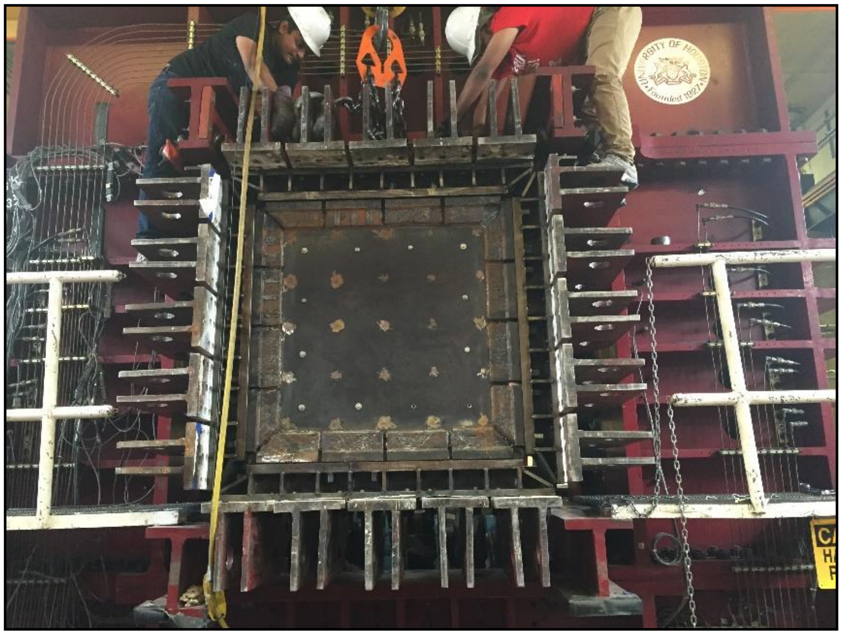

Figure 211. Placement of specimen S-UHPC-10 inside The Universal Panel Tester

Figure 211 shows the placement of specimen S-UHPC-10 inside the Universal Panel Tester. It can be observed that the steel inserts are welded to the specimen as opposed to being bolted in the case of specimen SC-45.

After setting up the specimen inside the Universal Panel Tester, instrumentation such as LVDTs, strain gages, smart aggregates and DIC were installed. The south side of the specimen is shown in Figure 212. A total number of four LVDTs, two in the horizontal direction and two in the vertical direction, were installed using triangular brackets. Furthermore, strain gages and smart aggregates were also installed to measure local strain and debonding, respectively. A speckle pattern was painted on the surface of the specimen for measuring deformations in 3D using the DIC system.

Figure 212. South side of specimen S-UHPC-10

The north side of the specimen is shown in Figure 213. Four LVDTs were installed in the horizontal direction, four in the vertical direction and two in the diagonal direction. In addition, smart aggregates (PZT) and strain gages were installed for measuring debonding and local strain, respectively.

The first phase of the experiment was controlled by a load-control procedure. The tensile and compressive stresses were applied proportionally. Unfortunately, when the control procedure was switched from load-control to strain-control, the jacks applied a non-uniform load which caused the specimen to fail locally. Therefore, the entire stress-strain curve could not be obtained.

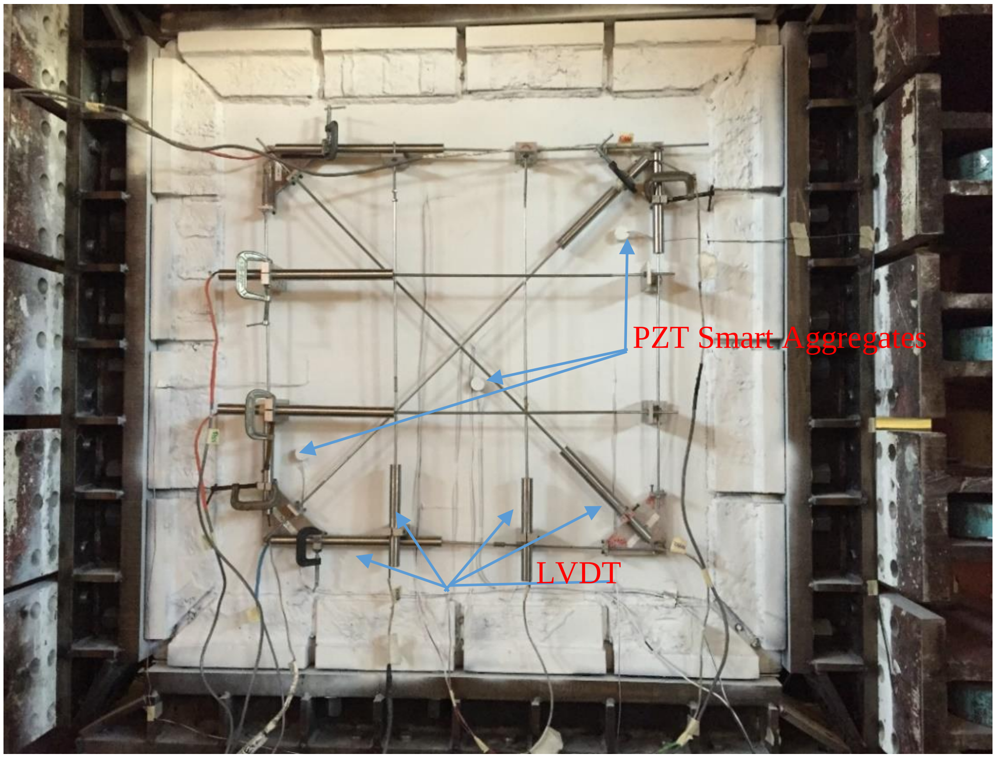

Figure 213. North side of specimen S-UHPC-10

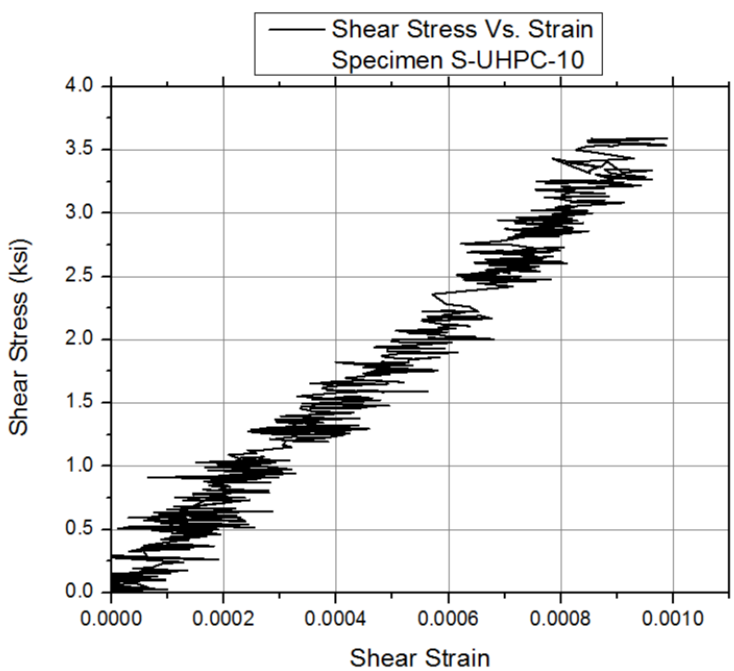

Figure 214. Shear stress-strain curve for S-UHPC-10

The shear stress-strain curve for S-UHPC-10 is shown in Figure 214. It can be seen from the curve that due to local failure only the elastic region of the shear stress-strain curve could be captured from the test. In addition, the tensile stress-strain curve and the compressive stress-strain curve are also plotted in Figure 215 and Figure 216.

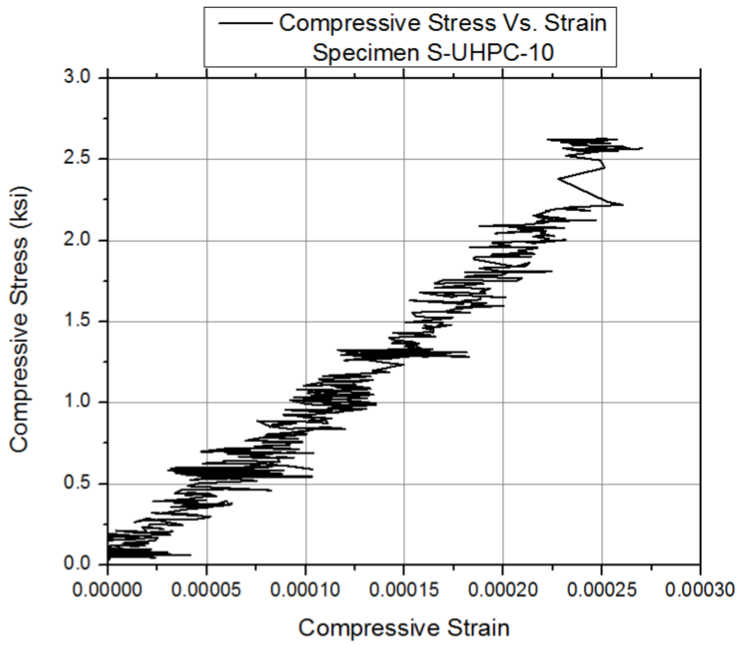

Figure 215. Compressive Stress Vs. Strain

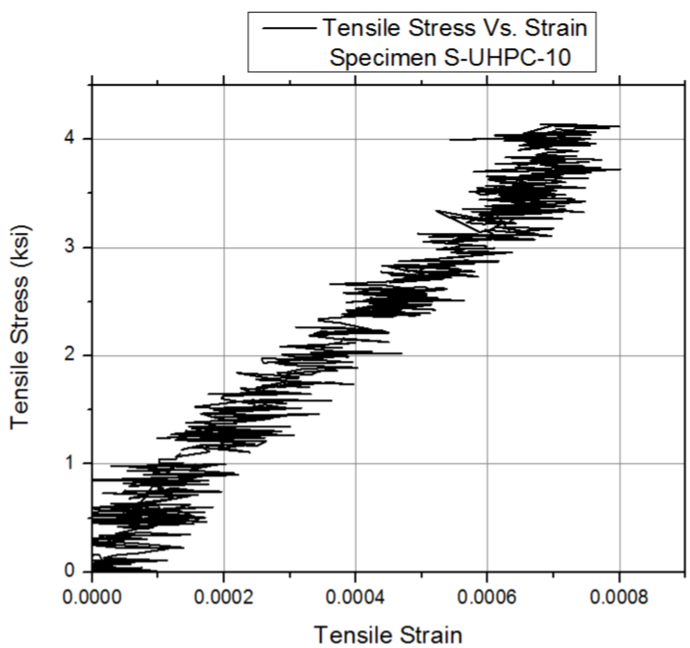

Figure 216. Tensile Stress Vs. Strain

5.4. Finite element simulation of SC/S-UHPC wall panels

In modeling SCS (Steel-plate Concrete Structures), the "smeared-crack" concept used in the reinforced concrete elements can be adopted. This concept allows the internally cracked SC composite to be treated as a simple, continuous material rather than a complicated, discontinuous composite. The salient advantage of this simplification is that mechanics-based analysis can be applied to predict the behavior of SC structures regardless of cracking. To implement this simplification, the material constitutive models must be based on the smeared (averaged) stress and strain relationship of the internally cracked SC elements. Therefore, the Cyclic Softened Membrane Model (CSMM), which was developed for reinforced concrete structures, can be extended to include the constitutive models of SC.

5.4.1. Fundamentals of 2D CSMM for Steel-plate Concrete

Coordinate systems

As shown in Figure 217, the Steel-plate concrete (SC) membrane element considered in this model consists of two outer layers of steel plate and an inner concrete layer. The steel plates are connected with the concrete by steel cross ties.

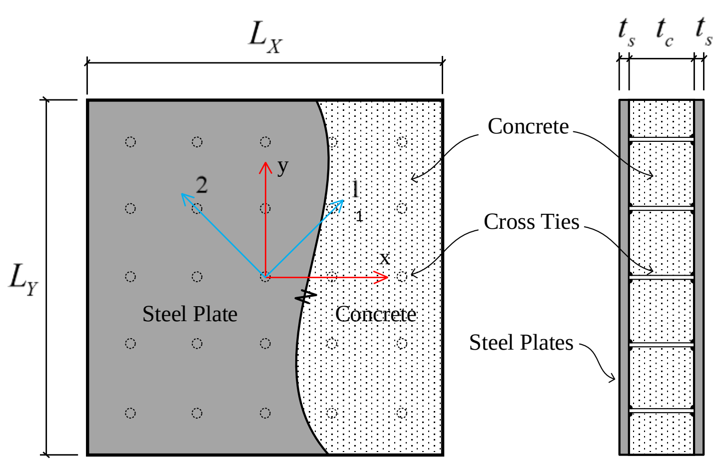

Figure 217. Steel-plate Concrete Element

Three Cartesian coordinates, x-y, 1-2 and $1'$-$2'$, are defined in the steel plane concrete elements, as shown in Figure 218. Coordinate x-y defines the local coordinate of the element. Coordinate 1-2 represents the principal stress directions of the applied stresses that have an angle θ_1 with respect to the x- axis. Coordinate $1'$-$2'$ represents the principal stress directions of the steel plates that have an angle θ_s with respect to the x- axis.

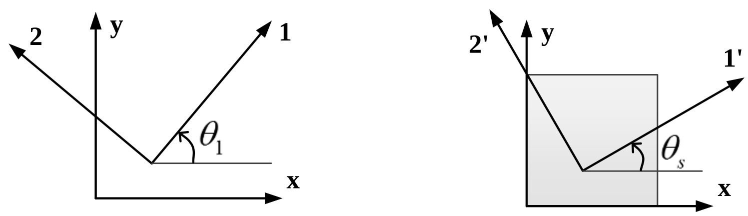

(a) Principal Stresses Direction of the Applied Stresses in Local Coordinate

(b) Principal Stresses Direction of the Steel Plates in Local Coordinate

Figure 218. Coordinate Systems for Steel Plate Concrete Elements

Equilibrium and compatibility equations

The stress states of the SC element are shown in Figure 219. The stresses of the element are assumed to be a combination of two components: concrete and steel plates.

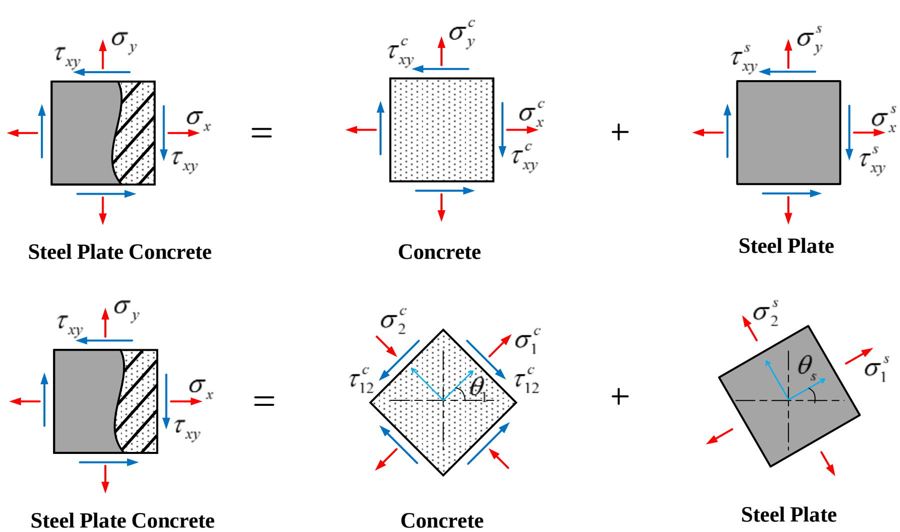

Figure 219. In-plane stress states in steel plate concrete element

The equilibrium equations that relate to the applied stresses of the element (σ_x, σ_y and τ_{xy}), to the internal principal stresses of concrete (σ_1^c, σ_2^c and τ_{12}^c), and the internal principal stresses of steel plate (σ_1^s, σ_2^s) are expressed as

$$\begin{Bmatrix} \sigma_x \\ \sigma_x \\ \tau_{xy} \end{Bmatrix} = \left[T\left(-\theta_1\right)\right] \begin{Bmatrix} \sigma_1^c \\ \sigma_2^c \\ \tau_{12}^c \end{Bmatrix} + \left[T\left(-\theta_s\right)\right] \begin{Bmatrix} \sigma_1^s \\ \sigma_2^s \\ 0 \end{Bmatrix} \tag{52}$$

where, $[T(-\theta_1)]$, $[T(-\theta_s)]$ is the transformation matrices from the 1-2 coordinate to the 1'-2' coordinate.

The compatibility equations, which represent the relationships between biaxial strains of other coordinates and the local biaxial concrete strains in the x-y coordinate (ε_x, ε_y and $0.5\gamma_{xy}$) are defined by the following equations:

$$\begin{Bmatrix} \varepsilon_1 \\ \varepsilon_2 \\ \frac{1}{2}\gamma_{12} \end{Bmatrix} = \left[T\left(\theta_1\right)\right] \begin{Bmatrix} \varepsilon_x \\ \varepsilon_y \\ \frac{1}{2}\gamma_{xy} \end{Bmatrix} \tag{53}$$

$$\begin{Bmatrix} \varepsilon_{1'} \\ \varepsilon_{2'} \\ 0 \end{Bmatrix} = \left[T\left(\theta_s\right)\right] \begin{Bmatrix} \varepsilon_x \\ \varepsilon_y \\ \frac{1}{2}\gamma_{xy} \end{Bmatrix} \tag{54}$$

Biaxial strains vs. uniaxial strains

In order to solve problems in 2-D, the biaxial strains need to be converted to uniaxial strains so that the unixial constitutive material models tested in laboratory can be used. For cracked concrete, the uniaxial strains are related to the biaxial strains by the Hsu/Zhu ratio matrix:

$$\begin{Bmatrix} \bar{\varepsilon}_1 \\ \bar{\varepsilon}_2 \\ 0.5\gamma_{12} \end{Bmatrix} = [V_c] \begin{Bmatrix} \varepsilon_1 \\ \varepsilon_2 \\ 0.5\gamma_{12} \end{Bmatrix}, \tag{55}$$

where

$$[V_c] = \begin{bmatrix} (1-v_{12}v_{21})^{-1} & v_{12}(1-v_{12}v_{21})^{-1} & 0 \\ v_{21}(1-v_{12}v_{21})^{-1} & (1-v_{12}v_{21})^{-1} & 0 \\ 0 & 0 & 1 \end{bmatrix} \tag{56}$$

In Equation 55 v_{12} is the ratio of the resulting tensile strain increment in the principal $1-$direction to the source compressive strain increment in the principal $2-$direction, and v_{21} is the ratio of the resulting compressive strain increment in the principal $2-$direction to the source tensile strain increment in the principal $1-$direction. Since there is no experimental data for the SC element, the values for v_{12} and v_{21} are adopted from the reinforced concrete element [155].

For steel plates the uniaxial strains are related to the biaxial strains by the Poisson's ratio matrix:

$$\begin{Bmatrix} \bar{\varepsilon}_{1'} \\ \bar{\varepsilon}_{2'} \\ 0 \end{Bmatrix} = [V_s] \begin{Bmatrix} \varepsilon_{1'} \\ \varepsilon_{2'} \\ 0 \end{Bmatrix}, \tag{57}$$

where

$$[V_s]=\begin{bmatrix}(1-v^2)^{-1} & v(1-v^2)^{-1} & 0\\ v(1-v^2)^{-1} & (1-v^2)^{-1} & 0\\ 0 & 0 & 1\end{bmatrix} \tag{58}$$

Constitutive Model of Concrete

Concrete in Compression and Tension

The cyclic uniaxial constitutive relationships of concrete with embedded reinforcement were proposed by Mansour and Hsu[147], as shown in Figure 220. The characteristics of these concrete constitutive laws include: (1) the softening effect on the concrete in compression due to the tensile strain in the perpendicular direction; (2) the softening effect on the concrete in compression under reversed cyclic loading and (3) the opening and closing of cracks, which are taken into account in the unloading and reloading stages. The equations of this model are summarized as follows

(Stage C1) $$\sigma^c = D\zeta f_c^{'}\left[2\left(\frac{\bar{\varepsilon}}{\zeta\varepsilon_0}\right)-\left(\frac{\bar{\varepsilon}}{\zeta\varepsilon_0}\right)^2\right],\quad 0\le|\bar{\varepsilon}|\le|\zeta\varepsilon_0|, \tag{59}$$

(Stage C2) $$\sigma^c = D\zeta f_c^{'}\left[1-\left(\frac{\bar{\varepsilon}/\varepsilon_0-1}{4/\zeta-1}\right)^2\right],\qquad |\bar{\varepsilon}|>|\zeta\varepsilon_0|, \tag{60}$$

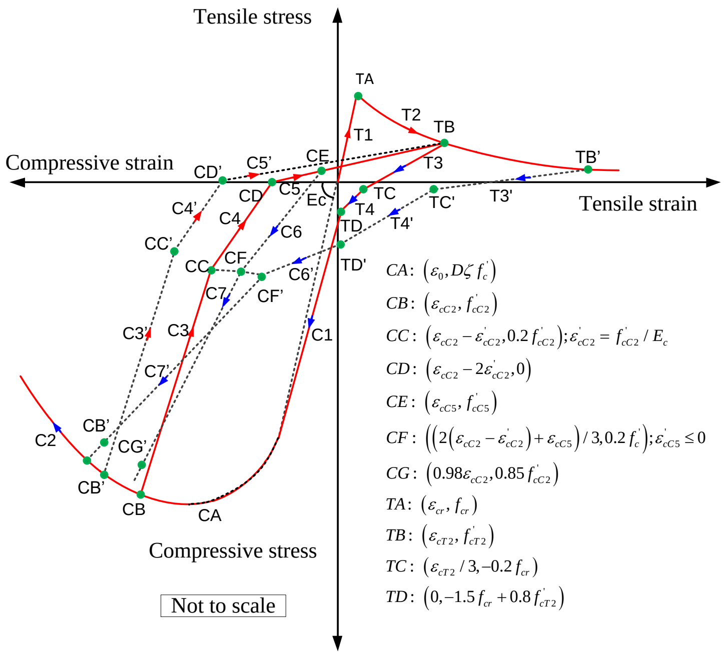

Figure 220. Cyclic smeared stress-strain curve of concrete

where,

$$\zeta=\left(\frac{5.8}{\sqrt{f_c^{'}(\mathrm{MPa})}}\right)\left(\frac{1}{\sqrt{1+400\bar{\varepsilon}_T}}\right)\left(1-\frac{|\beta|}{24^o}\right)\le 0.9, \tag{61}$$

$$D=1-0.4\frac{\varepsilon_c^{'}}{\varepsilon_0}\le 1.0, \tag{62}$$

$$\beta=\frac{1}{2}\tan^{-1}\left[\frac{\gamma_{12}}{\varepsilon_2-\varepsilon_1}\right], \tag{63}$$

(Stage T1) $\quad \sigma^c=E_c\bar{\varepsilon}\ ,\qquad$ if $\quad 0\le\bar{\varepsilon}<\varepsilon_{cr}\ ,$ (64)

(Stage T2) $\quad \sigma^c=f_{cr}\left(\dfrac{\varepsilon_{cr}}{\bar{\varepsilon}}\right)^{0.4}$, if $\quad \bar{\varepsilon}>\varepsilon_{cr}$, (65)

(Unloading and Reloading Stages) $\ \sigma^c=\sigma_i^c+E_{cc}\left(\bar{\varepsilon}_i-\bar{\varepsilon}\right),$ (66)

where $E_{cc}=\dfrac{\sigma_i^c-\sigma_{i+1}^c}{\bar{\varepsilon}_i-\bar{\varepsilon}_{i+1}}$. (67)

Concrete in Shear

The rational equation relating the shear stress of concrete (τ_{12}^{c}) and the shear strain (γ_{12}) in the $1\text{-}2$ coordinate system is given by

$$\tau_{12}^{c} = \frac{\sigma_1^c - \sigma_2^c}{2(\varepsilon_1 - \varepsilon_2)} \gamma_{12}, \tag{68}$$

where σ_1^c and σ_2^c are the smeared (average) concrete stresses and ε_1 and ε_2 are the biaxial smeared strains in the 1- and 2- directions of the principal applied stresses, respectively[155].

Constitutive model of steel plate

The constitutive model for mild steel used in steel plates is based on biaxial plasticity with Von Mises yield surface (Figure 221), associated flow and kinematic hardening[190]. The effective uniaxial stress strain relationship of the mild steel is assumed to be bilinear elastic followed by strain hardening, as shown in Figure 222.

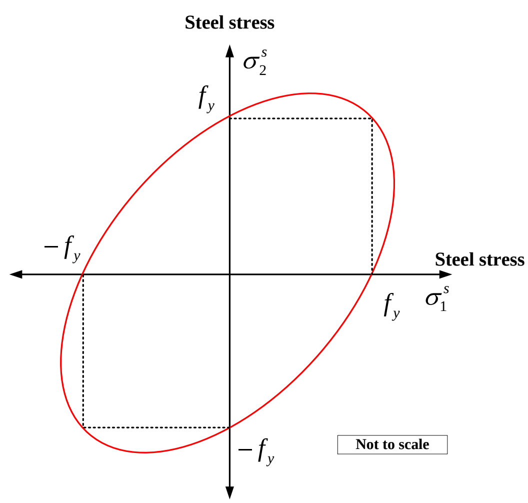

Figure 221. Von Mises yield surface for biaxial stress state [191]

To consider yielding of the steel plates under general biaxial stress conditions, the Von Mises criterion is used. Thus for steel with a uniaxial yielding strength f_y, the yielding criterion is given by:

$$(\sigma_1^s)^2 + (\sigma_2^s)^2 - \sigma_1^s \sigma_2^s = f_y^2, \tag{69}$$

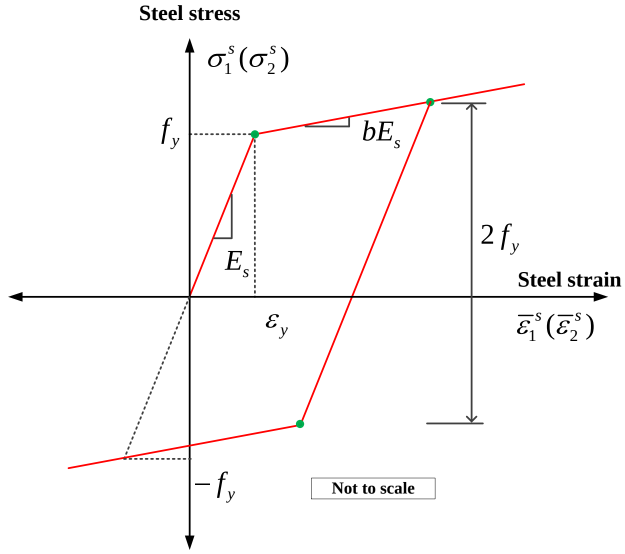

Figure 222. The effective uniaxial stress-strain curve of mild steel

5.4.2. Tangential Material Constitutive Matrix

The in-plane tangent material constitutive matrix $[\bar{D}]$ for a steel-plate concrete element is formulated as:

$$[\bar{D}] = \partial \begin{Bmatrix} \sigma_x \\ \sigma_y \\ \tau_{xy} \end{Bmatrix} \Big/ \partial \begin{Bmatrix} \varepsilon_x \\ \varepsilon_y \\ 0.5\gamma_{xy} \end{Bmatrix}, \tag{70}$$

$[\bar{D}]$ is evaluated by

$$[\bar{D}] = [T(-\theta_1)][\overline{D_c}][V_c][T(\theta_1)] + [T(-\theta_s)][\overline{D_s}][V_s][T(\theta_s)] \tag{71}$$

where $[\bar{D}_c]$ is the uniaxial tangential stiffness matrix of concrete and $[\bar{D}_s]$ is the uniaxial tangential stiffness of steel plates. The three matrices are evaluated as follows:

$$\left[\overline{D_c}\right]=\begin{bmatrix} \bar{E}_1^c & \partial\sigma_1^c/\partial\bar{\varepsilon}_2 & 0 \\ \partial\sigma_2^c/\partial\bar{\varepsilon}_1 & \bar{E}_2^c & 0 \\ 0 & 0 & G_{12}^c \end{bmatrix} \tag{72}$$

$$\left[\overline{D_s}\right]=\begin{bmatrix} \rho_s\bar{E}_s & 0 & 0 \\ 0 & \rho_s\bar{E}_s & 0 \\ 0 & 0 & \rho_s\bar{G}_s \end{bmatrix} \tag{73}$$

where $\bar{E}_1^c$ and $\bar{E}_2^c$ are the tangential uniaxial moduli of concrete in the 1 and 2 directions, respectively, evaluated at a certain stress/strain state. The off-diagonal terms $\partial\sigma_1^c/\partial\bar{\varepsilon}_2$ and $\partial\sigma_2^c/\partial\bar{\varepsilon}_1$ are obtained by using the uniaxial constitutive relationships and taking into account the state of the concrete stresses and uniaxial strains in the 1-2 directions, which are not zero because the stress and strain of the concrete in compression is softened by the orthogonal tensile strains. G_{12}^c is the shear modulus of concrete, taken as $\left(\sigma_2^c-\sigma_1^c\right)/\left(\varepsilon_2-\varepsilon_1\right)$. $\bar{E}_s$ and $\bar{G}_s$ are the uniaxial tangential modulus and shear tangential modulus for the steel plates. $\bar{G}_s$ is taken as $0.5\bar{E}_s/(1+v)$

.

5.4.3. Analysis Procedure

An iterative tangent stiffness procedure was developed to perform nonlinear analyses of SC structures using the CSMM element. An iterative analysis solution under a load increment using the Newton-Raphson method is used. Throughout the procedure, the tangent material constitutive matrix $[\bar{\mathrm{D}}]$ is determined first, and the tangent element stiffness matrix $[\mathrm{k}^e]$ and the element resisting force increment vector $\{\Delta f\}$ are calculated. Subsequently, the global stiffness matrix [K] and global resisting force increment vector $\{\Delta F\}$ are assembled. In each iteration the material constitutive matrix $[\bar{D}]$, the element tangent stiffness matrix $[k^e]$ and the global stiffness matrix [K] are iteratively refined until convergence criterion is achieved.

5.4.4. Implemented model in OpenSees

The CSMMLayerK01 is implemented into the OpenSees platform. The CSMMLayerK01 is related with SteelZ01, ConcreteZ01 and J2Plasticity to determine the tangent material constitutive matrix and calculate the stresses in the element at each layer. SteelZ01 and ConcreteZ01 are uniaxial material modules, implemented by Zhong[139]. J2Plasticity is an available ND material module in OpenSees. For each trial displacement increment in the analysis procedure, CSMMLayerK01 will receive the strains of the element and determine the uniaxial strains of the concrete and the biaxial strains of steel plates. Successively, these strains are sent to SteelZ01, ConcreteZ01 and J2Plasticity. For concrete, the CSMMLayerK01 will send the uniaxial strain and receive the tangent stiffness and uniaxial stress from the related uniaxial material objects. For steel plates, the CSMMLayerK01 will send the biaxial strain and receive the tangent stiffness and biaxial stress from the related biaxial material objects. After receiving the uniaxial stiffness and stresses of the concrete and steel plate, the tangent stiffness matrix will be evaluated and the stress vector will be calculated. An iterative procedure is defined to obtain the converged material constitutive matrix and stress vector for a given strain vector.

5.4.5. Validation of the Finite Element Model

The developed finite element program will be used for the analysis of SC and S-UHPC structures. The program will be verified by the results obtained from the experimental program.

Figure 223 compares the experimental results with the analytical results. It can be observed from the curves that the experimental data matches with the analytical results closely. However, the portion of the curve which corresponds to the yielding of the element does not match closely. This is due to the fact that the smeared yield strength of the steel plate is lower than the steel-plate material model implemented in OpenSees. Furthermore, it can be observed from the curves that the analytical model can accurately predict the elastic region and the peak shear stress and strain.

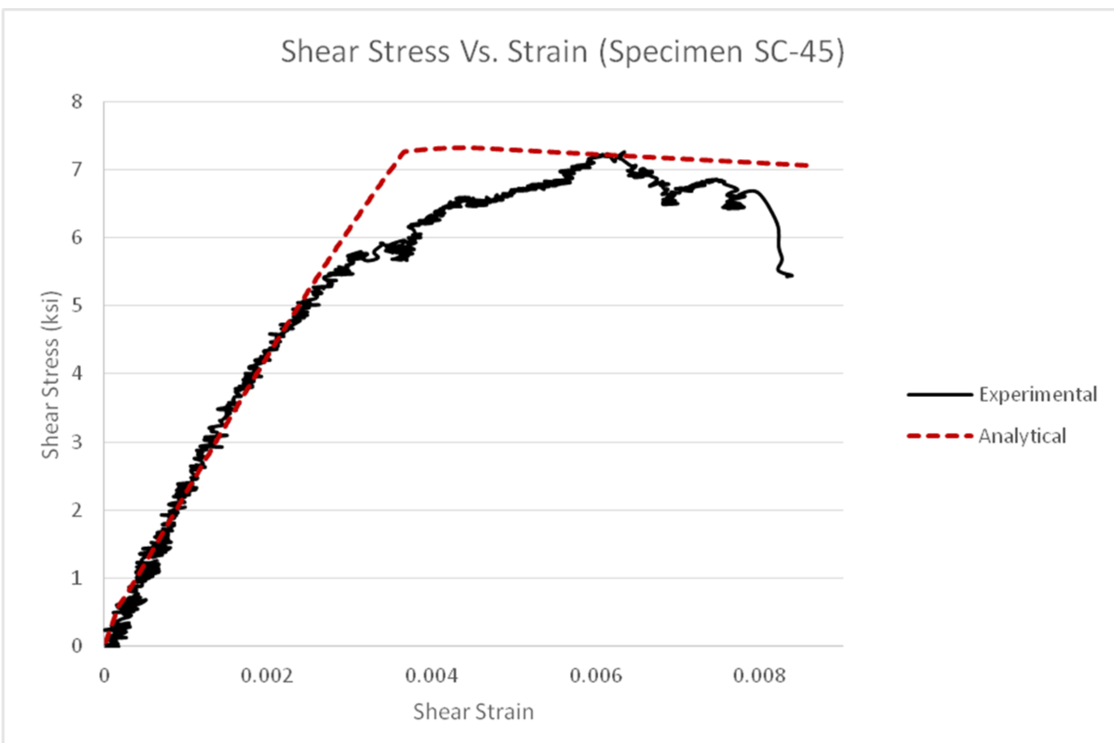

Figure 223. Experimental and analytical shear stress-strain curve for SC-45

Similarly, the compressive stress-strain and the tensile stress-strain experimental results were compared with the analytical results. The analytical results match closely with the experimental results as shown in Figure 224 and Figure 225.

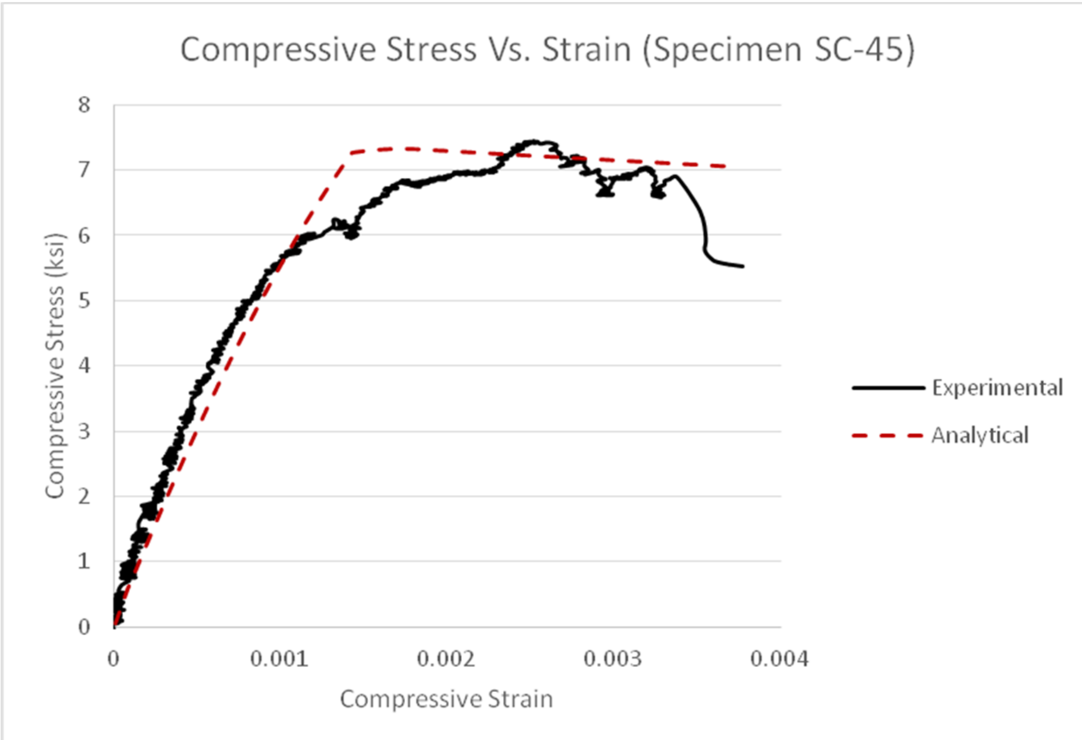

Figure 224. Experimental and analytical compressive stress-strain curve for SC-45

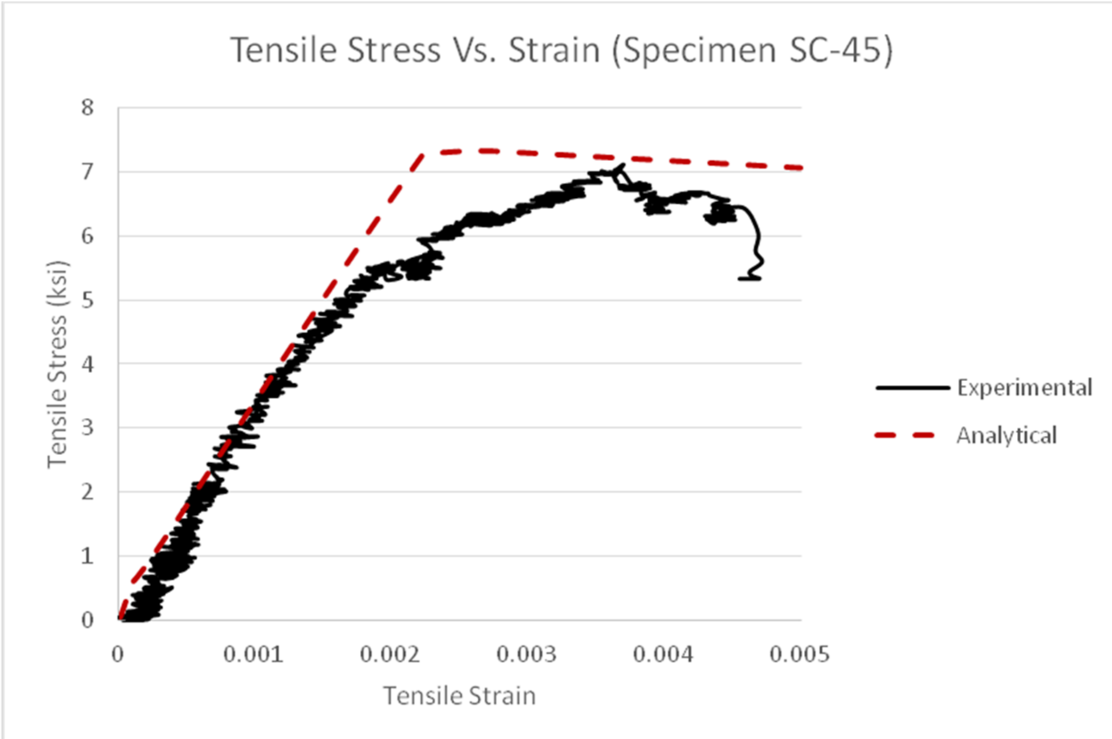

Figure 225. Experimental and analytical tensile stress-strain curve for SC-45

To compare the performance of the S-UHPC and SC wall panels, their analytical results are plotted and shown in Figure 226. From the curves, it can be observed that the performance of the S-UHPC is much higher than the SC due to the fact that the concrete strength in the S-UHPC wall panel is 22.23 ksi as opposed to 7.1 ksi in the case of the SC wall panel. As illustrated in Figure 226, the S-UHPC wall has higher stiffness and the peak shear stress is about 21% higher than that of the SC wall panel.

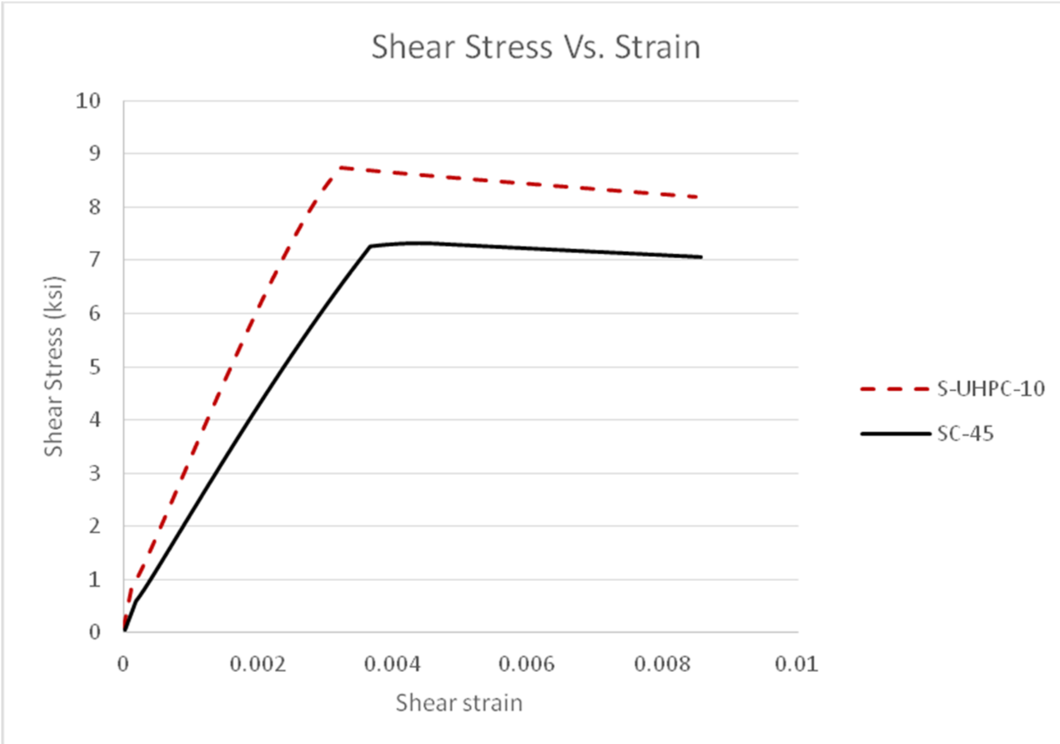

Figure 226. Comparison of S-UHPC and SC analytical results

5.5. Summary

The shear behavior of SC wall panels was understood by testing two SC (Steel-plate Concrete) wall panels using the Universal Panel Tester. The performance of SC and S-UHPC wall panels were compared. Based on the results, the S-UHPC wall panel had higher stiffness and increased shear carrying capacity than the SC wall panel. Furthermore, smart aggregates successfully captured the debonding between the steel-plates and concrete. In addition, the Digital Image Correlation (DIC) system measured the out-of-plane deformations in the steel plates.

Moreover, a nonlinear finite element program was developed to predict the behavior of the SC/S-UHPC wall panels. The developed finite element model was validated with the experimental results of the two SC walls. The analytical results matched the experimental results closely.

6. CONCLUSIONS

- Development of a new class of ultra-high performance concrete (UHPC) was achieved in this project. The material possesses a compressive strength of more than 22 ksi (150 MPa) with self-consolidating properties. This material is suitable for modular construction and can be mass produced by using a conventional concrete mixer and commercially available ingredients found in the United States.
- A microstructure study was carried out using X-ray micro-computed tomography (micro-CT) and a Scanning Electron Microscope. Three-dimensional morphological data on developed new UHPC material in comparison with regular conventional concrete was obtained. UHPC was found to have a significantly lower porosity and a discontinuous pore network. This gives a fundamental explanation with respect to the high strength and robust durability properties of UHPC compared with conventional concrete. Images taken by SEM gave proof of stronger hydration products on UHPC material with a larger amount and more solid structure of C-S-H layers compared to conventional mortar.
- Durability tests to evaluate the transport properties and dimension stability were performed on UHPC and normal concrete control specimens. These standardized tests include measurements on chloride diffusivity, water permeability, free and restrained shrinkage, alkali-silica reaction, accelerated corrosion and elevated temperature.
- UHPC possesses higher durability compared to conventional concrete in every experimental test, which include: significant lower chloride permeability and thermal conductivity, lower shrinkage and inactivity under exposure to alkaline environment. It also experiences significantly later corrosion failure compared to the control specimens under the accelerated corrosion test. An increase in compressive strength as high as 1.5

times its original strength was observed under elevated temperatures up to 300°C which is the normal operation temperature in a nuclear power plant, even though safety in the event of fire needs to be further studied. The improved durability observed in UHPC was due to a significant amount of pore reduction and high packing density of the material compared to normal concrete control specimens.

- The developed UHPC material was successfully used in the fabrication of SC modules. SC modules with cross ties were found to be one of the most efficient forms for constructing SC modules in terms of construction time, quality and cost. A thorough understanding of the flexural and shear behavior of the SC modules is critical to the success of the modular construction. This study investigated the structural performance of SC modules and identified the minimum amount of cross tie ratios in SC modules by experimentally testing a strip of the nuclear containment wall in out-of-plane shear.
- Based on the test results of specimens SC1 to SC6 for normal strength concrete and specimens S-UHPC-1 and S-UHPC-2 for ultra-high performance concrete, a minimum cross tie ratio for ductile shear failure is proposed. The proposed minimum amount of cross tie ratio for each of normal strength concrete and ultra-high performance concrete is described below.

For SC beams with normal strength concrete: $\boldsymbol{\rho_{t,min}}$=1.45*$\boldsymbol{\rho_{t,ACI}}$ for 2.0 < a/d < 4.0, or $\boldsymbol{\rho_{t,min}}$=1.25*$\boldsymbol{\rho_{t,ACI}}$ for a/d ≤ 2.0 and a/d ≥ 4.0.

For SC beams with Ultra-High Performance Concrete (UHPC): $\boldsymbol{\rho_{t,min}}$=1.10*$\boldsymbol{\rho_{t,ACI}}$ for a/d=2.5.

- An active sensing approach based on Smart Aggregates (SAs) is proposed to detect and monitor bond slip in SC beams. The initiation and development of bond slip in SC beams were captured successfully during the tests, which validated the applicability of the active sensing approach. This approach can provide early warning about the debonding of the steel plate and the concrete in SC beams before structural failure happens. Using the damage index, a quantitative study was conducted to compare the interfacial bond condition of SC beams equipped with different shear reinforcement ratios. Results show that cross ties can effectively improve the interfacial bond condition of SC beams and that cross ties as shear reinforcement can significantly improve ductility and shear strength of SC beams.

- Furthermore, a new material model was created to account for the bond-slip between the concrete and steel plate. The material model was incorporated in CSMM and implemented in OpenSees. A nonlinear finite element program was developed for the analysis of SC/S-UHPC structures based on the CSMM model. The developed finite element program was further validated by the experimental results of five SC and two S-UHPC beams. The analytical results show good agreement with the experimental data. The developed non-linear finite element program can provide researchers a powerful tool for the analysis of SC modules.
- The cylindrical wall in nuclear power plants is effective in resisting lateral loads originating from earthquake or wind. Because a large portion of the lateral shear forces are often assigned to such structures, it is important to understand their behavior under the predicted loads. The behavior of an element subjected to in-plane shear is characterized by shear stress vs. shear strain curve. An element subjected to pure shear does not fail immediately at the peak load but there exists a descending branch which indicates the ductility and energy absorption capacity of the element. The shear behavior of SC wall panels was

understood by testing two SC (Steel-plate Concrete) wall panels using the Universal Panel Tester. Based on the results, the S-UHPC wall panel had higher stiffness and increased shear carrying capacity than SC wall panel.

- Once again, smart aggregates successfully captured the debonding between steel-plates and concrete in SC/S-UHPC wall panels. In addition, the Digital Image Correlation (DIC) system was successful in measuring the out-of-plane deformations in the steel plates.
- Moreover, a nonlinear finite element program was developed to predict the behavior of the SC/S-UHPC wall panels. The developed finite element model was validated with the experimental results of two SC walls. The analytical results matched the experimental results closely.

7. REFERENCES

1. Okamura, H. and M. Ouchi, *Self-compacting concrete.* Journal of advanced concrete technology, 2003. **1**(1): p. 5-15.
2. Okamura, H., *Self-Compacting High Performance Concrete*, in *Concrete International*. 1997. p. 50-54.
3. Okamura, H. and M. Ouchi, *Self-compacting high performance concrete.* Progress in structural Engineering and Materials, 1998. **1**(4): p. 378-383.
4. Mehta, P.K. *High-Performance, High-Volume Fly Ash Concrete for Sustainable Development*. in *International Workshop on Sustainable Development and Concrete Technology*. 2004.
5. Mehta, P.K. and P.J. Monteiro, *Concrete: microstructure, properties, and materials*. Vol. 3. 2006: McGraw-Hill New York.
6. Graybeal, B., *Ultra-high performance concrete*. 2011.
7. de Larrard, F. and T. Sedran, *Optimization of ultra-high-performance concrete by the use of a packing model.* Cement and Concrete Research, 1994. **24**(6): p. 997-1009.
8. Nagaraj, T. and Z. Banu, *Generalization of Abrams' law.* Cement and Concrete Research, 1996. **26**(6): p. 933-942.
9. Rao, G.A., *Generalization of Abrams' law for cement mortars.* Cement and Concrete Research, 2001. **31**(3): p. 495-502.
10. ACI Committee 363, *State of the Art Report on High-Strength Concrete*, in *ACI Journal Proceedings*. 1984, ACI.
11. Yudenfreund, M., I. Odler, and S. Brunauer, *Hardened portland cement pastes of low porosity I. Materials and experimental methods.* Cement and Concrete Research, 1972. **2**(3): p. 313-330.
12. Yudenfreund, M., et al., *Hardened portland cement pastes of low porosity II. Exploratory studies. Dimensional changes.* Cement and Concrete Research, 1972. **2**(3): p. 331-348.
13. Roy, D.M., G.R. Gouda, and A. Bobrowsky, *Very High Strength Cement Pastes Prepared by Hot Pressing and Other High Pressure Techniques.* Cement and Concrete Research, 1972. **2**: p. 349-366.
14. Zadeh, D., A. Bahari, and F. Tirandaz. *Ultra-high performance concrete*. in *Excellence in Concrete Construction through Innovation: Proceedings of the conference held at the Kingston University, United Kingdom, 9-10 September 2008*. 2008. CRC Press.
15. Wille, K., A.E. Naaman, and G.J. Parra-Montesinos, *Ultra-high performance concrete with compressive strength exceeding 150 MPa (22 ksi): a simpler way.* ACI Materials Journal, 2011. **108**(1).
16. Wille, K., A.E. Naaman, and S. El-Tawll, *Optimizing ultra-high-performance fiber-reinforced concrete.* Concrete International, 2011. **33**(9).
17. Wille, K. and G.J. Parra-Montesinos, *Effect of beam size, casting method, and support conditions on flexural behavior of ultra-high-performance fiber-reinforced concrete.* ACI Materials Journal, 2012. **109**(3).
18. Schober, I. and U. Mader, *Selecting the optimum HRWR for SCC.* ACI Special Publication, 2006. **235**.
19. Dubey, R. and P. Kumar, *An experimental study for optimization of high range water reducing superplasticizer in self compacting concrete.* Frontiers of Structural and

Civil Engineering, 2013. **7**(1): p. 62-71.

20. Ganaw, A. and A. Ashour, *Rheological Properties of Mortars Prepared with Different Sands*. ACI Materials Journal, 2014. **111**(5).

21. Yahia, A., M. Tanimura, and Y. Shimoyama, *Rheological properties of highly flowable mortar containing limestone filler-effect of powder content and W/C ratio*. Cement and Concrete Research, 2005. **35**(3): p. 532-539.

22. Lange, D., et al., *Performance and acceptance of self-consolidating concrete: Final report*. 2008, Illinois Center for Transportation.

23. ACI Committee 237, *Self-Consolidating Concrete*. 2007, American Concrete Institute: Farmington Hills.

24. Larrard, F.D., *Ultrafine Particles for Making Very High Performance Concrete*, in *High Performance Concrete: from Material to Structure*. 1992, E & FN Spon: London. p. 34-47.

25. ASTM Standard C230, *Standard Specification for Flow Table for Use in Tests of Hydraulic Cement*. 2014, ASTM International: West Conshohocken, PA.

26. ASTM Standard C1611, *Standard Test Method for Slump Flow of Self-Consolidating Concrete*. 2014, ASTM International: West Conshohocken, PA.

27. ASTM Standard C617, *Standard Practice for Capping Cylindrical Concrete Specimens*. 2012, ASTM International: West Conshohocken, PA.

28. ASTM Standard C1231, *Standard Practice for Use of Unbonded Caps in Determination of Compressive Strength of Hardened Concrete Cylinders*. 2014, ASTM International: West Conshohocken, PA.

29. Stovall, T., F. De Larrard, and M. Buil, *Linear Packing Density Model of Grain Mixtures*. Powder Technology, 1986: p. 1-4.

30. Okamura, H., *Self-Compacting High-Performance Concrete*, in *Concrete International*. 1997. p. 50-54.

31. Su, N., K.-C. Hsu, and H.-W. Chai, *A Simple Mix Design Method for Self-Compacting Concrete*. Cement and Concrete Research, 2001. **31**: p. 1799-1807.

32. Domone, P.L., *Self-Compacting Concrete: An Analysis of 11 Years of Case Studies*. Cement and Concrete Composites, 2006. **28**: p. 197-208.

33. Brouwers, H.J.H. and H.J. Radix, *Self-Compacting Concrete: Theoritical and Experimental Study*. Cement and Concrete Research, 2005. **35**: p. 2116-2136.

34. Brouwers, H.J.H. and H.J. Radix. *Self-Compacting Concrete: the Role of the Particle Size Distribution*. in *First International Symposium on Design, Performance and Use of Self-Consolidating Concrete*. 2005. Changsha, Hunan, China.

35. Funk, J.E. and D. Dinger, *Perdictive Process Control of Crowded Particulate Suspensions: Applied to Ceramic Manufacturing*. 1928, Norwell: Kluwer Academic Publishers.

36. *Elkem Materials Mixture Analyzer*. 2014.

37. Tue, N.V., et al. *Influence of addition method of superplasticizer on the properties of fresh UHPC*. in *Second International Symposium on Ultra High Performance Concrete*. 2008.

38. EFNARC, *Specification and guidelines for self-compacting concrete*. 2002, European Federation of National Associations Representing for Concrete: UK. p. 32.

39. ASTM Standard C1621, *Standard Test Method for Passing Ability of Self-Consolidating Concrete by J-Ring*. 2014, ASTM International: West Conshohocken, PA.

40. ASTM Standard C231, *Standard Test Method for Air Content of Freshly Mixed Concrete by the Pressure Method*. 2014, ASTM International: West Conshohocken, PA.

41. *Computed tomography (CT) scans and cancer*. 2013, National Cancer Institute.

42. Hodge, A.C., et al., *Prostate boundary segmentation from ultrasound images using 2D active shape models: Optimisation and extension to 3D.* Computer Methods and Programs in Biomedicine, 2006. **84**(2-3): p. 99-113.

43. Landis, E.N. and D.T. Keane, *Tutorial review: X-ray microtomography.* Materials Characterization, 2010. **61**: p. 1305-1316.

44. Flannery, B.P., et al., *Three-dimensional x-ray microtomography.* Science, 1987. **237**(4821): p. 1439-1444.

45. Bentz, D.P., et al., *The visible cement data set.* Journal of Research of the National Institute of Standards and Technology, 2002. **107**(2): p. 137-148.

46. Galucci, E., et al., *3D experimental investigation of the microstructure of cement pastes using synchrotron X-ray microtomography* Cement and Concrete Research, 2006. **37**: p. 360-368.

47. Fan, S. and M. Li, *X-ray computed microtomography of three-dimensional microcracks and self-healing in engineered cementitious composites.* Smart Materials and Structures, 2015. **24**(1): p. 1-14.

48. Gastaldi, D., et al., *In situ tomographic investigation on the early hydration behaviors of cementing systems.* Construction and Building Materials, 2012. **29**: p. 284-290.

49. Brooks, R.A., *A quantitative theory of the hounsfield unit and its application to dual enery scanning.* Journal of Computer Assisted Tomography, 1977. **1**(4): p. 487-493.

50. Chang, S.G., B. Yu, and M. Vetterli, *Adaptive wavelet thresholding for image denoising and compression.* IEEE Transactions on Image Processing, 2000. **9**(9): p. 1532-1546.

51. Bentz, D.P., et al., *X-ray microtomography of an ASTM C109 mortar exposed to sulfate attack.* MRD Proceedings, 1994. **370**(1): p. 77-82.

52. Otsu, N., *A threshold selection method from gray-level histogram.* IEEE Transactions on Systems, Man, and Cybernetics, 1979. **SMC-9**(1): p. 62-66.

53. Ashby, M.F. and C.G. Sammis, *The damage mechanics of brittle solids in compression.* Pageoph, 1990. **133**(3): p. 489-521.

54. Liu, D.M., *Influence of porosity and pore size on the compressive strength of porous hydroxyapatite ceramic.* Ceramics International, 1997. **23**: p. 135-139.

55. Goldstein, J.I., et al., *Scanning electron microscopy and X-ray microanalysis. A text for biologists, materials scientists, and geologists*. 1981: Plenum Publishing Corporation.

56. Stutzman, P.E., *Scanning electron microscopy in concrete petrography.* National Institute of Standards and Technology, 2001. **2**.

57. *durability*. 2015, Merriam-Webster.com.

58. Hiller, K., *Strength reduction and length changes in porous glass caused by water vapor adsorption.* Journal of Applied Physics, 1964. **35**(5): p. 1622-1628.

59. Claisse, P.A., *Transport Properties of Concrete: Measurements and Applications*. 2014: Elsevier.

60. Stanish, K., R. Hooton, and M. Thomas, *Testing the chloride penetration resistance of concrete: a literature review.* Dep. Of Civil Eng., University of Toronto, 1997.

61. AASHTO T259, *Standard Method of Test for Resistance of Concrete to Chloride Ion Penetration*, in *Standard Specifications for Transportation Materials and Methods of Sampling and Testing*. 2000: Washington, DC.

62. ASTM Standard C1543, *Standard Test Method for Determining the Penetration of Chloride Ion into Concrete by Ponding*. 2010, ASTM International: West Conshohocken, PA.

63. ASTM Standard C1152, *Standard Test Method for Acid-Soluble Chloride in Mortar and Concrete*. 2012, ASTM International: West Conshohocken, PA.

64. Gailius, A. and M. Kosior-Kazberuk, *Monitoring of concrete resistance to chloride penetration.* Materials science, 2008. **14**(4): p. 350-355.

65. Lane, D.S., R.J. Detwiler, and R.D. Hooton, *Testing Transport Properties in Concrete.* Concrete international, 2010. **3**(11): p. 33-38.

66. ASTM Standard C1202, *Standard Test Method for Electrical Indication of Concrete's Ability to Resist Chloride Ion Penetration*. 2012, ASTM International: West Conshohocken, PA.

67. Nokken, M.R. and R.D. Hooton. *Development of early-age impermeability in high-performance concretes*. in *PCI Bridge Conference*. 2003. Orlando: PCI.

68. Whiting, D., *Rapid determination of the chloride permeability of concrete.* Final Report Portland Cement Association, Skokie, IL. Construction Technology Labs., 1981. **1**.

69. Yang, C.-C., *On the relationship between pore structure and chloride diffusivity from accelerated chloride migration test in cement-based materials.* Cement and Concrete Research, 2006. **36**(7): p. 1304-1311.

70. Joshi, P. and C. Chan, *Rapid chloride permeability testing.* Concrete Construction, 2002. **47**(12): p. 37-43.

71. Graybeal, B.A., *Material property characterization of ultra-high performance concrete*. 2006.

72. Graybeal, B. and J. Tanesi, *Durability of an ultra high-performance concrete.* Journal of materials in civil engineering, 2007. **19**(10): p. 848-854.

73. ASTM Standard C192, *Standard Practice for Making and Curing Concrete Test Specimens in the Laboratory*. 2013, ASTM International: West Conshohocken, PA.

74. Adámek, J., et al., *Three NDT Methods for the Assessment of the Concrete Permeability as a Measure of Durability*, in *Nondestructive Testing of Materials and Structures*. 2013, Springer. p. 293-302.

75. Germann Instruments, I., ,, *GWT-4000 Instruction and Maintenance Manual.* 2013.

76. Maroliya, M.M., *Estimation of Water Sorptivity as Durability Index for Ultra High Strength Reactive Powder Concrete.* International Journal of Engineering Research and Development, 2012. **4**(3): p. 53-56.

77. Aly, T. and J. Sanjayan, *Effect of Pore-Size Distribution on Shrinkage of Concretes.* Journal of Materials in Civil Engineering, 2010. **22**(5): p. 525-532.

78. Tazawa, E.-i., S. Miyazawa, and T. Kasai, *Chemical shrinkage and autogenous shrinkage of hydrating cement paste.* Cement and concrete research, 1995. **25**(2): p. 288-292.

79. ASTM Standard C157, *Standard Test Method for Length Change of Hardened Hydraulic-Cement Mortar and Concrete*. 2008, ASTM International: West Conshohocken, PA.

80. ASTM Standard C490, *Standard Test Method for Use of Apparatus for the Determination of Length Change of Hardened Cement Paste, Mortar, and Concrete*. 2011, ASTM International: West Conshohocken, PA.

81. Greenspan, L., *Humidity fixed points of binary saturated aqueous solutions.* Journal of Research of the National Bureau of Standards, 1977. **81**(1): p. 89-96.

82. Winston, P.W. and D.H. Bates, *Saturated solutions for the control of humidity in biological research.* Ecology, 1960: p. 232-237.

83. Wexler, A. and S. Hasegawa, *Relative humidity-temperature relationships of some saturated salt solutions in the temperature range 0 to 50 C.* Journal of Research of the National Bureau of Standards, 1954. **53**(1): p. 19-26.

84. ACI Committee 209, *Prediction of creep, shrinkage and temperature effects in concrete structures.* ACI Manual of Concrete Practice, 1997.

85. Branson, D.E. and M. Christiason, *Time Dependent Concrete Properties Related To Design-Strength and Elastic Properties, Creep, and Shrinkage.* ACI Special Publication, 1971. **27**.

86. Meyers, B., et al., *The Prediction of Creep and Shrinkage Properties of Concrete.* Iowa Highway Commission Final Report, 1970(70-5): p. 1-140.

87. AASHTO T334-08, *Standard Method of Test for Estimating the Cracking Tendency of Concrete*, in *Standard Specifications for Transportation Materials and Methods of Sampling and Testing*. 2012: Washington, DC.

88. Folliard, K.J., M.D. Thomas, and K.E. Kurtis, *Guidelines for the use of lithium to mitigate or prevent ASR*. 2003.

89. ASTM Standard C150, *Standard Specification for Portland Cement*. 2012, ASTM International: West Conshohocken, PA.

90. Wang, H. and J. Gillott, *Mechanism of alkali-silica reaction and the significance of calcium hydroxide.* Cement and Concrete Research, 1991. **21**(4): p. 647-654.

91. ASTM Standard C1260, *Standard Test Method for Potential Alkali Reactivity of Aggregates (Mortar-Bar Method)*. 2014, ASTM International: West Conshohocken, PA.

92. Ferraro, C.C., *Report of Investigation of 78 stone for the use as coarse aggregate in prestressed concrete*. 2005.

93. Hussain, S.E., *Corrosion resistance performance of fly ash blended cement concrete.* ACI Materials Journal, 1994. **91**(3).

94. Sahmaran, M., V.C. Li, and C. Andrade, *Corrosion resistance performance of steel-reinforced engineered cementitious composite beams.* ACI Materials Journal, 2008. **105**(3).

95. Fillmore, D., *Literature Review of the Effects of Radiation and Temperature on the Aging of Concrete*. 2004: United States. Department of Energy.

96. Hilsdorf, H., J. Kropp, and H. Koch. *The effects of nuclear radiation on the mechanical properties of concrete*. in *Proc. Douglas McHenry Int. Symp. on Concrete and Concrete Structures, ACI-SP, American Concrete Institute*. 1978.

97. Naus, D.J., *The Effect of Elevated Temperature on Concrete Materials and Structures-a Literature Review*. 2006, Oak Ridge National Laboratory (ORNL).

98. Xotta, G., et al., *Composite behavior of concrete materials under high temperatures.* International Journal of Solids and Structures, 2015. **64**: p. 86-99.

99. Copier, W., *The spalling of normal weight and lightweight concrete exposed to fire.* ACI Special Publication, 1983. **80**.

100. Bazant, Z.P. and M.F. Kaplan, *Concrete at high temperatures: material properties and mathematical models*. 1996: Longman Group Limited.

101. Schneider, U., *Concrete at high temperatures—a general review.* Fire safety journal, 1988. **13**(1): p. 55-68.

102. Bamonte, P. and P.G. Gambarova, *A study on the mechanical properties of self-compacting concrete at high temperature and after cooling.* Materials and structures, 2012. **45**(9): p. 1375-1387.

103. Khaliq, W. and V. Kodur, *Thermal and mechanical properties of fiber reinforced high performance self-consolidating concrete at elevated temperatures.* Cement and Concrete Research, 2011. **41**(11): p. 1112-1122.

104. Husem, M., *The Effects of High Temperature on Compressive and Flexural Strengths of Ordinary and High-Performance Concrete.* Fire Safety Journal, 2006. **41**(2): p. 155-163.

105. Sanchayan, S., N. Gowripalan, and S. Foster, *Mechanical properties of fibre reinforced reactive powder concrete after exposure to high temperatures.* 2013.

106. Sriskandarajah, S., *High Temperature Behaviour of Reactive Powder Concrete (RPC)*, in *School of CIvil and Environmental Engineering*. 2014, The University of New South Wales.

107. Bhat, P.S., V. Chang, and M. Li, *Effect of elevated temperature on strain-hardening engineered cementitious composites.* Construction and Building Materials, 2014. **69**: p. 370-380.

108. Bhat, P., *Cementitious Materials with Ultra-High Damage Tolerance for Hazards Mitigation*, in *Department of Civil and Environmental Engineering*. 2015, University of Houston.

109. Kodur, V.K.R. and M.A. Sultan, *Effect of Temperature on Thermal Properties of High-Strength Concrete.* Journal of Materials in Civil Engineering, 2003. **15**(2): p. 101-107.

110. Kodur, V. and W. Khaliq, *Effect of temperature on thermal properties of different types of high-strength concrete.* Journal of materials in civil engineering, 2010. **23**(6): p. 793-801.

111. Zanni, H., et al., *Investigation of hydration and pozzolanic reaction in reactive powder concrete (RPC) using 29 Si NMR.* Cement and Concrete Research, 1996. **26**(1): p. 93-100.

112. Cheyrezy, M., V. Maret, and L. Frouin, *Microstructural analysis of RPC (reactive powder concrete).* Cement and Concrete Research, 1995. **25**(7): p. 1491-1500.

113. Vodak, F., et al., *Thermophysical properties of concrete for nuclear-safety related structures.* Cement and concrete research, 1997. **27**(3): p. 415-426.

114. Sung, Y.-L., et al., *Fabricating optical lenses by inkjet printing and heat-assisted in situ curing of polydimethylsiloxane for smartphone microscopy.* Journal of biomedical optics, 2015. **20**(4): p. 047005-047005.

115. Xie, M., N. Foundoukos, and J. Chapman, *Static tests on steel–concrete–steel sandwich beams.* Journal of Constructional Steel Research, 2007. **63**(6): p. 735-750.

116. Subedi, N., *Double skin steel/concrete composite beam elements: experimental testing.* Structural Engineer, 2003. **81**(21): p. 30-35.

117. ACI Committee 349, *Code Requirements for Nuclear Safety-related Concrete structures: (ACI 349-06) and Commentary*. 2006, American Concrete Institute.:

Farmington Hills, Michigan.

118. ACI Committee 318, *Building Code Requirements for Structural Concrete (ACI 318-11) and Commentary*. 2005, American Concrete Institute: Farmington Hills, Michigan.

119. Varma, A.H., K. C. Sener, K. Zhang, K. Coogler and S. R. Malushte, *Out-of-plane Shear Behavior of SC Composite Structures.* International Association for Structural Mechanics in Reactor Technology 21, 2011.

120. Kani, G., *The Riddle of Shear Failure and Its Solution.* ACI Journal, 1964. **61**(4): p. 441-467.

121. Hsu, T.T., A. Laskar, and Y. Mo, *Shear Strengths of Prestressed Concrete Beams Part 2: Comparisons with ACI and AASHTO Provisions.* ACI structural Journal, 2010. **107**(3).

122. Laskar, A., T.T.C. Hsu, and Y.L. Mo, *Shear Strengths of Prestressed Concrete Beams Part 1: Experiments and Shear Design Equations."* ACI structural Journal, , 2010. **107**(3): p. 330-339.

123. ASTM Standard A572, *Standard Specification for High-strength Low-alloy Columbium-vanadium Structural Steel (A572/A572M-13a)*. 2014, ASTM: West Conshohocken, Pennsylvania.

124. Kuo, W.W., T.T.C. Hsu, and S.J. Hwang, *Shear Strength of Reinforced Concrete Beams.* ACI Structural Journal, 2014. **111**(4): p. 809-818.

125. Xu, B., T. Zhang, G. Song and H. Gu, *Active Interface Debonding Detection of a Concrete-filled Steel Tube with Piezoelectric Technologies using Wavelet Packet Analysis.* Mechanical Systems and Signal Processing, 2013. **36**: p. 7-17.

126. Feng, M.Q., F. De Flaviis, and Y.J. Kim, *Use of microwaves for damage detection of fiber reinforced polymer-wrapped concrete structures."* Journal of Engineering Mechanics, , 2002. **128**(2): p. 172-183.

127. *Non-Destructive Testing of Concrete Based on Analysis of Velocity Dispersion of Laser Ultrasonics*. 2006, ECNDT.

128. Yu, T.Y. and O. Buyukozturk, *A far-field airborne radar NDT technique for detecting debonding in GFRP-retrofitted concrete structures."* NDT & E International, 2008. **41**: p. 10-24.

129. Cheng, C.C., Y.T. Ke, and K.T. Hsu, *Using Lamb Waves to Evaluate Debonding of Steel Plate Strengthened Concrete.* Materials Transactions, 2012. **53**(2): p. 274-278.

130. Song, G., H. Gu, and Y.L. Mo, *Smart Aggregates: Multi-functional Sensors for Concrete Structures-a Tutorial and a Review."* Smart Materials and Structures,, 2008. **17**(3): p. 1-17.

131. Yan, S., et al., *Health monitoring of reinforced concrete shear walls using smart aggregates.* Smart Materials and Structures, , 2009. **18**(4): p. 1-6.

132. Wu, F. and F.K. Chang, *Debond Detection using Embedded Piezoelectric Elements in Reinforced Concrete Structures-Part I: Experiment.* Structural Health Monitoring, 2006. **5**(1): p. 5-15.

133. Kim, C.H., et al., *A Study of Fabrications of Steel Plate Concrete (SC) Modular Systems for Nuclear Power Plants*. 2007: Pyeongchang, Korea.

134. Yan, S., et al., *PZT-based Detection on Compactness of Concrete in Concrete Filled Steel Tube Using Time Reversal Method."* Mathematical Problems in Engineering 2014. **DOI: 10.1155/2014/909682**: p. 1-11.

135. Hou, Z., M. Noori, and R.S. Amand, *Wavelet-based approach for structural*

damage detection." ,. Journal of Engineering Mechanics, 2000. **126**(7): p. 677-683.

136. Samuel, P.D. and D.J. Pines, *Classifying Helicopter Gearbox Faults Using a Normalized Energy Metric.* Smart Materials and Structures, 2001. **10**(1): p. 145-153.

137. Song, G., et al., *Concrete Structural Health Monitoring using Embedded Piezoceramic Transducers."* Smart Materials and Structures, 2007. **16**(4): p. 959-968.

138. Ferguson, P.M. and A.P. Clark, *Diagonal Tension in Reinforced Concrete.* ACI Journal, 1951. **48**(2): p. 156-1 to 156-3.

139. Zhong, J., *Model-Based Simulation of Reinforced Concrete Plane Stress Structures*. 2005, Houston

140. Hsu, T.T.C. and Y.L. Mo, *Unified Theory of Concrete Structures*. 2010, Houston: John Wiley & Sons, Ltd.

141. Belarbi, A. and T.T.C. Hsu, *Constitutive Laws of Softened Concrete in Biaxial Tension-Compression.* ACI Structural Journal, 1995. **92**(5): p. 563-573.

142. Pang, X.B. and T.T.C. Hsu, *Behavior of Reinforced Concrete Membrane Elements in Shear.* Structural Journal of the American Concrete Institute, 1995. **92**(6): p. 665-679.

143. Pang, X.B. and T.T.C. Hsu, *Fixed-Angle Softened-Truss Model for Reinforced Concrete.* Structural Journal of the American Concrete Institute, 1996. **93**(2): p. 197-207.

144. Hsu, T.T.C. and L.X. Zhang, *Nonlinear Analysis of Membrane Elements by Fixed-Angle Softened-Truss Model.* Structural Journal of the American Concrete Institute, 1997. **94**(5): p. 483-492.

145. *Softened Membrane Model for Reinforced Concrete Elements in Shear,.* Structural Journal of the American Concrete Institute, 2002. **99**(4): p. 460-469.

146. Mansour, M. and T.T.C. Hsu, *Behavior of Reinforced Concrete Elements under Cyclic Shear: Part 1 – Experiments.* Journal of Structural Engineering, ASCE, 2005. **131**(1): p. 44-53.

147. Mansour, M. and T.T.C. Hsu, *Behavior of Reinforced Concrete Elements under Cyclic Shear: Part 2 - Theoretical Model.* Journal of Structural Engineering, ASCE, 2005. **131**(1): p. 54-65.

148. Fenves, G.L., *Annual Workshop on Open System for Earthquake Engineering Simulation*. 2001, Pacific Earthquake Engineering Research Center, UC Berkeley: Berkeley.

149. Hsu, T.T.C. and R.R.H. Zhu, *Softened Membrane Model for Reinforced Concrete Elements in Shear,.* Structural Journal of the American Concrete Institute, 2002. **99**(4): p. 460-469.

150. *Behavior of Reinforced Concrete Membrane Elements in Shear.* Structural Journal of the American Concrete Institute, 1995. **92**(6): p. 665-679.

151. Vecchio, F.J. and M.P. Collins, *Stress-Strain Characteristic of Reinforced Concrete in Pure Shear*. 1981, IABSE Colloquium, Advanced Mechanics of Reinforced Concrete, International Association of Bridge and Structural Engin: Delft.

152. Vecchio, F.J. and M.P. Collins, *Response of Reinforced Concrete to In Plane Shear and Normal Stresses*. 1982, University of Toronto, : Toronto, Canada.

153. Zhu, R.H., T.T.C. Hsu, and J.Y. Lee, *Rational Shear Modulus for Smeared Crack Analysis of Reinforced Concrete* Structural Journal of the American Concrete Institute, 2001. **98**(4): p. 443-450.

154. Zhu, R.R.H., *Softened-Membrane Model for Cracked Reinforced Concrete*

Considering Poisson Effect. 2000, PhD dissertation, Dept. of Civil and Environmental Engineering, University of Houston: Houston, TX.

155. Zhu, R.R.H. and T.T.C. Hsu, *Poisson Effect of Reinforced Concrete Membrane Elements.* Structural Journal of the American Concrete Institute, 2002. **99**(5): p. 631-640.

156. Mansour, M., J.Y. Lee, and T.T.C. Hsu, *Constitutive Laws of Concrete and Steel Bars in Membrane Elements under Cyclic Loading.* Journal of Structural Engineering, ASCE, 2001. **127**(12): p. 1402-1411.

157. *Behavior of Reinforced Concrete Membrane Elements under Cyclic Shear: Experiments to Theory*. 2001, PhD dissertation, Department of Civil Engineering, University of Houston: Houston, TX.

158. Belarbi, A. and T.T.C. Hsu, *Constitutive Laws of Concrete in Tension and Reinforcing Bars Stiffened by Concrete.* Structural Journal of the American Concrete Institute, 1994. **91**(4): p. 465-474.

159. Mo, Y.L., J. Zhong, and T.T.C. Hsu, *Seismic Simulation of RC Wall-type Structures.* Engineering Structures, 2008. **30**(11): p. 3167-3175.

160. Schulz, T.L., *Westinghouse AP1000 Advanced Passive Plant.* Nuclear Engineering and Design, 2006. **236**(14–16): p. 1547-1557.

161. Oesterle, R.G. and H.G. Russell, *Research Status and Needs for Shear Tests on Large-scale Reinforced Concrete Containment Elements.* Nuclear Engineering and Design, 1982. **69**(2): p. 187-194.

162. Walther, H.P., *Evaluation of Behavior and the Radial Shear Strength of a Reinforced Concrete Containment Structure*. 1990, University of Illinois: Urbana-Champaign, Champaign.

163. Hsu, T.T.C., A. Belarbi, and X. Pang, *A Universal Panel Tester.* Journal of testing and evaluation, 1995. **23**(1): p. 41-49.

164. Hsu, T.T.C., L.-X. Zhang, and T. Gomez, *A Servo-Control System for the Universal Panel Tester.* Journal of Testing and Evaluation, 1995. **23**(6): p. 424-430.

165. *A Servo-Control System for the Universal Panel Tester.* Journal of Testing and Evaluation, 1995. **23**(6): p. 424-430.

166. Rastogi, P. and E. Hack, *Optical Methods for Solid Mechanics: A Full-Field Approach*. 2012: John Wiley & Sons.

167. Choi, S. and S.P. Shah, *Measurement of Deformations on Concrete Subjected to Compression Using Image Correlation.* Experimental Mechanics, 1997. **27**(3): p. 307-313.

168. Ghrib, F., et al., *A Novel Technique for Displacement Measurements in RC Beams using Digital Image Correlation.* ACI Special Publication, 2014. **298**: p. 1-16.

169. Fard, M.Y., Y. Liu, and A. Chattopadhyay, *Characterization of Epoxy Resin Including Strain Rate Effects Using Digital Image Correlation System.* Journal of Aerospace Engineering,, 2012. **25**: p. 308-319.

170. Pan, B., et al., *Two-dimensional Digital Image Correlation for In-plane Displacement and Strain Measurement: A Review.* Measurement Science and Technology, 2009. **20**(6): p. 1-17.

171. Giachetti, A., *Matching Techniques to Compute Image Motion.* Image and Vision Computing, 2000. **18**(3): p. 247-260.

172. Tong, W., *An Evaluation of Digital Image Correlation Criteria for Strain Mapping Applications.* Strain, 2005. **41**(4): p. 167-175.

173. Pan, B., et al., *Two-dimensional Digital Image Correlation for In-plane*

Displacement and Strain Measurement: A Review. Measurement Science and Technology, 2009. **20**: p. 1-17.

174. Giachetti, A., *Matching Techniques to Compute Image Motion.* Image and Vision Computing, 2000. **18**: p. 247-260.

175. Tong, W., *An Evaluation of Digital Image Correlation Criteria for Strain Mapping Applications.* Strain, 2005. **41**: p. 167-175.

176. Pan, B., et al., *Full-field Strain Measurement using a Two-dimensional Savitzky-Golay Digital Differentiator in Digital Image Correlation.* Optical Engineering, 2007. **46**: p. 033601-1-033601-10.

177. Pan, B., et al., *Digital Image Correlation using Iterative Least Squares and Pointwise Least Squares for Displacement Field and Strain Measurements.* Optics and Lasers in Engineering, 2009. **47**: p. 865-874.

178. Pan, B., *Recent Progress in Digital Image Correlation.* Experimental Mechanics, 2011. **51**: p. 1223-1235.

179. Pan, B. and K. Li, *A Fast Digital Image Correlation Method for Deformation Measurement.* Optics and Lasers in Engineering, 2011. **49**: p. 841-847.

180. Bing, P., et al., *Performance of sub-pixel registration algorithms in digital image correlation.* Measurement Science and Technology, 2006. **17**(6): p. 1615.

181. Sutton, M.A., J.J. Orteu, and H.W. Schreier, *Image Correlation for Shape, Motion and Deformation Measurements*. 2009, New York: Springer.

182. Luo, P.-F., et al., *Accurate Measurement of Three-Dimensional Displacement in Deformable Bodies using Computer Vision.* Experimental Mechanics, 1993. **33**.

183. Luo, P.F., Y.J. Chao, and M.A. Sutton, *Application of Stereo Vision to Three-Dimensional Deformation Analyses in Fracture Experiments.* Optical Engineering, 1994. **33**: p. 981-990.

184. Pan, B., et al., *Accurate Measurement of Satellite Antenna Surface Using 3D Digital Image Correlation Technique.* Strain, vol., 2009. **45**: p. 194-200.

185. Berfield, T.A., et al., *Micro and Nanoscale Deformation Measurement of Surface and Internal Planes via Digital Image Correlation,"* Experimental Mechanics, vol. , 2007. **47**: p. 51-62.

186. Schreier, H.W. and M.A. Sutton, *Systematic Errors in Digital Image Correlation due to Undermatched Subset Shape Functions.* Experimental Mechanics, 2002. **42**: p. 303-310.

187. Lu, H. and P.D. Cary, *Deformation Measurements by Digital Image Correlation: Implementation of a Second-order Displacement Gradient.* Experimental Mechanics, 2000. **40**: p. 393-400.

188. Schreier, H.W., J.R. Braasch, and M.A. Sutton, *Systematic Errors in Digital Image Correlation Caused by Intensity Interpolation.* Optical Engineering, , 2000. **39**: p. 2915-2921.

189. Knauss, W.G., I. Chasiotis, and Y. Huang, *Mechanical Measurements at the Micron and Nanometer Scales.* Mechanics of Materials, 2003. **35**: p. 217-231.

190. Boresi, A.P., *Advanced Mechanics of Materials:* . 1993: John Wiley & Sons, Inc.

191. Chen, W.F. and D.J. Han, *Plasticity for Structural Engineers:* . 2007: J. Ross Publishing.